Forschungszentrum Karlsruhe

in der Helmholtz-Gemeinschaft

Wissenschaftliche Berichte

FZKA 6677

Comparison Report on the Blind Phase of the OECD International Standard Problem No. 45 Exercise (QUENCH-06)

W. Hering, Ch. Homann, J.-S. Lamy*

Institut für Reaktorsicherheit
Programm Nukleare Sicherheitsforschung

*delegate from EDF, France

Forschungszentrum Karlsruhe GmbH, Karlsruhe
2002

Impressum der Print-Ausgabe:

Als Manuskript gedruckt

Forschungszentrum Karlsruhe GmbH
Postfach 3640, 76021 Karlsruhe

Mitglied der Hermann von Helmholtz-Gemeinschaft
Deutscher Forschungszentren (HGF)

ISSN 0947-8620

Abstract

The International Standard Problem (ISP) No. 45 is part of the overall ISP program of the OECD/NEA and is dedicated to the behavior of heat-up and delayed reflood of fuel elements in nuclear reactors. ISP-45 is related to the out-of-pile bundle quench experiment QUENCH-06, performed at Forschungszentrum Karlsruhe (FZK), Germany, on December 13, 2000. Special attention was paid to hydrogen production.

To assess the ability of severe accident codes to simulate processes during core heat-up and reflood at temperatures above 2000 K, the behavior of the bundle during the whole experiment should be calculated on the basis of experimental initial and boundary conditions, but without knowing further experimental details (blind phase). In the blind phase 21 participants from 15 nations contributed with 8 different code systems (ATHLET-CD, ICARE/CATHARE, IMPACT/SAMPSON, GENFLO, MAAP, MELCOR, SCDAPSIM, SCDAP-3D).

After the end of the blind phase all measured data were made available and the participants were invited to deliver a second calculation, where this knowledge could be used (open phase). In this report, results of the blind calculations are presented, analyzed, and compared to experimental data. Additionally, post-test calculations using the in-house version SCDAP/RELAP5 mod3.2.irs are used for comparison.

During heat-up most results do not deviate significantly from one another, except as a consequence of some obvious user errors, so that a definition of a mainstream is justified. During quenching the lack of adequate hydraulic modeling becomes obvious: some participants could not match the observed cool-down rates, others had to use a very fine mesh to compensate code deficiencies. To overcome this insufficiency some newly developed reflood models were used in MAAP and MELCOR.

In QUENCH-06, the sufficiently thick oxide layers protected the cladding from melting and failure below 2200 K, so that no massive hydrogen release during reflood was found. This behavior could be simulated by most of the codes if no artificial shattering options were used. With respect to hydrogen production the mainstream shows a spreading of +/- 15 % prior to reflood initiation and a range of +/- 40 % after reflood. However, a group of SCDAPSIM users activated an extreme shattering option, which overestimates the produced hydrogen mass by a factor of 5. In the mainstream, most of the codes predict correctly that no bundle damage occurred, whereas others calculate slight material relocations, mainly due to overestimation of the cladding temperatures.

However, detailed inspection showed that the codes still have difficulties to predict correctly the bundle conditions prior to reflood. Another surprising aspect was that the energy balance has to be checked prior to further interpretation of the results. Lacking user experience to analyze such problems and to model them adequately was a main reason for larger deviations.

Vergleich der Ergebnisse der blinden Phase des Internationalen Standard Problems Nr. 45 der OECD (QUENCH-06)

Zusammenfassung

Das Internationale Standard Problem (ISP) No. 45 ist Teil des ISP Programms der OECD/NEA und zielt auf die Untersuchung des Kernverhaltens in Kernkraftwerken beim Aufheizen und verzögertem Fluten mit Wasser. ISP-45 wurde als Versuch No. 6 am 13. Dezember 2000 in der out-of-pile Versuchsanlage QUENCH im Forschungszentrum Karlsruhe durchgeführt. Ein wesentliches Ziel ist die Untersuchung der Wasserstoffquellterms beim Fluten.

Um den derzeitigen Stand der Kernschmelzcodes in Bezug auf Simulation der Kernaufheizung und schnellen Abkühlung durch Wasser (quench) adäquat beurteilen zu können, wurden nur die notwendigsten Anfangs- und Randbedingungen für die Rechnungen vorgegeben (Blinde Phase).

In der blinden Phase des ISP-45 nahmen 8 Code-Systeme teil (ATHLET-CD, ICARE/-CATHARE, IMPACT/SAMPSON, GENFLO, MAAP, MELCOR, SCDAPSIM, SCDAP-3D). Die Ergebnisse der Blind-Rechnungen der 21 Teilnehmer aus 15 Staaten werden mit den experimentellen Ergebnissen und den Resultaten der Nachrechnung mit SCDAP/RELAP5 mod3.2.irs verglichen. Während der Aufheizphase weichen die meisten Ergebnisse nur geringfügig voneinander, wobei offensichtliche Benutzer-Fehler ausgeklammert wurden. Dies rechtfertigt die Definition eines sogenannten „Hauptfeldes“. Während der Quench-Phase divergieren die Ergebnisse jedoch signifikant, was zum Teil auf eine unzureichende Modellierung der Thermohydraulik zurückzuführen ist. Um dieses Defizit zu umgehen, wurden neue Modelle in MAAP und MELCOR entwickelt und eingesetzt.

Im Versuch QUENCH-06, der eine Maximaltemperatur von ca. 2200 K erreichte, verhinderte eine ausreichend dicke Oxydschicht ein frühzeitiges Versagen der Hüllrohre und damit die Freisetzung von metallischer Schmelze. Daher ist die zusätzliche Wasserstofffreisetzung gering, sie kann mit den normalen Oxidationsmodellen weitgehend beschrieben werden. Im „Hauptfeld“ erhöhte sich die Streuung der freigesetzten H_2 – Masse von ca. +/- 15 % vor dem Fluten auf ca. +/- 40 % nach dem Test. Verschiedene Teilnehmer überschätzten jedoch deutlich den zusätzlichen H_2-Quellterm durch Einsatz eines sog. „Shattering models“, das künstlich die protektive Oxydschicht entfernt. Auch wurden Schmelzeverlagerungen und Debris-Bildung berechnet.

Eine detaillierte Untersuchung zeigte auch, dass die Codes noch Probleme mit der korrekten Berechnung des Bündelzustandes vor dem Fluten haben. Ein anderer überraschender Aspekt ist, dass die Energiebilanz sorgfältig überprüft werden muss, bevor man an die Interpretation der Ergebnisse gehen kann. Fehlende Erfahrung der Codebenutzer sowie Schwierigkeiten bei der Simulation der QUENCH-Anlage waren weitere Ursachen für die beobachtete Streuung der Ergebnisse.

Table of Contents

List of Figures

List of Tables

List of Abbreviations

AMM	Accident management measures
BDBA	Beyond Design Basis Accident
CSNI	Committee on the Safety of Nuclear Installations
CNSNS	Commission of Nuclear Safety and Safeguards, Mexico
CORA	Out-of-pile severe fuel damage tests performed at FZK, 1984-1992, http://hikwww4.fzk.de/irs/organisation/IRS1/CORA01.html
DBA	Design Basis Accident
DC	Direct current
DMX	Demultiplexed data format used for RELAP5
ECC	Emergency core cooling
ENEA	Ente per le Nuove Tecnologie l'Energia el'Ambiente, Italy
FZK	Forschungszentrum Karlsruhe, Technik und Umwelt, http://www.fzk.de/FZK2
GRS	Gesellschaft für Anlagen und Reaktorsicherheit, Germany
HR	Heater rod
IMF	Institut für Materialforschung, http://hbksun17.fzk.de:8080/imf/imf0.html
INEEL	Idaho National Engineering and Environmental Laboratory, Idaho Falls, USA, formerly INEL
INL	Token for INEEL
IRS	Institut für Reaktorsicherheit, http://hikwww4.fzk.de/irs/
ISP	International standard problem of the OECD/NEA
LOCA	Loss Of Coolant Accident
LOFT	Loss Of Fluid Test (Idaho National Engineering Laboratory, Idaho Falls, USA)
LWR	Light Water Reactor
NEA	Nuclear Energy Agency of the OECD: http://www.nea.fr , Issy les Moulineaux, France
NUKLEAR	Programm Nukleare Sicherheitsforschung at FZK
NUPEC	Nuclear Power Engineering Company, Tokyo, Japan
NSI	Nuclear Safety Institute, Moscow, Russia
n/a	not available
OECD	Organisation for Economic Cooperation and Development: http://www.oecd.org
op.	option
PCT	Peak core temperature
PSF	Projekt Sicherheitsforschung, predecessor of Programm Nuklear at FZK
PWR	Pressurized Water Reactor
QUENCH	Research programme at FZK, focused on investigations on material behavior during LWR reflood conditions: http://imf1-wt-server.fzk.de/quench/
RELAP5	old: Reactor Excursions and Leak Analysis Program, presently: Reactor Leak and Analysis Program, for LWR transients and SBLOCA

RMBK	Light Water Graphite Reactor (Russian abbreviation)
SBLOCA	Small break LOCA
SCD	Severe Core Damage
SCDAP	Severe Core Damage Analysis Package, (USNRC code, developed at INEEL)
SCDAP/RELAP5:	Coupled SCDAP and RELAP5 code to simulate reactor conditions up to SFD conditions
SFD	Severe Fuel Damage
t.b.d	to be defined
TC	Thermocouple
USNRC	United States Nuclear Regulatory Commission, http://www.nrc.gov

(Remark: URL-Addresses valid January 2002)

TOKENS

CMX	Commission of Nuclear Safety and Safeguards, Mexico City, Mexico
DMM	Dept. of Mechanical, Nuclear and Production Engineering, University of Pisa, Italy
DRS	CEA/DRS / IPSN, Cadarache France
EDF	Electricité de France, Clamart, France
ENE	Ente per le Nuove Tecnologie l'Energia el'Ambiente, Italy
FRA	Framatome-ANP, Paris, France
GRS	Gesellschaft für Anlagen- und Reaktorsicherheit, Garching, Germany
IJS	Institute Joséf Stephan, Ljubljana, Slovenia
INL	Idaho National Engineering and Environmental Laboratory, Idaho Falls, USA
ISS	Innovative Software Systems, Idaho Falls, USA
NEH	Nuclear Engineering University of Hacettepe, Turkey
NK(1,2,3)	NSI of RCC Kurchatov Institute, Moscow, Russia
NUP	Nuclear Power Engineering Company, Tokyo, Japan
REZ	Token for Nuclear Research Institute, Prague, CZ
RUB	Ruhr University Bochum, Department for Energy Systems and Energy Economics, Bochum, Germany
SES	Studsvik Eco & Safety , Nyköping, Sweden
SIE	Framatome-ANP Erlangen, formerly Siemens Nuclear Power, Erlangen, Germany
SNL	Sandia National Laboratories, Albuquerque, USA
UZA	University of Zagreb, Croatia
VTT	VTT ENERGY, Finland

DEFINITION OF TERMS

injection rate	mass flow rate delivered by the quench pump to the quench pipe in QUENCH facility
fast water injection	pressure driven water injection into the steam injection line to fill empty volumes and pipes
flooding rate	average rise of the water level in the test section: $\dot{Z} \approx \frac{\dot{m}(z)}{\rho \bullet A_{bundle}}$
cool-down rate	average rate of temperature decrease before the "quench point"
quench point	temperature and time of sharp change in cool-down rate due to partial wetting of the TC or cladding, breakdown of stable film boiling.
quench rate	fast cool-down of structures due to effective convective heat transfer (transition or nucleate boiling)
quench profile	axial distribution of quench times
LM501	pressure difference measurement across the whole test section. Under stationary conditions it can be transferred into a collapsed water level.
TFS	high temperature thermocouple mounted on cladding surface
TSH	high temperature thermocouple mounted on shroud outer surface
TCRC	TC in the center boring of the unheated fuel rod

Executive summary

In spite of great efforts in determining the hydrogen release, when the overheated core of a nuclear reactor is flooded with water as part of an accident management measure (AMM), knowledge is still too limited to predict this source term sufficiently well with computer programs. The International Standard Problem No. 45 (ISP-45) of the OECD/NEA is initiated to extend the database for such situations, in particular to identify key phenomena and to encourage an extended code validation so that the accuracy and reliability of the codes can be assessed. ISP-45 is based on the out-of-pile experiment QUENCH-06 performed at Forschungszentrum Karlsruhe, Germany, on December 13, 2000.

The main objective of QUENCH-06 is to investigate fuel rod bundle behavior up to and during reflood/quench conditions without severe fuel rod damage prior to reflood initiation. The main objective of the ISP-45 is to assess the reliability and accuracy of severe accident codes during quench phase.

In particular, in the QUENCH-06 experiment the conditions of a Design Basis Accident (DBA) plus an additional failure, leading to a delayed activation of the emergency core cooling (ECC) system, were investigated up to total reflood of the heated section of the bundle, starting with conditions representative for normal reactor operation. A pre-oxidation phase was used to establish a reactor specific oxide layer thickness of up to 250 µm. In the following transient phase electrical heating plus oxidation drove maximum cladding temperature to app. 2100 K. Increasing that temperature level prior to reflood would cause dissolution of the pellets by liquid Zr with subsequent melt relocation, hence conditions as simulated in QUENCH-02 and QUENCH -03 /3/, and in the previous ISP-31 (CORA-13) /12/.

Under the present conditions no severe bundle damage could happen. Water reflood was initiated, and most of the measured temperatures dropped nearly immediately to 400 K due to fast steam cooling caused by water evaporation. At reflood initiation fuel rod clad failure and slightly afterwards shroud failure were detected. About 250 s after reflood initiation the temperatures up to the level of the off-gas pipe decreased to saturation. Prior to reflood app. 31 g of hydrogen were produced and during reflood app. 4.6 g.

The fuel rod bundle remained intact even for temperatures as high as app. 2200 K /7/. This is mainly due to the fast reflood process and the limited axial extension of the hot zone. After the test the bundle remained intact as specified in the report on post-test analyses /7/.

The task of ISP-45 consisted in blind calculations of the whole test on the basis of general data of the facility like geometry, and of the specific experimental initial and boundary conditions, but further experimental data or results were not transmitted to the participants before these blind calculations were finished. Generally, it was a difficult task for most of the participants to simulate adequately the non-reactor specific features of the QUENCH facility; however, this is prerequisite for a sufficient code-to-data comparison, as was seen in previous ISPs (e.g. ISP-31, ISP-36, both at FZK).

ISP-45 started in October 2000 with the preparatory workshop at FZK, the blind exercise lasted from end of January 2001 up to the end of June 2001, and the Comparison Workshop was held at December 10-12, 2001. In total 21 participants from 15 nations used the detailed mechanistic codes ATHLET-CD, GENFLO, ICARE/CATHARE, IMPACT/SAMPSON, SCDAP-3D, and SCDAPSIM and the integral codes MAAP and MELCOR. Additionally, FZK posttest analyses were performed with an in-house version of SCDAP/RELAP5 mod3.2, which includes also the new reflood model of PSI /14/ plus FZK improvements /15/. About 400 variables were requested for the comparison; the most informative of them were used for this report, others were requested to facilitate our interpretation of the results. Based on this data global as well as detailed comparisons were performed.

Nearly all participants calculated the thermal-hydraulic conditions prior to reflood fairly well, except those who had difficulties in simulating the axial power distribution in the heater rods or to model the radiative heat transfer in the annular gap between shroud and cooling jacket in the upper electrode zone.

However, even without any calculated bundle damage, the calculated axial oxide layer thickness varied by a factor of app. 100 %. Evaluation of the delivered data shows that even at the end of the pre-oxidation phase, where a quasi steady state is reached in the bundle, the energy balance seems not to be fulfilled in each of the calculations. Some participants managed a fairly well energy balance: others fail, even with the same code version. As a consequence the energy balance of the different code systems should be checked carefully to identify the reasons of the observed variation by a factor of 3 compared to experimental values and post-test analyses.

As derived from the data, the simulation of the reflood phase is still weak. Several codes have no dedicated reflood models, others have models, which are not yet validated sufficiently on the basis of design DBA reflood experiments. That lack of knowledge leads to a wide scatter of results. Under these very transient conditions the individual models as well as their interplay between the models are still not sufficiently reliable.

Only from the calculation of the reflood water level, three groups of results can be distinguished:

- No significant rise in water level during reflood (possibly error in code usage or mass error in water balance),
- Strong deviation from expected flooding behavior, and
- Satisfactory match of maximum water level, but not of time for filling the whole test section.

Only the results of the latter group, which vary within 100 s, are discussed. Compared to the whole flooding time of app. 300 s, this error band amounts to 33 %. Final water level varies between 0.7 m and 1.4 m.

Prior to reflood initiation, 8 participants delivered results for the total hydrogen mass in the range of ± 15 % around the experimental value. This range spreads to ± 40 % after reflood mainly due to differences in modeling of the thermal-hydraulics conditions. Other participants might have used either inappropriate models or used shattering options in a

way that too much protective oxide scales are simulated to be removed and thus very high hydrogen releases are calculated.

A small group of participants calculated ballooning with subsequent clad failure early in the pre-oxidation phase and one participant calculated fuel rod damage and blockage formations during reflood phase.

In this way, the present lack of knowledge and hence the deficiencies in modeling become obvious, even in this experiment without significant bundle damage. As mentioned before, thermal-hydraulics of reflood processes still causes difficulties for several codes. Here modeling should take credit from best-estimated tools used in design basis accident analyses.

With respect to fuel rod behavior, a cautious statement of the ISP-45 together with other tests such as QUENCH-01 etc. is that if sufficient thick oxide layer have been formed on the metal, the fuel rods can withstand reflood situations with temperatures up to 2200 K. In such cases only a small amount of additional hydrogen is released. This can be simulated by most of the codes if no artificial shattering options are used. In case of melt release, the conditions are quite different and relevant experiments have shown significant hydrogen release during reflood. However, for these conditions a thermal-hydraulic model based on porous debris seems to be preferable, but this topic is outside the present investigations.

Based on the results of the blind phase it can be concluded, that the codes are able, excluding lacking user experience, to simulate roughly the reflood process of an intact fuel rod bundle, but in most cases not in the quality as required for DBA or licensing purposes. Hence, a wider code qualification plus code improvement with respect to reflood / quench simulation and transient oxidation of metallic melts should be recommended.

1 INTRODUCTION

An International Standard Problem (ISP) is defined as a broad comparison between experimental and analytical results derived from various computer codes. Especially in the field of beyond design basis accidents (BDBA), the reliability of code prediction has to be assessed for predictions of different phases of an accident and, moreover, for consequences occurring after operator interactions such as valve and/or emergency core cooling activation.

In the past Forschungszentrum Karlsruhe, Technik und Umwelt (FZK) has contributed several times to OECD/NEA international standard problems dedicated to fuel rod bundle behavior under various conditions. Two of them were devoted to reflood problems, namely the fuel rod bundle test in the REBEKA facility (ISP-14) and the PWR test in the CORA-facility (CORA-13, ISP-31). The experiment CORA-W2, ISP-36, was devoted to core degradation of a VVER type fuel rod bundle. The fourth one was a test on melt-concrete interaction, performed in the BETA facility (BETA V5.1, ISP-30).

The present international standard problem, ISP-45, is based on the out-of-pile experiment QUENCH-06 performed at Forschungszentrum Karlsruhe, Germany, on December 13, 2000. The main objective of this experiment is to investigate fuel rod bundle behavior up to and during reflood/quench conditions without severe fuel rod damage prior to reflood initiation. In particular the conditions of a Design Basis Accident (DBA) plus an additional failure, leading to a delayed activation of ECC, were investigated up to total reflood of the bundle, starting with conditions representative for normal reactor operation.

The task of ISP-45 consisted in blind calculations of the whole test on the basis of general data of the facility like geometry, and of the specific experimental initial and boundary conditions, but further experimental data or results were not transmitted to the participants before these calculations were finished.

The results delivered by the participants were checked and the global data were presented in a draft overview /9/ data which was sent to all participants in August 2001 (Table 1.1). Some participants could not deliver all results in time due to serious reasons, which were accepted after a brief check before the release of the experimental data. All participants were invited to perform open calculations and to present their results at ISP-45 Comparison workshop. In doing that they were asked to deliver a list of modifications as well as global results for comparison. Some participants sent us comments and error corrections after the release of that draft overview. Such comments are listed in the appendix; the original text and figures have not been changed.

The general intention of this report is to present all results delivered by the participants and to compare most significant data to allow each participant to check and validate his code, his input model, and the parameters he used for the blind phase calculations.

It is a pleasure that we could realize our intention to keep as many participants as possible within the exercise. Finally 21 participants from 15 nations delivered their results (section 3). Together with posttest analyses based on SCDAP/ RELAP5 mod 3.2.irs

(S/R5irs) calculations at Forschungszentrum Karlsruhe (FZK) and the experimental results this sums up to 23. During ISP-45 some delays occurred which are listed in Table 1.1.

Table 1.1 Initial and actual time schedule for the ISP-45

Initial time frame	Schedule / Meeting	Final time frame
Oct 13, 2000	Preparatory workshop: Definition of procedure, time schedule, participants, deliverable input (FZK) and results of calculations (participants).	
End of Oct.	Official confirmation of participation to OECD	Mid of Nov.
End Nov	**QUENCH-06 test conduct at FZK**	**Dec 13, 00**
End Jan 2001	Delivery of the experimental data by FZK to OECD:	End Jan 01
	plus: updated **ISP-45 Specification report** due to unexpected experimental conditions	April 01
May 2001	Delivery of calculated results by the participants to FZK Last contribution received	June 22, 01 July 2, 01
	Draft overview of global data delivered by FZK	**August 1st 01**
End Sep 2001	Delivery of FZK's preliminary comparison report to OECD	Nov 12 2001
	Delivery of the list of modifications for blind/open phase comparison to FZK	Nov 26 2001
Oct 18-19, 01	ISP-45 Comparison workshop at FZK	Dec 10-11, 01
Oct 16-18, 01	7th International QUENCH workshop at FZK	Dec 12-14, 01
Feb 2002	Final workshop together with informal ISP-46 meeting in Petten, NL	March 18, 2002

2 THE EXPERIMENT QUENCH-06

2.1 Description of the test facility

For the description of the ISP conditions the QUENCH facility can be split into two sections: the facility with all external devices and the test section itself. The overall description of the QUENCH facility is documented in several FZK Reports describing the commissioning tests /1/, experiment QUENCH-01 /2/, and the two experiments QUENCH-02 and QUENCH-03 /3/. In this report some additional information is given, including errata concerning the reports above mentioned. Some of this information is added for the sake of completeness, but not absolutely necessary for this ISP. The schematics shown in Figure 2.3 give an overview of flow paths, entrance and boundary conditions.

2.1.1 Inlet Section

The geometry of the bundle inlet is presented in Figure 2.1. The inlet pipe has an inner diameter of 0.054 m and a total length of 0.905 m between the valve and the wall of the lower plenum. The axial position of the inlet pipe centerline is at –0.412 m. The lower plenum has an inner diameter of 0.1053 m and contains a tube (outer diameter 0.0889 m, wall thickness 0.0025 m) with a number of holes to get a reasonable flow velocity profile in the bundle.

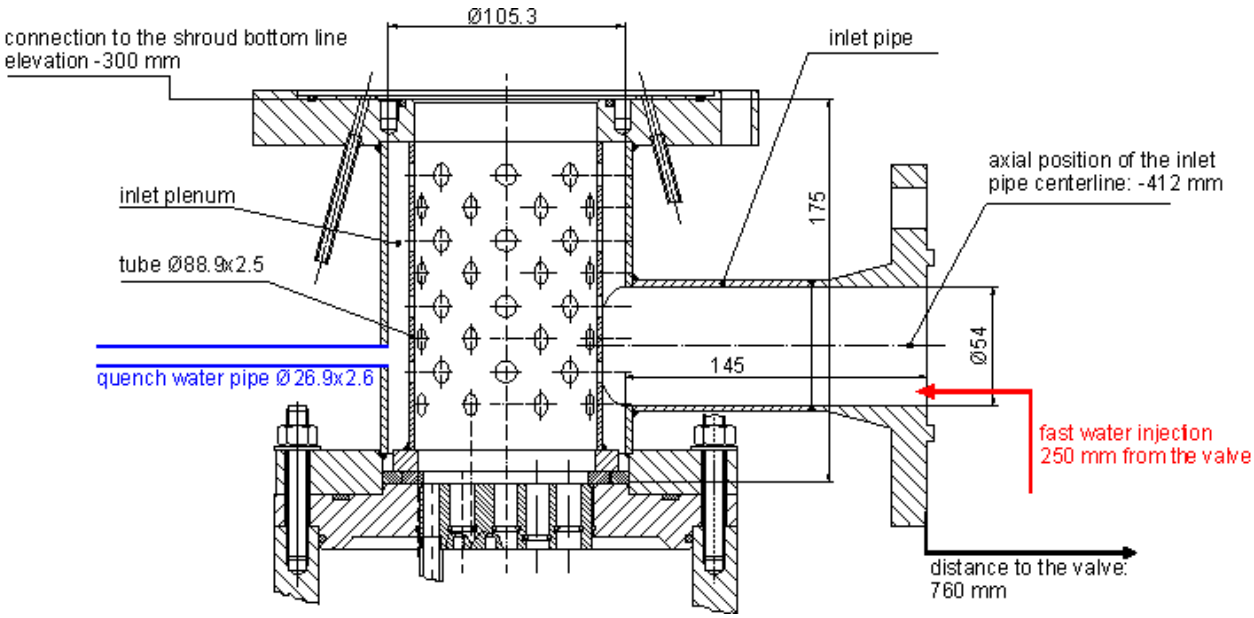

Figure 2.1 Detailed schematics of the lower plenum with fluid inlet pipe, fast water injection system (right), and quench water pipe (left).

During the post-test analyses of QUENCH-06 the comparison between measured data and those obtained by post-test calculations with SCDAP/RELAP5 mod 3.2.irs revealed some inconsistencies with respect to the reflood initiation. An unexpected time delay was found between calculated water level and that deduced from measured temperatures and differential pressure. To identify the origin of this delay, the lower plenum (Figure 2.1), the inlet pipes and the fast water injection system were included in much more finer in the existing detailed SCDAP/RELAP5 (Figure 2.2). After a series of calcu-

lations with the extended model and a profound comparison with assessed experimental data, the reason for the delay was identified.

Due to an unexpected leakage of a check-valve at the quench pump the quench inlet pipe must have drained out partially. Consequently, the mass flow rate in Figure 2.11 is only relevant at the position of the quench pump, where it is measured, and not at the entrance into the lower plenum, where it is needed. As a consequence, the fast quench water injection system had to fill up the lower plenum plus some parts of the quench water pipe. Together with water evaporation due to hot walls we could find out the observed delay. Based on the experimental data and the various S/R5 calculations the mass flow rate could be specified (section 2.3.2).

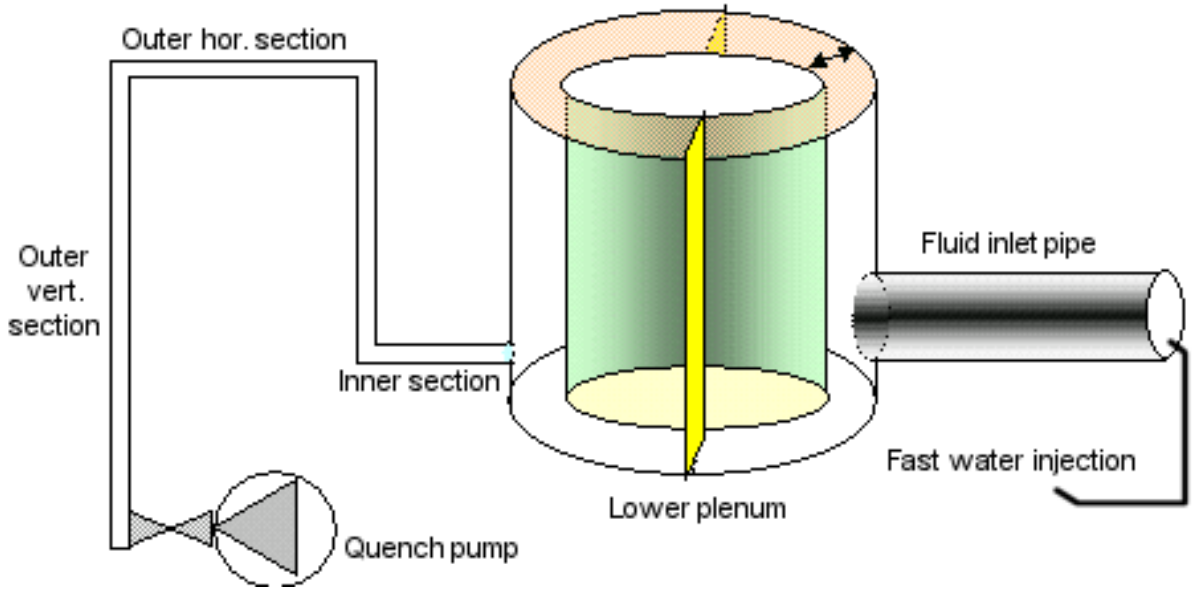

Figure 2.2 Detailed schematics of the inlet volumes including coaxial lower plenum with fluid inlet pipe, fast water injection system (right), and quench water pipe with realistic elevation changes (left).

2.1.2 Bundle Test Section

In radial direction the QUENCH fuel rod bundle (Figure 2.3 center) is composed of an unheated rod (Figure 2.5 left side) at center position, an inner ring of eight heater rods (Figure 2.5 right side) connected to one electric power supply, an outer ring of 12 heater rods connected to a second power supply system, and a set of four corner rods at the vacant rod positions of the bundle.

The 21 fuel rod simulators are filled with a mixture of 95 vol% argon and 5 vol% krypton at a pressure slightly above fluid pressure in the bundle and connected to a compensating volume at room temperature. More information on the internal structure of the heater rods as well as the unheated rod are given in /1/, /2/, and /3/. Details of the electric heating systems are summarized in /4/.

The bundle is enclosed in the shroud (Figure 2.4), which is composed of the Zircaloy liner (2.38 mm thick), a ZrO_2 fiber insulation and the inner cooling jacket, made of stainless steel. The thickness of the ZrO_2 fiber insulation was changed from 0.035 m in

QUENCH-01 (/2/, Fig. 6) to 0.037 m for all subsequent tests. Bottom of the insulation is located at –0.3 m. Location of the upper end of the insulation is at +1.024 m.

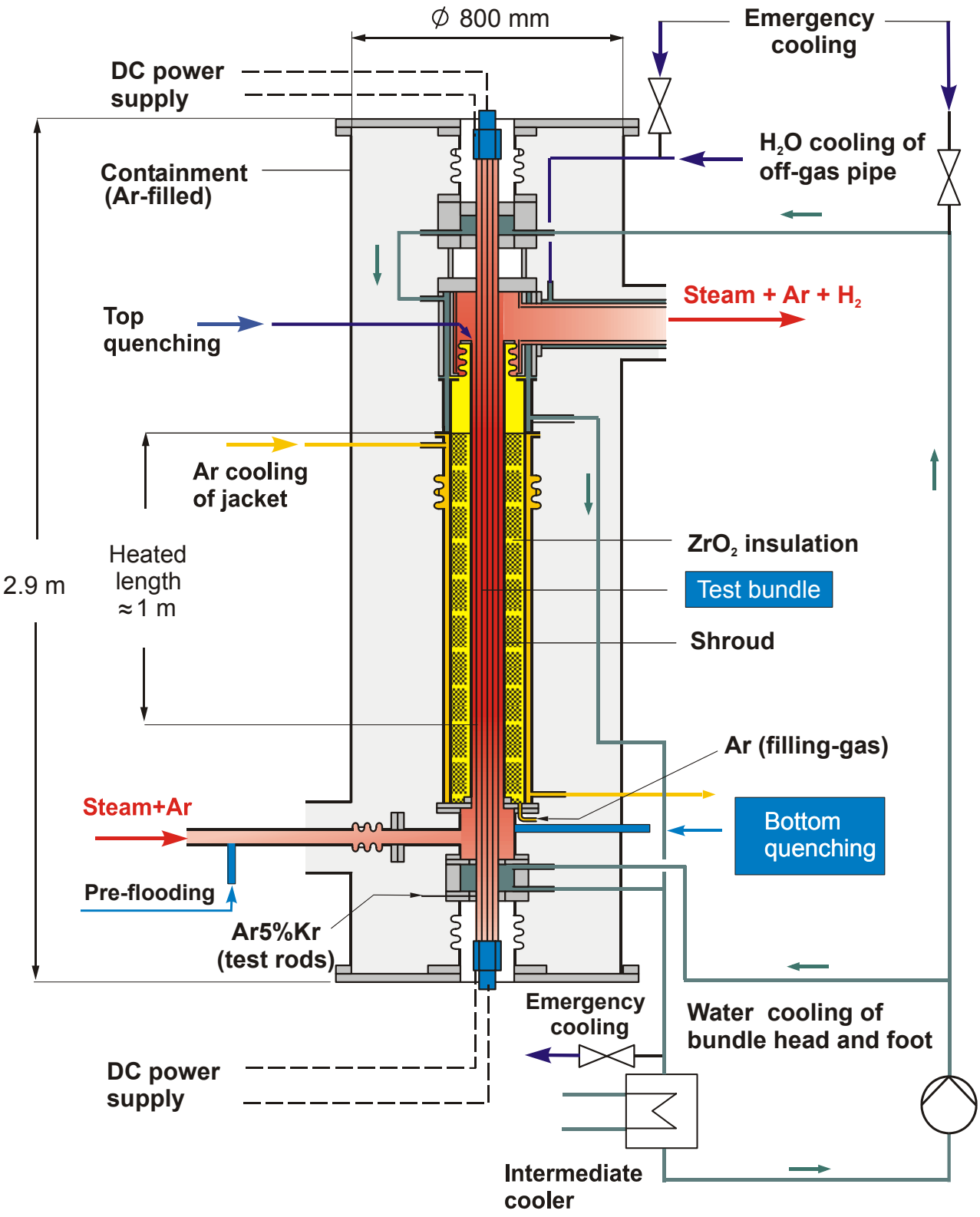

Figure 2.3 QUENCH flow paths: test section with fuel rod bundle, shroud, cooling jacket (argon and water), fill gas for the fuel rods, gas and quench fluid entrance conditions, and water cooling at the axial ends of the heater wires.

Properties and characteristics of the insulation provided by the manufacturer are taken from /6/. The region between the shroud and the inner cooling jacket, i. e. the ZrO_2 fiber insulation and the empty space above this insulation are flooded with argon before the test, the pressure being about 2 bar. In the fiber insulation convection may be inhibited due to the friction losses. In the empty space above, the main contribution of the radial heat losses is due to radiation, but natural convection may contribute to a certain extend. However, no information is available whether this argon remains stagnant during the whole test or whether a natural convection develops.

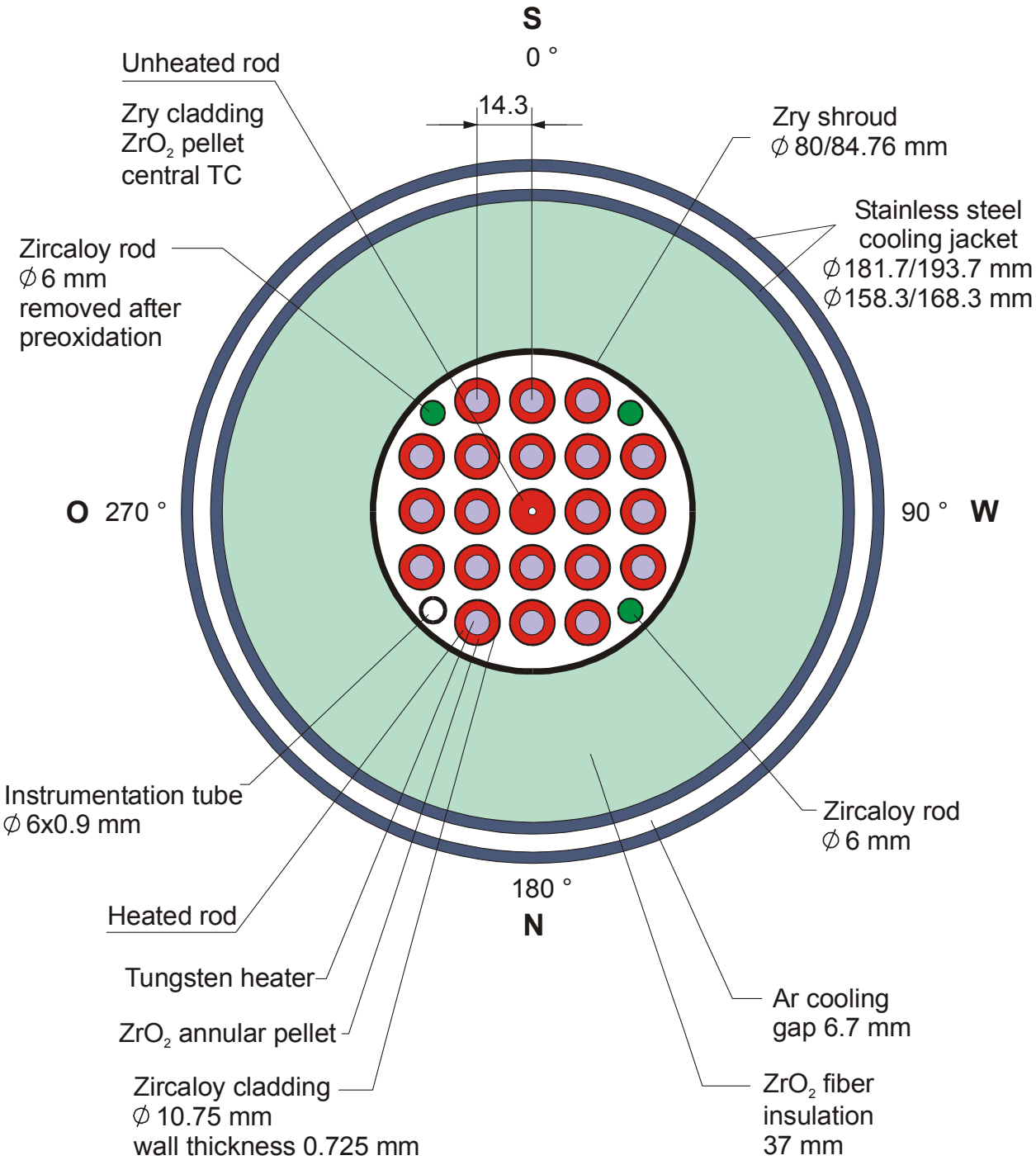

Figure 2.4 Bundle cross section and characteristic dimensions

2.1.3 Outlet Section

The bundle outlet geometry is sketched in Figure 2.3. Detailed drawings are published in /8/. Since nearly all participants did not simulate this section in detail, we refer to the description in /2/,/3/, or /7/.

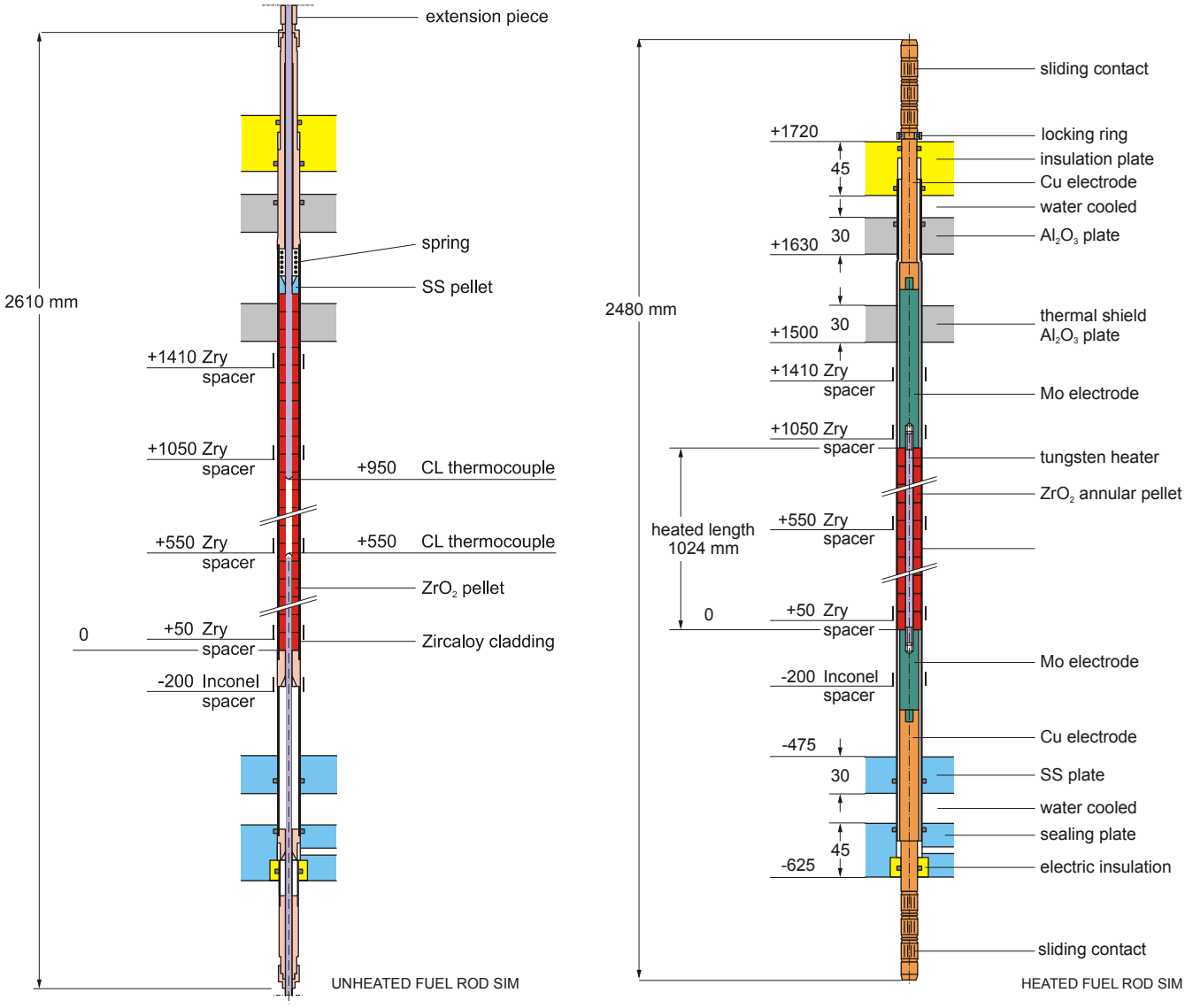

Figure 2.5 Detailed schematics of the QUENCH fuel rod simulators: unheated fuel rod (left) and heated fuel rod (right)

2.1.4 Cooling Jacket and Containment Geometry

The geometry of the cooling jacket and the containment (Figure 2.3) is given in /2/. Inner diameter of the cooling jacket is 0.1817 m. Containment wall thickness is 0.006 m.

2.1.5 Off-gas Pipe

The off-gas pipe mainly consists of a water-cooled inner pipe for the fluid leaving the bundle. This water-cooling is a countercurrent flow within the cooling jackets with a flow rate of app. 500 g/s at 300 K inlet temperature. The outer surface temperature of the in-

ner cooling jacket is at 300 K. Between the off-gas pipe and the inner cooling jacket there is stagnant argon. The dimensions of the structures are given in Table 2.1:

Mass spectrometer sampling position is located at the distance of 2.660 m from the beginning of the off-gas pipe (intersection with the QUENCH test section).

Table 2.1 Dimensions and materials of off-gas pipe

inner pipe	outer diameter 139.7 mm, wall thickness 4.5 mm total length 3.256 m
inner cooling jacket	outer diameter 154 mm, wall thickness 2 mm
outer cooling jacket	outer diameter 168.3 mm, wall thickness 5 mm
all materials	stainless steel

2.1.6 Electrical heating system

Indirect heating of the heater rods using tungsten and in the electrode zones molybdenum wires simulates the decay heat. The DC voltage measured in the facility includes the voltage drop at the sliding contacts at both ends of the rods, at wires which lead from the sliding contacts to the power supply, and at screws that fix the wires at their ends. This has to be taken into account to correctly model the input of electrical power into the bundle.

FZK has done the calculational analysis for all tests performed up to now and demonstrated that it is possible to reasonably well reproduce the temperatures and hydrogen production in all five tests, using one fixed value of this constant additional resistance. This value was estimated on the basis of calculations for QUENCH-01 and was fixed for all other code runs. This value is about 4 mΩ for the FZK in-house version of SCDAP/RELAP5 and might be different for other codes or other calculational domains.

Dimensions

The electrodes are plasma-coated with 0.2 mm ZrO_2. The coating is different for the upper and lower electrodes:

a) upper electrodes
Total length of the coating is 0.590 m, i.e. 0.576 m of the Mo electrode and 14 mm of the Cu electrode are coated.

b) lower electrodes
Total length of the coating is 0.593 m, i.e. 0.300 m of the Mo electrode and 0.293 m of the Cu electrode are coated.

Table 2.2 Resistivities for various heater rod materials

Material	**Resistivity** from /8/
Tungsten	$R_W = -2.61\cdot10^{-2} + 2.63\cdot10^{-4}\cdot T + 2.20\cdot10^{-8}\cdot T^2$
Molybdenum	$R_{Mo} = 2.29\cdot10^{-2} + 5.36\cdot10^{-5}\cdot T + 1.38\cdot10^{-7}\cdot T^2 - 2.22\cdot10^{-11}\cdot T^3$
Copper	$R_{Cu} = -7.89\cdot10^{-3} + 9.90\cdot10^{-5}\cdot T - 5.49\cdot10^{-8}\cdot T^2 + 3.16\cdot10^{-11}\cdot T^3$

where temperatures T are in [K] and resistivities R in [$\Omega\cdot mm^2/m$].

Room temperature data

Before test some fuel rod simulator resistances have been measured to give some information for input/model validation. The values are based on measurements of the simulators in the outer ring, since the inner rings are not accessible for sensing probes. The individual resistances vary between 2.95 and 3.23 mΩ per rod with an average value of 3.07 mΩ derived from all 12 rods. The sliding contacts have a static resistance of about 0.5 mΩ. For room temperature, the FZK/IRS SCDAP/RELAP5 mod 3.2 heater rod model predicts a total resistance of 2.95 mΩ for a rod without sliding contacts.

2.1.7 Experimental measurements and accuracy

For the QUENCH program the high temperature thermocouples were used based on the experience gained in the CORA program /12/, /13/. The details of mounting and internal structure can be found in /2/, /3/.

The fuel rod bundle and the shroud are equipped with high temperature TCs at various elevations and lateral positions. Besides the general accuracy is app. ± 50 K, the individual mounting as well as the fluid environment have to be taken into account: In gaseous atmosphere the temperatures measured by surface mounted high temperature TCs show an app. 50 K lower value than the corresponding cladding temperature. In two-phase flow environment, however, the 2 mm thick TC blocks the flow cross section substantially as an obstacle in the path of the water droplets. In that case TC then indicates liquid temperature without much delay. The droplet at a TC can evaporate before the water bulk arrives, so that the TC shows more elevated values afterwards, but probably below rod surface temperature. If that fin effect becomes dominant, the real temperature may vary between saturation (wetted TC) and the temperature measured in vapor atmosphere. Inner TCs do not suffer from such difficulties, but they show a delay due to thermal inertia of the surroundings. For clarification, temperatures measured by wall TC such as TSH have to be used preferentially for two phase flow conditions. If possible, both TC types should be used for comparison at a given elevation.

The quadrupole mass spectrometer (QMS) is used to detect the concentrations of several gas species in the off-gas pipe. Its accuracy is 5 %, the minimum detectable value for H_2O and H_2 is given to 20 ppm, that for non-condensable gases app. 1 ppm. In the beginning of the experiment steam measurements have to consider local steam condensation at cold off-gas pipe structures.

Time delay of measurements is negligible for TCs and impressed mass flow rates. The time delay gas detection systems has been measured during calibration test in which gas was injected into the test section. The time delay for the QMS is app. 5 s, that of the CALDOS depends on the fluid velocity in the off-gas pipe. Moreover, the signal form is affected by dilution effects in the argon steam, and hydrogen atmosphere.

Fluid mass flow rates of argon and steam are impressed by the pump whose make-up rate is calibrated. In case of steam, the delay due to evaporation process is negligible here. Post test analyses include non-destructive and destructive processes to identify the bundle state but are not yet finished completely.

2.2 QUENCH-06 test results

The QUENCH-06 test results are documented in detail in /7/, so that only a brief description will be given in this section, including the data specified as input data for the blind phase exercise.

2.2.1 Test Conduct

The ISP-45 experiment QUENCH-06 was successfully performed at FZK on December 13, 2000 /5/. In Table 2.3 the times of the various events and phases are listed.

As in the previous QUENCH experiments, the bundle was heated initially by a series of stepwise increases of electrical power from room temperature to ~600 °C in an atmosphere of flowing argon (3 g/s) and steam (3 g/s).

Pre-oxidation phase

The bundle was stabilized at this temperature for about two hours, the electrical power being about 4 kW. During this time the operation of the various systems was checked. Shortly before the end of this phase data acquisition was started. At the end of the stabilization period the bundle was ramped by stepwise increases in power up to about 11 kW to reach an appropriate temperature for pre-oxidation. The temperature level was maintained for about 1 hr by control of the electrical power to reach the desired oxide layer thickness.

Transient phase

At 6000 s, after the pre-oxidation phase, the electrical power was ramped at 0.3 W/s per rod to start the transient phase in the same way as in QUENCH-05. At 6620 s a corner rod was withdrawn to check the amount of oxidation at that time. The quench phase was initiated when pre-defined criteria similarly to QUENCH-05 were reached; therefore the cooling initiation conditions for these two tests are virtually identical.

Reflood phase

Within 5 s app. 4 kg of water were injected to rapidly fill the lower parts of the set-up (fast water injection system). At the same time the quench pump was started to inject water from the bottom of the test section at a rate of ~40 g/s. About 20 s later the electrical power was reduced to 4 kW within 15 s to simulate decay heat level. Quenching of the test section was completed within ~250 s; the steam mass flow rate and electrical power were then shut off, terminating the experiment. During the quench phase argon injection was switched to the upper plenum to continue to provide carrier gas for a quantitative hydrogen detection.

From the pressure histories at least one rod and the shroud were detected to fail shortly after the initiation of the quench phase. The lowest position of that hole is at 0.87 m bundle elevation. The fiber insulation shows only a slight intrusion of water.

Table 2.3 Events and phases of QUENCH-06

Time	Event	Phase
0	Start of data acquisition	
30	Heat up to about 1500 K	pre-oxidation
1965	Pre-oxidation at about 1500 K	
6010	Initiation of power transient	
6620	Initiation of pull-out of corner rod (B)	power transient
7179	Quench phase initiation Shut down of steam supply Onset of fast water injection Onset of quench water injection Detection of clad failure First temperature drop at TFS 2/1	reflood
7181	Steam mass flow rate zero	quench
7205	Onset of electric power reduction	
7221	Decay heat level reached	
7430	Onset of final power reduction	
7431	Shut down of quench water injection	
7431	Electric power < 0.5 kW	
7435	Quench water mass flow zero	
11420	End of data acquisition	

2.2.2 Final state

After the test the QUENCH-06 bundle /7/ plus the Zircaloy shroud appeared nearly intact up to 0.85 m. The outside of the shroud was only slightly oxidized up to that elevation. Between 0.85 m and app. 1.0 m the Zircaloy showed melting and melt relocation traces as well as a breach above 0.87 m as mentioned in section 2.2.1. The fuel rods show the same axial dependency except for the absence of melt traces in the section between 0.85 an 1.02 m.

No local melt formation, relocation or blockage formation could be detected during post-test analyses. The bundle remained intact except for local cladding failure. A more detailed description of the final state can be found in the QUENCH-06 experiment documentation /7/ or in the OECD report /22/.

2.3 ISP-45 Specification for blind calculations

ISP-45 was performed as a blind exercise so that only the initial conditions as well as boundary conditions were provided to the participants. Furthermore, the results of previous QUENCH experiments were made available to the participants to allow an adjustment of their codes and input decks of the QUENCH facility.

2.3.1 Initial and boundary conditions

As boundary conditions, necessary to perform ISP-45, data measured during the test or derived from those data, were given /8/. They were stored in file q06_boundcond.dat to be transmitted to the participants of ISP-45 in electronic form. In the same way the initial conditions (Figure 2.6) were stored in q06_inicond.dat. Moreover, for MELCOR users, the measured voltage was added (q06-voltageatplug.dat).

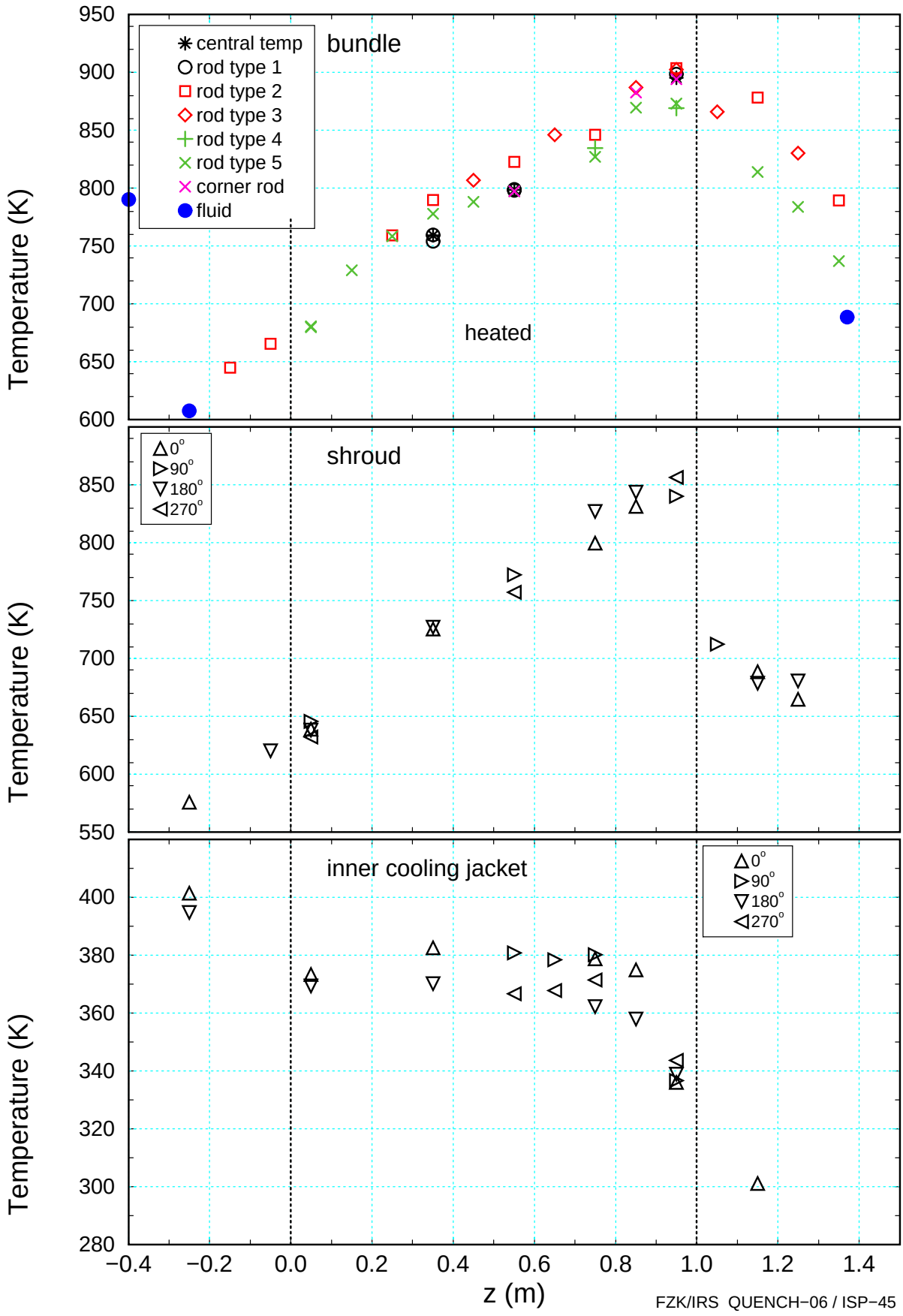

Figure 2.6 Axial temperature profiles measured in the bundle (top), shroud (center), and in the inner cooling jacket (bottom) at = 0 s.

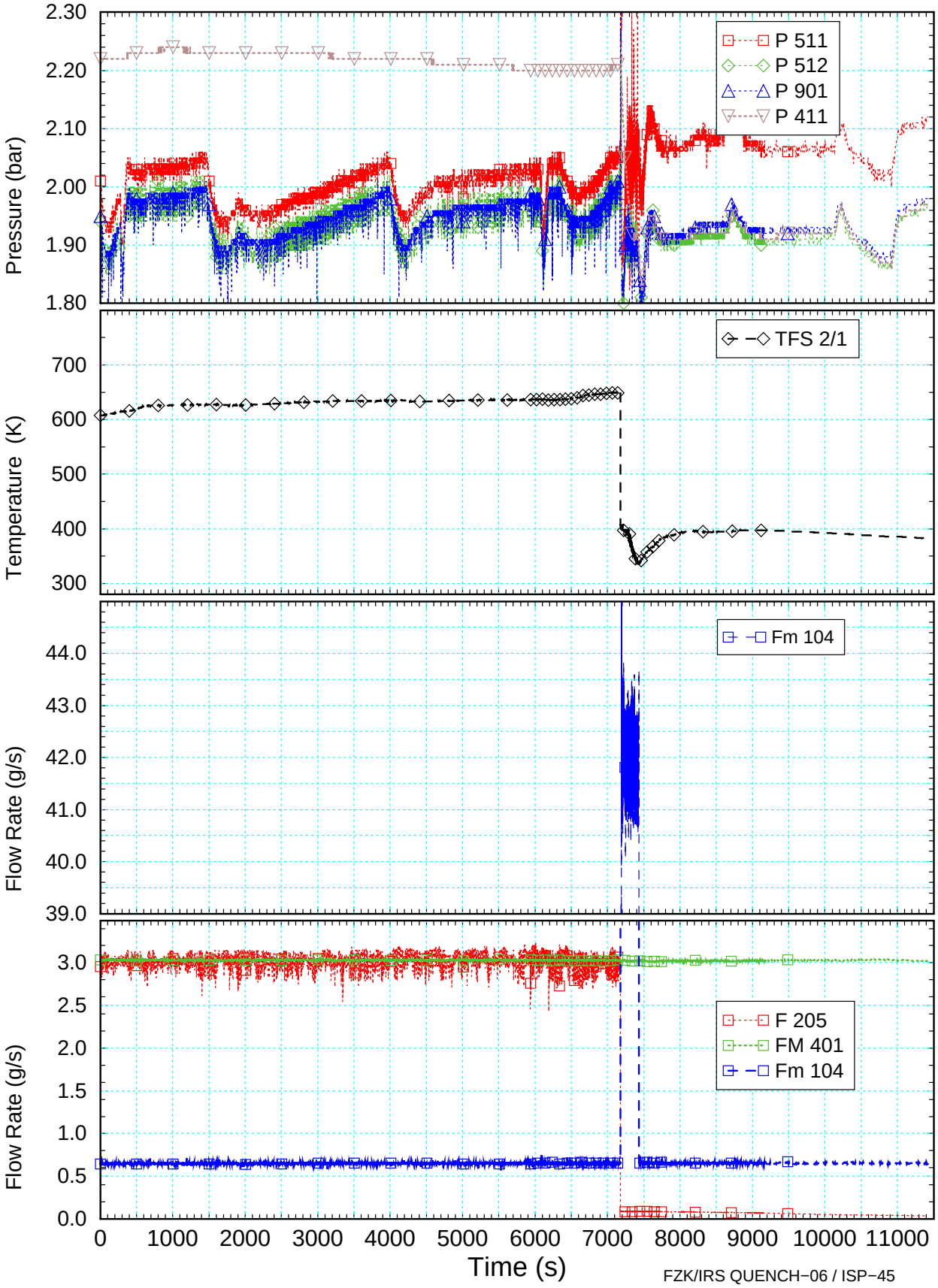

Figure 2.7 System and fuel rod inner pressures (top), fluid inlet temperatures (below) and fluid inlet mass flow rates for steam, argon, and quench water (bottom).

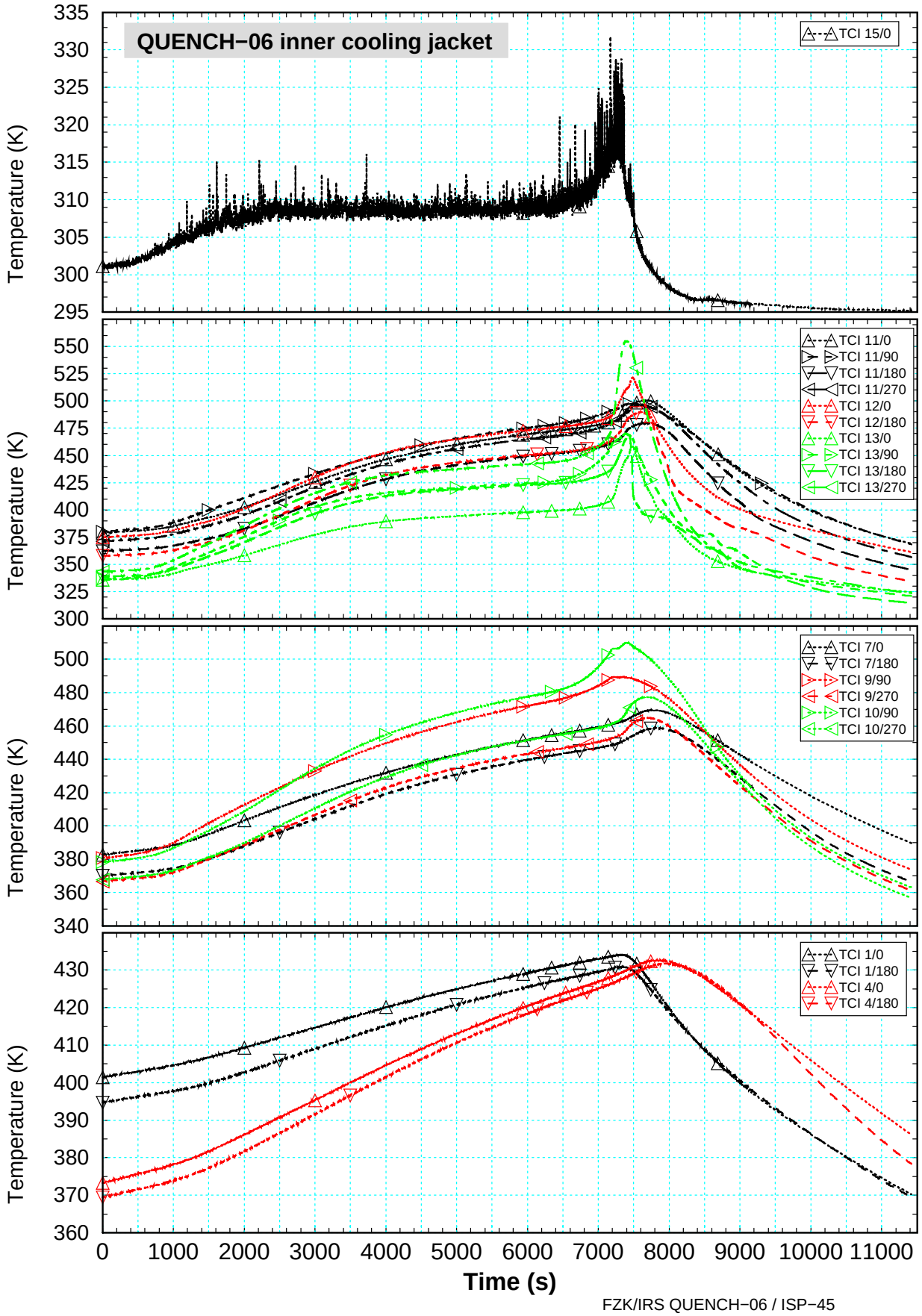

Figure 2.8 Inner cooling jacket temperatures measured by TCI thermocouples at various elevations during QUENCH-06 experiment.

The data file (q06_boundcond.dat) includes all data up to 11420 s for:

- mass flow rates at bundle inlet of argon (FM 401), steam (F 205), and quench water (Fm 104)
- fluid temperature at –0.25 m (TFS 2/1)
- pressure at bundle inlet (P 511) and outlet (P 512), behind the condenser (P 901), and fuel rod inner pressure (P 411)
- electrical power of the inner (E 505), outer (E 506) heated rods and sum (Ptot) as well as voltage at power supply plugs (E304 / E305) shown in Figure 2.9 and Figure 2.10
- temperatures at inner cooling jacket (TCI nn), with nn = 1…21.

The first three lines of that file contain the channel number, the designation of the instrument and the physical unit.

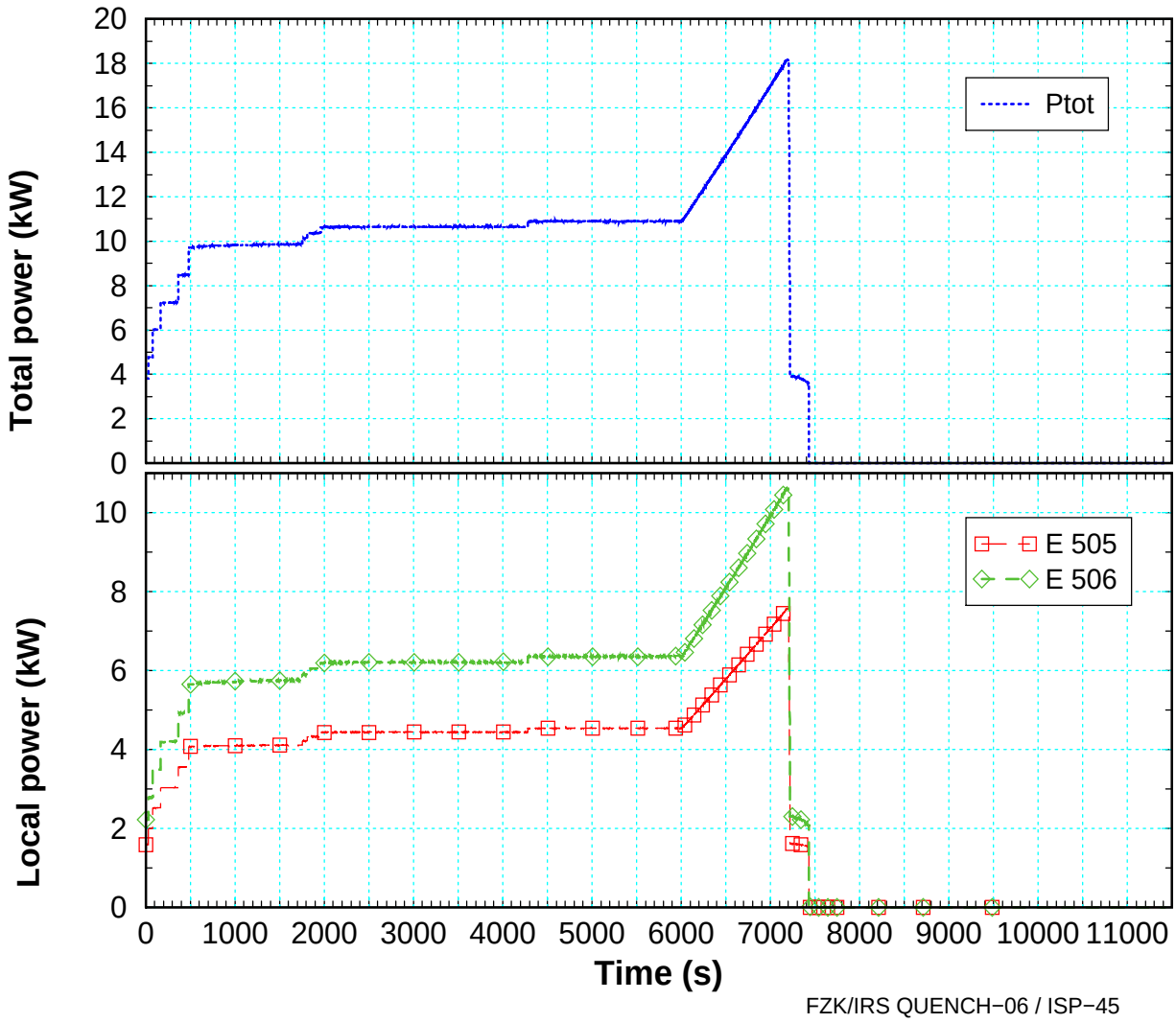

Figure 2.9 Total electric power (top) and electric power for inner and outer ring (bottom)

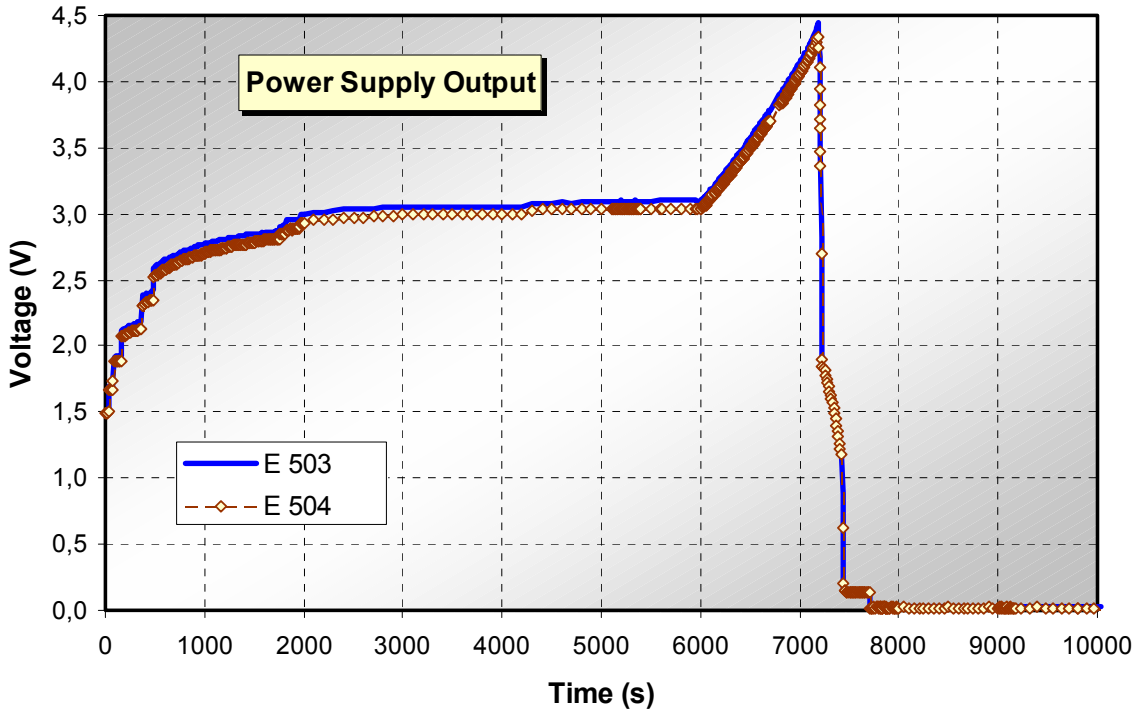

Figure 2.10 Voltage output of power supply system for inner and outer heat rods

2.3.2 Initial reflood conditions

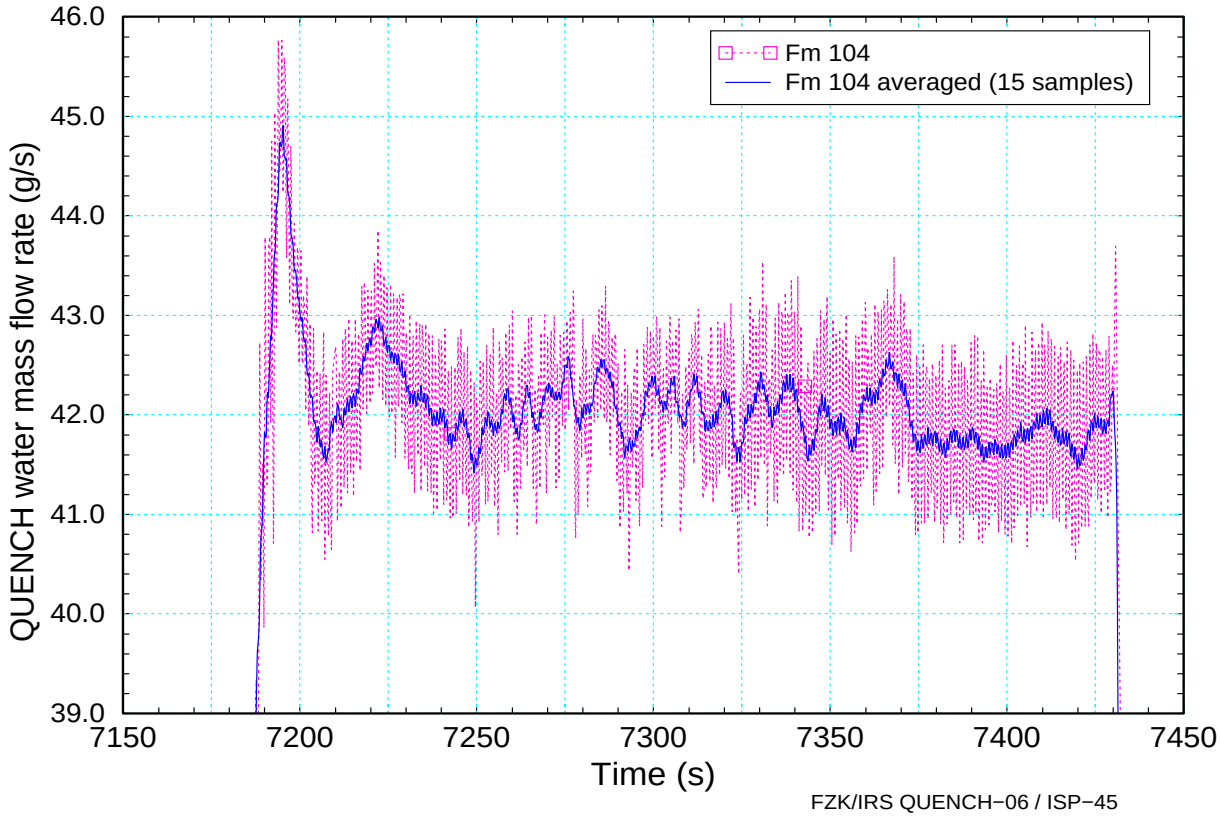

Figure 2.11 Quench water history, measured value and average values

Since thermocouple T 511 is not representative for bulk fluid temperature at bundle inlet, the only available information is the fluid temperature at elevation -0.25 m (TFS

2/1). Fluid inlet temperature should be adjusted such that calculated values agree with that measured value. The water used for rod cooling may be assumed to be at room temperature. Plots of the data contained in the file are given in Figure 2.8 to Figure 2.11.

Figure 2.11 is a magnified copy of the quench water mass flow rate (lower center of Figure 2.7). In this figure, the solid curve indicates a running average over 15 samples, a time interval of several seconds. In Figure 2.12 (a) the mass flow rate conditions are shown. The dashed line represents the fast water injection and the long dashed line the pump mass flow rate as specified in Figure 2.11. The mass flow rate at top end of the lower plenum (solid line) results from S/R5 calculations.

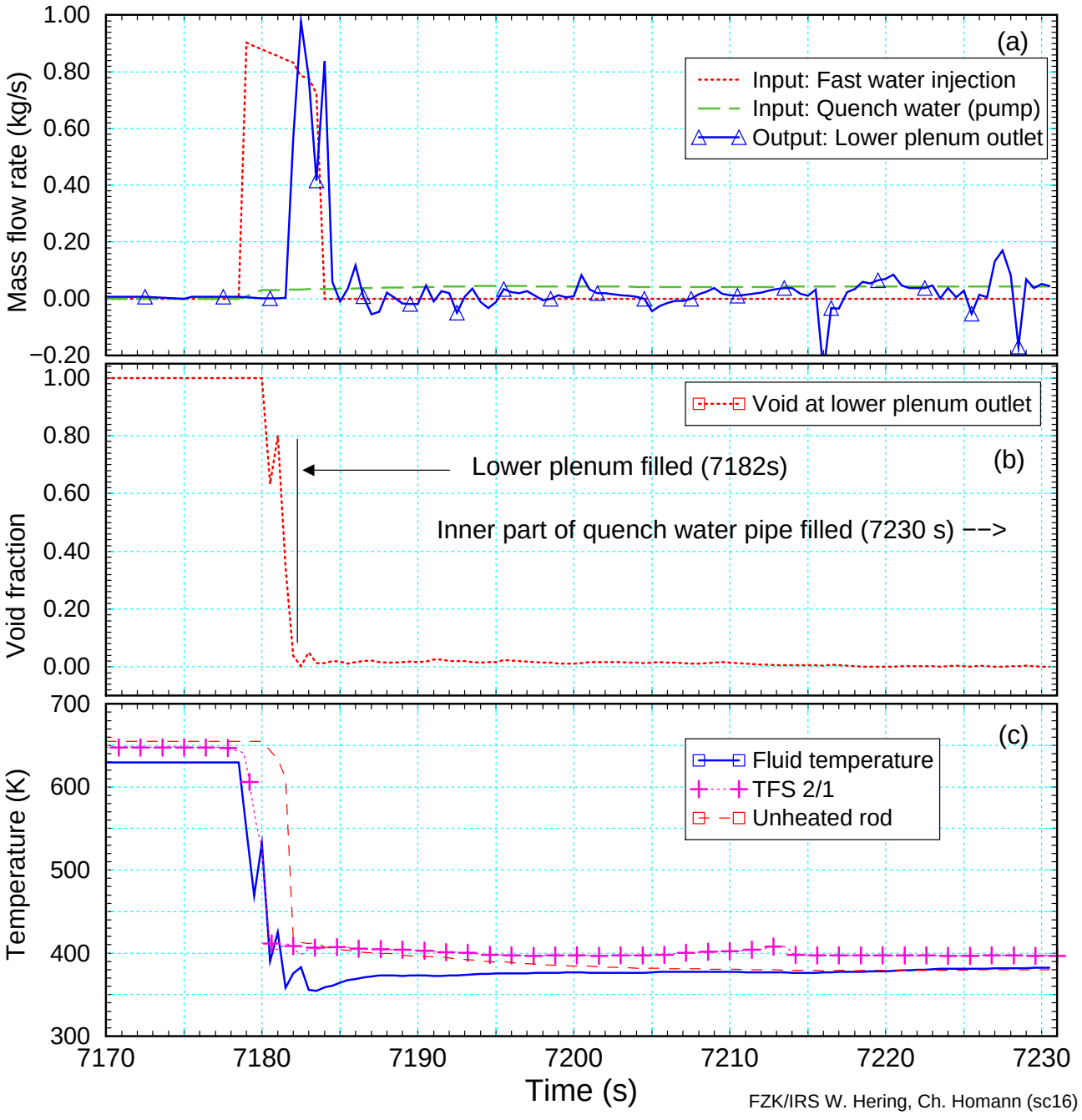

Figure 2.12 Mass flow rates (a), void (b) and temperatures (c) calculated by SCDAP/RELAP5 for the outlet of the lower plenum at -0.3m.

At app. 7182 s the lower plenum is nearly filled as shown by the calculated void fraction (Figure 2.12 b) but the quench water inlet pipe is still voided so that the net mass flow rate is lower than the injected mass flow rate up to app. 7230 s (Figure 2.12 a). After that time, the inlet mass flow rate follows substantially the specified data. Finally Figure 2.12 c shows the good agreement between the calculated fluid temperature and the specified fluid inlet temperature (TFS 2/1, Figure 2.7).

As mentioned in the ISP-specification report /8/, the unexpected draining of the quench water pipe was detected after test. Post-test analyses with S/R5irs were performed at FZK to identify the water mass in the various pipes of the steam and quench inlet system. In Figure 2.13 the measurements and post test analyses of the reflood progress are shown. From the pressure difference sensor (Lm501) a very sharp peak at 7180 s indicate the very violent water injection and cannot be interpreted as a water level. To eliminate the pressure spikes (noise) low-pass filtering was performed leading to the curve. "ISP-45: Lm501". The result of the S/R5 post test analysis (sc16 final) is based on a detailed simulation of all pipes and volumes in the hydraulic system of the QUENCH facility and is in the vicinity of the detected wetting signals derived from different types of thermocouples. Most reliable are the shroud outer surface thermocouple (TSH) which are not influence by dispersed droplet flow.

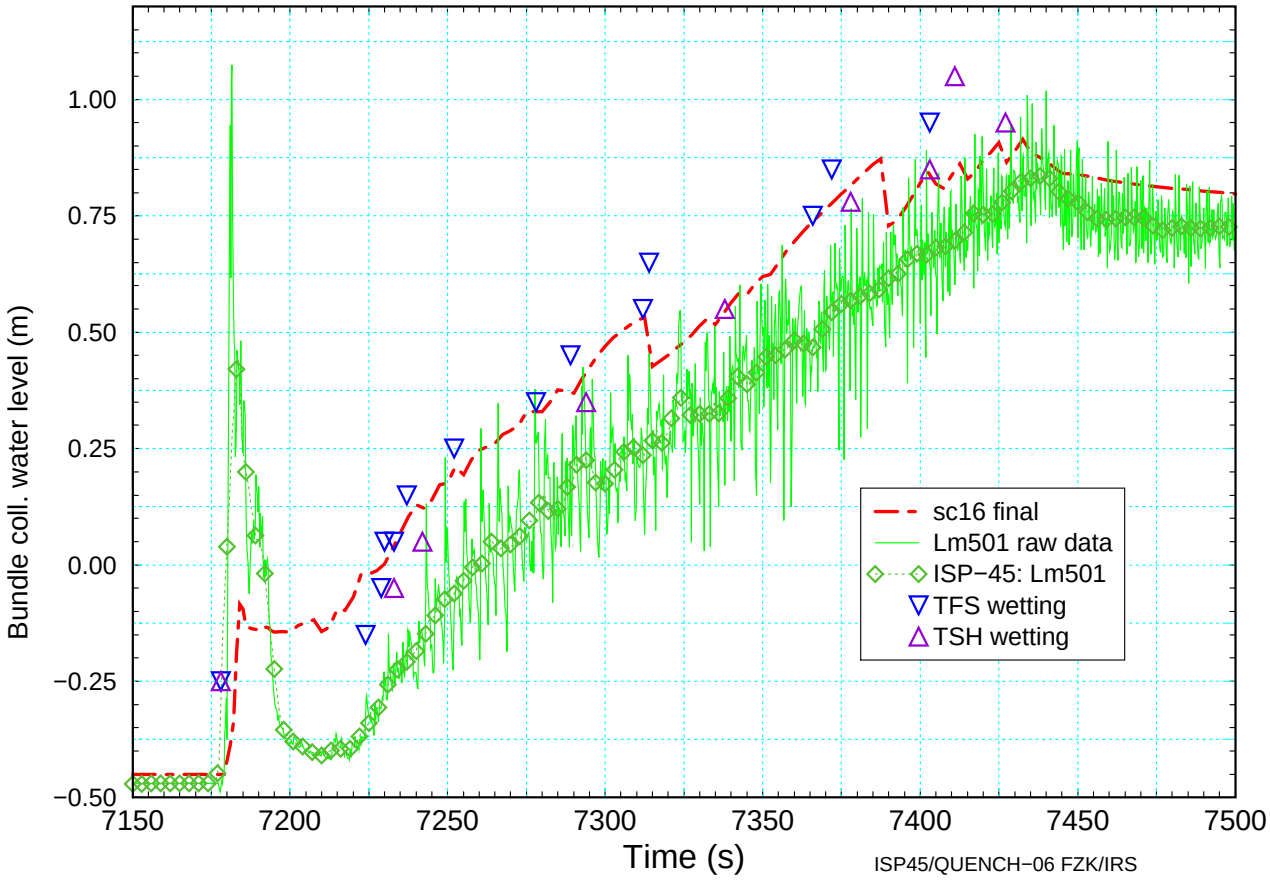

Figure 2.13 Calculated water level increase compared with experimental measurements and thermocouple readings.

3 CODES AND PARTICIPANTS

A large variety of data sets in different conditions were delivered from the 21 participants listed in Table 3.1. Since we wanted to keep as many participants as possible in the ISP-45 we did not refuse bad data formats and/or miss-aligned data. Besides the specified ASCII tables and the DMX files we got RELAP 5 strip files and MELCOR printout and even one complete "restart plot-file". We corrected obvious miss-typing in the variable names. Surprisingly some participants did not match the specified time vector which caused additional efforts and increased the data storage. We tried to use the inappropriate time vectors if they were in ascending order. The remaining inconsistencies found during data assessment are outlined in Table 8.6 in the appendix (section 8.1.1).

Table 3.1 Final list of participants and their organizations

Token	*Analyst(s)*	*Organisation*	*Address*	
CMX	Nunez-Carrera A.	Nat. Commission of Nuclear Safety and Safeguards (CNSNS)	Dr. Barragan 779, Col Narvarte; 03020, MEXICO D.F.	MX
DMM	Leonardi M.	University of Pisa	Via Diotisalvi, 2 - I-56126 Pisa	I
DRS	Mélis S. Zabiego, M.	IPSN/DRS/SEMAR/LECTA	Cadarache Bat 700; 13108 St Paul Lez Durance	F
EDF	Lacour V., Pineau D.	Electricité de France (EDF)	1 avenue du Général de Gaulle; 92141 Clamart	F
ENE	Bandini G.	ENEA	Via Martiri di Monte Sole 4; 40129 Bologna	I
FRA	Caillaux A.	Framatome-ANP, Paris	TOUR FRAMATOME; 92084 Paris La Defense	F
GRS	Erdmann W.	Gesellschaft für Anlagen- und Reaktorsicherheit (GRS)	Schwertnergasse 1; 50667 Köln	G
IJS	Stanojevic M. Leskovar, M.	Institut Jožef Stefan	Ljubljana, Slovenia	SI
INL	Coryell E.	Idaho National Engineering and Environmental Lab.	Idaho Falls, ID	USA
ISS	Allison C. Honaiser, E.	Innovative Systems Software University of Florida, Tampa	1284 South Woodruff; 83404 Idaho Falls, ID	USA
NEH	Niyazi Sokmen C.	Nuclear Engineering, University Hacettepe	Beytepe, Ankara, 06532	TR
NK1	Pylev S.	NSI of RRC "Kurchatov Institute"	123182 Kurchatov sq.1; Moscow, Russia	RU
NK2	Tomachik D.	NSI of RRC "Kurchatov Institute"	123182 Kurchatov sq.1; Moscow, Russia	RU
NUP	Ikeda T.	NUPEC (Nuclear Power Engineering Corporation)	17-1, 3-chome Toranomon; Minato-ku, Tokyo, 105-0001	JP
REZ	Duspiva J.	Nuclear Research Institute, Rez	250 68 Rez near Prague	CZ
RUB	Reinke N.	Ruhr-University Bochum; Institute for Energy Systems and Energy Economics	Building IB 4/126; 44780 Bochum	G
SES	Sponton L.	Studsvik ECO & Safety AB	SE 611 82 Nyköping	S
SIE	Plank H.	Framatome-ANP, Erlangen	Freyeslebenstr. 1; 91058 Erlangen	G
SNL	Cole R.	Sandia National Laboratories	PO Box 5800-0739; Albuquerque, NM 87185-0739	USA
UZA	Debrecin N.	University of Zagreb	Unska 3; 10000 Zagreb	CR
VTT	Hämäläinen A.	VTT Energy	PO box 1604; 02044 VTT	FIN
FZK	Homann Ch.	Forschungszentrum Karlsruhe, Institute for Reactor Safety	PO Box 3640; 76021 Karlsruhe	G

3.1 Codes

In the ISP-45 the 21 participants used 8 different codes as shown in Table 3.2. They can be grouped into two families:

- Integral code systems (I) which are designed for complete reactor analyses and
- detailed codes (D) which are often used to assist and analyze integral experiments.

Table 3.2 List of codes and code options used in for ISP-45 calculations

Code	Type	Token	Analyst(s)	Thermohydraulics general	Thermohydraulics reflood	Clad failure temp.[K]	Oxidation low / high	Remarks
ATHLET-CD	**D**	**GRS**	Erdmann	2p, 1D, 5eq.	Inv. annul. flow	2400 K	C / UH	based on Q-01
		RUB	Reinke	"	"	2400 K	C / UH	based on Q-01
GENFLO	**D**	**VTT**	Hämäläinen	2p, 2D, 5eq.	qft	n/a	UH	UH mod * 0.2
ICARE/	**D**	**DRS**	Zabiego	2p, 1D, 6eq.	Inv. annul. flow	2300	UH	
CATHARE		**ENE**	Bandini	"	"	2300	UH	simpl. crack op.
IMPACT/ SAMPSON	**D**	**NUP**	Ikeda	3p, 2D, multi-field	n/a	n/a	C / UH	
MAAP 4.04	**I**	**EDF**	Pineau	1p+1p, 1D	simpl.qft	2500	C / UH	MAAP4.04c
		FRA	Caillaux	"	mixture level	2500	C / BJ	
MELCOR	**I**	**IJS**	Stanojevic	2p, 1D, 6eq.	no	2500	C / UH	*decay power*
Me 1.8.5QZ		**NK2**	Tomachik	"	no	2250	C / UH	
Me 1.8.5RB		**REZ**	Duspiva	"	simplified qft	deactivated	C / UH	new HR model
		SES	Sponton	"	"	2500	C / UH	"
		SNL	Cole	"	"	2500	C / UH	"
SCDAPSIM	**D**	**CMX**	Nunez-Carrera	2p,1*D,6eq	n/a	n/a	C / UH	*FZKA 6566*
		DMM	Leonardi	"	"	2200	C / UH	"
		ISS	Honaiser	"	"	2500	C / UH	"
		NEH	Sokmen	"	"	2500	C / UH	"
		NK1	Pylev	"	"	2500	C / UH	"
		SIE	Plank	"	"	2200	C / UH	"
		UZA	Debrecin	"	"	2500	C / UH	"
SCDAP-3D	**D**	**INL**	Coryell	2p,1*D,6eq	n/a	n/a	Diff.Model (Olander)	"
S/R5.irs	**D**	**FZK**	Homann/ Hering	2p,1*D,6eq	PSI / FZK	2350	C / UH	FZKA 6566

Oxidation correlation: ***BJ: Baker/Just*** ***C: Cathcart*** ***UH: Urbanic/Heidrick***

Thermal-hydraulics: p: phase D: dimension eq: equations

1*D: 1D + cross-flow capability

n/a: no sufficient information given qft: quench front tracking

Me 1.8.5RB Melcor code version with qf tracking and beta HR model

Me 1.8.5QZ Melcor original version without explicit reflood model and HR model

MAAP4.04c EDF MAAP4.04 code version with qf tracking, C/UH oxidation correlation

3.1.1 General code features

For the pre-quench phases only a single phase 1-dimensional representation of thermal-hydraulics is required. However, in the quench phase the codes require capabilities to simulate 2 phase flow and to track the water level. From literature /10/ it is known that

a maximum zone length of 0.07 m should not be exceeded to track the various fluid states sufficiently. In case of larger zones, averaging of temperatures and heat fluxes smear the very pronounced temperature drop (quenching) leading to reduced cool-down rates.

In essence the thermal-hydraulic capabilities of the codes can be described briefly as follows (Table 3.2):

- ATHLET-CD and GENFLO use a 5 equation representation of two-phase thermal-hydraulics, the single momentum equation is extended by a drift flux correlation coupling both phases. For reflood situations a dedicated quench front tracking model derived and validated from design bases reflood experiments is available.
- ICARE/CATHARE is based on the French thermal-hydraulic code CATHARE, which uses a 6 equation system and mass balances for non-condensables in the vapor and solutes in the liquid phase. The CATHARE code also allows 1-D multi channel flow in the core region.
- IMPACT/SAMPSON is rather a new modular approach started around 1994. Thermal-hydraulics is modeled based on multi-field, multi-component, multi-velocity field in three phases (gas, liquid, plus solid particles) and in two dimensions. Mass conservation is calculated for each species independently.
- The MAAP code originally only handles one fluid in each cell, either fluid or vapor. Some improvements of EDF allow cells with both phases to simulate a rising water level during reflood. The phases are separated depending on the local void fraction.
- The MELCOR code uses a 6 equation representation of two phase thermal-hydraulics with two independent momentum equations. The major distinction from more detailed codes is in the "flow regime map" for the coupling of the phases by exchange of momentum. MELCOR's "map" is extremely simple, and is intended only to give good results for the limits of counter-current flow and low-velocity entrainment.

Three of the detailed codes are based on the thermal-hydraulic code system RELAP5 (SCDAP-3D, SCDAPSIM, SCDAP/RELAP5 mod 3.2 (S/R5irs)) which uses a 6 equation system and mass balances for non-condensables in the vapor and solutes in the liquid phase. In the FZK version (S/R5irs) the PSI/FZK reflood model has been activated, which gives better results for the quench temperatures using the semi-mechanistic Chen transition boiling model.

3.1.2 Code options selected

Especially the integral codes use a set of default parameters. If participants modified one of these, this should have been specified. In the third and fourth section of Table 3.2 the clad failure criteria and the oxidation correlation are given as far as delivered by the participants.

Clad failure

In all codes the clad failure criterion is a user defined parameter which strongly influences the further progress of the bundle damage, because of U-Zr-O melt relocation

into colder parts of the core/bundle. From FZK single rod experiments a certain dependency of the clad failure temperature on the heat-up rate was detected. This may explain the common observation of different clad failure temperatures used in simulation of reactors and integral experiments.

From physics the melting of the α-Zr(O) weaken the ZrO_2 layer since in liquid metallic Zr the oxygen diffusion coefficient is much higher than in solid state. In addition the ZrO_2 stability is rather low above 2700 K. Therefore, a physically sound parameter range is between 2330 K and 2700 K. To avoid melt relocation some participants increased the clad failure temperature allowing for continuous oxidation.

Oxidation correlation

Nearly all participants used the Cathcart (C) correlation for the low temperature regime of Zircaloy oxidation (Table 3.2), except for ICARE/CATHARE and GENFLO, which both use Urbanic/Heidrick (UH). In the high temperature regime mostly the correlation of Urbanic/Heidrick is used which tends to under-predict the oxide layer growth.

Besides, Baker/Just (BJ) is used by the MAAP code. In the temperature range of QUENCH-06, the differences between UH and BJ are not very pronounced for a large part of the experiment, so that the source of exothermal energy should be similar.

In SCDAP-3D an integral diffusion model for oxidation is implemented, which applies Fick's law of diffusion and the phase diagram of the oxidic and metallic portions of the cladding to calculate the rate of oxygen uptake in the cladding. From that Zr-O phase diagram the oxygen concentrations at phase boundaries were derived, the diffusion coefficients were taken from Olander /11/.

3.1.3 Dedicated models for reflood conditions

Some of the codes have powerful thermal-hydraulics package (S/R5, SCDAPSIM, ICARE/ CATHARE) others use simplified models which work sufficiently in the SFD range, but have problems with the two-phase flow conditions.

All codes which are based on RELAP5 mod3.2 include a sophisticated reflood model developed at PSI /14/ and extended at FZK /15/. This model, originally developed for DBA analyses has to be activated by a trip and works efficiently on RELAP5 heat structures.

- The MELCOR thermal-hydraulics package is developed at SANDIA national laboratory based on two independent momentum equations. In the ISP-45 contest, two MELCOR code versions participate. IJS and NK2 used original MELCOR 1.8.5 (QZ) and REZ, SES, and SNL used an improved MELCOR 1.8.5 MELCOR 1.8.5 (RB) version /16/ which includes a simplified water level tracking model (Table 3.2).
- The original MAAP which is used by FRA only allows either water or steam in one mesh. The heat transfer to the fluid is a function of the fuel rod state and the conditions in the fluid. The EDF version of the MAAP code includes a simplified reflood model is based on four two phase flow regimes. The transition between these re-

gimes are calculated using local state variables, critical heat flux, and minimum film boiling temperature.

- GENFLO also includes a quench front tracking model, which has been assessed against various DBA reflood tests.
- The reflood model of the IMPACT/SAMPSON code selects the heat transfer coefficients depending on the flow conditions comparable to the solution in RELAP5.

3.2 Modeling of test section

In previous ISP exercises, such as ISP-31 (CORA-13, /12/) or ISP-36 (CORA-W2, /13/), most of the participants were only able to simulate the heated section of the CORA bundle which extends to 1.0 m, and the number of axial zones were mostly fixed to ten. The upper electrode zone, which makes about 20% of the total length could not be simulated.

In the ISP-45 all participants were able to simulate the heated section plus the molybdenum electrode zones extending the length of the simulated test section to 1.6 m as can be seen in Table 3.3. Integral experiments such as QUENCH or Phebus FP can be analyzed sufficiently using a 1-D approach, since the length of the test section (1.6 m) is much larger than the radius (0.04 m). Cross flow effects such as occurred in some CORA experiments are not possible. So most of the participants use several rings for the bundle components in one single fluid channel, except for NUP, EDF and FRA, use 3 fluid channels. A large number of participants also include the external cooling channel (Table 3.3) with Argon and water in the upper electrode zone and consider the absence of the fiber insulation in the shroud above 1.0 m.

The detailed code systems generally use 0.1 m zone lengths in the heated sections and various lengths in the electrode zones which often include the copper sections too. As sketched in Table 3.3 nearly all participants simulated the bundle using all five components: unheated rod (Un), inner and outer ring of heater rods (He), corner rod (Cr), and shroud (Shr).

- The ATHLET-CD input deck from GRS originally derived from previous CORA calculations was extended for analyses of various QUENCH experiments. RUB increased in the upper electrode zone the convective heat transfer to the shroud artificially (Table 3.3).
- In the GENFLO code the electric power is distributed homogeneously over the heated length of the tungsten since no dedicated heater rod model is available to simulate the temperature driven negative feedback. Due to this fact, the temperatures in the lower part of the bundle are overestimated.
- The ICARE/CATHARE calculation by DRS is based on a fine mesh originated from CEA studies with ICARE2 to achieve a better representation of the axial temperature profiles prior to reflood. Similar experience was obtained with the 32 nodes input deck used at FZK.
- The ICARE/CATHARE input deck of ENE input deck tripled the number of axial zones so that in the heated section 0.033 m long zones were achieved. To account

for the convection in the gap above 1.0 m the Zry emissivity at the shroud outer surface was adapted (as indicated by Ar+ in Table 3.3) .

- IMPACT/SAMPSON model includes three flow channels, 1. center: including the unheated rod, 2. middle: including the inner ring of heated rods, and 3. outer: with outer ring and the shroud.
- The MAAP code users have only limited degree of freedom to design own input decks, since large parts are coded in the program itself. The FRA input deck is based on an EPRI version for CORA experiments.

Table 3.3 Modeling of the QUENCH test section by ISP-45 participants

Code	Token	Nodalisation axial	Nodalisation radial	Simulated length [m]	Components Un He Cr Shr	Shroud Upper electr.	Shroud outer bound.	Remarks Special features	Remarks Special options
ATHLET-CD	**GRS**	20	4	-0.475 ...1.5	**1 2 0 1**	Ar*	Ar / W	$\lambda_{(ZrO2)}$+50%	Rv=5.0mΩ
	RUB	19	4	-0.475 ...1.5	**1 2 0 1**	Ar*	Ar		Rv=4.2mΩ
GENFLO	**VTT**	17	4	-0.2 ...1.5	**1 2 0 1**	n/a	n/a	no specific HR-model	
ICARE /	**DRS**	66	5	-0.47 ...1.47	**1 2 1 1**	Ar*	prescribed	$\lambda_{(ZrO2)}$+80%	Rv=4.2mΩ
CATHARE	**ENE**	42	5	-0.45 ...1.5	**1 2 1 1**	Ar+	prescribed	3 channels	Rv=4mΩ
IMPACT / SAMPSON	**NUP**	19	5	-0.3 ...1.5	**1 2 $^3/_4$ 1**	Ar	Ar / W	3 channels	Rv=5mΩ
MAAP 4.04	**EDF**	58	4	-0.46 ...1.51	**0 3 0 1**		prescribed	3 channels	no Rv
	FRA	50	4	-0.475 ...1.5	**0 3 1 1**		prescribed		Rv=4mΩ
MELCOR	**IJS**	19	5	-0.475 ...1.5	**1 2 0 1**	Ar	Ar / W		*decay heat*
vers. 1.8.5QZ	**NK2**	18	4	-0.475 ...1.5	**1 2 0 1**	n/a	Ar+steam		
ver. 1.8.5RB	**REZ**	20	5	-0.475 ...1.6	**1 2 1 1**	Ar	prescribed		Rv=2.5mΩ
	SES	16	4	-0.6 ... 1.79	**1 2 0 1**	Ar*	Ar		Rv=4.2mΩ
	SNL	22	5	-0.475 ...1.5	**1 2 1 1**	Ar*	Ar / W	*off-gas pipe*	Rv=3mΩ
SCDAPSIM	**CMX**	16	5	-0.3 ...1.3	**1 2 1 1**	Ar*	Ar / W	*ISS based*	*O-30*
	DMM	16	5	-0.25 ...1.6	**1 2 1 1**	Ar*	Ar / W	$\lambda_{(ZrO2)}$+80%	Rv=4.3mΩ
	ISS	16	5	-0.3 ...1.3	**1 2 1 1**	Ar*	Ar / W	0.86*Po(el)	Rv=2.5mΩ
	NEH	16	5	-0.3 ...1.3	**1 2 1 1**	Ar*	prescribed	*ISS based*	
	NK1	16	5	-0.3 ...1.3	**1 2 1 1**	Ar*	n/a	*ISS based*	
	SIE	19	5	-0.485 .1.52	**1 2 1 1**	Ar *	Ar / W	$2.2 * \lambda_{(ZrO2)}$	
	UZA	16	5	-0.3 ... 1.3	**1 2 1 1**	Ar*	Ar / W	*ISS based*	*O-30*
SCDAP-3D	**INL**	16	5	-0.25 ...1.35	**1 2 1 1**	n/a	n/a	*ISS based*	Rv=4.2mΩ
S/R5.irs	**FZK**	16 32	5 3	-0.45 ...1.6	**1 2 1 1** **1 1 0 1**	Ar & rad	Ar / W W		Rv=4.2mΩ

Argon gap:
- Ar* Argon with modified heat conductivity
- Ar+ Argon with modified radiation (see text)
- O-30 Option 30 used, no radiation in bundle
- prescribed Temperatures given in the specification report used

External cooling:
- Ar / W Argon below 1.0 m, water above
- W Water cooling at shroud outside
- HR electric heater rod
- $^3/_4$ simulation of corner rod removal

- MELCOR input deck from REZ has been developed and validated for QUENCH-01 experiment. It serves as basis for the input decks of SNL, which developed the

MELCOR reflood model. However, some problems arise due to the inadequate modeling of axial power release. In MELCOR six thermal-hydraulic cells (CVH, FL package) are used but in the bundle model (COR package) a much finer discretization is used. The thermal-hydraulic boundary conditions for the COR structures are interpolated base on the CVH values. Other MELCOR users (NK2, IJS, SES) developed input decks with a finer CVH nodalization.

- Nearly all participants using SCDAPSIM or SCDAP-3D (except for SIE and DMM) rely on an input deck developed by University of Florida (E. Honaiser), which was distributed as part of SCDAPSIM package (ISS, C. Allison).

3.3 Participants experience

To participate successfully in an OECD International Standard problem the organizations as well as the users know that sufficient experience in analysis of test facilities as well as nuclear power plants is prerequisite. In ISP-45, the user's experience ranged from beginners to code developers, who know the code deficiencies perfectly. Therefore, the participants were grouped according to their experience, of course with some reservation.

The first group indicated by "D" comprises all code developers such as DRS (ICARE/CATHARE), GRS (ATHELT-CD), INL (SCDAP-3D), ISS (SCDAPSIM), NUP (IMPACT/ SAMPSON), and SNL (MELCOR). Two other participants were also ranked as "D" because they developed models or improved their code EDF (MAAP4) and RUB (ATHLET-CD).

Since the code developers also validate their codes, they were also considered to be a more experienced users ("E"). In this context, more experienced users are defined to have already analysed either CORA experiments or other QUENCH experiments. Also experience with analyses of experiments in the French Phebus facility were taken into account. Participants in this group are: ENE, FRA, REZ, SES, DMM, and SIE.

The third group indicated by "G" for general, combines all users which are not so experienced in analysing integral severe accident experiments or nuclear power plants. In this category the participants CMX, IJS, NEH, NK1, NK2, UZA, and VTT were placed.

4 RESULTS OF BLIND PHASE

In order to establish a broad data basis for a coherent assessment of the code predictions, a series of calculated data was requested to the participants. In total more than 400 different physical quantities were plotted as graphics. The whole list of the delivered data and its qualification is listed in the appendix in Table 5.1 - Table 8.6. This section comprises the delivered results of various codes, experimental results, and the FZK post test analyses using SCDAP/RELAP5 mod 3.2.irs.

In section 4.1 the global results up to quench initiation is discussed in more detail allowing a brief overview about the quality of the data collected within ISP-45. A coarse energy balance reveals quality and accuracy of codes and input model. In section 4.4 various axial profiles such as cladding temperature, electrical power, oxide layer thickness are discussed for the end of the pre-oxidation phase (6000 s), the time of corner rod removal (6620 s), and prior to reflood initiation (7170 s). Though in QUENCH-06 the bundle remained essentially intact, some participants calculated melt release and relocation. Therefore, the bundle degradation is highlighted in section 4.5 mainly focused on the pre-reflood period of the experiment. For the reflood phase, discussed in section 4.6 the code predictions are checked, with special emphasis on the thermal-hydraulics and the hydrogen release. A presentation of final state of QUENCH-06 follows in 4.7.

In the legend of all graphics shown in this section, all participants are listed. Each participant is identified by its token and the curves are characterized by symbol, color, and line style. Experimental results are identified by (-E-) or by opaque symbols. The FZK post test calculations can be identified by (-C-) symbol.

If the participants did not deliver the desired results or the data could not been read, a suffix ".0" was added to the token in the legend. This allows unique line properties for each participant. Furthermore an extension ".1" indicates a change of original database by FZK e.g. when bundle power obviously referred to single rod power, whereas most of the participants referred to bundle power (Figure 4.15).

4.1 Global results up to quench initiation

In order to meet the objectives of the ISP-45, the variables calculated comprise global parameters needed mainly for the energy balance, the heat input by electrical power and oxidation, heat stored in the structures, and heat losses to the fluid and in radial direction through the shroud. The code improvements /4/ made at FZK/IRS and sent out to MELCOR, SCDAP and SCDAPSIM code developers include a feature to identify and print these data. In most of the delivered data the values show a low scattering, which was used to define a "mainstream". Generally the deviations in the mainstream are considered to be negligible under the conditions of ISP-45.

As specified in /8/, all calculations begin at the end of the stabilization period when the bundle is ramped by stepwise increases in power in order to stabilize the axial maximum temperature at the 1473 K level.

4.1.1 Peak bundle temperature

To get a first overview of the results of the blind phase of ISP-45 the maximum temperature in the bundle (Tbp) is shown in Figure 4.1. The values calculated by the participants are compared with the experimental data (TIT A/13; -E-), a thermocouple in a corner rod at 0.95 m, and the results of FZK post-test calculations (fzk; -C-). In the ISP-45 Specification Report /8/ the maximum initial temperature was given in Figure 3.1 (/8/) to 900 K. Nearly all participants start with that value except for VTT and NK2. The strong deviation of DRS at t=0 originates from the non-monotonous time vector which partially devaluates their results.

First heat-up

During first heat-up phase the temperature curves spread significantly, especially since at 1000 s a temperature escalation is calculated by IJS, driving maximum temperature up to 2370 K, mainly caused by an inadequate use of the MELCOR decay power module instead of the electric heater rod module ELHEAT, as mentioned by IJS.

Steepest temperature increase was calculated by CMX with 0.5 K/s and slowest increase comes from RUB with 0.3 K/s.

Pre-oxidation phase

After 1965 s the pre-oxidation phase starts with a temperature plateau of 1500 K as can be seen in Figure 4.1. Two participants overshoot the desired temperature plateau drastically, INL up to 2000 K mainly due to problems with the diffusion oxidation model, and NK1 up to 1800 K, the reason being unclear. Both calculations are based on the ISS input deck. The ISS tendency to overshoot the temperature ramp is not so pronounced, but still detectable. The main reason may be that the SCDAP shroud model calculates radial heat conduction in slab geometry, whereas the QUENCH shroud insulation is cylindrical with a thickness of 0.38 m, which is comparable to the inner shroud radius. The deviation can be assessed to app. 40 % with respect to volume and surface.

After 4000 s the GRS peak temperature exceeds the main stream by app. 50 K. The origin of the glitches in the UZA data at 3900 s and 5195 s driving maximum temperature up to 1510 K and 1850 K, respectively, is also unclear.

Final heat-up

At 6000 s the electrical power is increased for the final heat-up phase. Except for NK1 and GRS all results are in the range of 1350 K to 1530 K. First smooth reactions of the codes can be noticed 100 s later, slowly increasing temperature as observed in the experiment. When the maximum temperature exceeds 1850 K various steep temperature increases were found due to transition to high temperature oxidation regime.

However, at 6400 s the INL curve starts unexpectedly with a temperature escalation of app. 2.0 K/s driving temperature straight up to 1900 K and with app. 1 K/s to 2150 K at 7170 s. At 6570 s and at 6840 s glitches in NK1 are observed.

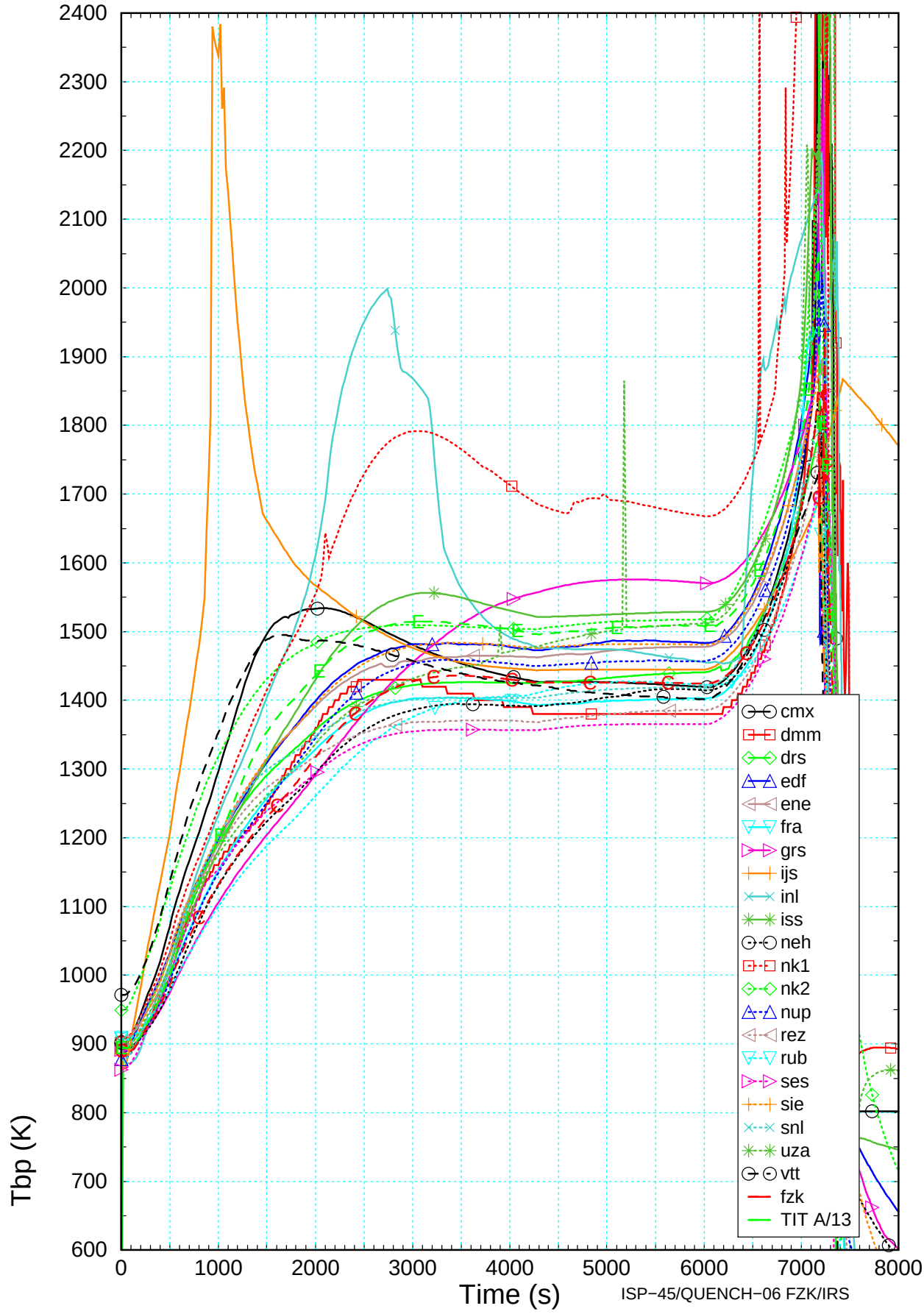

Figure 4.1 Maximum temperature calculated by the participants, post-test calculations with S/R5irs (-C-), and derived from the QUENCH-06 experiment using a thermocouple at 0.95 m (TIT A/13, -E-)

4.1.2 Power data

The knowledge of the power effectively dissipated in the modeled zone is of utmost importance and has to be investigated carefully. Due to thermal feedback mechanisms, small variations may affect the results significantly.

Electrical power input

In the ISP-45 Specification Report /8/, electrical power of the inner (E505) and outer (E506) heated rods as well as total power input (Ptot) and voltage at power supply plugs (E304/E305) have been given as redundant boundary conditions. With the material property data of copper, molybdenum and tungsten and an external resistance of 4 mΩ per rod as specified in /8/ a realistic power balance should be feasible.

Participants were asked to deliver electrical power released in the heated as well as in electrode sections. In Figure 4.2 to Figure 4.4 results calculated by the participants are compared with the results of FZK post-test calculations since no experimental data are available.

First, is must be stated that DMM, NK1, REZ, SES, UZA and VTT did not deliver the requested data and SIE furnished erroneous data for electrical power generation in the lower electrode zone. As mentioned before, DRS curve is not ascending monotonously. Therefore, results look somewhat strange and the thick line corresponds in fact to several lines. CMX values do not correspond in shape with the others and might be attributed to temperature curves. This discussion has to be carried further in the future. As regards IJS results, an over-prediction, maybe linked to equivalent material properties and heating system modeling, is also detected.

First heat-up phase

Up to the end of the heat-up phase, at about 1965 s, all curves spread significantly around the reference FZK curve in a large range of magnitude. INL and ISS estimate an increase in heating power in the lower electrode zone leading to overestimated values after 500 s (app. 12% of the total power released in the bundle instead of a mean value of 6%). DRS curve shows an opposite behavior underestimating values in the lower electrode zone (app. 3% instead of 6%). Those out-of-the-way results could have a common explanation linked to their heater rod modeling.

In the heated zone (Figure 4.3), three participants tend to over-shoot the desired electrical power plateau as was already observed for the peak cladding temperature, INL up to 8900 W, NK2 and ISS in a lower manner up to 8450 W. On the other hand, other participants delivered results which agree quite well.

In the upper electrode zone (Figure 4.4), INL, ISS and NEH under-predict clearly the electrical power release in the bundle (app. 7% of the power released in the bundle instead of a mean value of 14%). On the contrary, DRS and NK2 show an overstated amount of electrical power released in the bundle (app. 28% instead of 14%).

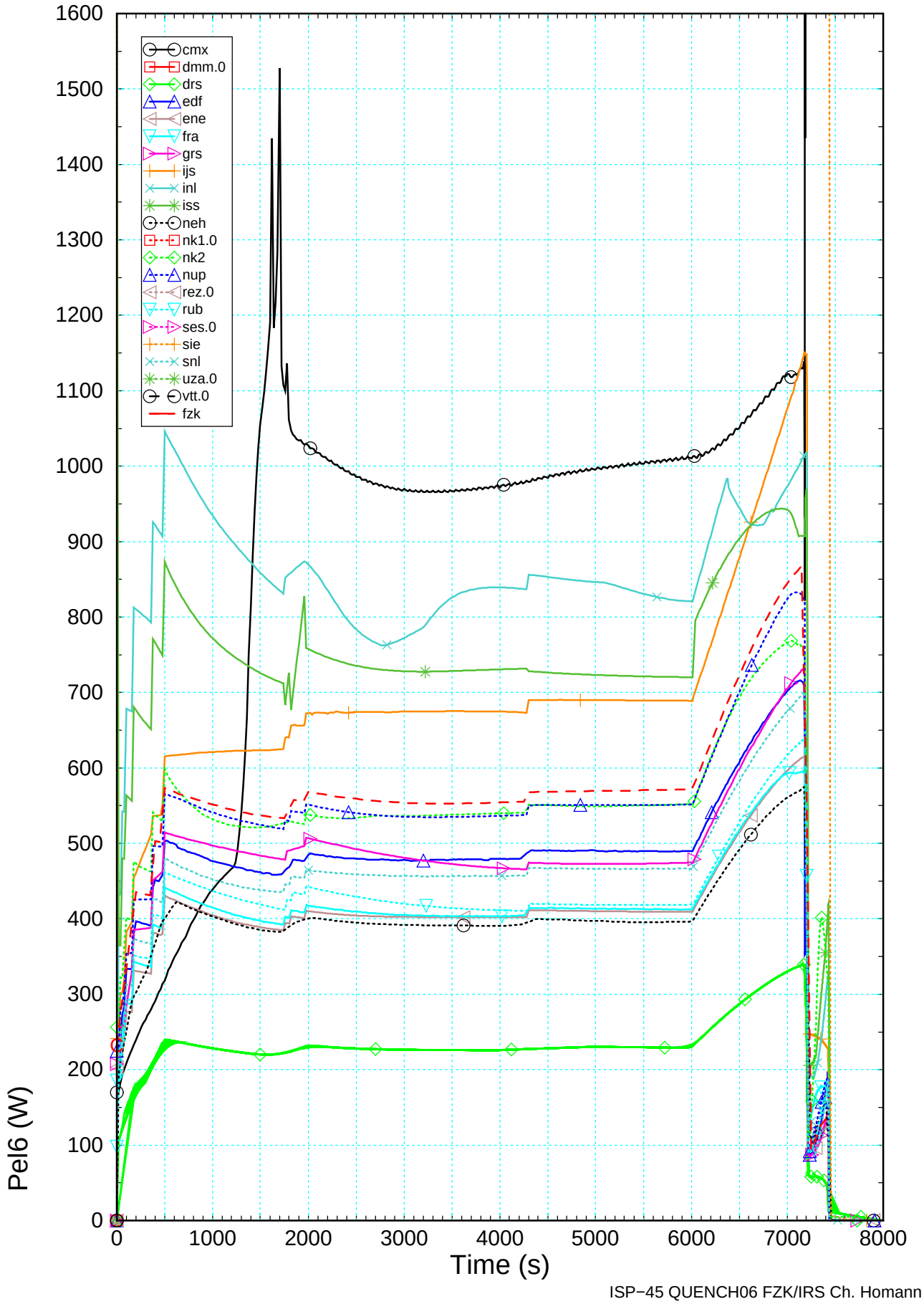

Figure 4.2 Survey of electrical power released in the lower electrode zone compared to results of FZK post test calculations (- - -).

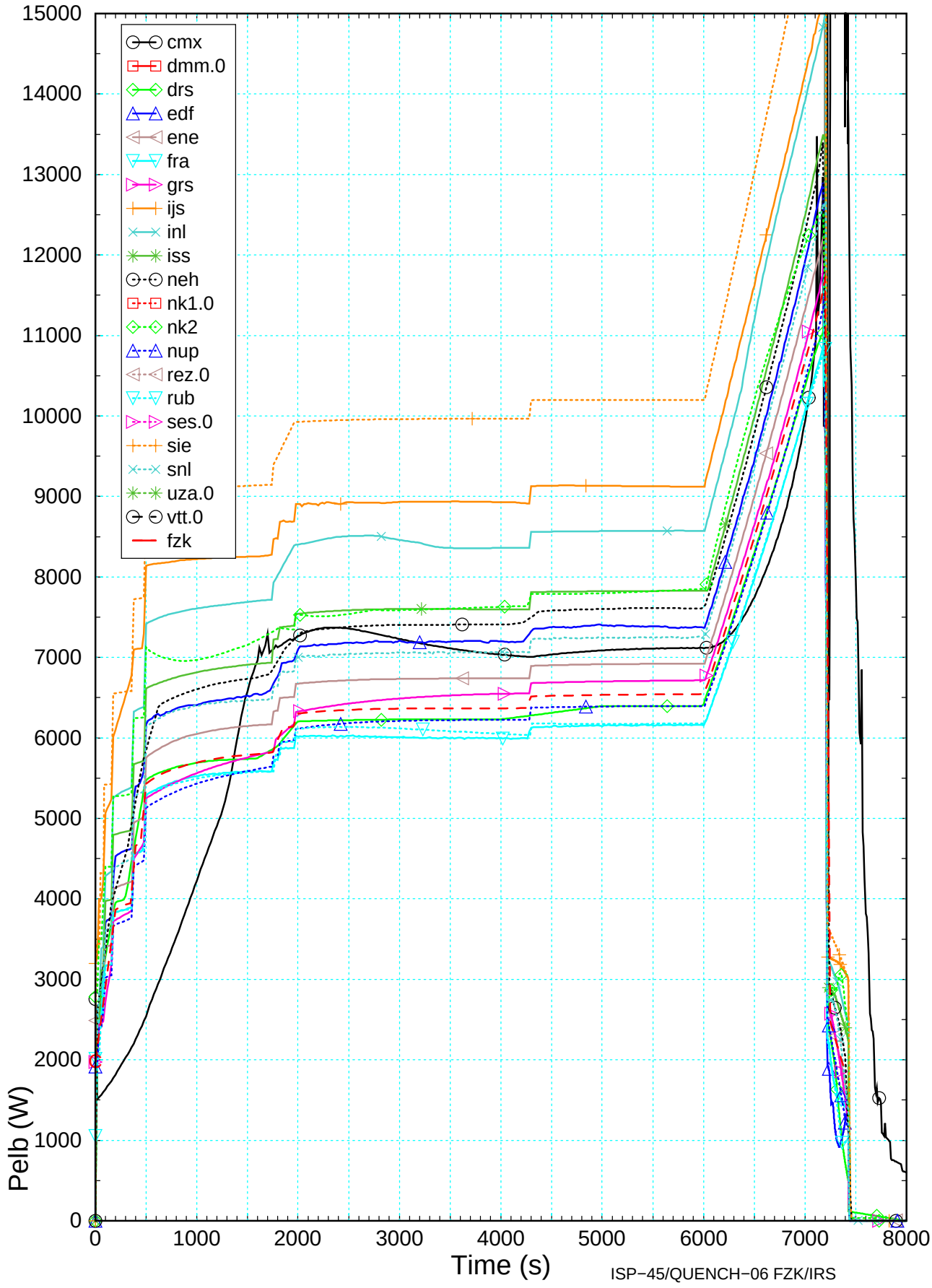

Figure 4.3 Survey of electrical power released in the heated zone compared to results of FZK post test calculations (- - -).

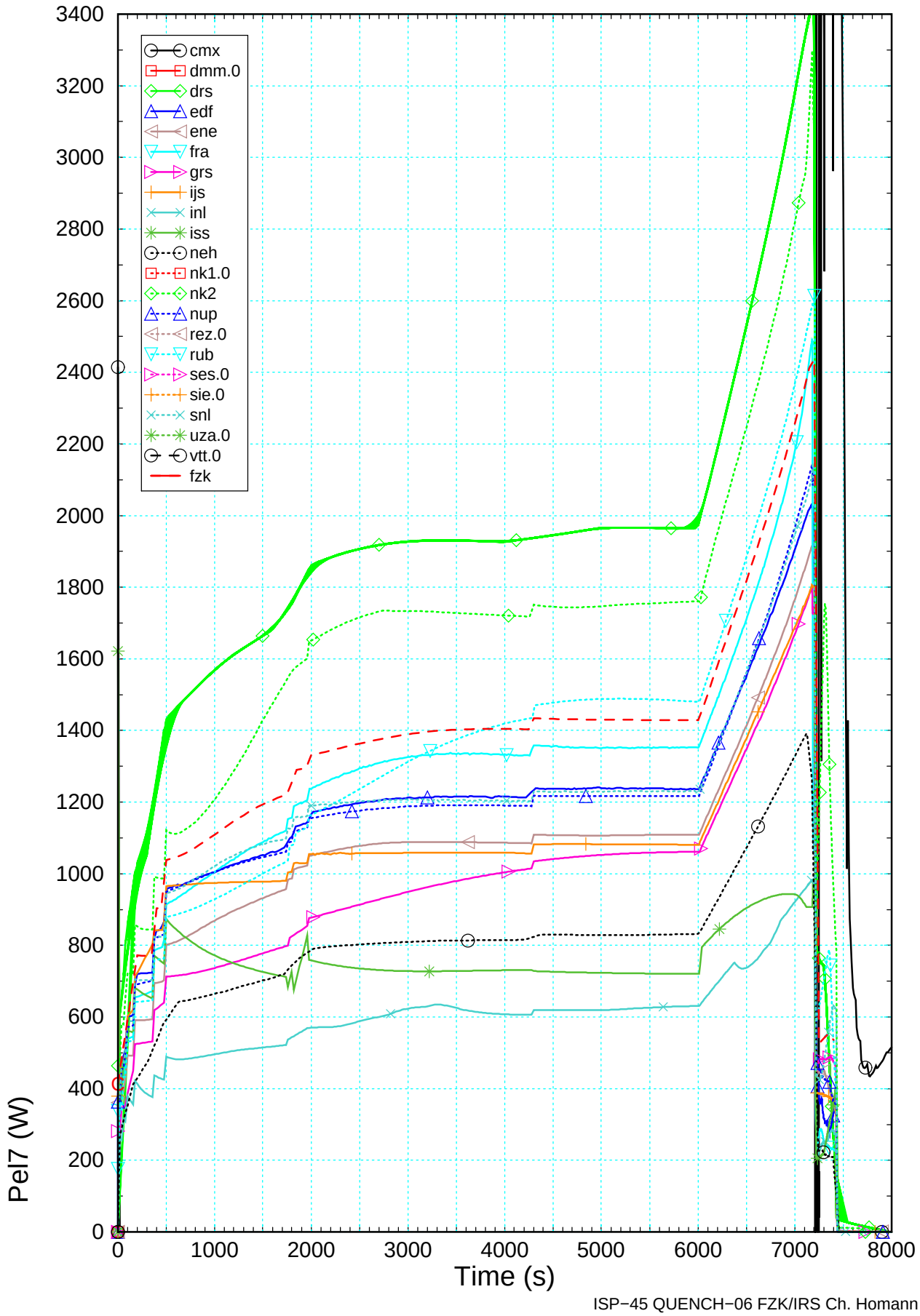

Figure 4.4 Survey of electrical power released in the upper electrode zone compared to results of FZK post test calculations (- - -).

Pre-oxidation phase

Then, during the pre-oxidation phase, the electric power is at app. 8700 W for the heated zone. The temperature is maintained constant for app. 4000 s by control of the electrical power and, in all zones, curves are nearly to maintain the same expected stabilized shape with the exception of INL and ISS. Besides, GRS and RUB show a curious increase in the upper electrode zone (Figure 4.4) from 2000 s up to 4800 s even if their data stay in an acceptable range of magnitude.

Final heat-up phase

At last, we can notice that at the beginning of the transient phase (6010 s) the initiating heat-up rate is quite well achieved in the heated zone (Figure 4.3) for the major part of participants. However, the electrode zones (Figure 4.2 and Figure 4.4) show deviations from expected power increase. Furthermore, sudden short drops were found for ISS at 7000 s and INL at 6400 s which may be caused by temperature escalation.

Exothermal power

All participants delivered results of exothermal power generated by oxidation. In Figure 4.5, results calculated by the participants are compared with the results of FZK post-test calculations (FZK ; -C-) and the experimental data (P.chem).

First, it is noticed that a sharp peak, probably due to post-processing errors, is observed in the first time step of EDF curve and VTT probably sent wrong data with several orders of magnitude lower than experimental data.

First heat-up phase

Whereas the experimental data indicate that the onset of significant oxidation starts at 6000s with the temperature escalation, IJS shows an erroneous sharp peak synonym of strong oxidation of the bundle starting after approximately 1000 s. Some short peaks also appear in NK2, REZ and SES curves all along this phase.

CMX calculated enhanced oxidation between 500 s and 3200 s increasing bundle temperature with app. 0.5 K/s as shown in Figure 4.1 whereas RUB, which is characterized by the slowest temperature increase (0.3 K/s) consequently shows the smallest oxidation power.

Oxidation power calculated by DRS and ENE is slightly overestimated at low temperatures (<1200 K), one explanation may the use of the U/H oxidation correlation.

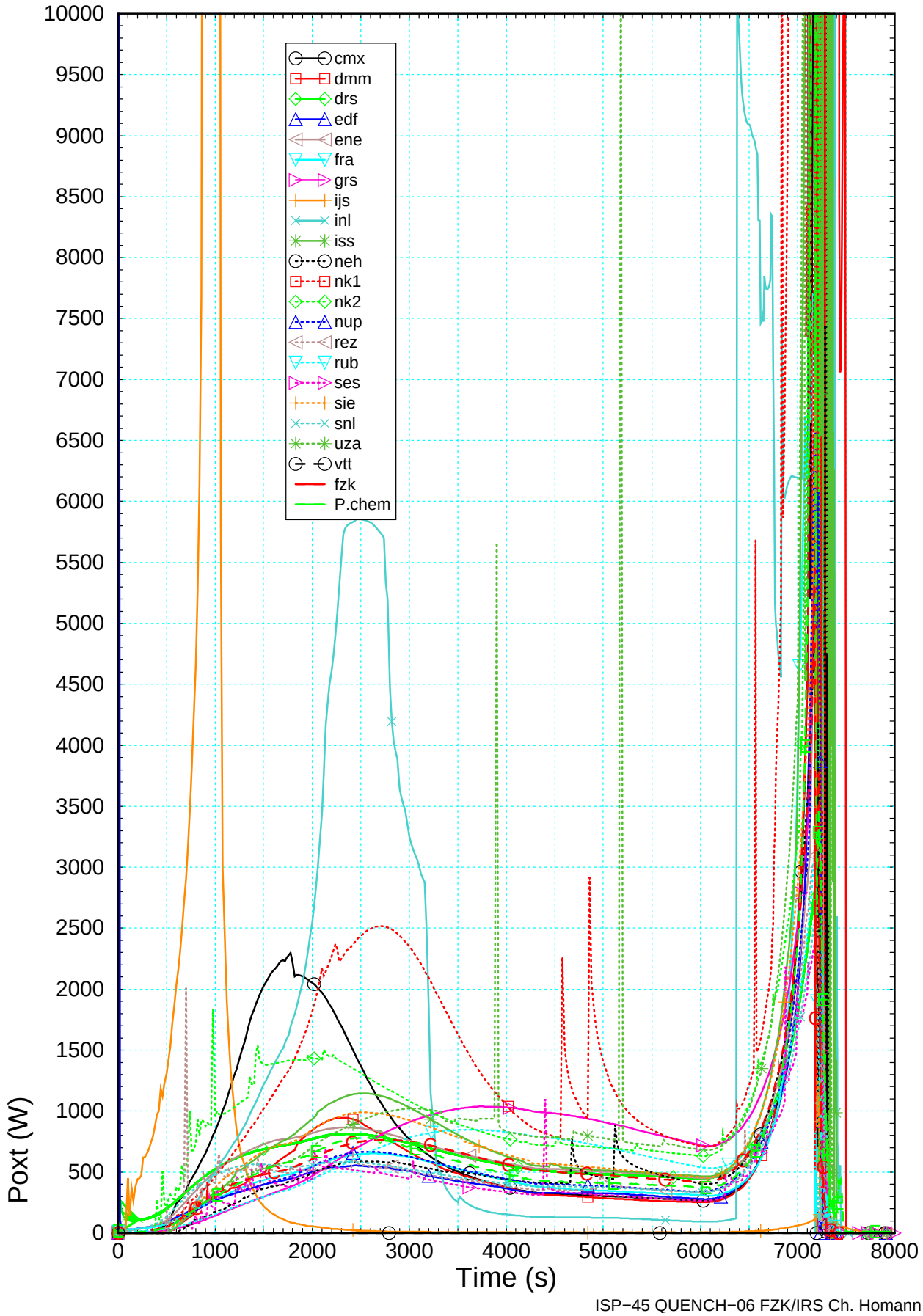

Figure 4.5 Reaction power released by zirconium oxidation compared to results of FZK post test calculations (-C-).

Pre-oxidation phase

NK1 and INL show strongly overestimated oxidation as was already predictable from previous section. GRS, NK2, and ISS seem to adopt the same behavior but with lower amplitude. Unexpected local glitches appear in SES and UZA curves (up to 10600 W for UZA at 5200 s), the origin is quite unclear at the moment and may be associated to numerical problems. NK1 and NEH curves show sudden power peaks beginning at 4600 s, a typical release behavior which gives hints for a calculated cladding failure and a material relocation.

Final heat-up phase

300 s after the beginning of final heat-up, exothermal power calculated by INL shows an unphysical sharp increase which cannot be explained. As already mentioned in section 4.1.1, NK1 maximum temperature curve shows a deviation from the general slope of exothermal power at 6000 s. NK2 and UZA revealed a similar behavior as NK1 during the temperature escalation.

Heat losses through shroud

For a complete energy balance as intended in section 0, the radial heat losses have to be quantified. Therefore, all participants except ENE, SES and SNL delivered data about heat losses through the inner surface of the shroud (Figure 4.6). As no experimental data is available, all results have been compared with the results of FZK post-test calculations (FZK ; -C-).

First, it must be underlined that all calculations do not begin with the same initial heat losses through the shroud due to different results of prior stabilization calculations. Indeed, while major part of curves begins with zero values, some initial values are slightly different and vary from –250 W (NK2) to 2700 W (VTT). Besides, DMM, INL and REZ curves have to be checked carefully because of energy balance discrepancies.

First heat-up phase

As can be seen in Figure 4.6 the predictions of the shroud heat loss spread significantly during the first heat-up phase. 1000 s after beginning of the first heat up phase, the IJS curve deviates significantly from the expected bundle behavior. An unexpected spike also appears at the end of the first heat-up phase in CMX curve. It cannot be explained so far. In addition DRS, EDF, SIE, and VTT over-predict heat losses maybe due to problems in the modeling of the shroud liner and fiber insulation.

Pre-oxidation phase

All reliable heat loss curves increase with the bundle mean temperature given in Figure 4.1 achieving stationary values after app. 3000s. Thus, this indicates near (quasi) steady state conditions in the bundle.

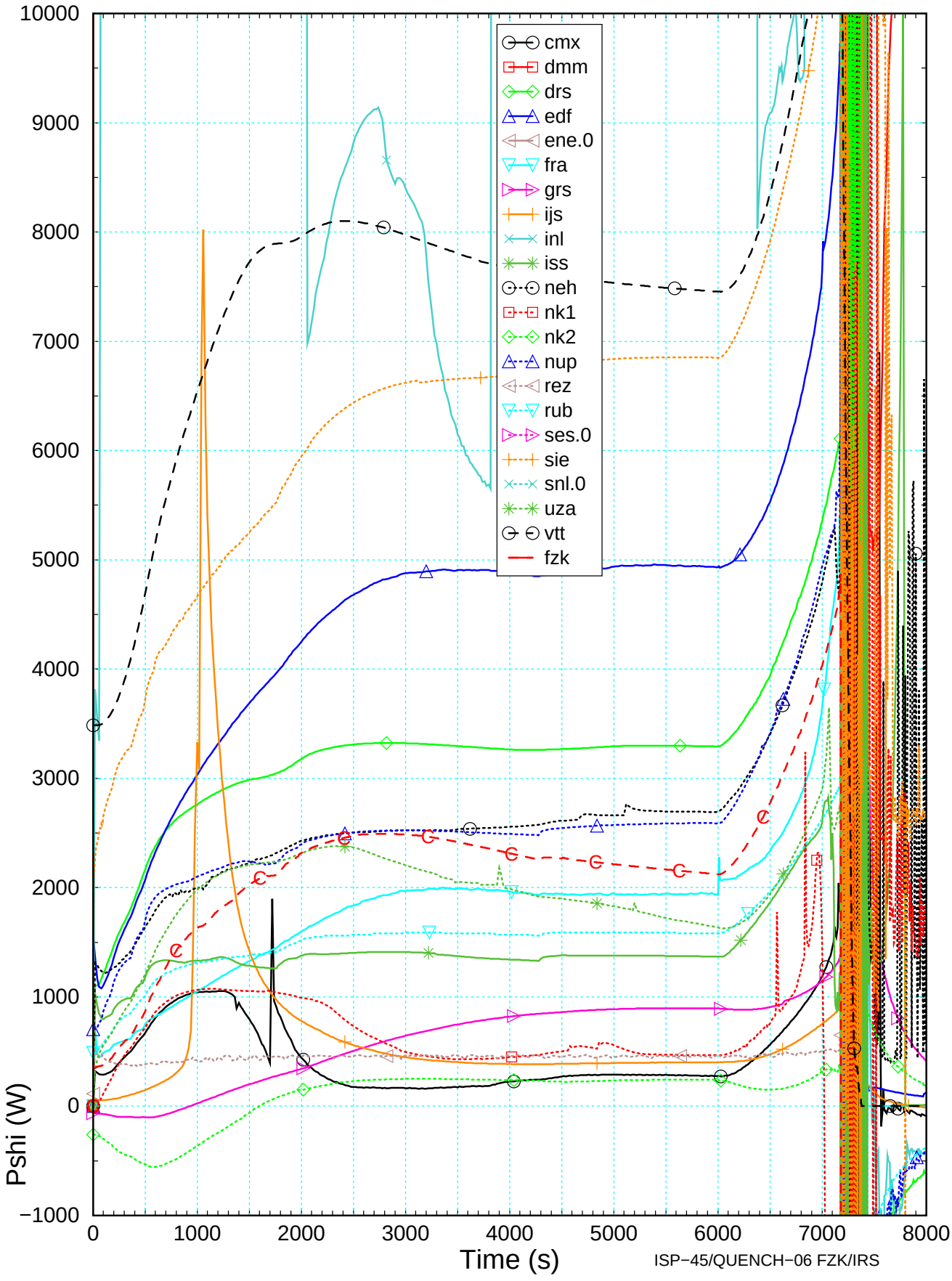

Figure 4.6 Heat losses integrated over whole shroud inner surface compared to results of FZK post test calculations (-C-).

Final heat-up phase

The final heat-up phase starts slowly with power increase at 6010 s and is accelerated by the additional energy release due to Zircaloy oxidation of fuel rods and shroud as can be seen in Figure 4.10. All curves behave similar by except NK2 which shows an opposite curvature. Meanwhile, after 6500s, sharp peaks and a sudden unexpected drop occurs in NK1 curve. Regarding ISS and UZA curves, the same unexpected phenomenon seems to happen about 50 s before quenching.

4.1.3 Steam mass flow rate at bundle outlet

In the ISP-45 specification /8/ only the steam mass flow rate was asked because the Argon flow is stationary. Data calculated by participants and FZK (FZK ; -C-) are given in Figure 4.7. Indeed, there is no experimental data reliable.

Even if nearly all participants delivered steam mass flow values of 3g/s +/- 5 %, two participants, ISS and NK1 must have included the Argon part, so that they end up with 6 g/s. Also CMX and VTT calculated more than 6 g/s. Moreover, unexpected results were delivered by IJS and NK2 with values between 3 g/s and more than 6.7 g/s. The IJS data clearly indicates steam starvation at app. 1000 s and the curve shows a tremendous noise up to quench initiation. The main origin is that water was injected unintentionally. The VTT plot also show a constant decrease up to 5500 s and after 6000 s an unexpected increase, may be due to an early reflood initiation. All reliable results show a significant steam consumption after 6300 s caused by the increased oxidation in the bundle.

4.1.4 Bundle outlet temperature

To complete a global energy balance, the amount of convective heat losses has to be checked. Since the fluid inlet temperature was specified in /8/ (TFS 2/1) only the fluid temperature (Tfg9) at the bundle outlet is missing. All participants delivered that data. However, data of IJS is outside the expected range and those of ISS and DMM are quite stationary, so that a post-processing error has to be assumed. Thermocouple T512, dedicated to measure fluid temperature at the outlet, is situated in a rather cold environment outside the bundle, so that only results of post-test analyses with S/R5irs are used for comparison in Figure 4.8.

As mentioned in section 4.1.1 the initial temperatures vary in a wide range between saturation temperature (VTT, 380 K) and 860 K (NK2). Remarkable deviations are the drop of the INL gas temperature after 3200 s and the pretty low gas temperatures of REZ. Main contribution of the low REZ values is the supplementary simulation of the rather cold off-gas pipe. Steepest temperature increase in the final heat-up phase is calculated by NK1.

Gas temperature variations in the post-test calculations with S/R5irs amount to +/- 20 K between different calculations at a given time in the pre-oxidation phase. So, assuming that the fluid thermal properties are comparable, these data can be interpreted and used for comparison as the calculated energy loss to the fluid during the pre-oxidation phase, neglecting the hydrogen, which is still rather small in this phase.

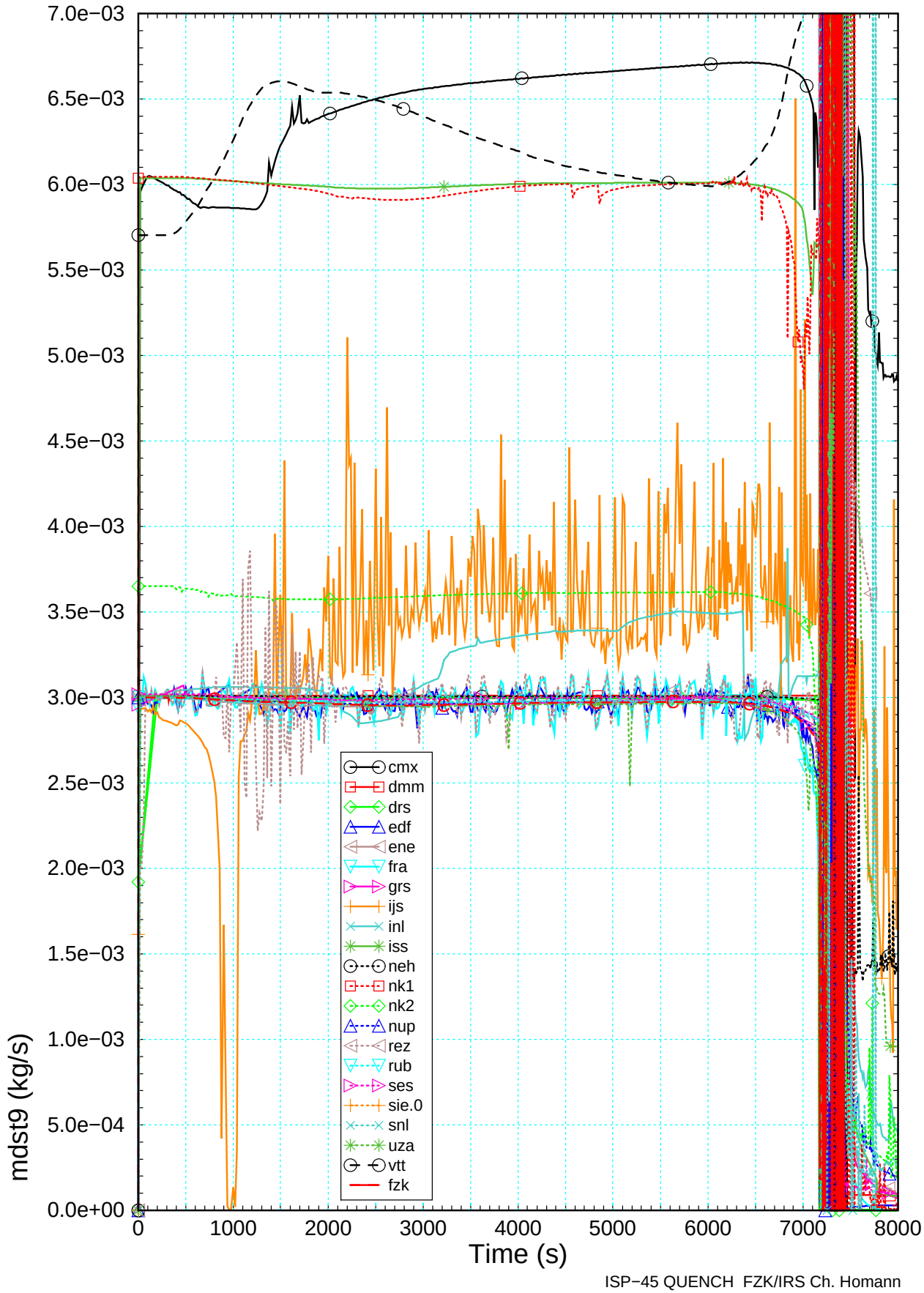

Figure 4.7 Steam mass flow rate (mdst9) at the bundle outlet calculated by participants and by FZK post-test analyses (-C-).

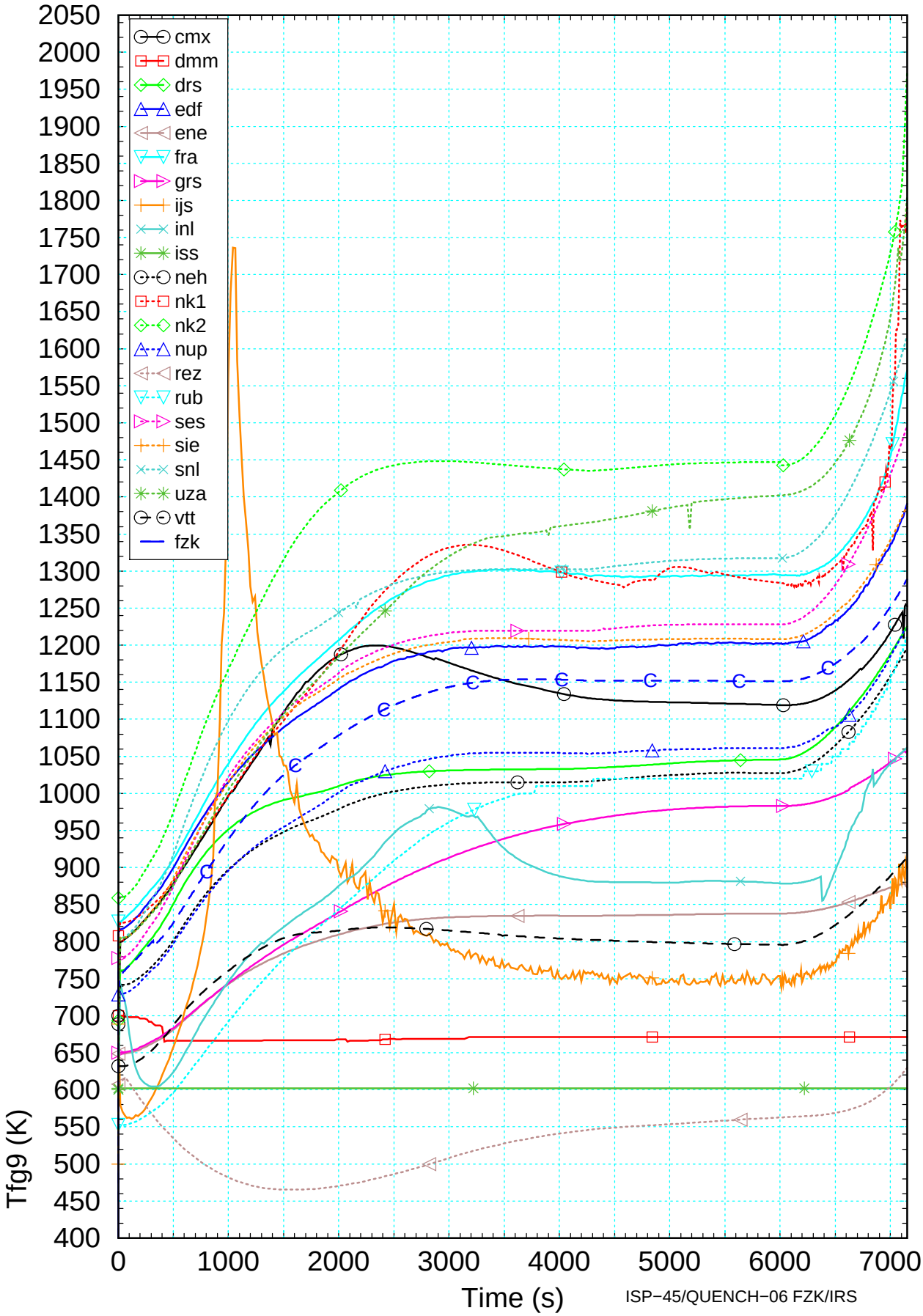

Figure 4.8 Fluid temperature at the bundle outlet (Tfg9) calculated by participants and by FZK post-test analyses (-C-).

The wide spread of the temperatures (app. 400 K) may be explained by differences in the modeling of the test section, the electric and exothermal power release as well as thermal-hydraulics limitations of the codes. Moreover, this strong temperature spread can be explained by difference in modeling of the heat transfer between shroud outer surface and inner cooling jacket by radiation. Some participants considered that peculiarity and increased the radial heat losses (Pshi) artificially thus decreasing the bundle outlet gas temperature (Tfg9).

4.1.5 Hydrogen source and total mass

Hydrogen source term

The data for the hydrogen source was already shown in Figure 4.5 because the exothermal power is strictly proportional to the released hydrogen, but here the magnification is increased so that the spreading becomes more visible. Generally the temperatures in the test section are too low for significant oxidation before app. 500 s, but not for IJS which shows a dramatic increase starting from the beginning.

Neglecting the spikes and glitches which were already discussed in section 0 the spread of the data is very large during first heat-up phase, extending up to 3000 s. Assuming that the Zircaloy oxidation model is implemented correctly, the steep increase in hydrogen release may originate from errors in the energy balance so that the exothermal energy is not released but stored in the cladding leading to the observed temperature excursion.

The initiation of reflood can be seen in the results by very strong variations due to the used shattering models. After 7500 s no hydrogen release was calculated.

Hydrogen mass

The total hydrogen mass is one of the target results of the ISP-45. The mass spectrometer data of QUENCH-06 are listed in Table 4.1 and are given in Figure 4.10. These values are already corrected to account for measuring errors. They do not include the stored hydrogen which amounts to additionally 3.5 %.

A clear mainstream can be detected which comprises the results of 14 participants. Two others are in the vicinity and 4 participants delivered data which were influenced by either code errors or misinterpreted specification.

As discussed in section 4.1.1 the Zircaloy oxidation during the steep temperature increase calculated by IJS at 1000 s is caused by uncontrolled oxidation which is only limited by steam starvation at 1064 s. During this short time period nearly all hydrogen is produced.

Similar conditions are observed for INL where 0.046 kg were calculated up to 3260 s. Also CMX, NK1, NK2, and VTT deviate significantly from the experimental data before reflood initiation.

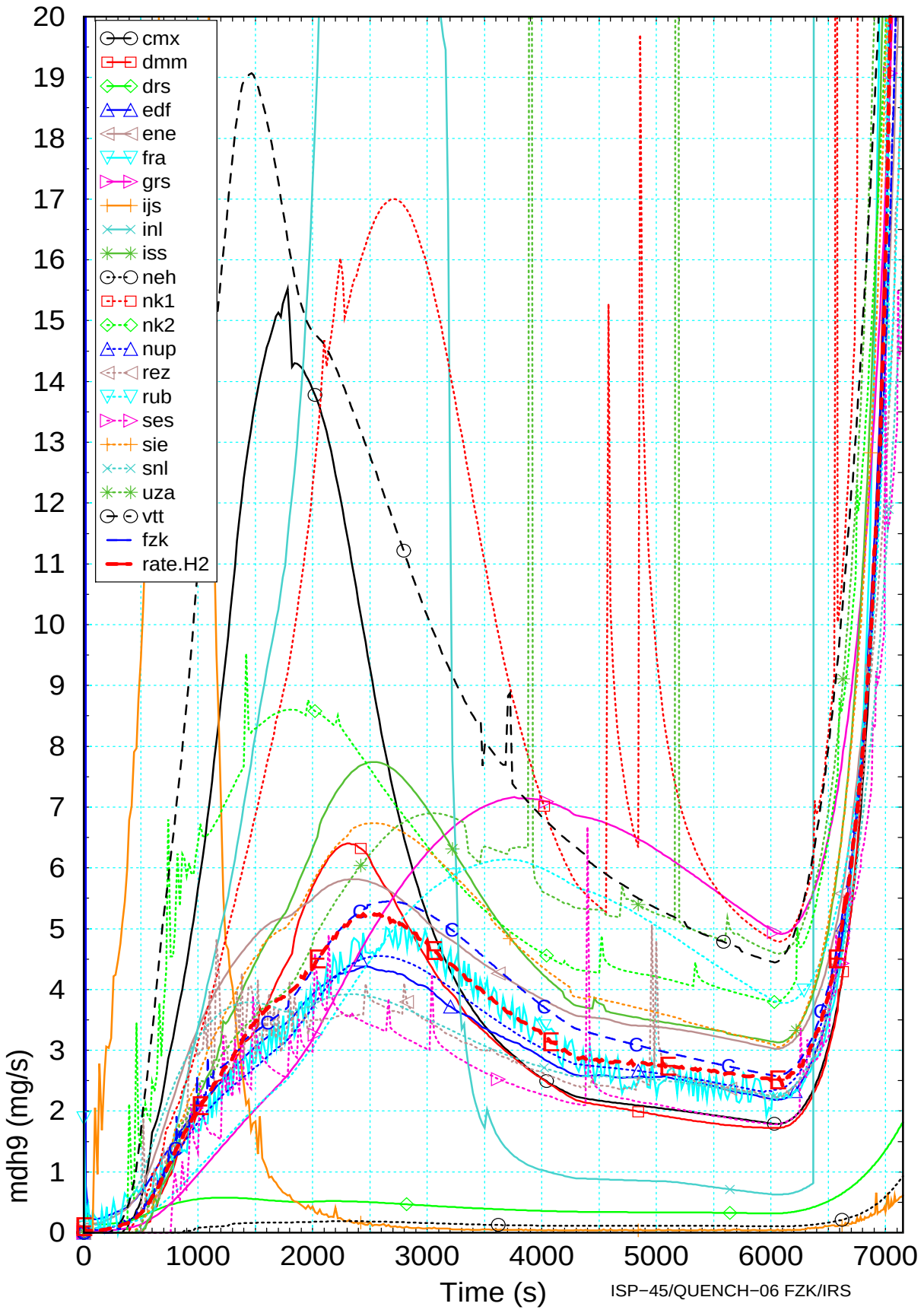

Figure 4.9 Hydrogen source at bundle outlet (mdh9) calculated by the participants and compared with measured data (-E-) and post-test calculations with S/R5 (-C-).

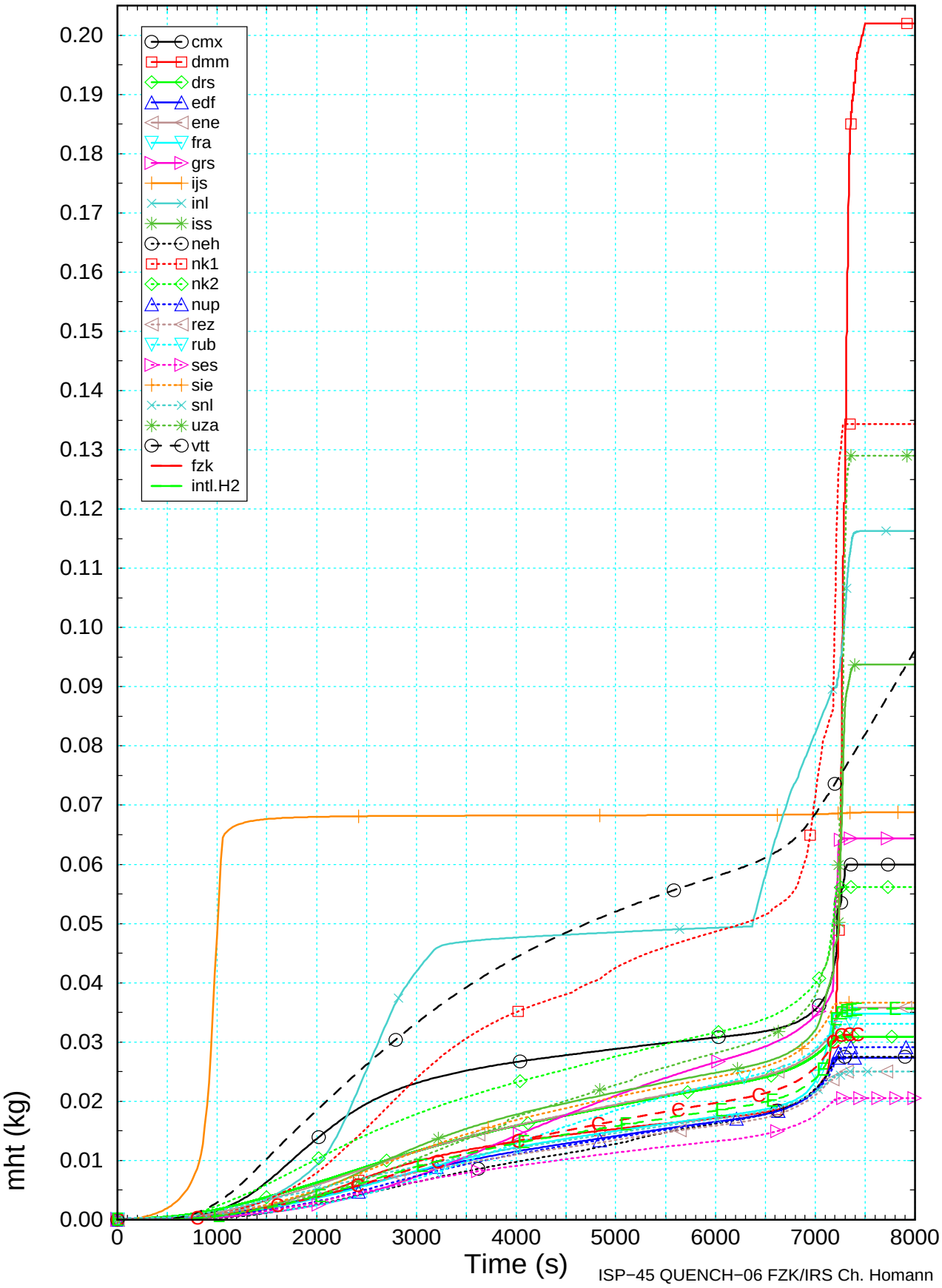

Figure 4.10 Total hydrogen mass calculated by the participants and compared with measured data (-E-) and post-test calculations with S/R5 (-C-).

The range of results delivered by the participants (Table 3.2) is given for four times in Table 4.1. The tendency to over-predict the hydrogen productions is obvious, especially in the quench phase (last column of Table 4.1). The extreme value at 8000 s represents a nearly complete oxidation of the Zircaloy inventory of the bundle. The values calculated for the reflood phase are discussed in detail in section 4.6.5.

Table 4.1 Assessment of hydrogen mass and its distribution during course of ISP-45.

Time	**2000 s**	**6000 s**	**7170 s**	**8000 s**
Experiment	4 g	18 g	31 g	35.6 g
Mainstream Min	2 g -50%	13 g - 30%	20 g - 37%	20 g - 42%
Mainstream Max	6 g +50%	32 g + 56%	50 g + 67%	134 g + 285%
Extreme Value	*68 g*	*68 g*	*95 g*	*202 g + 480%*

The accuracy of the mass spectrometer can be assumed to +/- 5 % (section 2.1.7). The scatter of FZK post test calculations ranges between 0.028 kg and 0.046 kg.

4.2 Fluid mass balance

As discussed in the previous section (section 4.1.3) the fluid conditions at the inlet were predefined by the specification report. The fluid is composed of 3 g/s argon plus 3 g/s steam. At the end of the test section, at least the argon mass flow rate should be maintained. To check the fluid mass balance in the test section, we used the steam mass flow (mdst9, Figure 4.7) and the hydrogen mass flow rate (mdh9, Figure 4.9) to check the mass balance of thermal-hydraulics part and oxidation models.

In both figures, some strange plot can be seen. If these deviations originate only from oxidation, they should vanish in Figure 4.11. For most of the participants the residual values are close to the input value of steam. Two participants delivered the total mass flow rate at bundle outlet, composed of steam, argon, and hydrogen (ISS, NK1).

Others show a strong drift (CMX, INL, VTT) during pre-oxidation as discussed earlier. In case of DMM a deviation is observed at app. 2200 s and after 6500 s, indicating mass balance errors caused by steam removal and hydrogen release, probably due to enhanced oxidation.

One participant (IJS) calculates very strong oscillations due to the unintended injection of water into the test section, which causes evaporation and/or condensation problems /21/.

The experimental value, mass flow rate of steam plus hydrogen, measured by the mass spectrometer in the off-gas pipe deviates from the ideal line due to steam condensation. The condensed water flows to the main steam condensor and is considered in the global water balance.

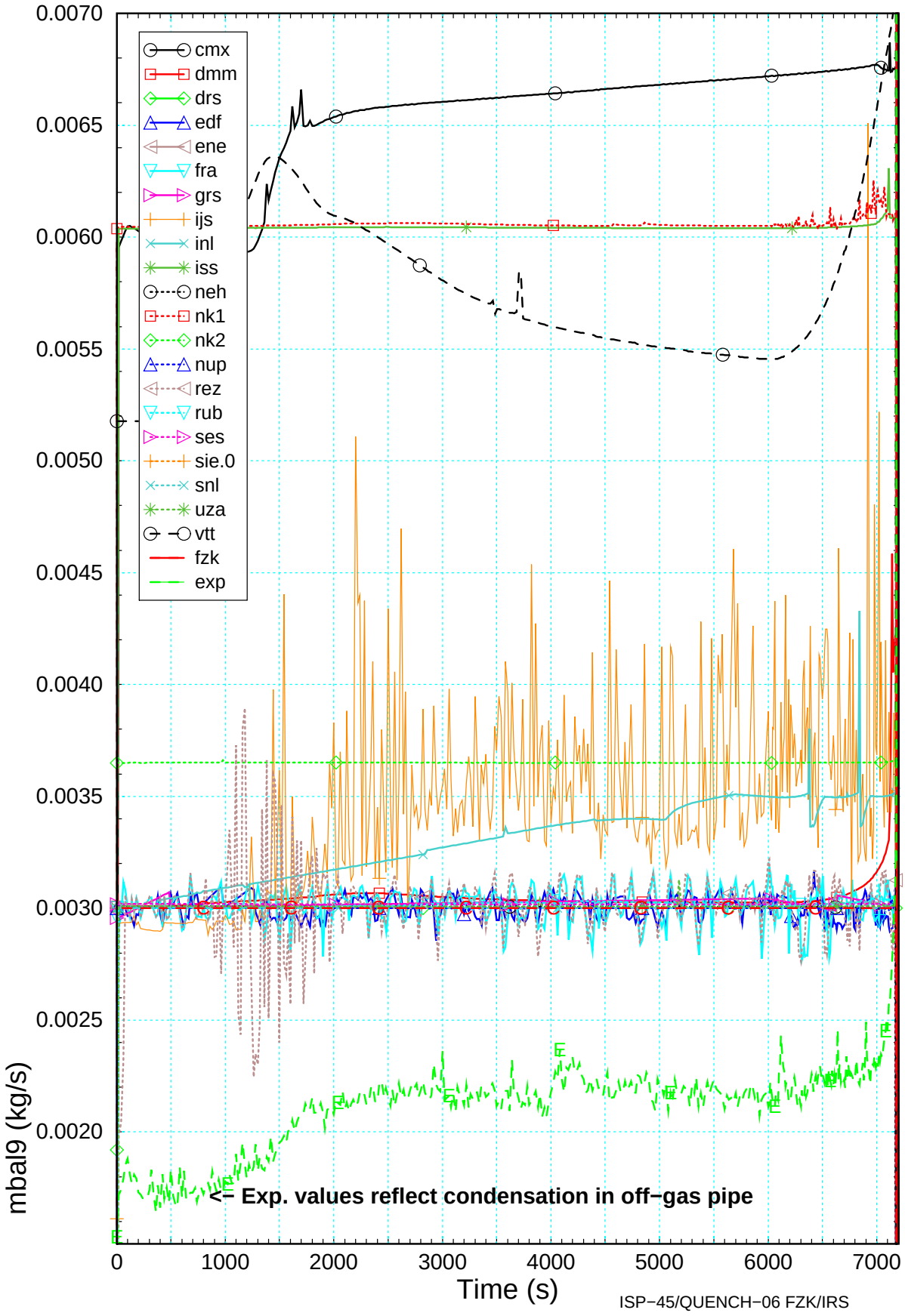

Figure 4.11 Fluid mass balance (mdst9 + 9*mdh9) calculated by the participants and compared with measured data from experiment (-E-) and post-test calculations with S/R5 (-C-).

4.3 Global energy balance

The list of the global data allows to check the energy balance and so to assess the achieved quality and the reliability of the simulations. For comparison purpose a coarse energy balance can be described by:

$$P_{elt} + P_{oxt} - P_{axt} - P_{shi} - H_{diff} = P_{bal} = P_{store} \quad (4.1)$$

with $P_{elt} = P_{el6} + P_{elb} + P_{el7}$

The energy source P_{elt} (sum of P_{el6} (Figure 4.2), P_{elb} (Figure 4.3), and P_{el7} (Figure 4.4)) is the total electric energy released in the test section as shown in Figure 4.12 bottom. The other energy source, which is the exothermal power P_{oxt} shown in Figure 4.5, amounts to only app. 700 W during pre-oxidation phase as shown in Figure 4.12.

The energy sinks are given by P_{shi} (Figure 4.6), P_{axt}, P_{fluid}, and P_{store} as shown in Figure 4.12 bottom. P_{axt} is the axial heat loss due to heat conduction in the molybdenum electrodes of the heater rods assessed by 1-D heat conduction calculation. Contribution of heat conduction in ZrO_2 pellets or in the Zry cladding can be neglected.

P_{fluid} is the heat transferred to the fluid via convection and radiation. The convective term can be calculated from the data given assuming that all participants used same material properties of steam and argon. It also includes the radiation absorption in the fluid. Since the hydrogen mass flow rate (Figure 4.9) is less than 1 %, it will be neglected in the following discussion. Hence P_{fluid} is reduced to H_{diff} which can be calculated as follows:

$$H_{diff} = \Delta H_{Ar} * \dot{m}_{Ar} + \Delta H_{Steam} * \dot{m}_{Steam} \quad (4.2)$$

with $\Delta H = H_{out} - H_{in}$

H steam or argon enthalpy.

For H_{in} the fluid temperature in the first elevation is used as delivered by the participants (Figure 4.13). At this elevation the fluid inlet temperature is defined in /8/ based on the TFS 2/1 reading and it should be matched by the participants, but evidently not in all cases. For H_{out} the variable Tfg9 is used as calculated by each participant.

In order to confirm Eq. (4.1) the results of FZK post-test calculation are used. In Figure 4.12 top, the contribution of the argon and the steam mass flows are shown. Below, H_{diff} is compared to the result of RELAP5 variable q (P_{bun} in Figure 4.12 bottom) which sums up all heat transferred from all surfaces to the fluid. As can be seen in Figure 4.12 bottom, that value (P_{bun}) equals to the estimated enthalpy difference (H_{diff}). This demonstrates that the contribution of the hydrogen can be neglected and the enthalpy difference according to Eq. (4.2) is adequate to balance heat losses to the fluid and to compute the power balance P_{bal}. Based on P_{bun} the power balance P_{bal2} is calculated . In brief, but both power balance values are identical, both do not equal to zero as indicated in Figure 4.12 bottom.

The main part of that difference is attributed to the storage term, P_{store}, which characterizes the increase in inner energy of fluid and structures in case of heat-up. In the fast heat-up phase, this term deviates significantly whereas during the pre-oxidation phase the value decreases to the error level of this coarse energy balance since the temperatures in the bundle are no strictly stationary. P_{store} amounts to app. 500 W (app. 6 % of the total energy source), which is in the range of the oxidation power P_{oxt} during pre-oxidation phase.

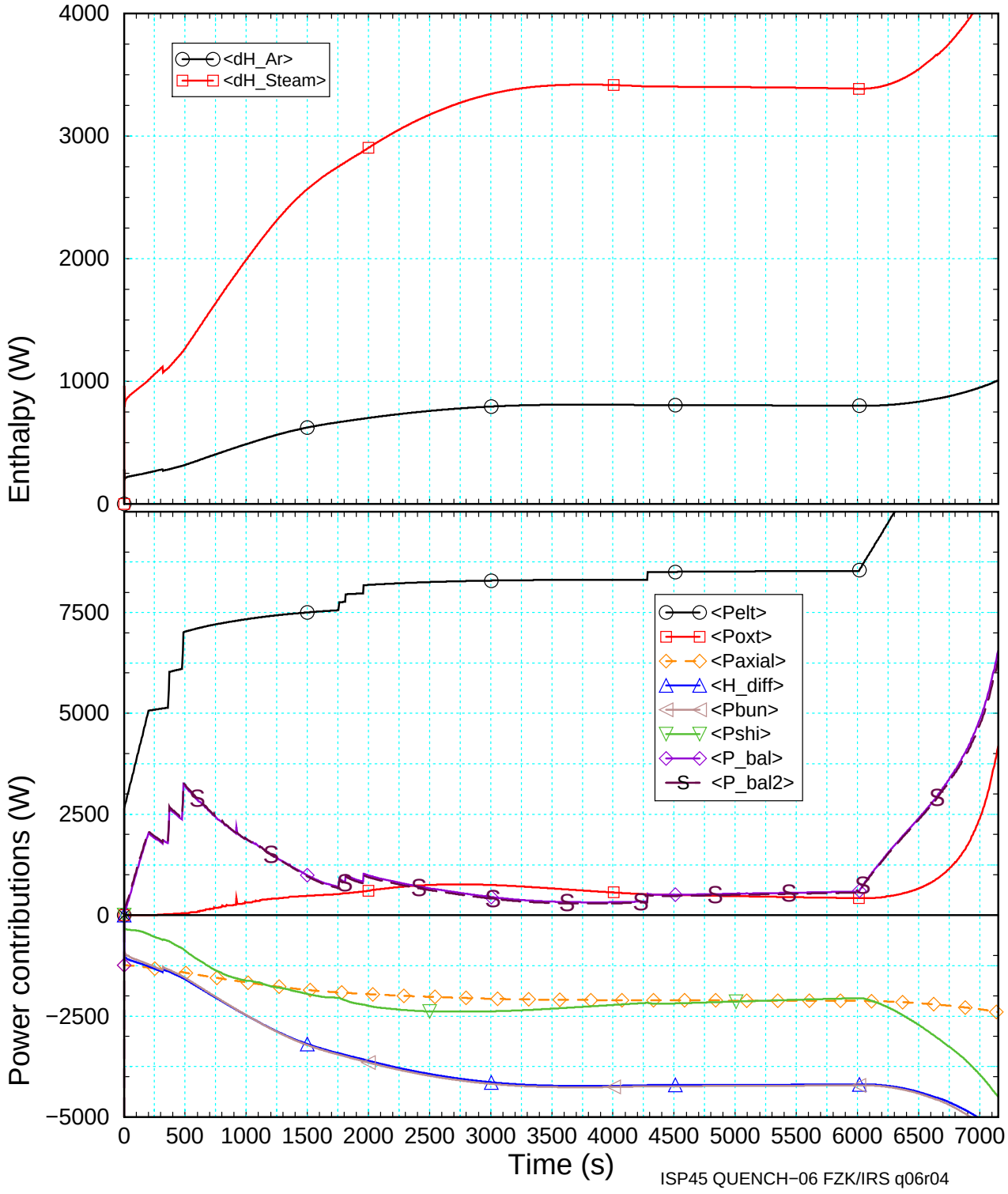

Figure 4.12 Global power balance derived from FZK post-test calculations: top: fluid enthalpy (Steam plus argon) increase along the test section and (bottom) power balance.

Based on these equations, a coarse power balance was performed for all participants and summarized in Figure 4.15. Since the axial nodalization varies between participants influencing the axial heat flux to water cooled ends, such heat losses due to axial heat conduction in the electrodes were not considered. From our experience these heat losses sums up to app. 2000 W for both, the upper and the lower connections of the heater rod molybdenum wires to the water cooled ends. Also, this sink term is rather stationary as can be seen in Figure 4.12 bottom, because the axial boundary temperatures do not vary strongly during test. Even during final heat-up phase, this term only increases by 20 %. For a more detailed analysis the variation of the local temperatures in the bundle due to oxidation or convective cooling should be considered, too. But this is beyond schedule.

Since all terms required for the energy balance (Eq. 4.1) were already discussed in the previous section (4.1.2) only the inlet temperature remains. So, calculated vapor temperatures at the lowest node (01) as well as the initially defined input temperature TFS 2/1 are given in Figure 4.13. Then, in order to identify the reasons of the discrepancies the intermediate result of the energy balance H_{diff} is given in Figure 4.14. Finally, the results of the coarse power balance are given in Figure 4.15.

Fluid inlet temperature

If the fluid input does not match the initially defined input temperature, the inlet enthalpy term in Eq. 4.2 becomes wrong. Such happened to DMM and INL whose values decrease constantly with time, and to CMX and IJS whose temperatures drop during first 2000 s to app. 400 K.

FRA, RUB, and SIE used lower values which follow the temperature history of the specified input temperature. The purpose of these deviations is unclear. Except for these participants the fluid temperatures do not vary more than 10 % compared to the experimental value TFS 2/1, so that a rather good adjustment of the input model for the QUENCH facility can be stated.

Enthalpy difference

In Figure 4.14 two values for enthalpy differences are given, H_{diff1} for the whole bundle (top) as used in the power balance and in the lower figure H_{diff2}, the enthalpy difference from the entrance (TFS 2/1) up to the 13th axial level at 0.95 m. The latter graphic was created to exclude possible difficulties arising from the cold shroud in the upper electrode zone.

For H_{diff1} (Figure 4.14 top) a mainstream is found within a scatter band of 15 % at the end of the pre-oxidation phase, located between the measured electrical power input P_{tot} and the post test calculations of FZK as a lower value. Indeed, the FZK value may be a lower bound because of the effective heat transfer by radiation to the water cooled cooling channel outside the shroud. Besides, comparing the heat transfer to the fluid with the electrical power /8/ released in the same section, CMX, INL, ISS, NK1, RUB, and VTT over predicted convective losses significantly.

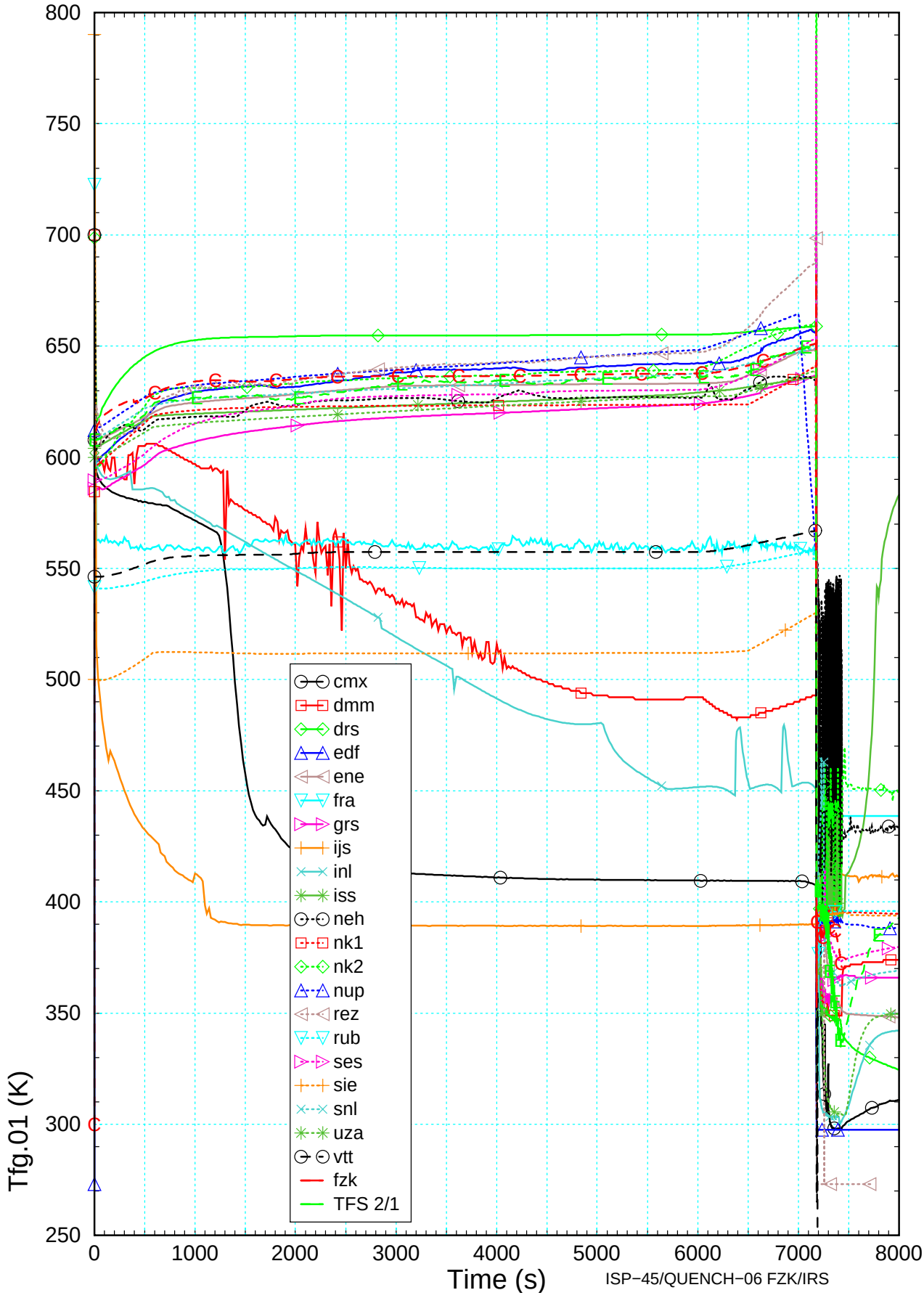

Figure 4.13 Fluid inlet temperature (Tfg_01) at lowest bundle elevation calculated by the participants compared with post-test calculation with S/R5 (-C-) and delivered fluid inlet temperature derived from TFS 2/1.

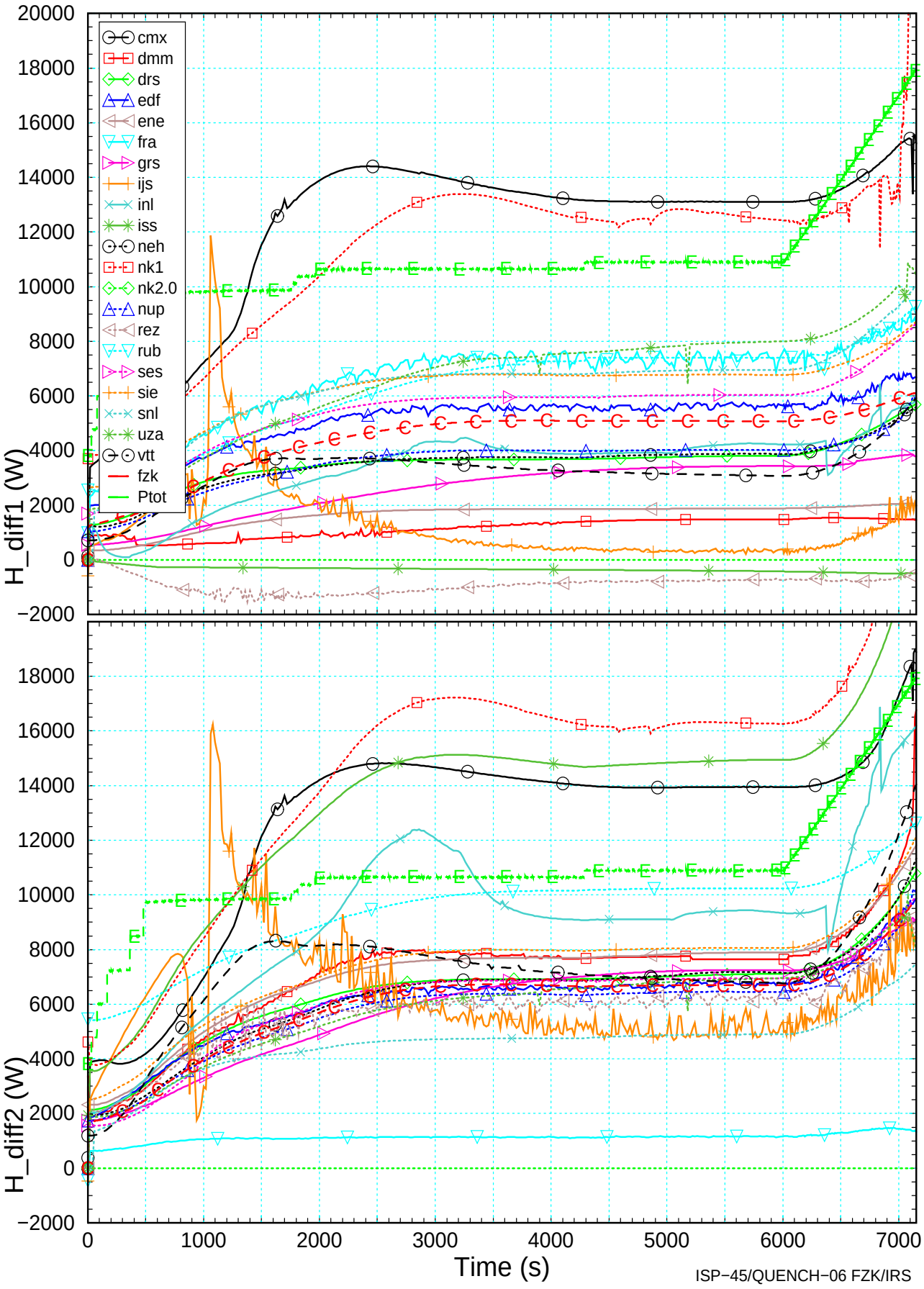

Figure 4.14 Enthalpy difference computed for the whole bundle (H_diff1, top) and for the test section up to 1.0 m (H_diff2, bottom) compared with the electrical heat input (-E-) and the post-test calculation with S/R5 (-C-).

This may arise due to the upper electrode zone as can be seen in Figure 4.14 bottom, in which only CMX, DMM, ISS, and VTT exceed the electrical power. In this case the FZK results are in the middle of the mainstream of similar depth as found for H_{diff1}. In the heated section Figure 4.14 bottom, DMM, ENE, ISS, and REZ under-predict convective heat losses. Moreover, VTT has two handicaps, first: no dedicated heater rod model, and secondly an overestimated growth rate of their oxidation model.

Taking into account that the modeling of rather a small integral test facility is much more difficult due to large influence of the radial boundary conditions compared to a nuclear power plant, the results of DRS, EDF, FRA, GRS, INL, NEH, NUP, SIE, SES, SNL, and UZA are acceptable.

Power balance

For the power balance, only data which were requested in /8/ and shown in section 4.1 were used. Also only the quasi-stationary time interval between 2000 s and 6000 s was considered for discussion. Furthermore, one additional assumption was made with respect to argon. For simplicity we assumed for all participants a mass flow rate of 3 g/s and a constant Cp value of 520 W/kg*K. This amounts to heat flux density rate of 1.56 W/s*K.

As mentioned earlier, an acceptable power balance should lead to a residual storage value between 1500 W and 3000 W for the temperature plateau in the pre-oxidation phase but quite a different situation was found for the power balance Pbal as shown in Figure 4.15. In this region only results of DRS, NEH, NUP, RUB, SNL, and FZK are found.

From this energy balance, five candidates should have cooled down the bundle, because of negative residual values, may be due to sign error. For another class of participants the power balance amounts to values which are comparable to the electric heat input, so that a detailed discussion is obvious due to basic error in simulation of single phase thermal-hydraulics and heat fluxes.

In a first glance we did not identify a code specific tendency, such as integral codes versus detailed codes, so that user effects may have contributed most. To identify the origins of these deviations we will repeat this analysis with data obtained from open calculations.

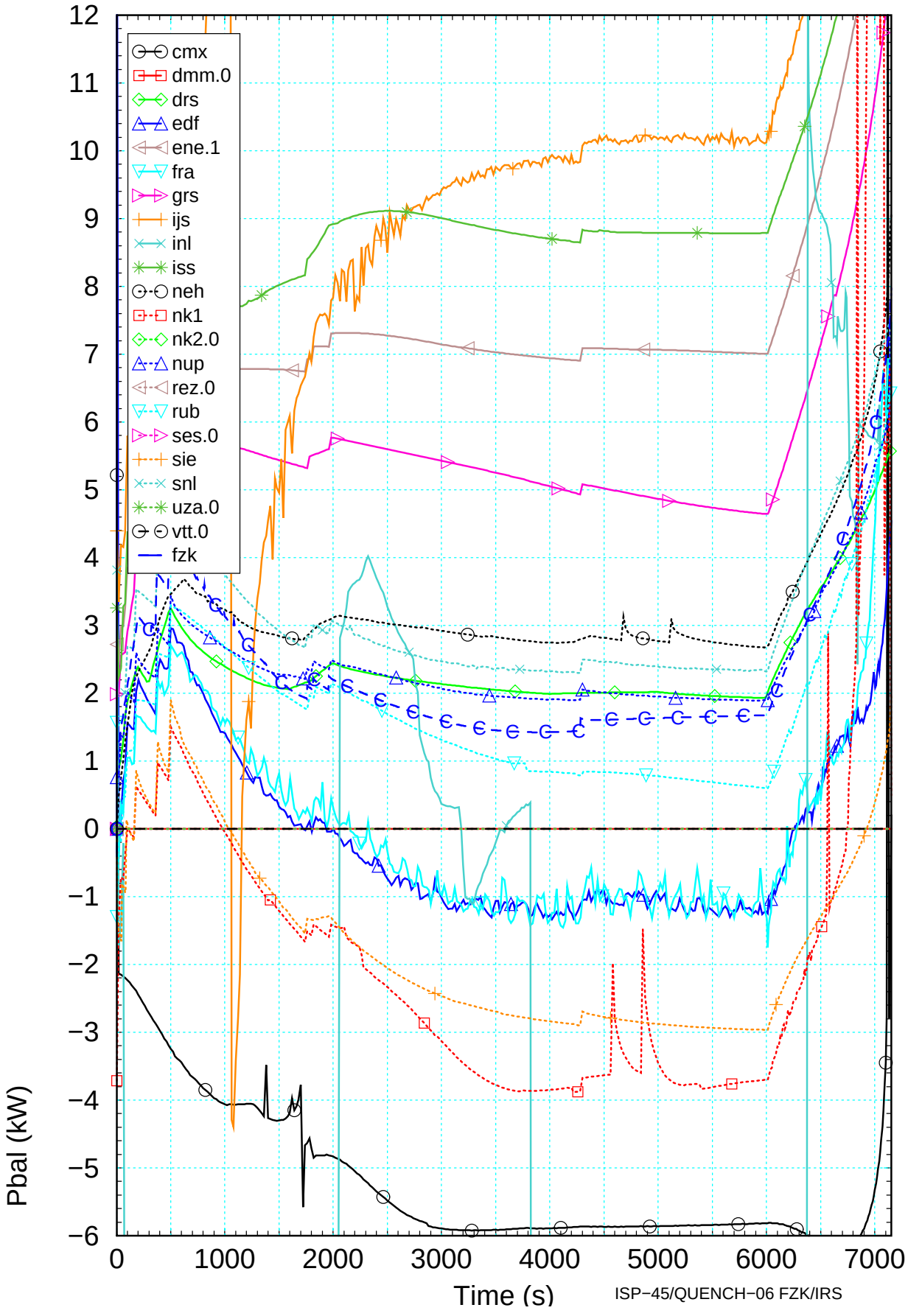

Figure 4.15 Power balance derived from data delivered by the participants without consideration of axial heat losses in the copper wires (Paxial) compared with post-test calculation with S/R5 (-C-).

4.4 Axial profiles

4.4.1 General

In the final transient phase the rapidly increasing temperatures and the enhanced oxidation cause uncertainties in the description of the bundle state. To allow a better interpretation of the bundle state, the participants were asked to deliver axial profiles for the electric power, various bundle and shroud temperatures, and oxide layer thickness for various bundle components at four times as shown in Table 4.2. This amounts to 55 axial profiles from which a subset of 12 are discussed here. The others are shown in the appendix in section 8.3. The discussion of the axial profiles at 8000 s is given in section 4.7.

Table 4.2 Times and events of axial profiles

	Time	Specification / event	Quantity
1	6000 s	end of pre-oxidation phase (section 4.4.3)	Pel (iax), Tc (ic,iax), δ_{ox} (ic,iax), $\dot{m}$ (H_2)
2	6620 s	corner rod withdrawn (section 4.4.4)	Pel (iax), Tc (ic,iax), δ_{ox} (ic,iax), $\dot{m}$ (H_2)
3	7170 s	Just before reflood initiation (section 4.4.5)	Pel (iax), Tc (ic,iax), δ_{ox} (ic,iax), $\dot{m}$ (H_2)
4	8000 s	End of cool-down, final bundle state (section 4.7)	Tc (ic,iax), δ_{ox} (ic,iax), m $_{(Zry)}$ (iax)

with:

iax: the axial resolution as specified in /8/
ic: unheated rod, inner/outer ring, corner rod, and shroud.
Tfg: fluid, gas / vapor temperatures
m (Zry) axial mass profile in case of calculated relocations

In Figure 4.16 the relevant experimental data and FZK post-test calculations are given for the three times listed in Table 4.2 for shroud, heater rods, corner rods, and for the cooling channel inner and outer wall temperatures. The post test calculations, shown in the plots by solid, dotted and dashed lines, are based on the FZK facility model which has a 16 axial zone nodalization and five thermal-hydraulic systems including the laboratory atmosphere, because the radial heat losses out of the bundle depend ultimately on the ambient temperature. In the cooling jacket the argon and water systems are simulated as realistically as possible to allow for pre-test calculations.

Measured fluid inlet and outlet temperatures are given by solid circles at their axial location, the different types of rod thermocouples are indicated by similar symbols, all without lines.

Comparing the three measured axial temperature profiles with results of S/R5 it can be stated that even the well adapted code S/R5 still has difficulties to explain the measured temperature increase prior to reflood initiation. A better representation can be obtained in increasing the axial resolution from 16 to 32 axial zones. In the upper heated section the large radial temperature gradient could not be simulated correctly, mainly because of only two rings of heated rods. At lower temperatures the radiative heat flux seems to be under predicted and above 1400 K vice versa.

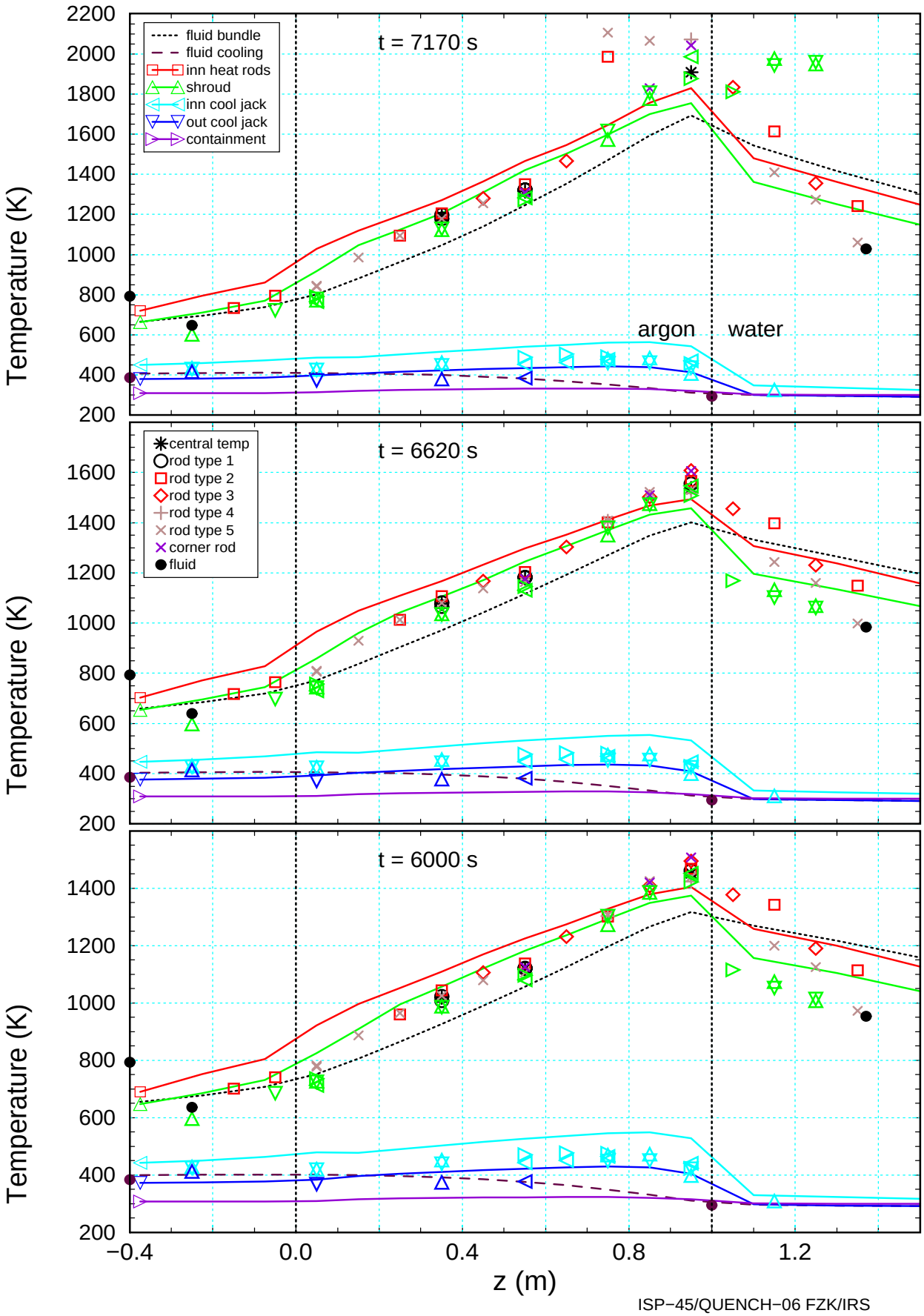

Figure 4.16 Axial temperature profiles measured in the bundle for: top: 7170 s, center: 6620 s, and bottom: 6000 s compared with results of the post test calculation using S/R5.

4.4.2 Data quality

As mentioned earlier, the axial profiles are foreseen to allow a detailed comparison over the whole length of the simulated test section. These results are compared with the measurements and the results of FZK post test calculations. In the following figures the minimum and maximum experimental data will be printed as opaque symbols (diamond). They include heater rod and shroud temperatures as well.

For the axial power profiles, some participants evidently sent only single rod power. For comparison we multiplied their data with the number of heater rods (20). The respective participants are indicated in the legend by a ppp.1. Others (CMX, ISS, NK1, SES, and SIE) did not deliver results concerning the axial power profile. The power values sent by NEH were zero and FRA might have trouble with the scaling factor because data showed unrealistic values. The VTT code GENFLO didn't include a heater rod model to calculate the axial power distribution as can be seen in Figure 4.18. Therefore these results will be not considered in the detailed comparison, however, it emphasizes the necessity of the modeling of physical effects, even if they are not relevant for reactor applications.

The oxide layer profile data are lacking for EDF (not modeled), NK1, and SIE for the unheated rod. Local hydrogen mass flow rates are missing for CMX and ENE. The users of SCDAPSIM (DMM, ISS, NEH, NK1, SIE) delivered local hydrogen source data and the FRA values showed an offset which could be identified as the argon gas, because MAAP is not able to simulate more than one non-condensable gas.

Finally, CMX always shows lowest temperatures of the unheated rod, app. 100 K lower than most of the participants, which may be attributed to errors in the power balance as mentioned in section 0.

4.4.3 End of the pre-oxidation phase

At 6000 s the temperature plateau of the pre-oxidation phase ends and the axial profiles discussed in this section define the starting conditions for the final transient. The axial clad temperature profiles calculated for the unheated rod in the center of the bundle are shown in Figure 4.17 and compared with the measured temperatures in the bundle. The axial profile of the electric power and the calculated oxide layer thickness are shown in Figure 4.18 and Figure 4.19, respectively. The clad temperatures for the heater rods in the inner and outer ring, the corner rods, and the shroud as well as the fluid temperatures are given in section **8.3** in the appendix.

Temperature

The maximum measured temperature of app. 1500 K (Figure 4.1) is located at 0.95 m and the average axial temperature gradient amounts to 750 K/m. The minimum and maximum temperatures (Figure 4.17) measured in the bundle show rather a small spreading (< 50 K), except for the upper electrode zone, since the absence of the shroud insulation consequently increased the radial heat losses. This annular gap was intended to protect the heater wires from being damaged by extreme temperatures.

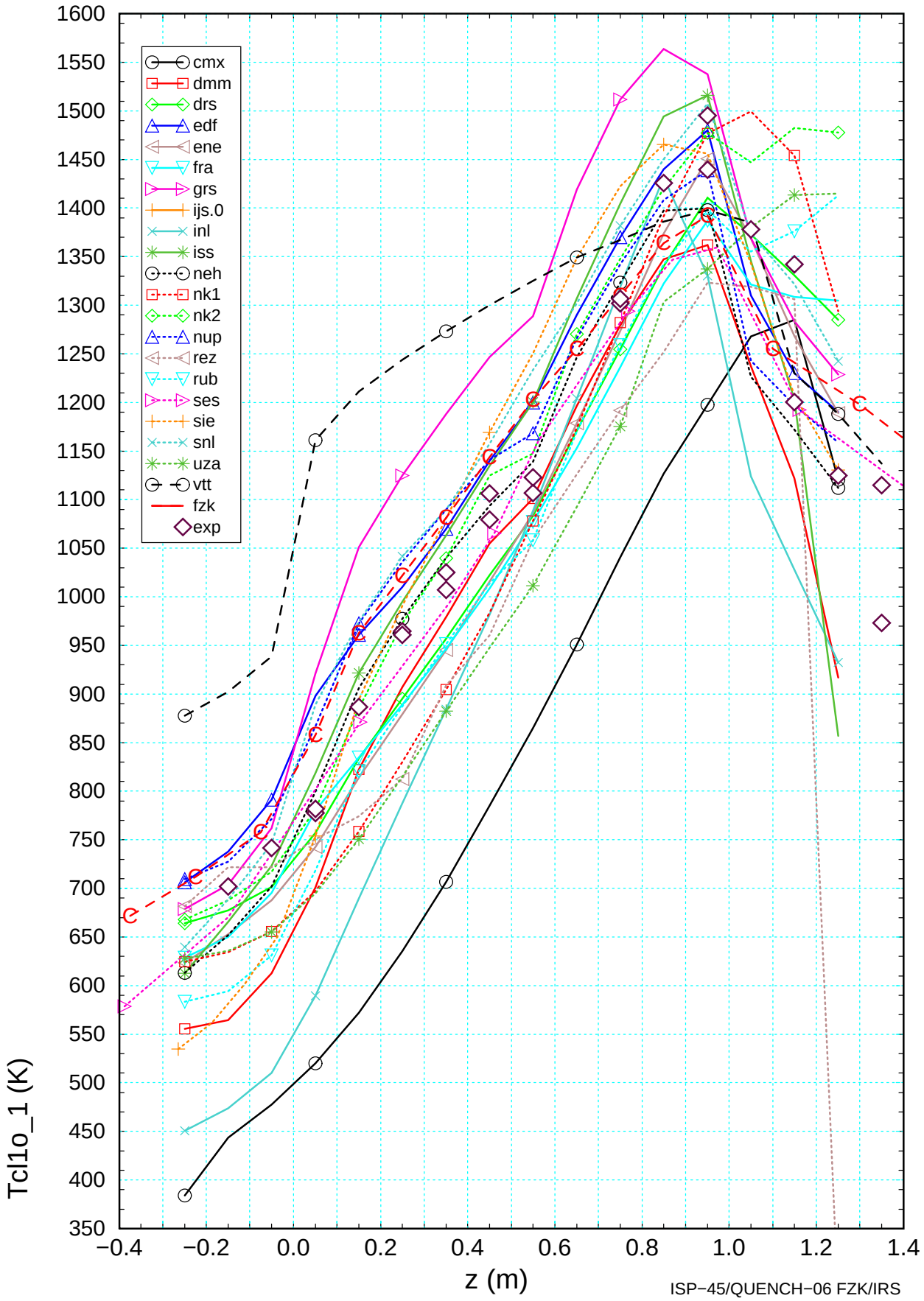

Figure 4.17 Axial surface temperature profile of the unheated power profile calculated by the participants for t=6000s compared with measurements and results of FZK post-test calculations (-C-).

Above 1300 K, temperature differences of the unheated fuel rod and adjacent heater rods are rather small due to effective radiative heat transfer. However, some differences can be found with respect to position of maximum temperature and power. For discussion, the unheated rod was selected because of its more reactor specific type. The relevant heater rod data are given in the appendix, the deviations from unheated rod behavior are discussed in the text.

The temperature level calculated by the participants (T_{unh}< 1570 K, T_{heater} < 1660 K, Figure 8.2) indicates that no bundle damage has occurred so far. In the heated zone of the test section, a temperature band of 250 K width includes nearly all participants. Despite this large discrepancy, the axial temperature gradient is met quite well by these participants (mainstream). The maximum temperature is calculated at 0.95 by all of the participants except for GRS and INL whose temperature and power has a maximum at 0.85 m, app. 0.1 m below.

In the upper electrode zone, the results spread to 600 K depending on the accuracy of modeling of axial heat conduction and/or radial heat losses to the shroud. The cladding temperatures calculated by DMM, INL, ISS, and NK1 tend to be under-predicted. The reason may be linked to different axial boundary conditions required for adequate axial heat conduction and hence modifying the power level at the ends of the heater rod. In case of CMX a strong under-prediction of 150 K is noticed plus an axial shift of 0.2 m towards the upper end of the unheated rod. The axial shift is unclear but may be due to an error during post-processing. In that case the CMX data would fit to the mainstream.

On the other side FRA, NK2, RUB and UZA calculations tend to underestimate radial heat losses due radiation in the annular shroud gap so that their temperatures are higher than expected. REZ has delivered a zero for the uppermost temperature of the unheated rod which is caused by an unexpected code error.

The radial temperature gradient in the bundle can be derived comparing unheated fuel rod temperature (Figure 4.16) and the inner ring heater rod temperature (Figure 8.2). At z=0.05 m both rods show similar scatter, from 650 K to 850 K and at 0.95 m a band between 1300 K and 1480 K, the unheated rod is 50-100 K colder as the heater rod. This flat radial temperature profile is mainly due to the thick shroud insulation and to some extent to the one channel thermal-hydraulic approach used in nearly all SFD codes. In the electrode zones these values exceed 300 K due to different boundary conditions.

Electrical power

In the axial power profile (Figure 4.18) the three heater rod sections can be identified clearly by the level of the linear power. At a first glance the power curves show axial dependent distortions affected by either oxidation or convective heat losses. The scatter band starts in the lower section of the heated zone with app. 15 % and end at 0.85 m with app. 37 % neglecting the modified data (".1") of INL, NK2, and RUB (assumed number of heater rods: 20). Nevertheless the power scatter at the axial ends is smaller than the temperature scatter discussed before. The shift in the electric power between upper and lower electrode zone is due to the temperature dependency to the molybdenum wire.

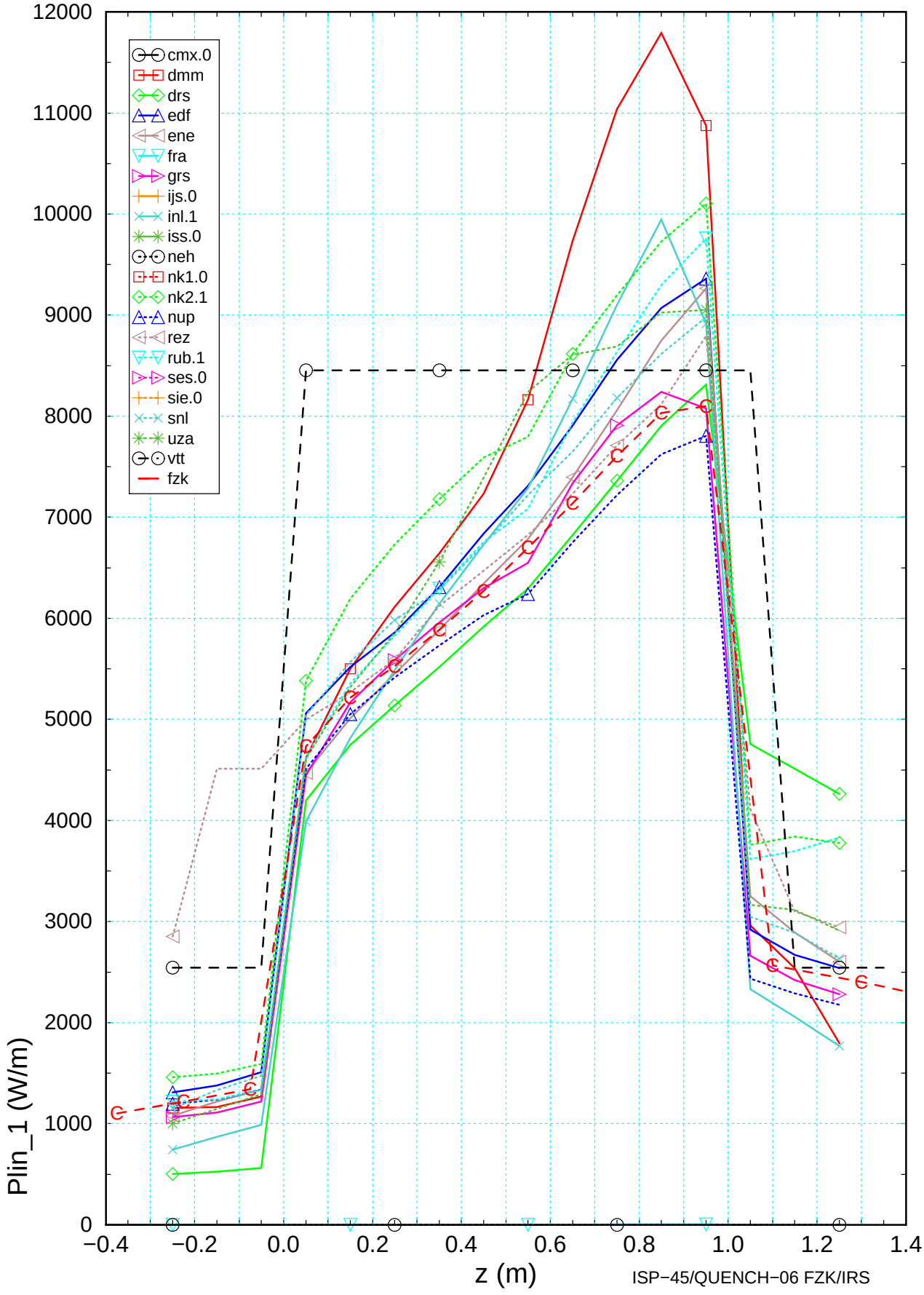

Figure 4.18 Axial power profile calculated by the participants for t=6000s compared with results of FZK post-test calculations (-C-).

Generally all participants calculated the maximum power at 0.95 m except for DMM and GRS which have the power spot at 0.85 m. Concerning DMM, it may be caused by a false temperature dependent specific resistance of the tungsten wire since the oxide layer thickness (Figure 4.19) does not reflect increased oxidation. Besides, DMM mentioned that the heat exchange from the upper electrode section to the shroud has been "enhanced" to better model the temperature behavior of the upper electrode zone.

EDF slightly over predicts the power released in the test section because they didn't consider the external resistance, however, with decreasing influence by increasing temperatures (section 2.1.6).

The VTT code GENFLO has been developed essentially for reactor purposes, in order to analyze plant transients and design basis accidents. Since VTT did not participate in previous FZK-ISPs such as CORA-13 /12/ or CORA-W1 /13/, there was no need for a dedicated heater rod model to calculate the axial power profile as a function of the local heater rod temperature. The lack of this feedback mechanism increases the temperature in the half of the heated section. The axial temperature profile only reflects convective heat losses and oxidation power, as in a reactor or in in-pile test.

The uncertainties of the shroud insulation also include the material properties of the ZrO_2 fiber material which change with temperature and fill gas, as observed in CORA tests.

Oxide layer thickness

During the pre-oxidation phase a maximum oxide layer thickness of app. 150 µm should have been produced as intended by the experimental staff. A first glance on the calculated axial oxide layer profiles (Figure 4.19) revealed that there might be still problems with the oxidation models. Indeed, at peak value (z=0.95m) the oxide layer thickness mostly ranges from 140 µm to 260 µm. A wide scatter in the upper electrode zone is found as mentioned earlier for the temperature.

In the heated zone the axial dependency of the oxide layer profiles is similar for nearly all participants. Excluding VTT, whose oxide growth rate might not be accurate and INL, which has difficulties with the diffusion model leading to nearly complete oxidation at 0.85 m, the oxide layer thickness reflects the series of uncertainties starting from power, convective heat loss, to relevant oxide growth rate. Concerning INL, the mechanistic diffusion model available in SCDAP-3D tends to generate discrepancies in the energy balance and the cladding temperature increase (section 3.1). It allows an auto-catalytic behavior of the oxidation reaction with the local heat generation in the bundle being highly sensitive to the temperature distribution.

A remarkable deviation of the axial oxide layer profile is found for CMX with a maximum value at 1.150 m elevation as mentioned earlier.

NK2 tendency to drastically under-predict the oxide layer growth is quite unclear since that calculation shows the same over-predicted maximum temperature and hydrogen generation as e.g. ISS and GRS. It may be due to a post-processing scaling factor error.

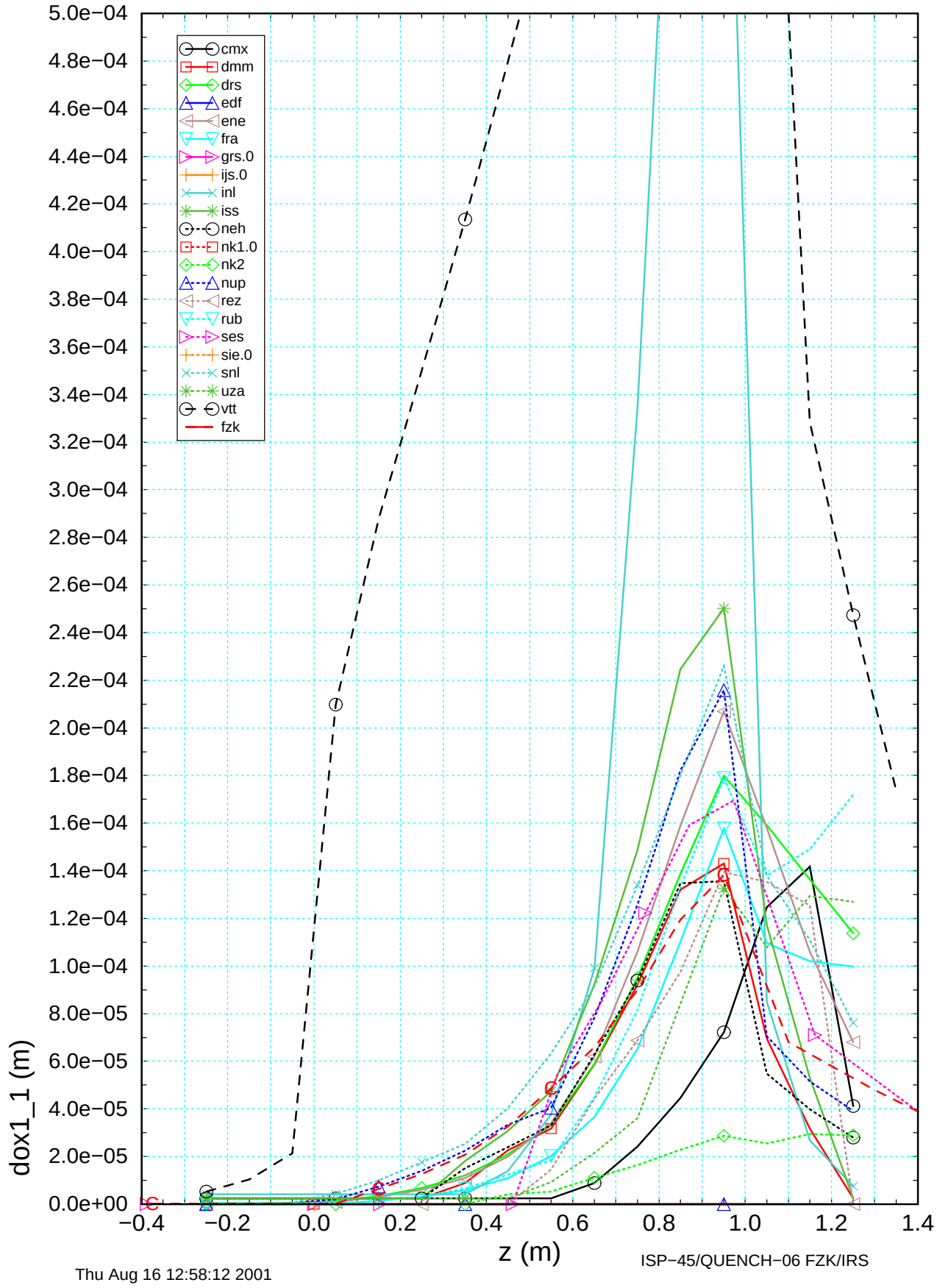

Figure 4.19 Axial oxide layer profile calculated by the participants for t=6000 s compared with the results of FZK post-test calculations (-C-).

4.4.4 Removal of the corner rod

Approximately 600 s after the end of the pre-oxidation phase, the corner rod was withdrawn to allow determination of an axial profile of oxide layer thickness. At that time the upper third of the heated zone has exceeded 1500 K so that the temperature escalation due to exothermal oxidation starts there, spreading out both upwards and downwards, dividing the heated section of the bundle into three different zones which will be discussed later.

Electric power input

At previous time (6000 s), the initial heat-up of the bundle was determined mainly by the electrical power input (0.3 W/s per rod) whereas now, the local temperature increase is accelerated by the exothermal Zircaloy/steam chemical interaction.

Compared to 6000 s the power input (Figure 4.20) has been increased by app. 50 % driving the maximum temperature into the heated section from 1450 K to 1650 K whereas the temperature range at the axial ends remained nearly unchanged. The shape resembles that discussed for 6000 s with one significant difference. In the heated section the results of all participants are in the mainstream or nearby, except for INL, RUB, and VTT. However, the spreading at the axial ends has been increased by app. 30 % due to the higher power input.

In the power curves (Figure 4.18) as well as in the temperature curves the influence of the Zry grid spacer at 0.55 m (Figure 2.5) can be seen, decreasing locally the clad temperature and hence the released electrical power.

Temperature

A similar picture as seen at 6000 s can be found for the temperature profiles at 6620 s (Figure 4.21) when the corner rod was removed from the bundle. The maximum measured temperature of app. 1600 K (Figure 4.1) is located at 0.95 m. The average axial temperature gradient amounts to 800 K/m. At that position the maximum radial temperature gradient was measured to app. 85 K in the heated zone, due to onset of oxidation at the heater rods. In the upper electrode section that value increase to app. 150 K.

The temperature spread of around 250 K at 6000 s for the mainstream of 15 participants' results in an equivalent spread of app. 250K, 620 s later. Temperatures above 1500 K calculated by participants in the mainstream can be found in the interval 0.8 to 1.0 m, with a peak temperature at 0.95 m of app. 1600 K.

In detail the influence of the oxidation becomes visible, e.g. the temperature peak of DMM is now at 0.95 m whereas the power peak is located app. 0.1 m below as can be seen in Figure 4.20. The peak temperature of INL reaches app. 1850 K at 0.75 m, may be caused by steam starvation above due to violent oxidation. In the upper electrode zone NK1 which has problems in modeling the energy balance calculated a peak temperature of 1700 K at 1.05 m.

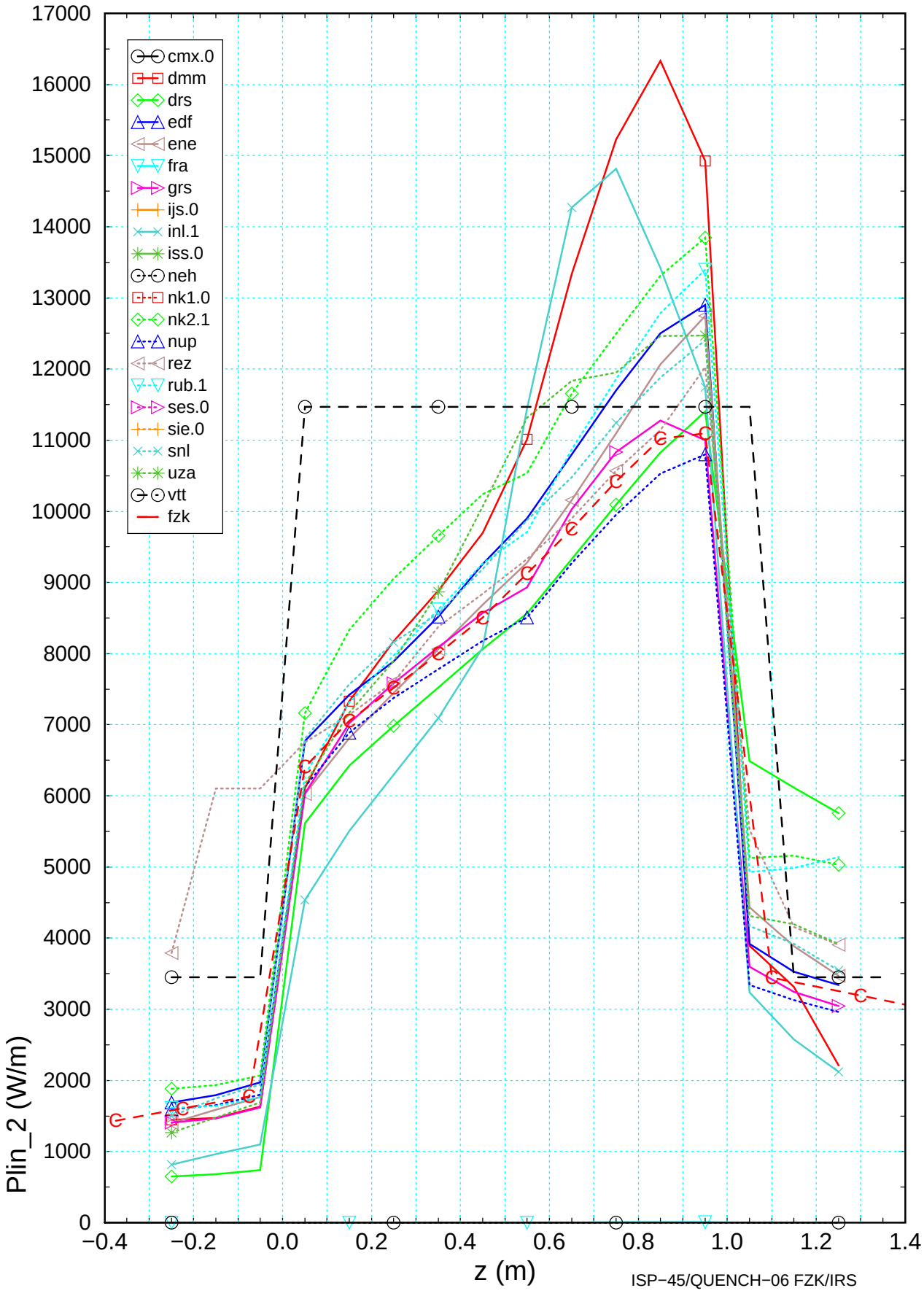

Figure 4.20 Axial power profile calculated by the participants for t=6620 s compared with results of FZK post-test calculations (-C-).

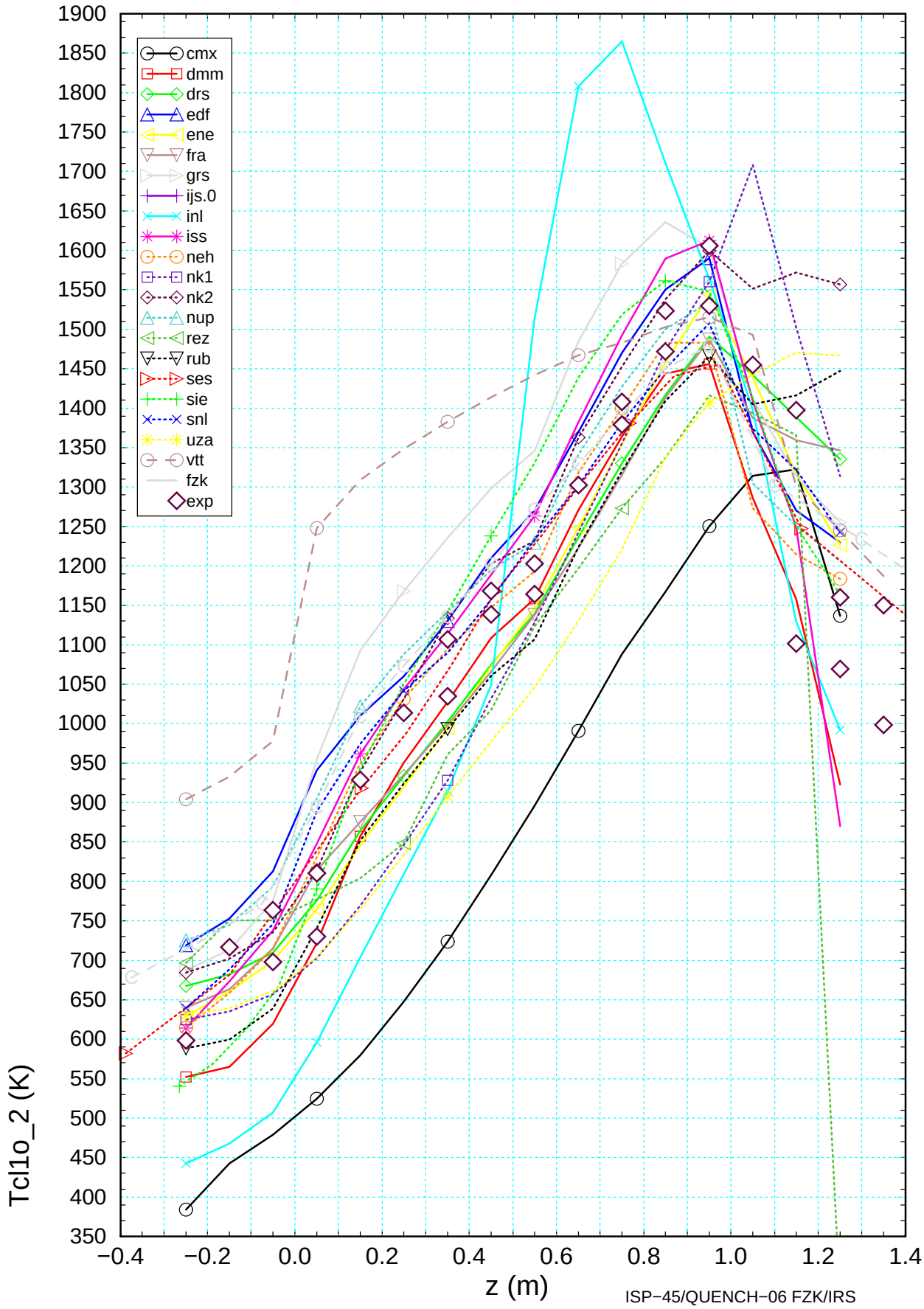

Figure 4.21 Axial surface temperature profile of the unheated fuel rod calculated by the participants for t=6620 s compared with measurements and results of FZK post-test calculations (-C-).

Oxide layer thickness

In Figure 4.22 the maximum and minimum values for the oxide layer thickness derived from different destructive measurements are shown by diamond shaped symbols. Considering the existing scatter in the calculated oxide layer thickness the measured values can be used as reference values for the unheated rod, too. At a bundle elevation of 0.95 m most of the calculated values for the corner rod (Figure 8.14 in section 8.3) vary between 140 µm and 280 µm, those for the unheated fuel rod between 140 µm and 320 µm, respectively. Nearly all code predictions are within a scatter band of +/- 40%.

In both values (dox1_2, Figure 4.22 and dox4_2, Figure 8.14) the difference in the slope of the oxidation profile is obvious. Nearly all calculations predict a lower elevation for onset of oxidation (0...0.4 m) compared to the experiment (0.6 m). One possible explanation of this deviation below 0.5 m may be linked to temperatures (Figure 4.21) below 1100 K where the oxidation correlation overestimates the oxidation.

Nevertheless, the prediction capability of the Cathcart rate equation used up to 1850 K for the Zircaloy oxidation kinetics by nearly all participants is quite reasonable for the intact bundle geometry.

4.4.5 Prior to reflood initiation

In the time interval between the corner rod withdrawal and the reflood initiation, heat generated by the highly exothermal oxidation of Zircaloy by steam substantially contributes to the heat-up of the bundle. This drives the temperature at 0.75 m up to 2000 K just before reflood and the increases considerably the scatter of the calculations.

That temperature level is achieved by a fast heat-up rate of > 2.0 K/s as can be depicted from Figure 4.1. The average axial temperature gradient amounts to 950 K/m in the lower half of the heated zone and more than 2000 K/m in the upper third, due to the temperature escalation. In the lower half the radial temperature spreading is nearly maintained as before, whereas above 0.7 m extreme values of 200 K are measured. In the upper electrode zone that variation shows a dramatic value of more than 500 K.

At the begin of reflood, which will be discussed in section 4.6, the experimental temperatures correspond to design basis accident (DBA) conditions which extend up to mid of the bundle. At reflood initiation time the following situation is found: at 0.0 m the wall superheat is app. 300 K, in the center of the bundle app. 900 K, and in the hottest position app. 1600 K. Based on the temperature level, which is below the melting temperature of oxygen stabilized α-Zr(O), and the stability of slowly grown ZrO_2 scales the fuel rod claddings should still be intact, which is confirmed by inner fuel rod pressure measurements /7/.

Temperature

Up to the time of the experimentally detected temperature excursion (app. 7000 s), nearly all heat-up rates are quite well estimated compared to experimental results. Quite larger deviations are detected afterwards, mainly due to the more or less abrupt change between the low and high temperature oxidation correlations used in the codes.

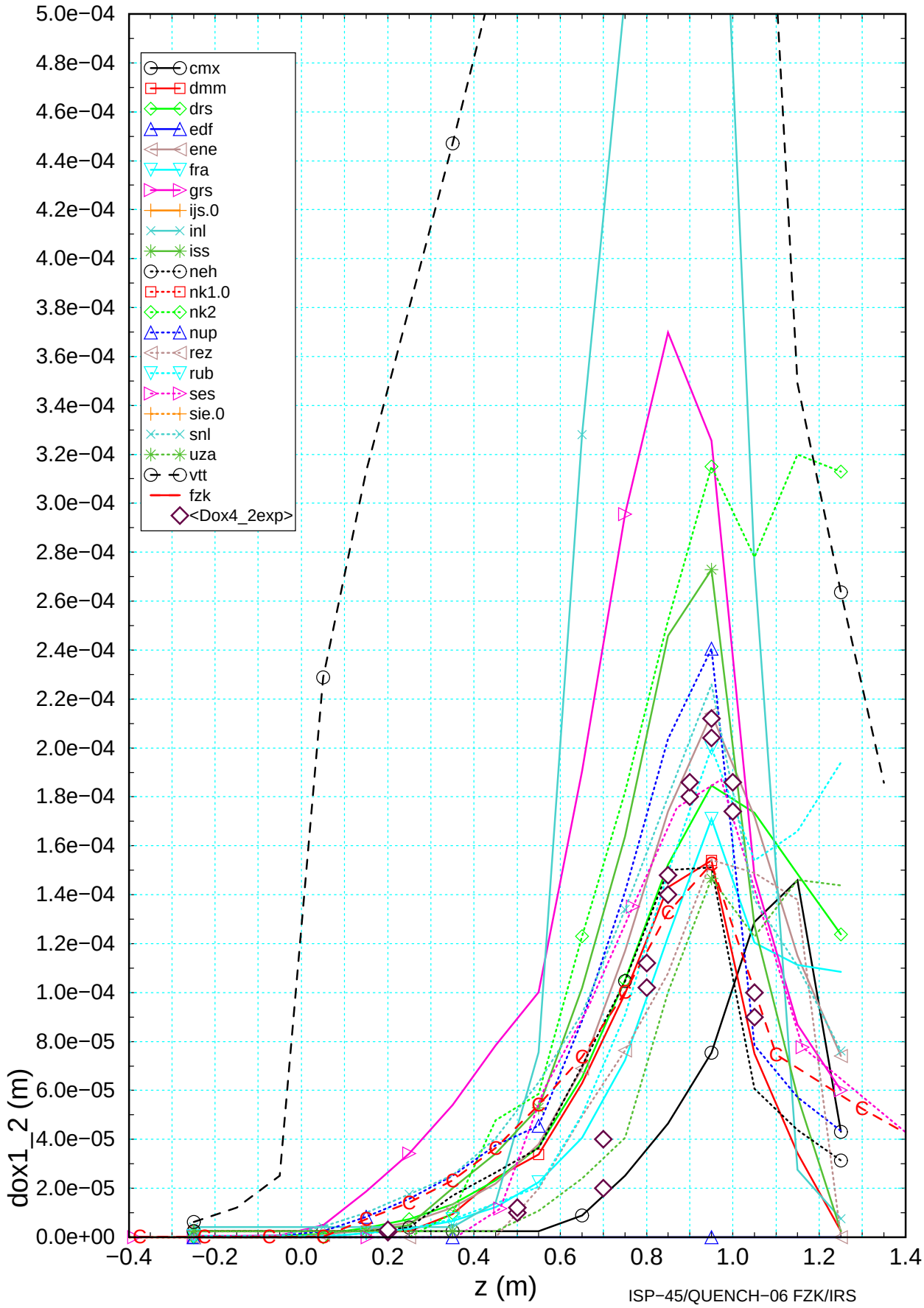

Figure 4.22 Axial oxide layer profile calculated by the participants for t=6620 s compared with experimental minimum and maximum values (diamonds) and the results of FZK post-test calculations (-C-).

Besides, the sudden increase in the heat release of the exothermal Zircaloy/steam reaction at the switch temperature may cause energy balance problems, because the heat release by radiation and convection requires some time. In case of a nearly adiabatic insulation by a Zircaloy shroud which also starts to heat-up, the heat is mainly removed by the fluid. Therefore, bundle insulation as well as local heat generation both of which are difficult to model determine the heat-up rate.

For DMM, since the calculated temperature profile begins to deviate from the expected values after the onset of temperature escalation for all bundle components (up to 2400 K for the shroud in Figure 8.19), ZrO_2 thin layers are deemed to have failed because the fixed cladding failure temperature limit of 2200 K is exceeded at around 7140 s.

An unclear temperature escalation in the shroud begins in the NK1 calculation before the quenching initiation leading to maximum temperatures of around 2900 K, 100 s before the quenching initiation. The absence of hydrogen generation in the upper plenum (between 0.95 m and 1.05 m elevation in Figure 8.16) indicates a complete oxidation of all bundle components in this region.

The axial temperature profiles of NK1 and UZA show rather cold lower ends, whereas the very high peak temperature are produced. In essence the temperature at 1.35 m varies from 950 K (ISS) to 2120 K (NK2), neglecting the negative value of REZ.

Electric power input

As mentioned before the axial power profile (Figure 4.24) also reflects the local energy balance, especially additional power released by the Zry oxidation. Below 0.5 m nearly all participants in forming the mainstream are close together, the scatter is only 1800 W/m (10 % of maximum value). However, in the upper third the values spread, also enforced by power redistribution.

The strong deviations observed for INL and NK2 have to be checked by the users.

Oxide layer thickness

Unfortunately no experimental data are available at that time, so that a reliable description of the pre-reflood situation may rely on the corner rod data extracted 550 s earlier, however, in case of a temperature escalation this time interval may lead to more than 1000 K difference.

Based on post-test calculations with Russian mechanistic SVECHA code /17/ which uses the measured temperature and oxide scales measured at the corner rod at 6620 s as input conditions a supporting axial oxide layer profile is estimated and used for comparison at 7170 s. A second curve shows the results of SVECHA code calculations starts from the beginning. Both curves show, that the uncertainty of the derived values is increased, however, the error is acceptable, mainly due to the reasonable reliability of SVECHA below 1800 K.

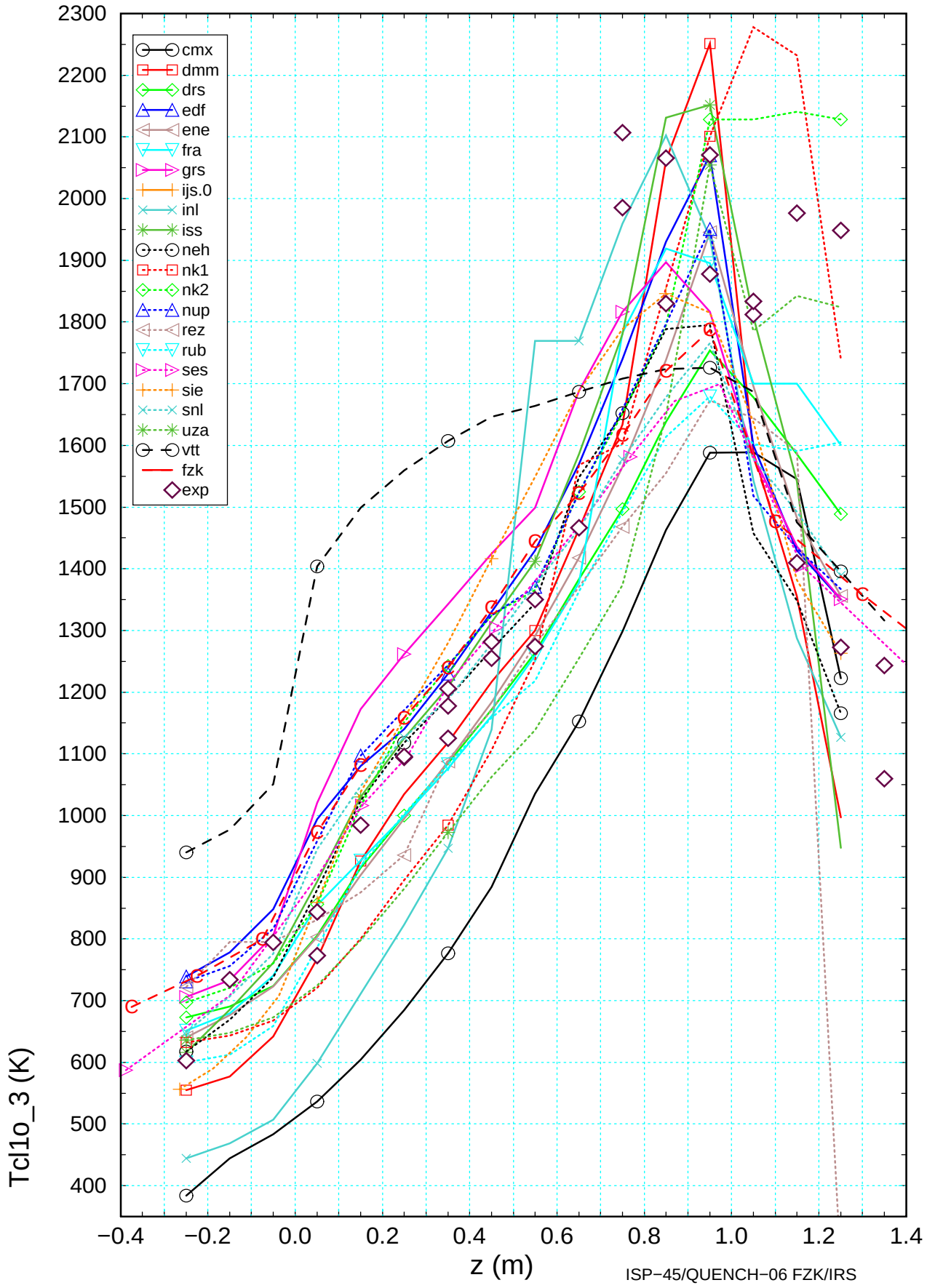

Figure 4.23 Axial surface temperature profile of the unheated fuel rod calculated by the participants for t=7170 s compared with measurements and results of FZK post-test calculations (-C-).

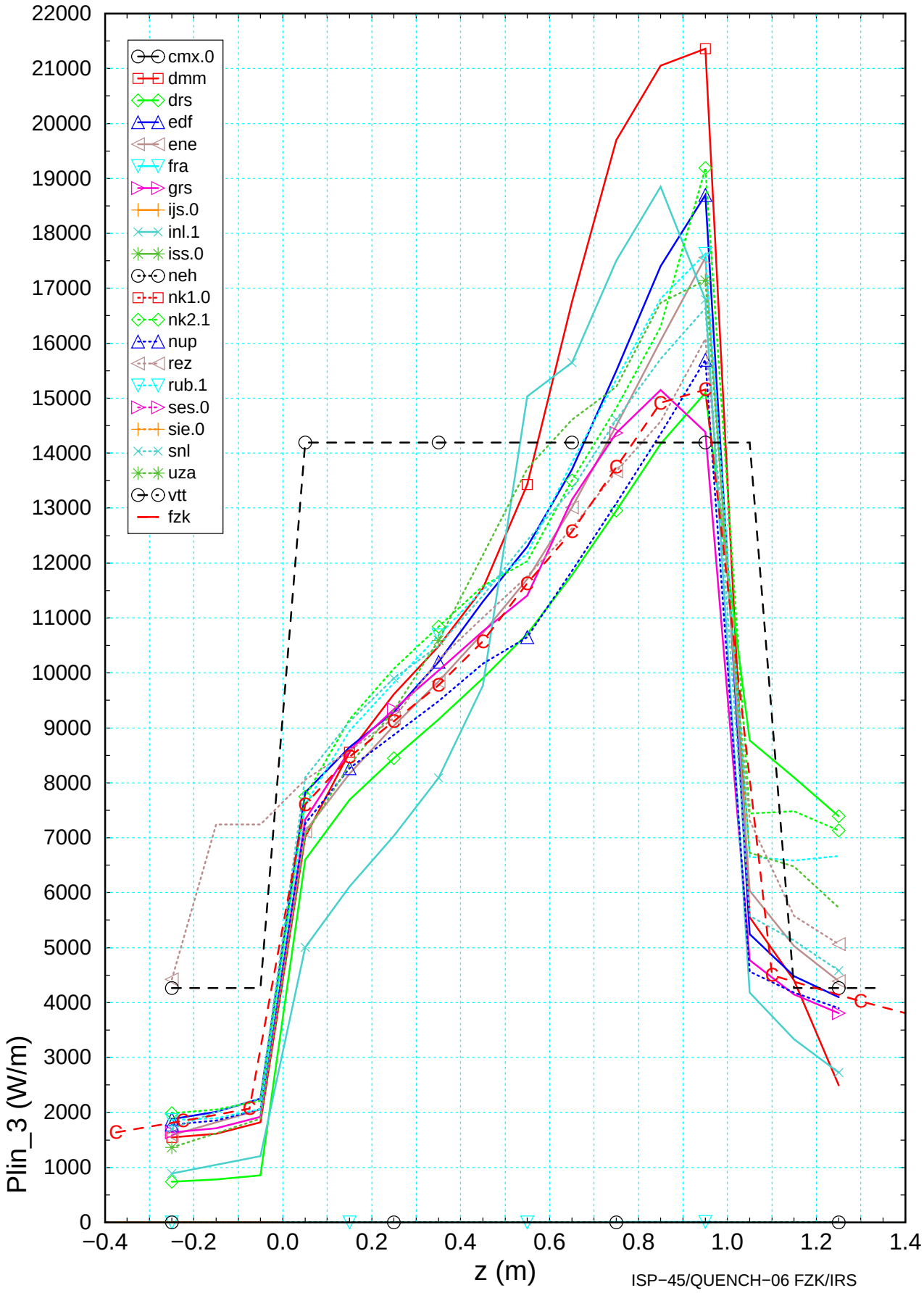

Figure 4.24 Axial power profile calculated by the participants for t=7170 s compared with results of FZK post-test calculations (-C-).

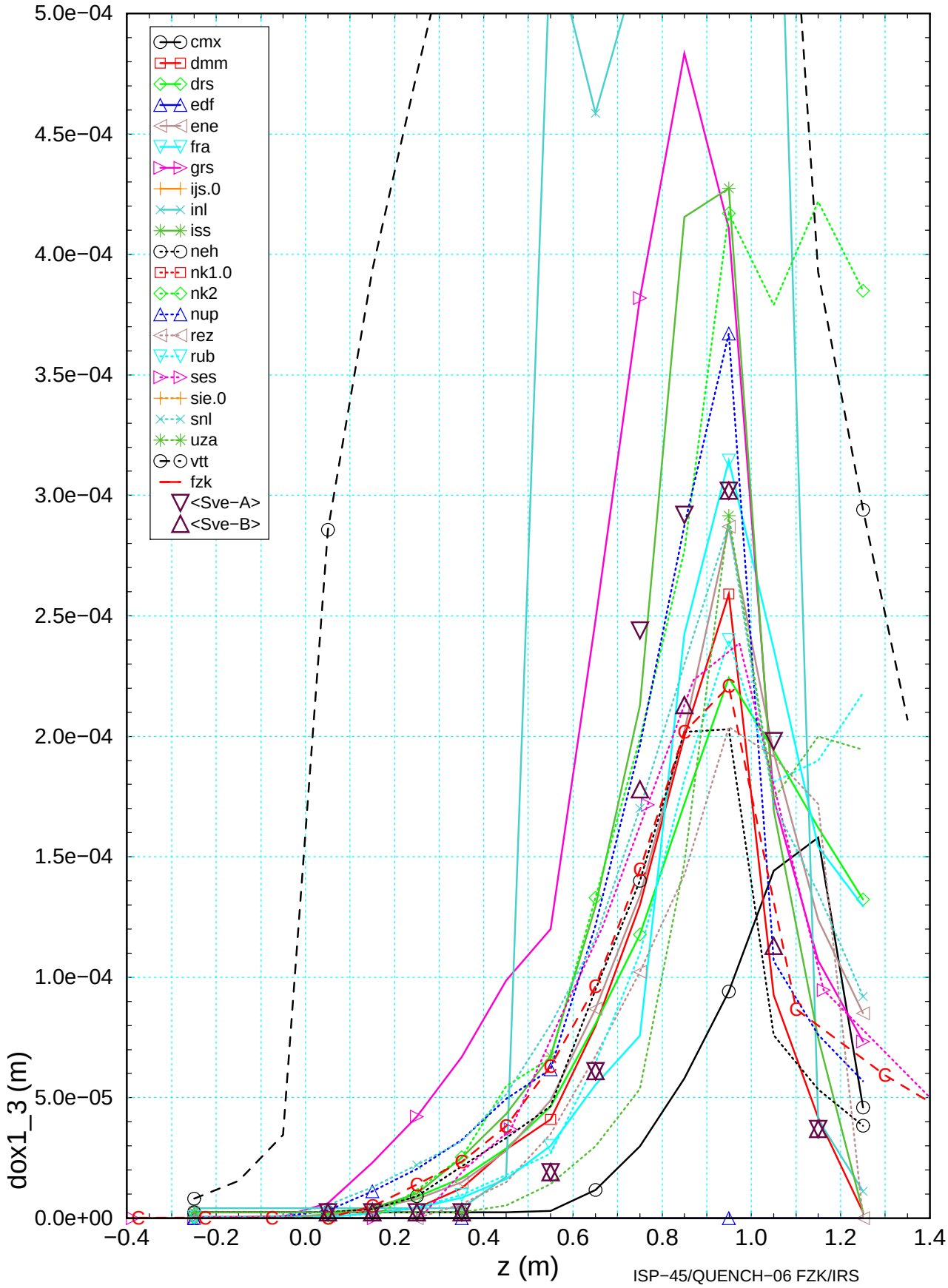

Figure 4.25 Axial oxide layer profile calculated by the participants for t=7170 s compared with experimental based calculations using SVECHA (symbols) and results of FZK post-test calculations (-C-).

Besides, the calculated oxide scales confirm the strong dependency on the axial temperature profile dividing the bundle in three different zones. Nearly all calculations show that in the lower part of the bundle (up to 0.2 m elevation) the claddings are still slightly oxidized (< 50 µm) whereas in the middle and upper parts a pronounced core oxidation process is found to have occurred.

At 0.95 m the variation between the participants amount to 200 µm, which is 50% of the maximum value. The cladding oxidation reaction is even stopped by a lack of non-oxidized materials for the extreme cases of VTT and INL.

4.5 Bundle degradation up to reflood initiation

In the QUENCH Program two tests (QUENCH-02 and QUENCH-03, /3/) showed significant bundle degradation due to high temperature, however, main bundle damage was initiated prior to reflood initiation. From the post-test examination of QUENCH-06 /7/ no significant bundle damage is found.

4.5.1 Experimental findings

After the test (section 2.2.2) the QUENCH-06 bundle shows only localized damage of the shroud in the upper third of the heated section. Since no significant temperatures increase was observed during reflood which may have triggered bundle damage, it is assumed that the fuel rod bundle was essentially intact at time of reflood initiation /7/.

From on-line measurements fuel rod cladding failure was detected just after reflood initiation at 7179 s, originated by thermal shock (clad rupture). The cladding temperatures were significantly below any liquefaction temperatures, however, local melting of metallic Zircaloy cannot be excluded so far. But that metallic ZrO-Zr melt was retained within relative stable ZrO_2-scales of more than 300 µm thickness.

4.5.2 Calculated bundle damage

No sufficient information were delivered by EDF, ENE, ISS, NK1, NK2, RUB, SES, SIE, SNL, and VTT. The fluid flow area data of DRS, REZ, and FRA deviate from specified geometry of the intact bundle.

From the various data (af, mzry, mzro, etc.) versus time, an overview was extracted as shown in Table 4.3. In the first column the axial node indicates at which elevation the participants calculated fuel rod or shroud damage. Next the assumed or identified phenomena are given together with the token of the participant who calculated the damage. In the last column a brief attempt was made to explain and to quantify the calculated results. From Af slope an identification of the basic mechanism is feasible (ballooning, melt relocation). Generally all participants kept the QUENCH facility intact. Neglecting a distortion of Af of 10 %, the lower five zones remained intact for all participants. The results of IJS are excluded from the discussion, because the code calculated melt relocation and release down to 0.15 m at 1000 s.

Table 4.3 Overview of local effects derived from time dependant data delivered by the participants

#	Effect	Participant	Remark
16	melting ballooning ?	IJS NEH, UZA FRA	assumed ZrO_2 pellets nearly all melted at 1000 s NEH: 1500s-2500s and UZA: 3000 s - 3500 s small unexpected increase of Af
15	melting ballooning ?	IJS CMX,NEH,UZA FRA	assumed ZrO_2 pellets nearly all melted at 1000 s ballooning between 1000 s and 3500 s small unexpected increase of Af
14	melting ballooning	IJS CMX, UZA, DMM, FZK FRA	assumed ZrO_2 pellets completely melted at 1000 s 10 - 20 % ballooning < 5% ballooning small unexpected increase of Af
13	ballooning	DMM, FZK, CMX,NEH,UZA	up to 20 % up to 10 %
12	blockage ballooning	IJS CMX, NEH, UZA DMM	intermediate blockage at 1000 s + subsequent relocation 5 % reduction between 1000 s and 1500 s (and 3500 s) 20 % reduction between 1000 s and 1500 s
11	ballooning blockage ?	DMM, CMX, NEH, FZK, UZA FRA IJS	nearly all participants up to 15 % (1000 s to 3000 s) 20 % at 7200 s blockage formation plus subsequent re-melting
10	blockage ballooning	IJS CMX, UZA	50 % blockage at 1000s 5 % reduction between 1000s and 1500s (3000s)
9	blockage ballooning ?	IJS DMM,NEH,FZK CMX, UZA	40 % blockage at 1000s ballooning between 1000s and 3500s ballooning with subsequent clad relocation
8	blockage ballooning	IJS CMX, UZA,NEH, FZK, DMM	50 % blockage at 1000s 5 % reduction between 1000s and 1500s (3000s)
7	blockage ballooning	IJS CMX, UZA	20 % blockage at 1000s 5 % reduction between 1000s and 1500s (3000s)
6	blockage	IJS	12 % blockage at 1000s
5	blockage	IJS	8 % blockage at 1000s
4	blockage spacer ?	IJS IJS, NEH, DMM, REZ, FRA	first blockage at 1000s initial value 0.0024 m² initial value 0.0026 m²
3	blockage	FRA	slight blockage at 7200s
2	-		intact bundle: no variation of Af
1	-		intact bundle: no variation of Af

Please note: ? : No clear indication of the basic process

No data available from EDF, ENE, ISS, NK1, NK2, RUB, SES, SIE, SNL, and VTT. In the experiment Zircaloy spacers are located in axial zone 9,14, and 16, the Inconel spacer is located in level 4.

Clad failure

In the experiment fuel rod cladding failure was detected at the onset of reflood at 7179 s (section 0), mainly caused by thermal shock. One second later the shroud failed too. This quantity was not asked by the participants due to difficulties in modeling the small plena and the rather large volumes of the fuel rod pressure system, which remains at room temperature level. However, the participants were asked to explain the position and type of clad failure calculated by their code (section 4.6 in /8/). Some participants mentioned that they had to reduce the inner rod pressure to avoid early clad failure as observed in early S/R5.irs calculations.

In all codes participating in the ISP-45 the clad failure calculated by bounding user values, such as local cladding temperature and oxide layer thickness. The temperature value range is reasonable between 2200 K and 2500 K, compared to earlier ISPs (ISP-31).

Melt formation and release

Nevertheless some participants calculated temperatures high enough to produce clad failure with subsequent melt release and relocation.

In some cases blockages at the upper most elevation was observed, probably due to code error. The melt accumulates in the 15th and 16th axial zone (CMX, IJS, NEH, UZA).

Formation of debris

No direct experimental information are available for the bundle state prior to reflood. As mentioned in section 2.2.2 no visible blockage formation was found in QUENCH-06 after the test, so that this holds true for the bundle state prior to reflood. More detailed information about the pots-test bundle state are available in /7/.

In Figure 4.41 the free flow cross sections are shown for the final bundle state. The results of the code calculations will be discussed in section 4.7.3. Table 4.3 gives time and location of calculated debris formation and in Figure 4.43 the accumulated mass is given for each axial zone.

4.6 Reflood phase

The main objective of the test ISP45 (QUENCH 06) was to investigate the behavior on reflood and hydrogen release. Therefore, the following section is divided into global data to identify whether or not the participants adopted the FZK QUENCH-06 reflood conditions and local data taking into account the axial temperature profile (section 4.4.5) and the hydrogen production (section 4.1.5) prior to reflood a rough selection will be given. A more detailed discussion on cool-down simulation will follow depending on available data.

4.6.1 Water balance

A global estimation of water masses used during bundle reflood in QUENCH-06 revealed no large discrepancies. During quench phase, the quench pump (F104) fed in 10.6 l water. The water volume injected into the test section by the fast injection system is app. 4 l (4.17 l in the S/R5irs simulation). After the test, the remaining water in the test section amounts to app. 6 l and that in the off-gas condenser to app. 8 l. The water in the test section also includes the filled quench inlet pipe as explained below.

4.6.2 Water level in the experiment

As mentioned in the ISP-45 specification report /8/, the unexpected draining of the quench water pipe was detected after test. Post-test analyses with S/R5irs were performed at FZK to identify the water mass in the various pipes of the steam and quench inlet system.

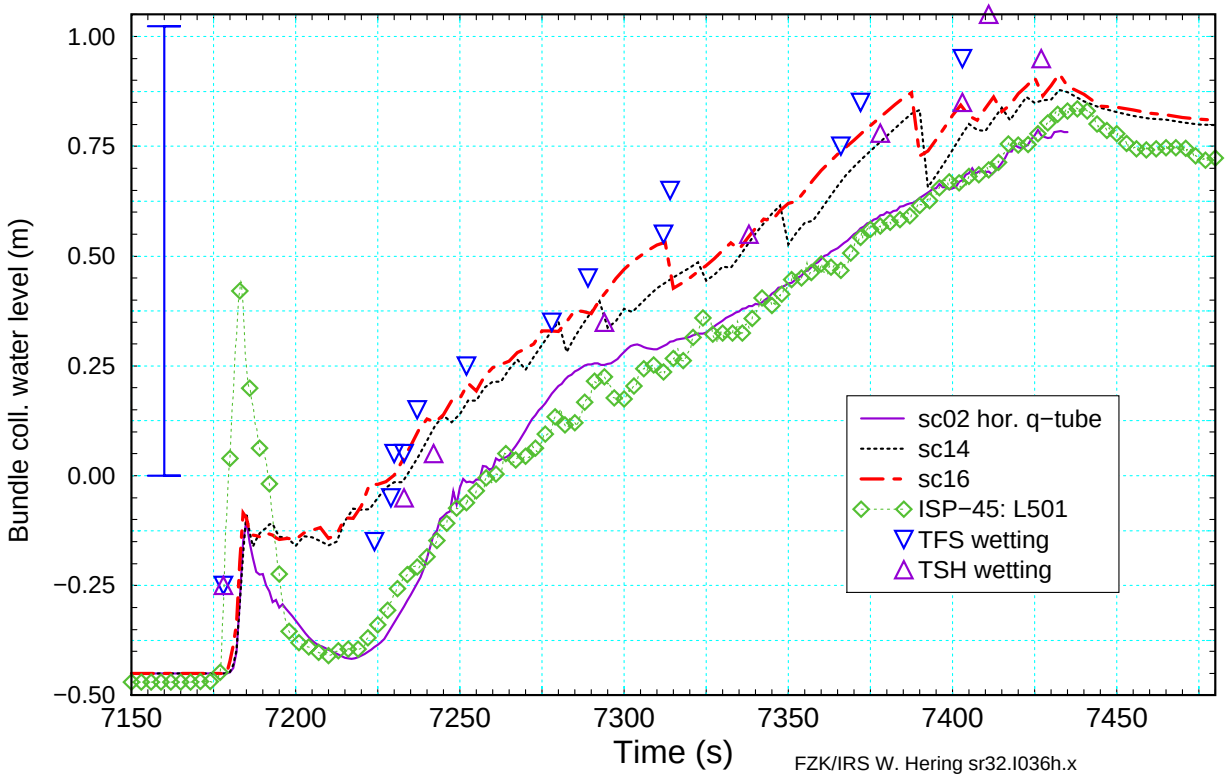

Figure 4.26 Calculated water level increase compared with experimental measurements and thermocouple readings.

From the experiment the position and times of thermocouple wetting (triangles) mark an upper bound for the quench water level. The TSH signals are valid for the onset of nucleate boiling, whereas the surface mounted TFS thermocouples give hints of the elevation of the droplet zone in the two phase region. In this sense, the TSH line is considered to be the lowest elevation for "wetting". A detailed description can be found in /7/. The lower bound is given by the signal of the water level tracking using a differential pressure sensor (L501) as shown in Figure 4.26.

In a first calculation the quench inlet pipe was modeled only in the entrance level without any vertical bending (sc02). The results of S/R.irs fits well with the pressure transducer signal (L501), however, don't match the thermocouple readings. Further calculations (sc14, sc16) simulated the vertical bending of the quench inlet pipe correctly, so that the rise velocity as well as thermocouple readings could be explained. The calculation sc16 used a finer mesh in the quench inlet pipe to achieve a better modeling of the 2-D geometry.

4.6.3 Comparison of calculated water levels

All participants calculated the reflood phase with more or less success. Among all participants INL, NK1, NK2 and SES did not deliver the collapsed water level progression data. The FRA water level is affected by the limited thermal-hydraulic reflood capability of MAAP. Besides, DMM delivered a plot with a step-like shape but it is only due to the decimal accuracy of all its quench data. IJS calculated rather early (at 1000 s) a massive core blockage (section 4.5.2) leading to a nearly uncoolable configuration. So it was decided not to discuss IJS results in detail.

The remaining data are compared with the results of the FZK post-test calculation sc16 already seen in previous section (fzk ;-C-). The results concerning the wetting of thermocouple (TFS at fuel rod cladding and TSH at shroud inner surface) and the differential pressure sensor (Lm501 averaged; diamond) are also included to generate an experimental range of uncertainty for the accuracy of the calculated water levels. The indications from the TFS are used as an uppermost limit (triangle up opaque symbol) and those of the TSH as a lower limit for a kind of swell level.

To identify the difficulties of simulation of the fast water injection, the collapsed water level is shown up to 7220 s in Figure 4.27. A whole comparison of the ISP-45 reflood phase is presented in Figure 4.28.

Fast water injection

The reflood phase starts at app. 7179s with the activation of the fast water injection which has been taken into account by nearly all participants. Due to the high injection rate enhanced boiling and water entrainment take place along the cooling channel. But even if the experimental results demonstrate that the fast water supply is enough to fill almost instantaneously the lower part of the bundle, the code predictions spread significantly. Thus attention may be focused first on the selected reflood conditions and then on the way the quench experiment is modeled by the participants.

As can be seen in Figure 4.28 nearly all participants (except NUP) simulated water injection between -0.475 m and -0.3 m depending on the selected nodalization scheme.

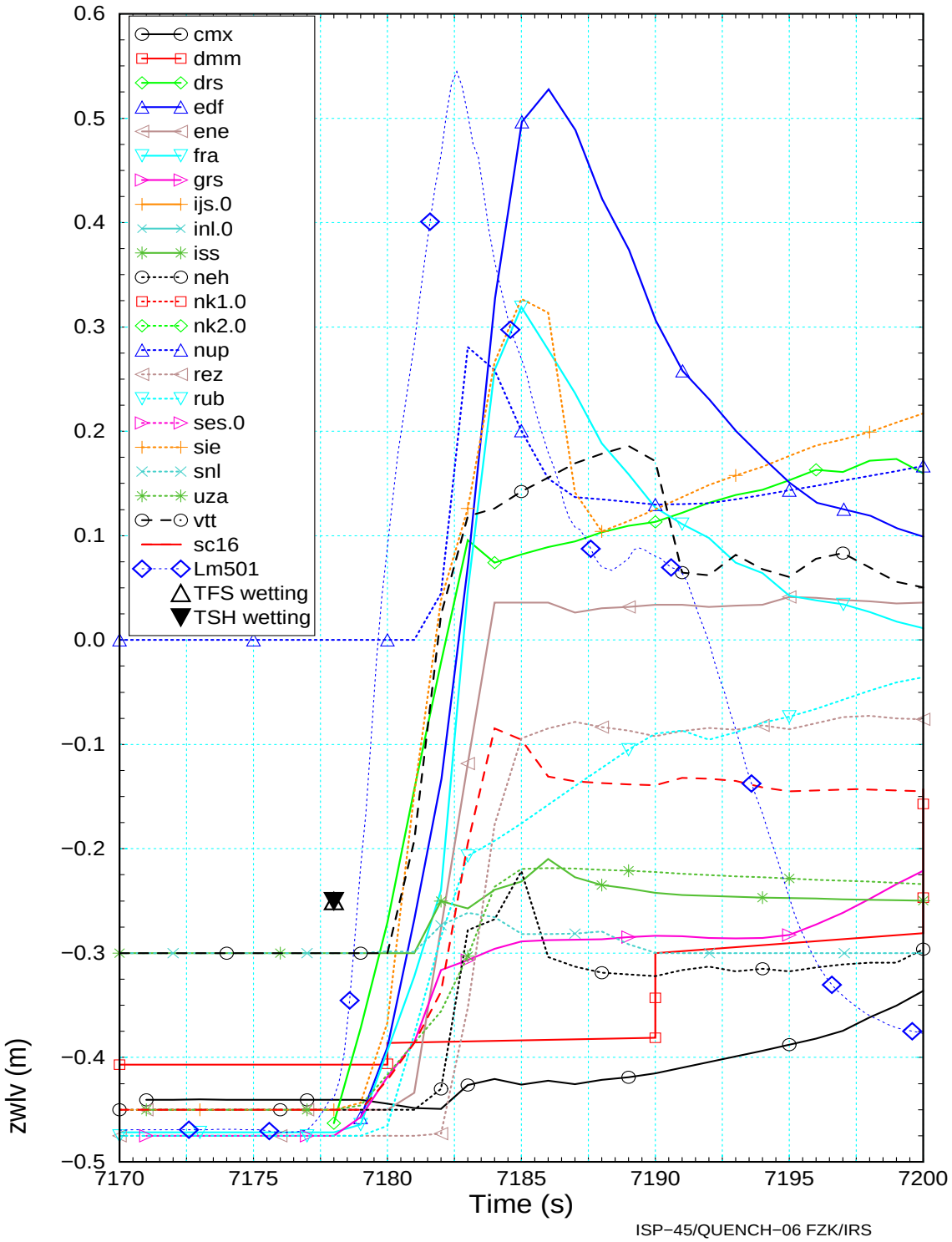

Figure 4.27 Calculated collapsed water levels compared with experimental measurements and results of post-test calculation (sc16, - - -) during fast water injection.

As an example, ISS, UZA, and VTT used simpler nodalization which starts at -0.3 m. The elevations calculated by VTT were corrected by hand in both figures (Figure 4.27 and Figure 4.28) to avoid an obvious elevation shift of 0.5 m compared to the reference as derived from VTTs information file. The SNL plot starts also at -0.3 m but shows an unexpected delay of app. 70 s as can be seen clearly in Figure 4.28. However, the overall behavior at the end of the reflood phase is estimated surprisingly well. Furthermore, NUP calculated the reflood phase with modified boundary conditions which specify the water mass flow rate as an input from the outlet of the lower plenum (0.0 m).

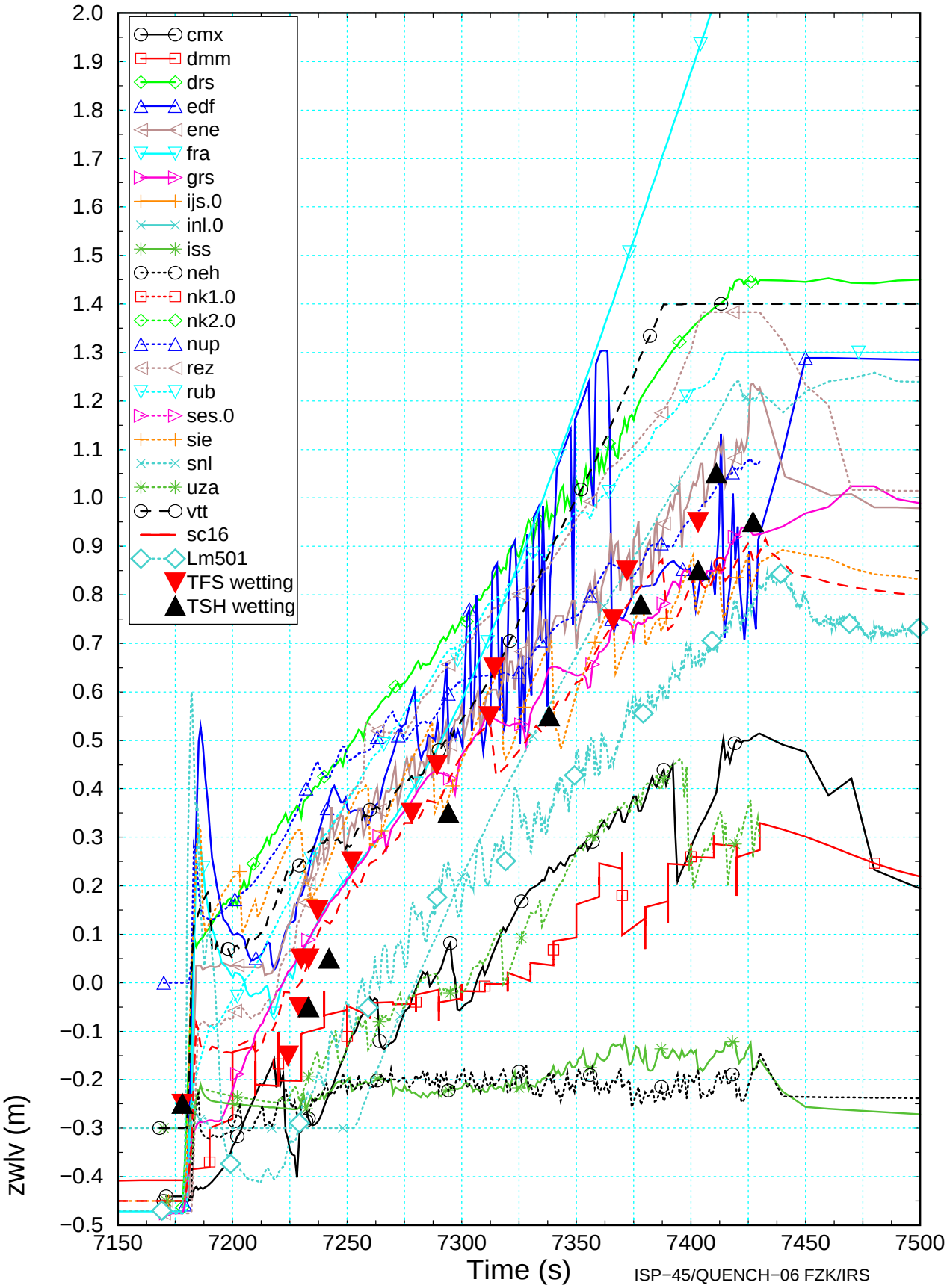

Figure 4.28 Collapsed water level calculated by the participants and compared with experimental measurements, thermocouple readings, and results of post-test calculations (-C-).

Five seconds after reflood initiation, 5 participants calculated a 0.5 m drop in the collapsed water level. One explanation may be fast evaporation together with the old reflood mass flow rate (see sc02 in Figure 4.26).

Water injection by quench pump

Then the fast water injection is followed by a relatively moderate flooding rate of app. 0.015 m/s starting at app. 7200 s. At a first glance, a clear mainstream formed by 10 participants can be seen in the vicinity of the experimental results. However, the overall flooding rate of this mainstream appears to be slightly overestimated looking at the results of S/R5 post test calculations and the TCs.

The scatter band including those participants starts in the lower section of the heated region with a rather “low” uncertainty of app. 0.3 m, but it spreads to app. 0.7 m in the hot spot (above 0.5 m Figure 4.28). This may be explained by calculation of different evaporation rates due to different axial temperature profiles prior to reflood initiation. It was assumed that all participants used the same quench water mass flow rate as specified in /8/.

Due to increased evaporation by higher surface temperatures, the overall flooding velocity of this mainstream tend to slow down above app. 0.5 m. However, a group of 4 curves (DRS, FRA, RUB and VTT) show nearly linear flooding rates up to the bundle outlet. Besides, the calculated values of those 4 participants indicate a complete flooding up to the simulated bundle outlet (off-gas pipe), which is positioned at different axial levels (between 1.3 m and 1.5 m excluding FRA).

At 7431 s the quench water injection was stopped and the electric heating was reduced to 1 W/rod as can be seen in Figure 4.28. Afterwards a smooth decrease of the experimental data indicates that not all heat is removed from the bundle and the shroud. The plots of DRS, GRS, RUB and VTT show a completely filled bundle confirming that there may be again either over-flooding into the off-gas pipe or a problem in the energy and/or mass balance of their codes.

A second group is formed by CMX, DMM, and UZA showing a reduced flooding capability so that even not the whole heated length of the test section was flooded. Apparently, their reflood models might have difficulties associated with the mass conservation.

At last, NEH and ISS, show no increase of the water level at all up to the end of the reflood phase. Here a data error or a post processing error has to be assumed since they calculated cool down rates which sound reasonable as can be seen in Figure 4.34.

In addition, some curves show strong oscillations which originate from two-phase flow which prevails near the flooding front. Possible reasons may be too large axial nodes or oscillations in the heat flux and boiling rate due to changes between different heat transfer modes. Since none of the participants used codes which have a mesh refinement capability the maximum zone size should not exceed 0.07 m /10/. However, the rewetting of the hot spot in the upper third of the bundle calculated by EDF shows steep spikes in a range of app. 0.3 m, probably caused by a stability problem of the new reflood model implemented in EDF MAAP version.

4.6.4 Discussion of temperature history

Maximum bundle temperature

The maximum temperature is a non-localized data during reflood phase so that a detailed discussion (section 4.6.4) has to use the local temperatures which are given in the appendix in section 8.3.3 together with measured temperature. However, it shows clearly the difficulties of simulating bundle behavior under reflood conditions when temperatures have already reached 2000 K or above before onset of water injection. Figure 4.29, a magnified version of Figure 4.1, illustrates the diverse cool-down behaviors.

Participants who obviously overestimated the amount of oxidation calculated temperatures far above measured values, so that a maximum temperature difference of 1300 K can be found as outlined in Figure 4.29. So, two distinct groups of results can be identified: a rather wide mainstream of 13 participants which did not calculate a temperature escalation during reflood and 7 calculations which show a strong over-prediction.

As already known from flooding experiments under DBA conditions, the cool-down curve has two sections. At high surface temperatures the heat flux is dominated by convective heat transfer to the vapor and radiation to small water droplets. Below the so called minimum film boiling temperature the heat flux is dominated by heat transfer to single phase liquid. Also an intermediate section exists which shows strongly increasing heat transfer due to radiation to droplets and partial wetting by single droplets (e. g. transition boiling). The intersection of the coarse extrapolation of the latter both cool-down rates defines the so called quench point. This behavior can be found by the more reliable shroud TC and most of the participants as shown in Figure 8.31 to Figure 8.34 for elevations between 0.5 m and 1.15 m.

In the experiment the melting point of metallic β-Zircaloy (2033 K) was already exceeded before reflood initiation (Figure 4.29). Indeed, bundle peak temperature excursions during reflood occurred in 7 calculations including GRS and a divergent band of 6 SCDAPSIM calculations. At least 3 of them show onset of melt formation and oxidation in the hot spot, NK1 up to 7255 s and DMM and UZA up to app.7350 s. In addition, at least 2 SCDAPSIM users (DMM and NK1) already exceeded their cladding failure temperature (i.e. DMM: 2200 K and NK1: 2500 K) prior to water injection.

The driving mechanism for the steep temperature increase is the overestimation of the energy release by the oxidation as indicated in Figure 4.30. Together with inefficient cooling the temperature can trigger severe bundle damage and debris formation as observed by some (7) participants, especially if the shattering option is used to completely remove the protective oxide layer. The 6 diverting SCDAPSIM calculations mentioned earlier have also a common deficiency enhancing temperature escalation in the upper part of the bundle during the transient phase (Figure 4.30) mainly caused by an obvious lack of adequate modeling of either the axial heat transfer to the water cooled ends or the radiative heat transfer in the shroud in the upper electrode zone (/18/). Consequently, the oxidation in the upper electrode zone is overestimated contributing significantly to the high increase of the hydrogen production during the quenching.

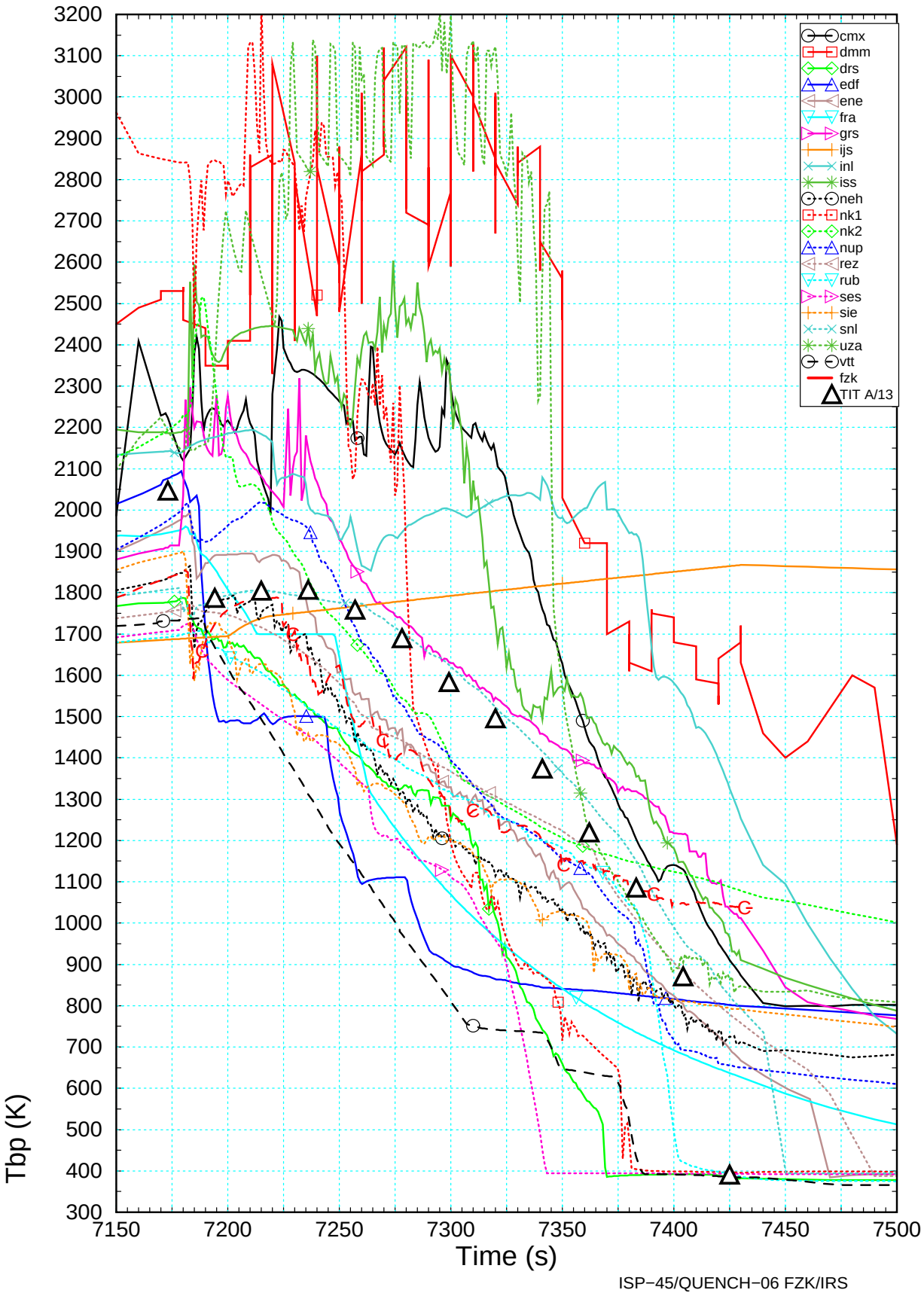

Figure 4.29 Maximum core temperature during reflood compared to thermocouple reading TITA/13 (triangle) and to FZK post-test calculation (-C-)

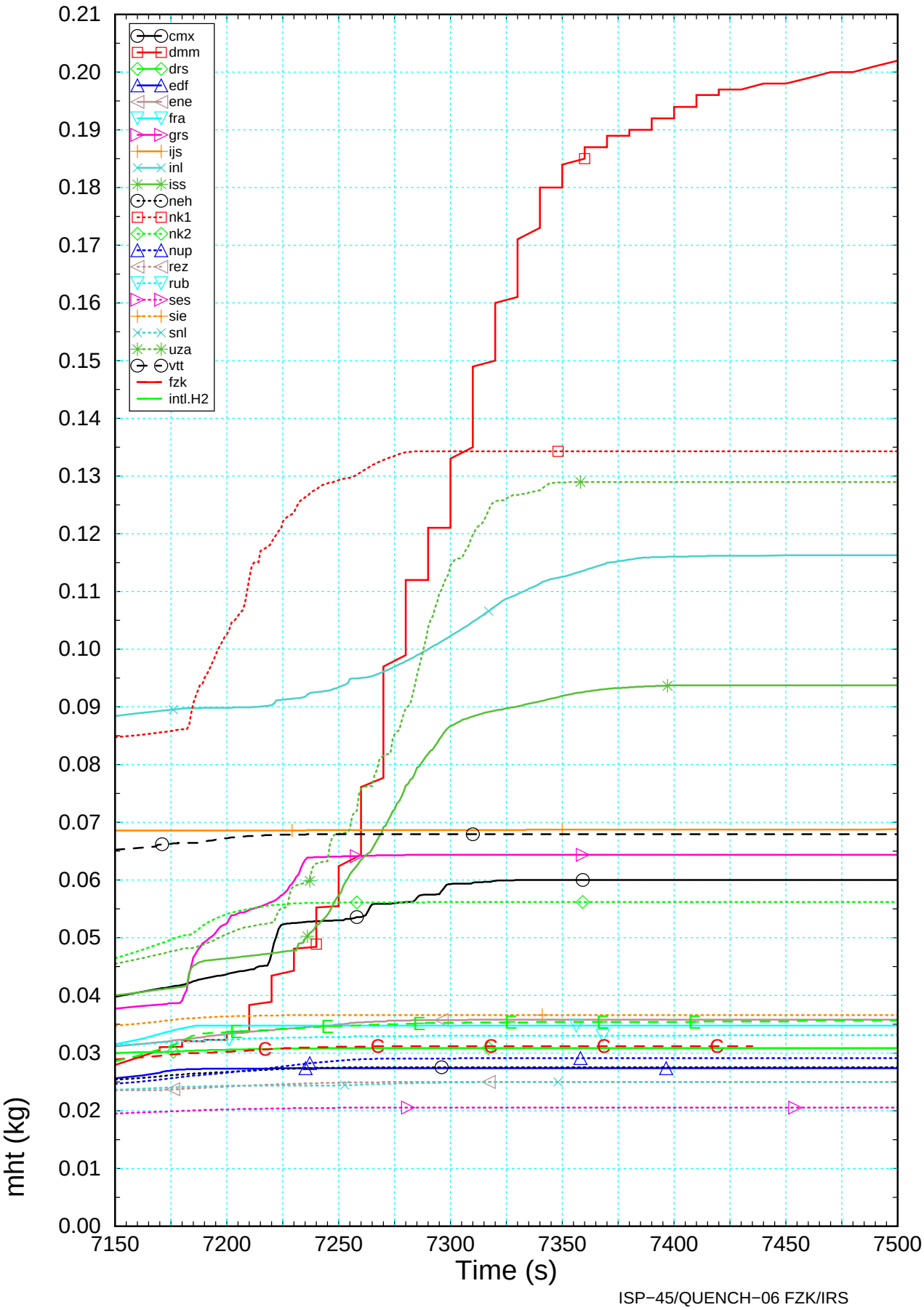

Figure 4.30 Hydrogen mass during reflood calculated by the participants and compared with data from experiment (-E-) and post-test calculations with S/R5 (-C-).

Local temperature increase during reflood / quench

The local cladding temperatures give a more detailed picture of bundle behavior during reflood. So Figure 4.31 to Figure 4.38 have been selected to show the thermal behavior at different elevations in the lower electrode zone (-0.25m, -0.15 m), in the lower half of the heated section characterized by a bundle peak temperature lower than 1500K (0.15 m, 0.35 m, 0.55 m) at reflood initiation, in the upper half of the heated section (0.75 m, 0.95 m), and in the upper electrode zone (1.15 m, 1.25 m). For selected elevations the shroud surface temperatures as well as the cladding oxide thicknesses are included in the appendix (section 8.3) for completeness.

Lower electrode zone

First the FRA cladding temperatures in Figure 4.31 as well as in Figure 4.32 clearly indicates that the convective heat transfer calculated by this MAAP calculation did not consider two-phase fluid conditions properly. No quench point is calculated and the cladding temperature drops in a smooth curve to saturation level. Such a behavior is obviously not realistic. Therefore, the results of this calculation will not be discussed in detail further-on.

As can be seen in Figure 4.32 for elevation –0.15 m, major part of the other calculations do not agree quite well with experimental data so that either the wetting times as well as the saturation temperature were not met. Even at that rather low temperatures, which are in the DBA regime, some codes still have difficulties with reflood thermal-hydraulics. In Figure 4.32 the measurements of TFS 2/2 is given, which shows fast cool-down due to the fast water injection with subsequent heat-up (to 500 K) before quench pump starts final reflood of the bundle. As can be seen, 5 participants indicate this initial prompt cooling to saturation temperature for all nodes in the lower electrode zone (Figure 4.32).

The other participants did not reproduce this initial temperature drop suggesting a possible misinterpretation of the fast injection rate, the volume in the lower plenum and/or have problems with this fast flooding process. Indeed, CMX, DMM, ISS and NEH use nodalizations which extend only partly into the lower electrode zone. The temperature in the first node of their simulator rods (Figure 4.31) is consequently used as a boundary condition to take into account the heat conduction in the water sink downside /18/.

In parallel, CMX electrical power input does not correspond in shape with the others (Figure 4.2, Figure 4.3 and Figure 4.4) contributing evidently to an unrealistic energy balance during reflood. Hence, due to this erroneous power input the positive feed back on temperatures in the bundle may induce a quite unrealistic temperature distribution over the whole bundle during reflood.

Besides, the initial wall temperature history at the bundle inlet gave large deviations up to the end of the heat-up phase (section 4.4.5). So, at 7179s, although a main stream of 16 participants show more or less realistic cladding surface temperatures in a “quite large” temperature band of 150 K width at elevation -0.15 m, REZ temperature is strongly too high (975 K instead of the expected TC value of 780 K) due to the rather coarse meshing in the lower electrode zone.

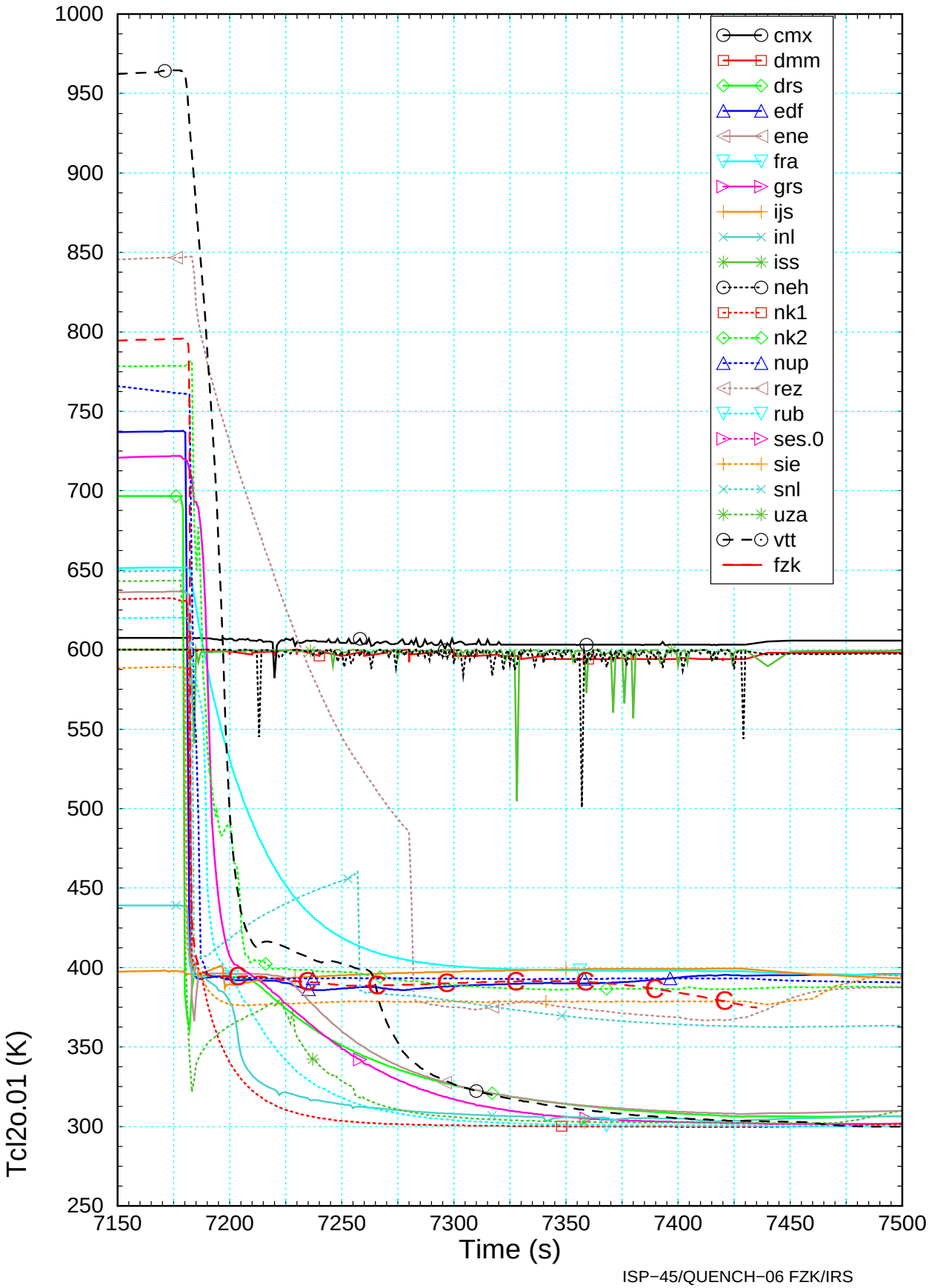

Figure 4.31 Cladding temperature at elevation –0.25 m (First Ring) calculated by the participants and compared to the results of FZK post-test calculation (-C-).

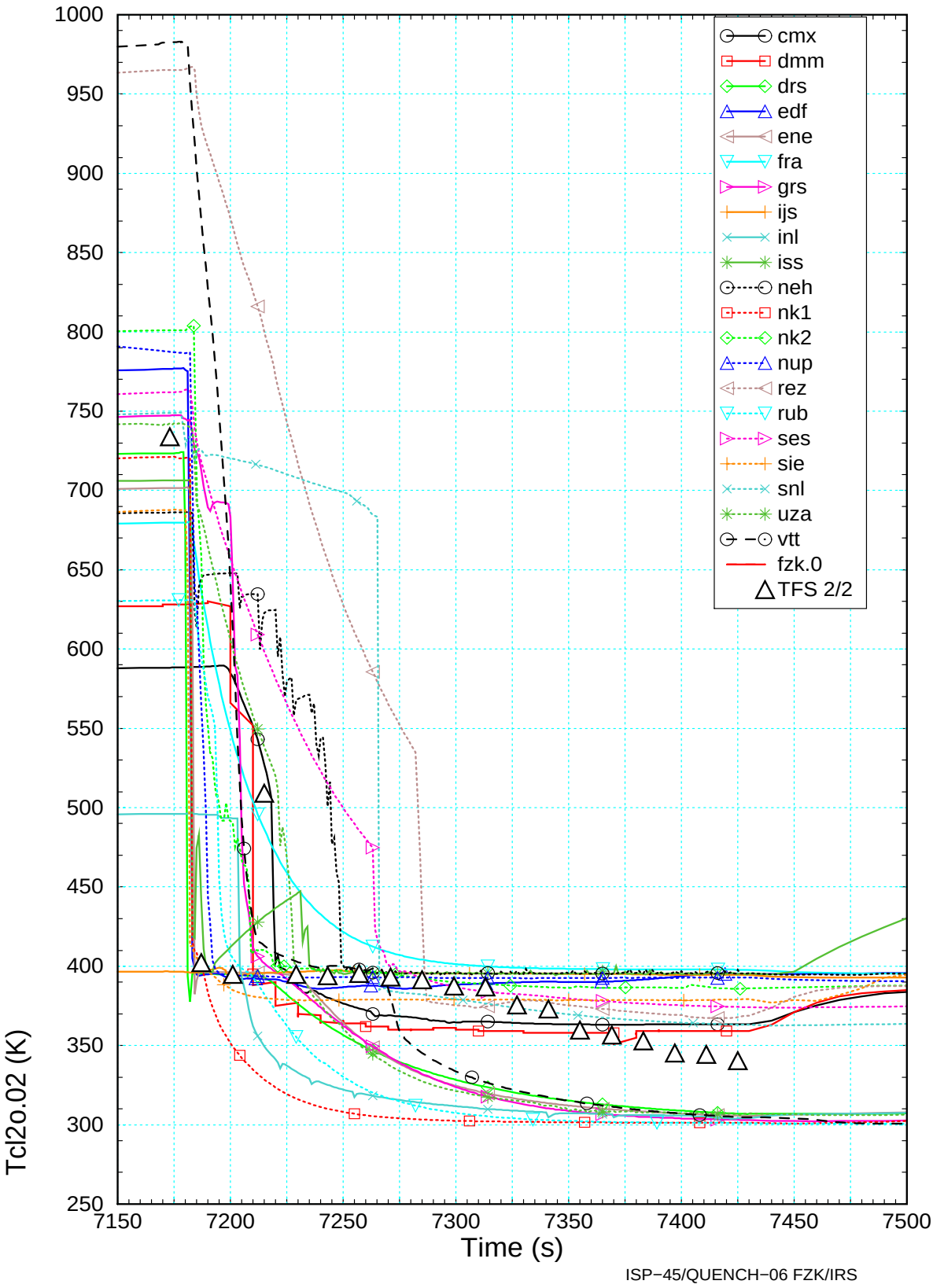

Figure 4.32 Cladding temperature at elevation –0.15 m (First Ring) calculated by the participants and compared to experimental results TFS2/2.

Moreover, SNL confirms the significant delay in initial propagation of quench front mentioned earlier (see section 6.3.1) by a slower temperature drop even if this deficiency is partially overcome by the use of an input parameter determining the quench front progression (Figure 4.32).

Heated section

Concerning the wide mainstream of 13 curves which do not show significant temperature escalations, 4 of them (DRS, EDF, RUB and SES) show a common tendency to overestimate the quench efficiency in the heated section (Figure 4.33 to Figure 4.36). The mean cooling rate of this group is quite higher than others so that wetting is calculated app. 40 s earlier compared to others. No temperature excursion is predicted during the quench phase. Consequently, those participants calculate a rather low hydrogen release between 20 to 80 % of the expected value.

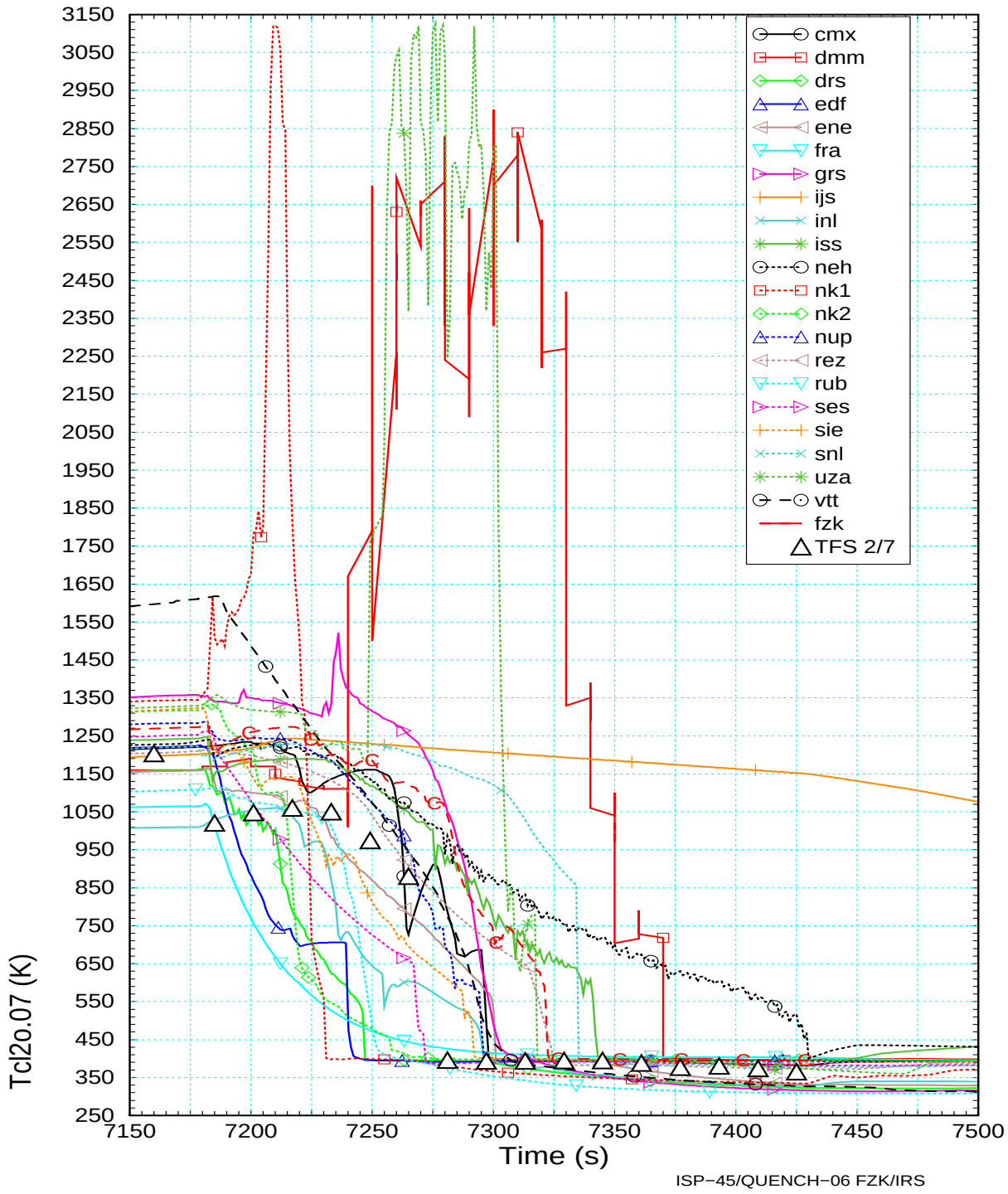

Figure 4.33 Cladding temperature at elevation 0.35 m (First Ring) calculated by the participants and compared to experimental results TFS2/7.

In essence, there is no obvious lack in the standard oxidation models up to the end of the heat-up phase but the use of such correlation during the very transient conditions of the reflood phase is still unexplained.

In addition, no quench induced cracking was taken into account, so that only the temperature increase due to the increased steam availability during the quench phase was calculated contributing to this slight under-prediction of the bundle temperatures in the heated zone. NK2 which over-predicted the bundle peak temperature at time of water injection (2150 K) did not use the new MELCOR reflood model but calculated an additional hydrogen release of 5g H_2 during reflood, which is quite close to the experimental value (Table 4.4).

Lower part of the heated region

In the lower third of the heated section (up to 0.55 m, Figure 4.34), the temperature plots of ISS, NEH, and SNL show a delayed cooling, the saturation level is reached app. 100 s later as in the experiment. Since no blockage was calculated in this elevation (Table 4.2) this behavior cannot be explained at the moment.

As explained by SNL their simplified reflood model is based on a maximum temperature against which a quench front can advance. It includes the effects of axial heat conduction within a rod from the unquenched portion to the quenched region, and represents the temperature of the unquenched portion of a rod above which this conduction transports more heat to the quenched region than can be removed there /16/.

The GRS curve show that the diffusion resistance of the oxide layer is another important sensitivity parameter for the calculation of the thermal behavior of the bundle. A reduction of the protective oxide layer thickness to 20 μm is used in this calculation to simulate the influence of the thermal stresses during cladding quench. However, the temperatures are not high enough in the lower half part and the oxide layer thicknesses are lower than 300 μm required for crack induced oxidation.

The simulation of the so called "shattering" phenomenon contributes significantly to the temperature increase in the lower half of the bundle as can be seen in Figure 4.33 (0.35 m) and in the upper half (Figure 4.34 above 0.5 m). The sharp bent in the slope of the temperature curves give hints of the usage of a global shattering approach.

So, generally speaking, the uncertainty in the water injection at bundle inlet during reflood due to heat exchanges with hot structures of the inlet circuit and lower plenum induces an inaccuracy in the water temperature and thus in the evaporation rate. This affects the cool-down rate which stops or, in case of "shattering options" promotes the oxidation process.

If oxidation excursion is calculated in the bundle a similar behavior is observed for the shroud. A high peak is observed at 0.25 m for DMM (section 8.3), 0.45 m for ISS, and 0.55 m for GRS (Figure 4.34).

The high energy release by the oxidation process is mainly due to the large mass of Zircaloy available for oxidation in this slightly oxidized region even if molten but localized within the protective oxide scale.

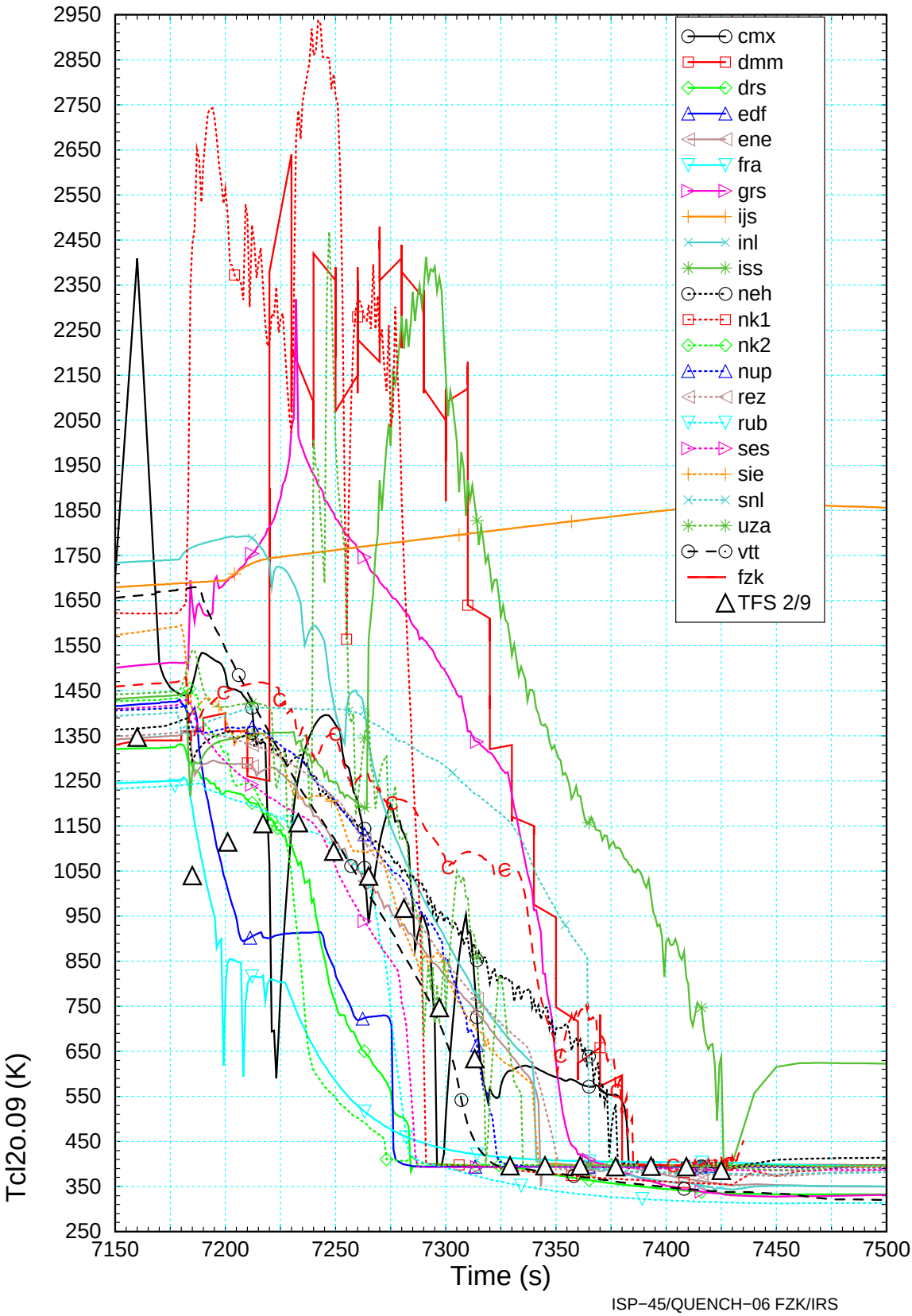

Figure 4.34 Cladding temperature at elevation 0.55 m (First Ring) calculated by the participants and compared to experimental result TFS2/9 and that of FZK post-test calculation (-C-).

Upper part of the heated region

At time of reflood initiation nearly all calculations except for DMM, INL, ISS, NK1 and UZA, indicated only localized damage in the upper third of the heated section and the temperatures were significantly below any liquefaction temperature. But at 0.95 m elevation, the scatter band including those participants amounted to 300 K at 7170 s (Figure 4.36).

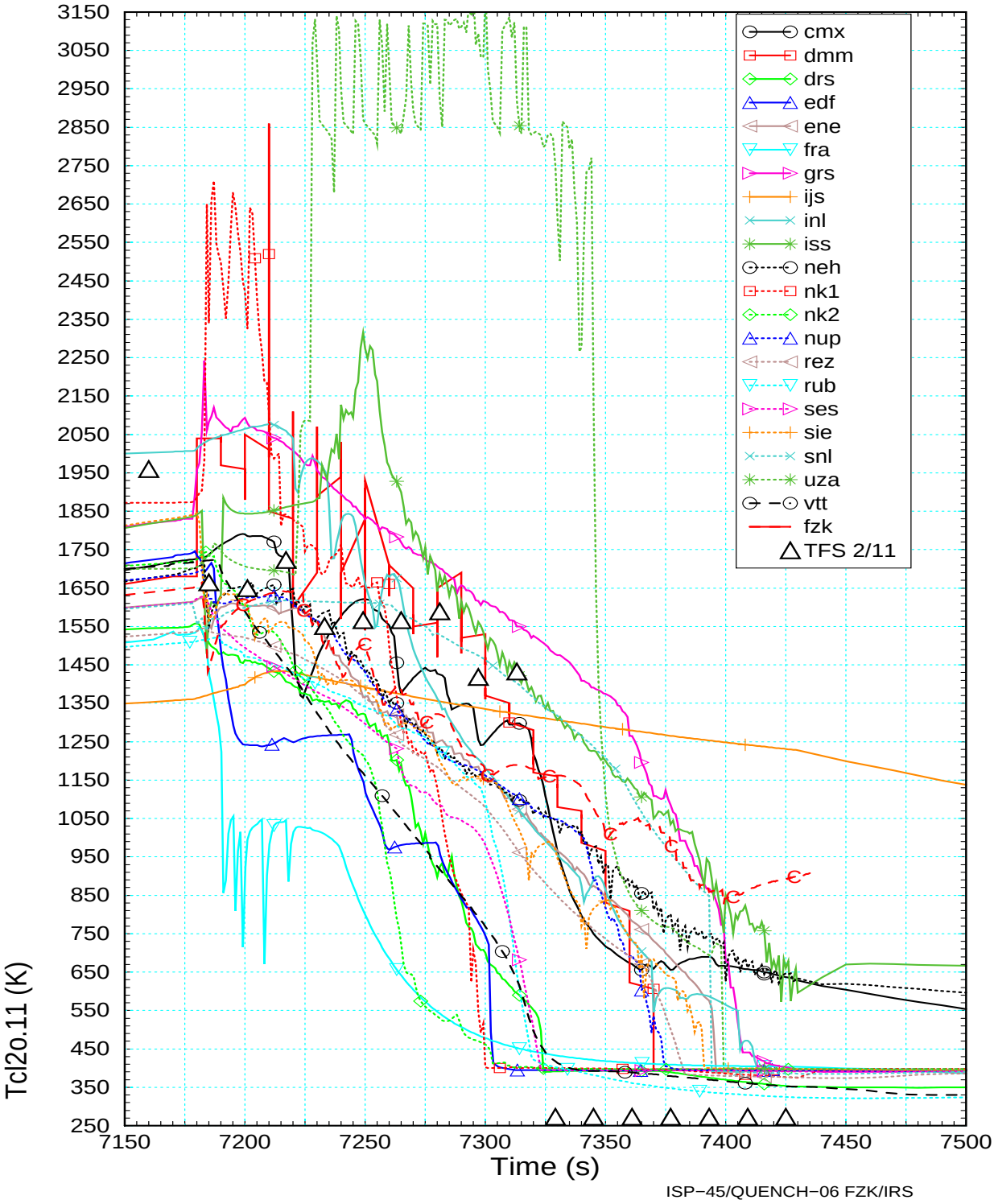

Figure 4.35 Cladding temperature at elevation 0.75 m (First Ring) calculated by the participants and compared to experimental result TFS2/11 and that of FZK post-test calculation (-C-)

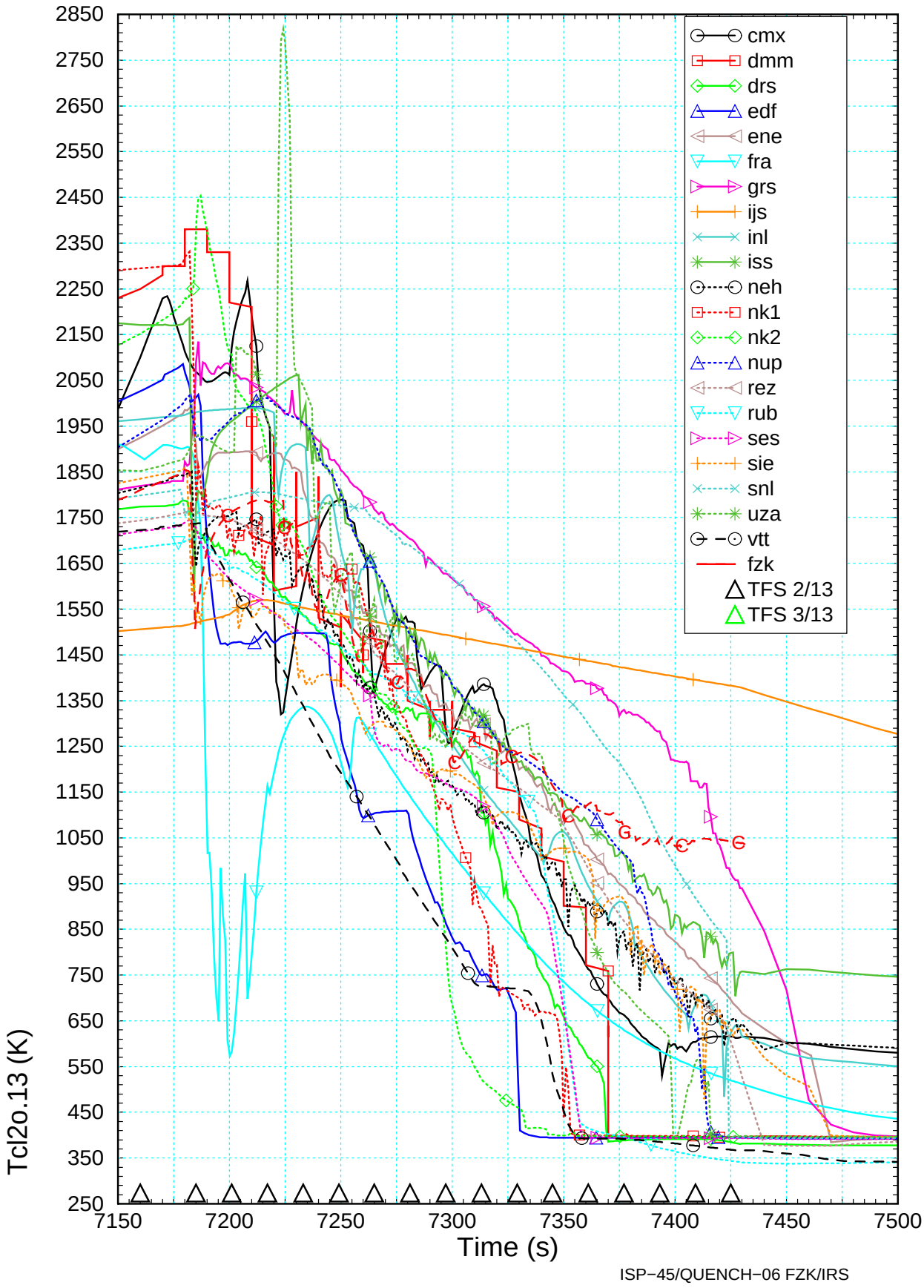

Figure 4.36 Cladding temperature at elevation 0.95 m (First Ring) calculated by the participants and compared to experimental results TFS[2;3]/13 and the results of FZK post-test calculation(-C-).

App. 200 s later this wide band extends to 600 K (excluding FRA) indication that temperatures are strongly influenced by artificially triggered oxidation (Figure 4.30). DMM, ISS, and UZA deviated already from the expected values after the onset of temperature escalation (6000 s) indicating possible melting. A possible relocation of metallic melts seems to be stopped quickly by the fast cooling rate because the temperature escalation is terminated within less than 100s for all of them. As a consequence the water front progression upwards is influenced but it does not explain the unreliability of the collapsed water level calculations of those participants (Figure 4.28).

In the extreme cases of INL and NK1, relocation of molten Zircaloy appears to be prevented due to the strongly over-predicted oxidation observed after the onset of temperature escalation, the oxide thicknesses being highly superior to 300 µm (see appendix section 6.4).

Even neglecting the extreme cases which were influenced by the oxidation accelerated by a shattering option, it can be stated in brief: The temperatures calculated in the hot spot in the upper third of the heated section confirm that the strong dependency of bundle degradation from the thermal-hydraulic conditions in the fluid channel is not yet solved reliably.

Upper electrode zone

The cool-down rates are still not well estimated in the upper part of the bundle reflecting the high degree of uncertainty associated to the flooding rates calculated up-stream. Nevertheless, uncertainties in definition of the state of the bundle prior reflooding also takes part in the inadequate heat and mass balance calculations of the participants.

SCDAPSIM users (except SIE) approximate more or less accurately the upper boundary condition for axial heat conduction in the heater rods (use of a guess for the temperature at the top of the electrode zone) and the radiative exchange between shroud and inner cooling jacket. This leads to a large distortion in calculated axial power and temperature profiles prior to reflood initiation (Figure 4.23, and Figure 4.24).

At this stage, the temperatures spread up to 1165 K at the top of the upper electrode zone as seen in Figure 4.38. Thus, NK1 and UZA show a common tendency to overestimate the temperature increase in that zone, probably linked to the cladding oxidation (Figure 4.37 and Figure 4.38). In Figure 4.37 the single triangle (TFS2/15) marks the sudden temperature drop at app.7180 s measure by the surface mounted TC. It indicates the steam and droplet flow caused by the fast water injection.

Besides, CMX, ISS, and NK1 used input nodalizations which extend only part way in the upper electrode zone leading to the observed low artificial cladding temperatures fixed as boundary condition for heat conduction at 1.25 m (Figure 4.38). It caused the observed high inconsistencies in the energy balance close to the outlet.

In addition, CMX power input adopts an unexpected temperature-like shape in the upper unheated zone during reflood (Figure 4.4) which contributes to a temperature escalation up to 2450 K (Figure 4.37) at 1.15 m bundle elevation.

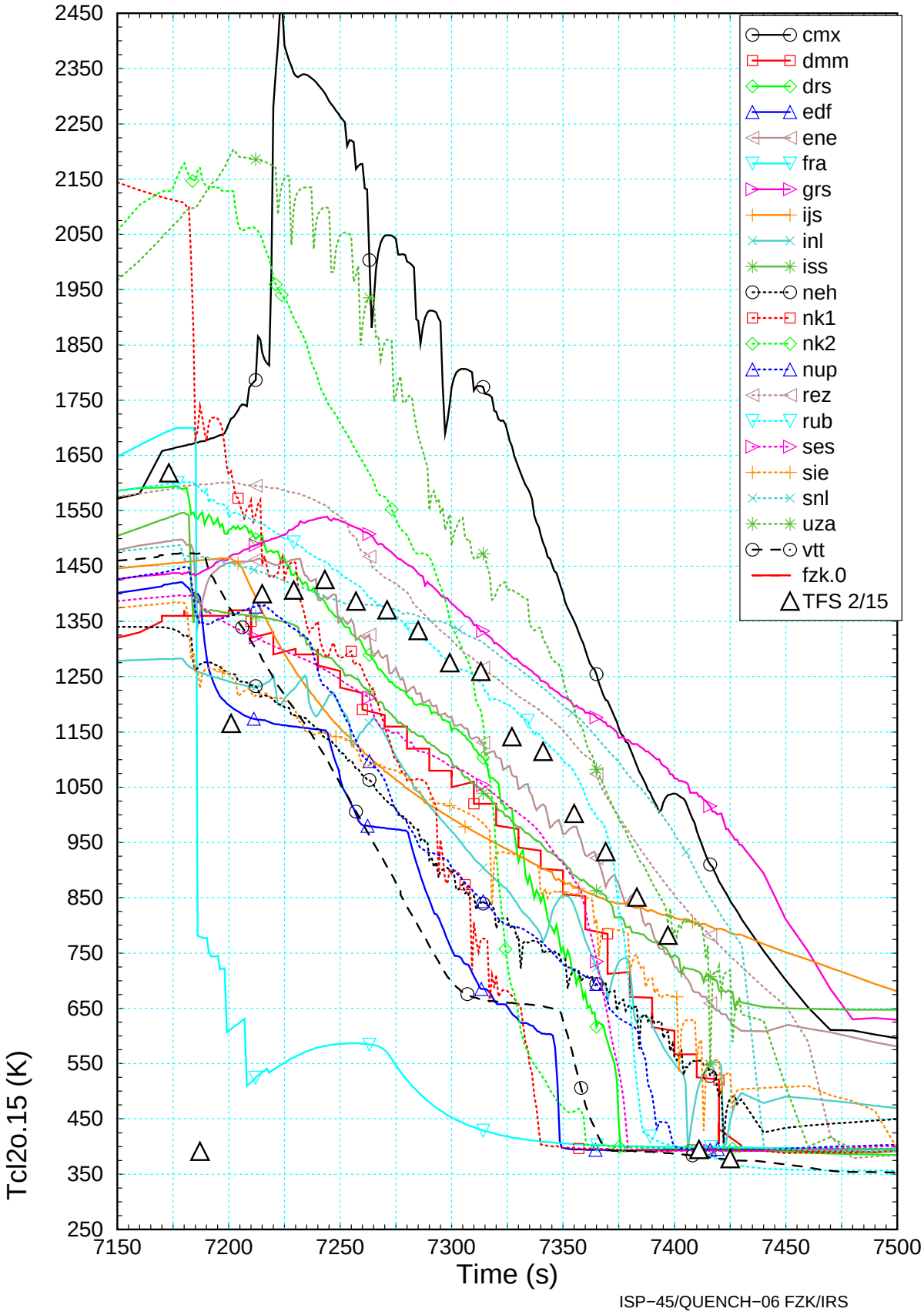

Figure 4.37 Cladding temperature at elevation 1.15 m (First Ring) calculated by the participants and compared to experimental result TFS2/15 and the results of FZK post-test calculation (-C-).

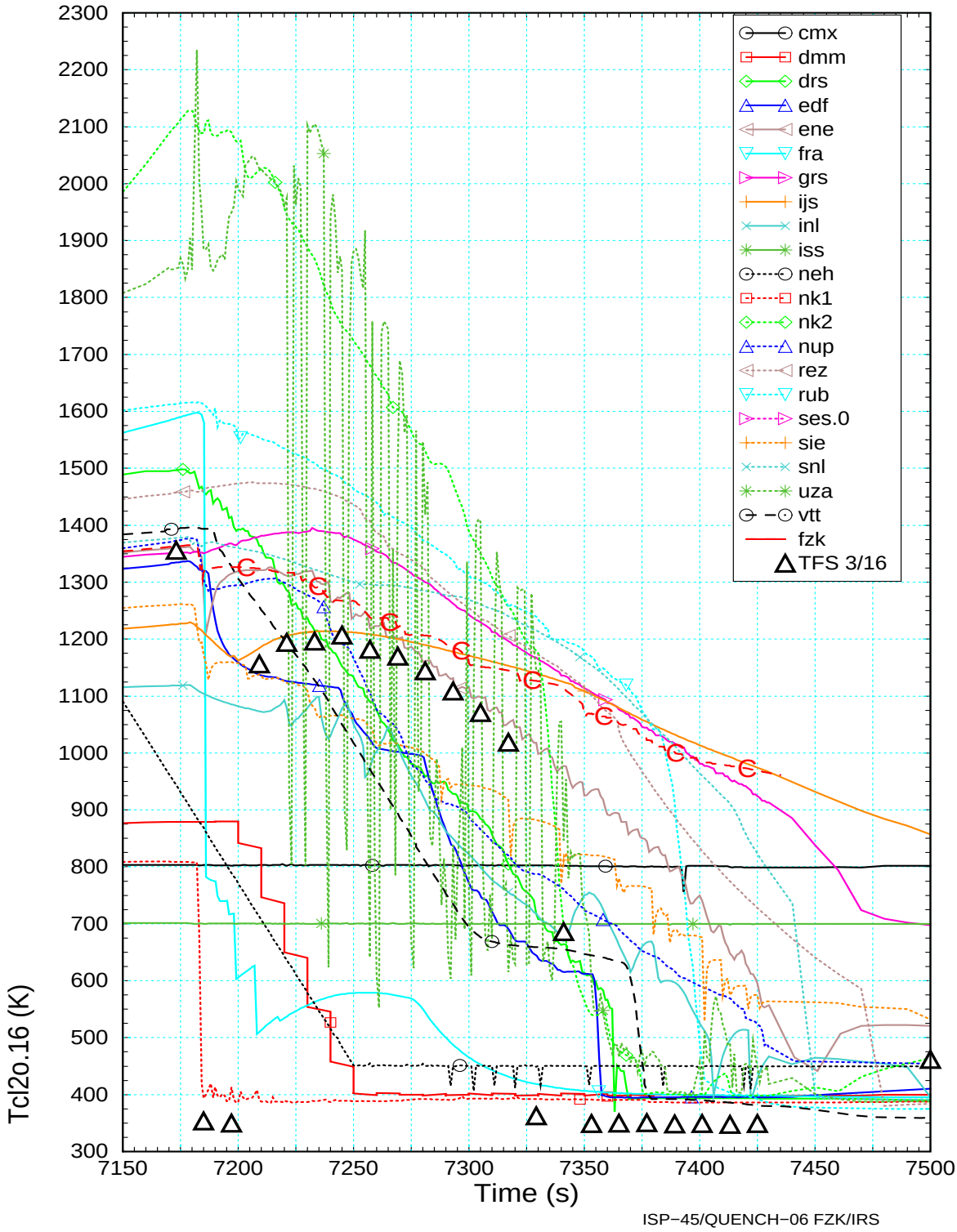

Figure 4.38 Cladding temperature at elevation 1.25 m (First Ring) calculated by the participants and compared to experimental result TFS3/16 and the results of FZK post-test calculation (-C-)

4.6.5 QUENCH front progression

To identify the capabilities of the thermal-hydraulic code packages the development of the quench front (zTq) was asked /8/. Data, delivered BY DRS, EDF, FRA, GRS, IJS, NEH, NUP, REZ, RUB, SNL, and VTT are shown in Figure 4.39 for the reflood phase. The results of IJS are calculated by a MELCOR version without a dedicated reflood

model so that the very noisy signal was removed. The data vector of NEH only contained zeros. The axial offset in the VTT results was corrected subtracting 0.5 m. The other participants did not deliver data.

The experimental data are derived from TSF thermocouples indicated by -e- and shroud thermocouples TSH -E-, respectively. Their slopes are approximated by thick straight lines. The results of TCRI/C thermocouples which are used for support, are indicated by " s ".

As mentioned in section 4.6.2 the TSH signals are representative for the onset of nucleate boiling, whereas the surface mounted TFS thermocouples give hints of the elevation of the droplet zone in the two phase region. In this sense, the TSH line is considered to be the lowest elevation for "wetting". As can be seen clearly the distance between both lines is affected by the mass flow rate G. During the short period of fast water injection, that distance increases to app. 0.5 m but after 7250 s it decreases to 0.1 m - 0.2 m.

First, there is a tendency to slightly over-predict the quench progression during fast water injection leading to an offset of app. 0.2 m. A fraction of fast injected water evaporates in contact with the hot structures of inlet pipe and enters the bundle as vapor at app. 400K (section 2.3.2). That vapor muss flow rate may be the origin of the observed deviations in the local void fraction calculation of some participants (DRS, EDF).

Two MELCOR results (SNL and REZ) show an unexpected delay of app. 80 s until the quench front starts to propagate upwards. At that time the quench front (zTq) is calculated to be app. 1 m below the collapsed water level (zwlv) as can be seen in Figure 4.27. This is rather unrealistic, especially since the surface temperatures are rather low below 0.5 m and the flooding rate after 7250 s is rather stationary (app. 40 g/s). Below 0.5 m these plots are out of the mainstream, mainly linked to the over-predicted fixed temperature against which a quench front can advance as assumed in the simplified reflood model.

Three curves, two MELCOR results, SNL and REZ as well as one MAAP results (FRA) are out of the mainstream, mainly due to lacking or erroneous reflood models. The MELCOR results show an unexpected delay of app. 80 s. The results of ATHLET-CD code calculations of GRS and RUB are somewhat contradicting, which could be explained by the artificial oxide scale cracking used by GRS. Indeed, GRS quench front met the TSH line while RUB overestimated. The results of EDF, DRS, and VTT also overestimated the quench front velocity in the bundle, EDF together with VTT mostly above 0.5 m.

Above 0.25 m, the result of the FZK calculation, which was used to define the water mass flow rate at the bundle entrance follows roughly the TFS line. The spreading of all slopes in Figure 4.39 is rather small considering the differences in the surface temperatures prior to reflood which are of 500 K and more (Figure 4.23). Indeed, the heat removal of the highly oxidized and overheated fuel rods and the shroud became more complicated due to changes in material composition and surface geometry. The calculated oxide layer thicknesses varying by a factor of 100% (Figure 4.25) along the bundle length may change strongly the axial and radial heat conduction at the clad surface.

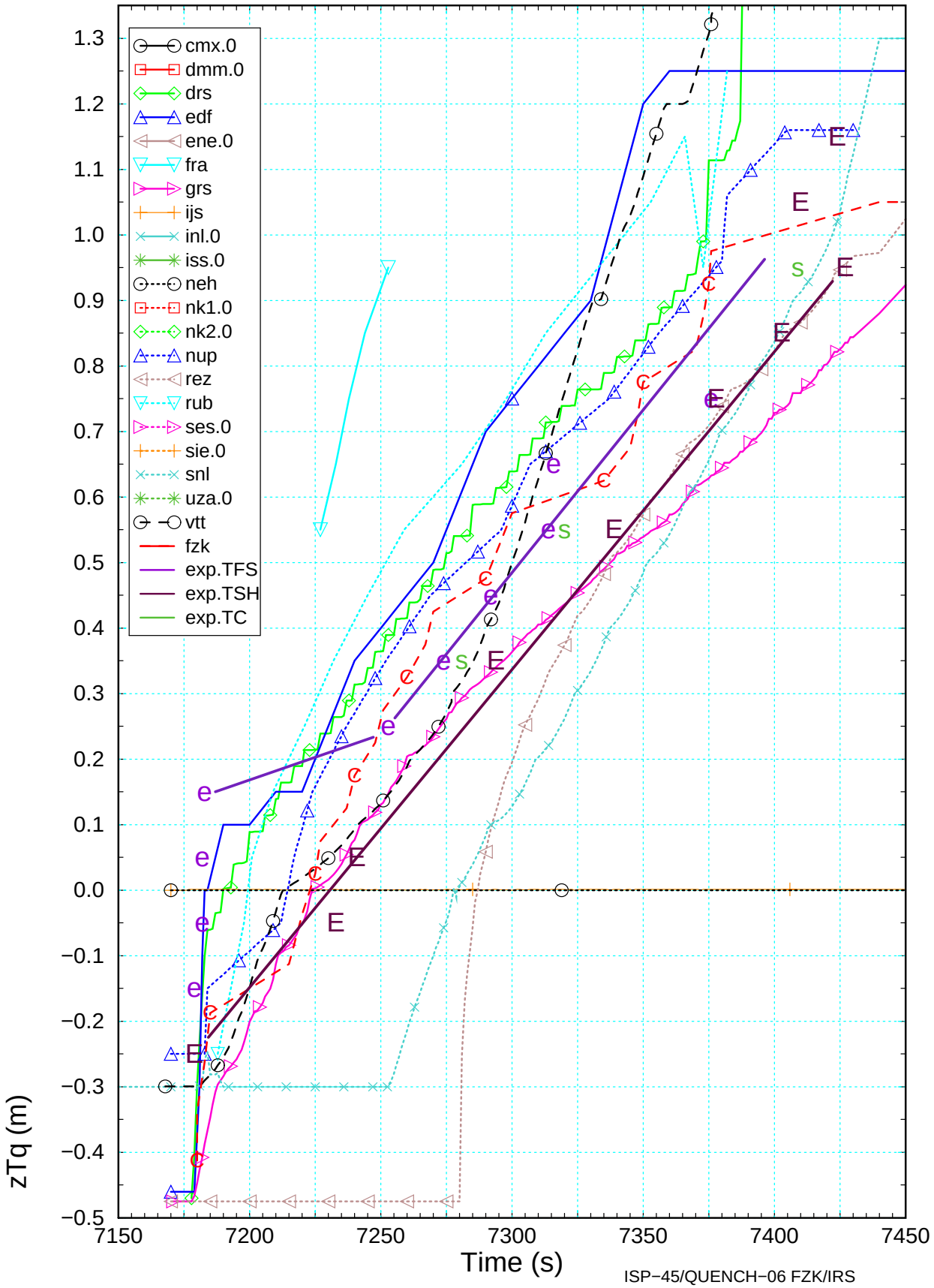

Figure 4.39 Development of the quench front calculated by various participants and compared to experimental results derived from TFS (-e-), TSH (-E-), and TCR (s) thermo-couples and the results of FZK post-test calculation (-C-).

On the other side, the quench temperature reflects the capability of the models to simulated the fuel rod behavior plus the very turbulent two phase flow in the cooling channel. Here codes with thermal-hydraulic code packages developed for DBA are advantageous. Especially if the strongly varying radial heat fluxes can be calculated in a fine axial mesh as mentioned in /10/. Since mesh refinement techniques are not available so far, the axial mesh length should be restricted to 0.075 m (3").

In the final ISP-45 OECD report /22/ this question will be addressed in more detail, especially addressing the relationship between zwlv and zTq which gives hints about the quality of the reflood model.

4.6.6 Hydrogen release during reflood / quench

In particular, the QUENCH-06 experiment was performed to assess SFD computer codes under reflood conditions, especially fuel rod behavior under transient cool-down conditions and hydrogen release. So, a special emphasis on the accumulated hydrogen generation for the bundle plus shroud during reflood is given in this section. All available results are compared to FZK post-test calculation (-C-) and data from experiment (-E-) in Figure 4.30.

As shown in Table 4.4 only a few grams of hydrogen have been released during reflood. The calculated hydrogen production spreads of around 20 g observed for the mainstream of 14 participants at 7179 s and around 180 g for 8000 s (Table 4.1). The scatter band which started with a range of uncertainty of app. 67 % at 7179 s has grown up to more then 480 % 420 s later. No specific code tendency could be identified. Thus, thermal-hydraulic modeling, activation of shattering options by the user, or severe bundle damage prior to reflood initiation have to be considered. In Figure 4.40 the oxide layer growth during reflood is shown for nearly all participants.

First, most of the participants, the so called mainstream, did not calculate significant oxide layer thickness increase.

Second, a large increase is found only above 0.35 m as mentioned before. This indicated that a minimum oxide layer thickness is implemented in the shattering options of the different codes, or that the option must obey to a temperature criterion. In Figure 4.40 a decrease in the oxide layer thickness is given, which only can be explained by local melt relocation removing a large part of the oxide layer.

Indeed, the code user has a great influence on the calculated results, e.g. by activation of the shattering option. Therefore, at the end of this analysis, 3 general tendencies are underlined.

First, 7 participants (EDF, FRA, REZ, RUB, SES, SNL, and VTT) did not apply shattering options. Their average hydrogen mass (Table 4.4) form a narrow group around the experimental value. NK2 may adopt the same configuration but due to absence of a reflood model they highly over-predict temperature during quenching.

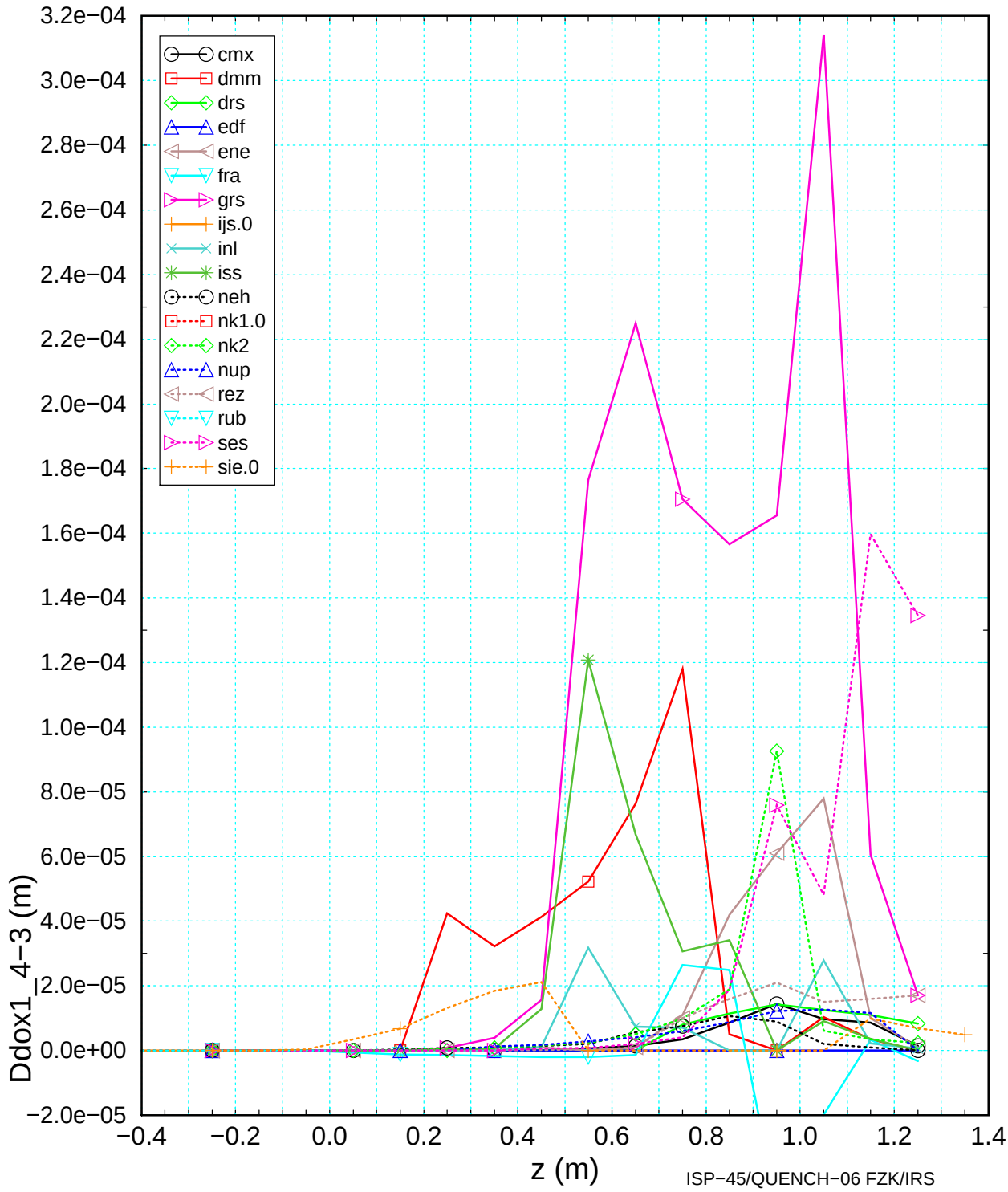

Figure 4.40 Oxide layer growth calculated for the central unheated rod during quench process showing the influence of the options used (shattering etc.)

A second group of 5 participants (DRS, ENE, NEH, NUP and SIE) have activated their shattering options and predicted more or less realistically the bundle state prior to reflood initiation (mean peak bundle temperature of app. 1900 K and mean maximum oxide thickness of app. 300 µm at 7179 s Figure 4.25 and Figure 4.42) thus leading to reasonable results as shown in Table 4.4.

Table 4.4 Hydrogen source term during flooding of ISP45

		bundle state prior to reflood (t=7179s)			final bundle state (t=8000s)	
code	**participant**	**Tbp K**	**δox μm**	**mht_1 g**	**mht_2 g**	**shattering option**
QUENCH-06		***2050***	***≅ 300 (#)***	***31***	***4,6***	
quenching at Tbp < 2050K : total 14 calculations						
ATHLET-CD	**RUB**	1675	250	32	1	(-)
GENFLO	**VTT**	1725	330	66	1,8	(0) (*)
MELCOR	**REZ**	1750	260	23,5	1,3	(0)
ICARE/ CATHARE	**DRS**	1775	250	30,5	0,5	(-)
MELCOR	**SES**	1775	250	20	0,5	(0)
MELCOR	**SNL**	1800	310	24	1,1	(0)
SCDAPSIM	**NEH**	1825	220	26	1,2	(+)
S/R5.irs	***FZK***	***1825***	***220***	***30***	***1,2***	***(+)***
SCDAPSIM	**SIE**	1875	300	41	0,8	(+)
MAAP 4.04	**FRA**	1900	310	34,5	0,5	(0)
ATHLET/CD	**GRS**	1900	510	39	27	(++)
ICARE/ CATHARE	**ENE**	1950	310	32	3,5	(+)
IMPACT/ SAMPSON	**NUP**	1950	400	25,5	3	(+)
MAAP 4.04	**EDF**	2050	370	27,5	0,2	(0)
quenching at 2050 < Tbp : total 7 calculations						
SCDAPSIM	**UZA**	2100	360	47,5	80	(+)
SCDAP-3D	**INL**	2150	680	90	26	(+) (**)
SCDAPSIM	**ISS**	2175	450	42	53	(+)
MELCOR	**NK2**	2175	630	50	5	(0)
SCDAPSIM	**CMX**	2225	320	42	18	(+) (*)
SCDAPSIM	**DMM**	2275	280	32	175	(+)
SCDAPSIM	**NK1**	2300	1100	86	50	(+)

(#) preliminary value from SVECHA
(+) shattering option activated
(++) shattering amplified by user
(-) shattering option deactivated
(0) shattering not available
(*) erroneous axial dynamic power redistribution
(**) erroneous heater rod model

IJS excluded due to early blockage formation
δox : oxide layer thickness
mht_1 : Accumulated H_2 mass up to reflood
mht_2 : Accumulated H_2 mass starting at reflood

The third group is constituted with 6 SCDAPSIM users (CMX, DMM, ISS, GRS, NK1, and UZA) which were already out of the mainstream prior to reflood initiation at 7179 s. Indeed, each of them showed strongly enhanced temperature escalations in the upper part of the heated section during the heat-up phase. This led to high axial temperature gradients of 2000 K/m for CMX up to 40000 K/m for the extreme case of DMM. They consequently over-estimate the hydrogen generation by reducing the protective oxide layer by the clad shattering option.

GRS may be included in the third group due to the artificial decrease of its protective oxide layer to 20 μm which amplifies also the over-prediction of the hydrogen release during the quench phase (app. 27 g in Figure 4.30) and INL shows the same tendency probably due to its diffusion model effect on the oxidation process even for highly oxidized claddings.

4.7 Final state

4.7.1 Free bundle cross section

As mentioned in section 2.2.2 no bundle damage except for cladding rupture at reflood initiation was found /7/. Consequently, the change between initial conditions of the free flow area (af) and the final state is limited to the location of ballooning and clad rupture.

As can be seen in Figure 4.41 the mainstream of the results are close to the intact bundle flow cross section area of 0.003 m². Two results ENE and FRA, show cross sections app. one order of magnitude smaller which may be explained by post processing errors.

Nearly all participants show some slight reduction in the free flow area due to local ballooning. The extreme reduction above 1.0 m cannot be explained based on our available data, one explanation is a unintended collapse of the fuel rod segments in the upper electrode zone by an unexpected user error.

4.7.2 Axial profile of oxide scales

In Figure 4.42 the oxide layer profiles calculated for the final state of the QUENCH-06 bundle are shown. The large variations are caused by superposition of several uncertainties starting from user input, oxidation model, activation of the shattering option, and melt formation and relocation.

Indeed, excluding participants with code difficulties (VTT: inaccurate oxide growth rate) and those which did not deliver results (IJS, NK2, SNL), the relevant oxide thickness show three different zones along the axial elevation.

In the lower part of the heated zone (< 0.5 m), even if nearly all calculations showed that the claddings were slightly oxidized at 7179 s, a strong difference in the slope of the oxidation profile is obvious at the end of the calculation. Since all codes except for the SCDAP-3 (INL) rely on correlations, a initial oxide layer thickness is required. Also the used Cathcard correlation overestimates the growth rate at low temperatures.

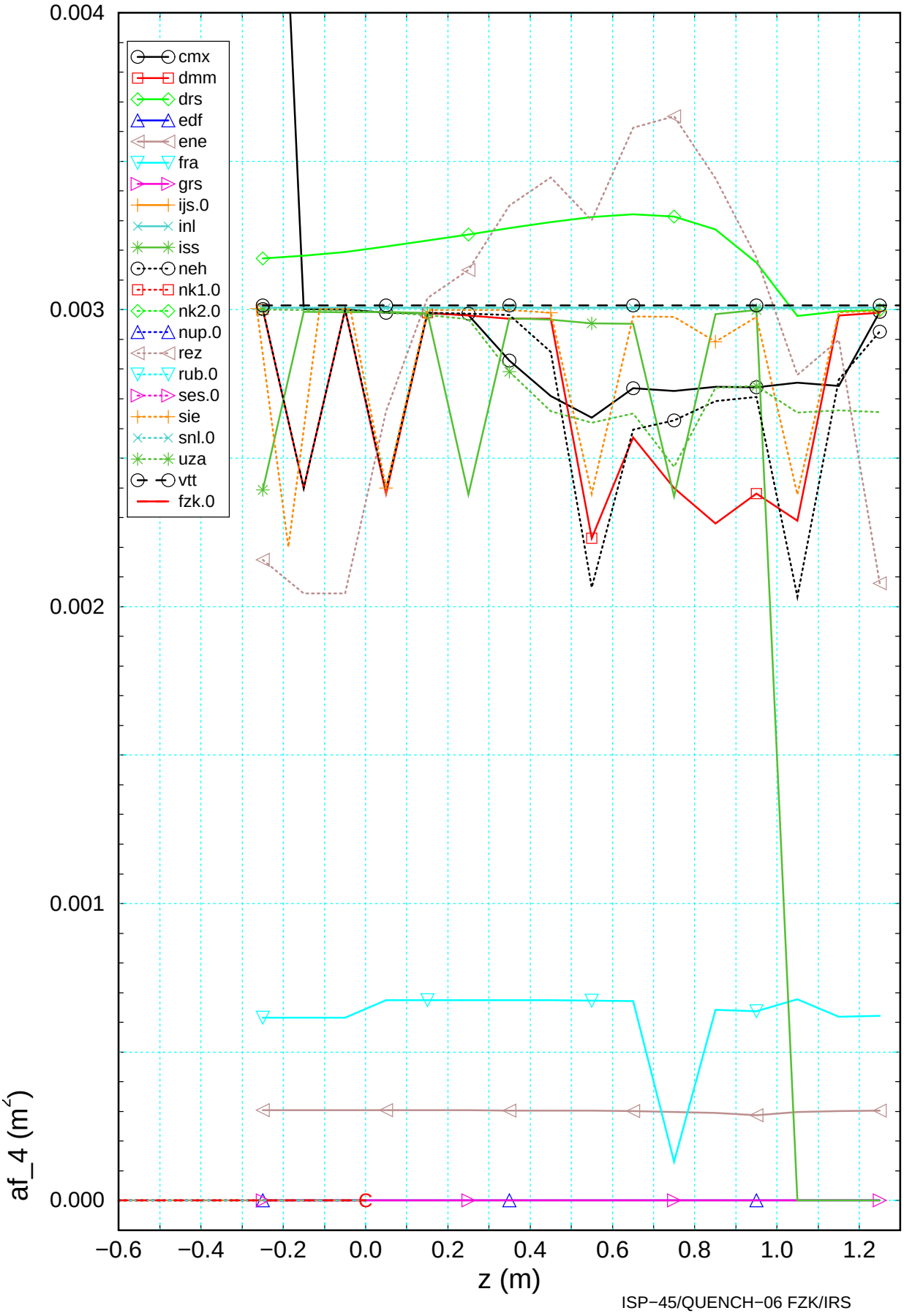

Figure 4.41 Axial fluid cross section profile calculated by the participants for t=8000 s.

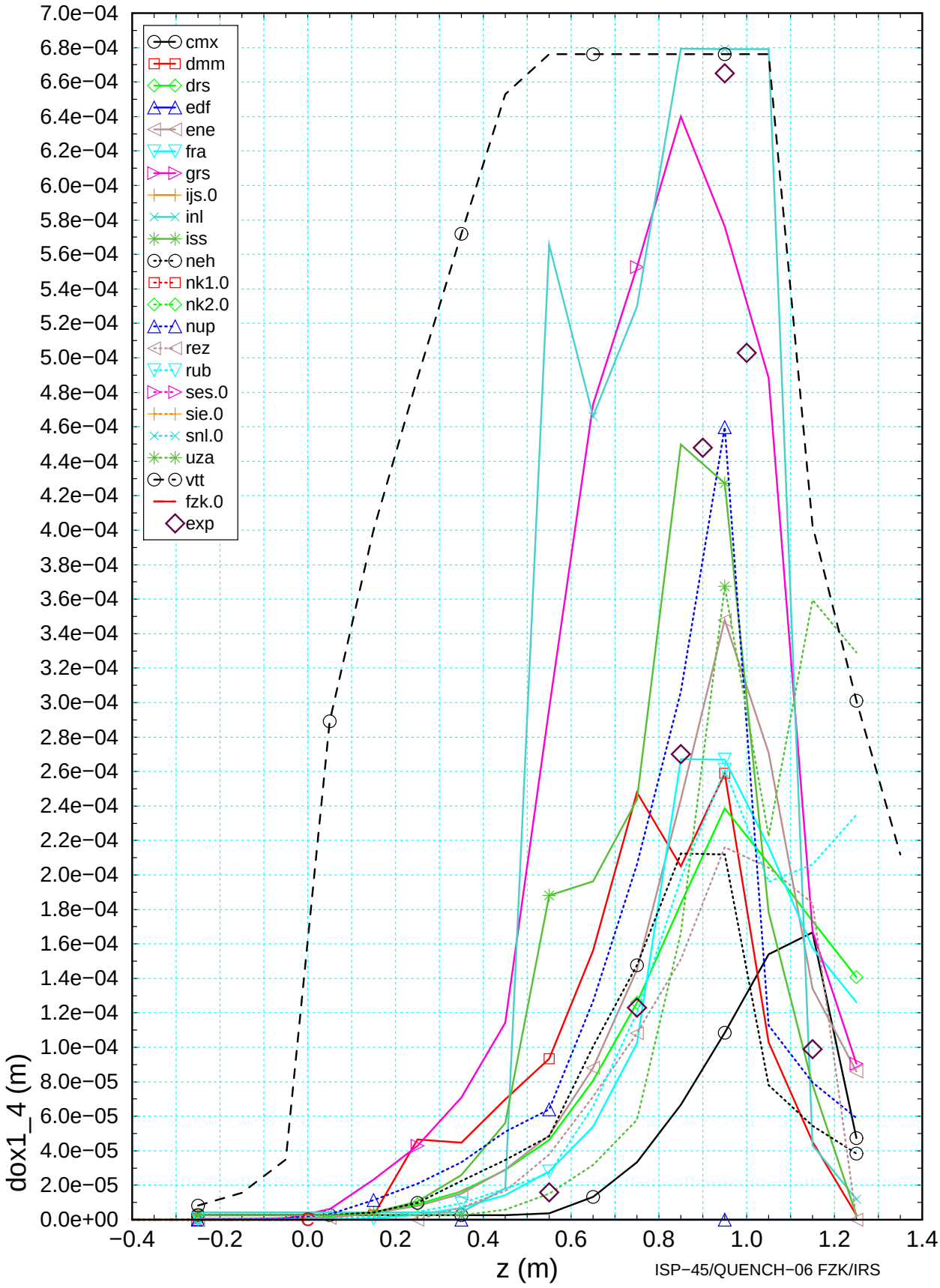

Figure 4.42 Axial oxide scale profile of the central unheated rod calculated by the participants for t=8000 s compared to experimental results

A more pronounced bundle oxidation is found to have occurred during reflood for DMM, GRS, ISS, NEH, NK1, and UZA. The SCDAPSIM users strongly over-predict the amount of clad shattering, the axial extension as well as the local amount of hydrogen released additionally, which becomes obvious in Figure 4.40.

Moreover, GRS tends to clearly over-predict the oxide growth rate over the whole bundle confirming the unreliability of its artificial decrease of the diffusion resistance of the oxide shell under such reflood conditions.

At 0.95m, the values for the heated rod ranges between 230 μm and 1100 μm and those for the unheated fuel rod from 110 μm to 660 μm. Nevertheless, whereas all values were in a scatter band of +/-70 % at 7179 s, it rises only to +/-75 % at the final state. In fact, for participants showing strong heat-up during the power transient (DMM, ISS, INL, NK1 and UZA), no significant oxidation is found to have occurred in the hot spot. Concerning the extreme cases of INL and NK1, the cladding oxidation was already stopped by a lack of unoxidized materials before water injection but, for others, such a situation can be explained only by assuming that a massive blockage may have covered a part of the coolant cross-section area in the hot spot knowing that the relocated material may have protected the cladding from steam exposure.

On the other side, DRS, EDF, RUB and SES under-predict their oxide growth rate over the whole heated section. Therefore knowing that embrittlement mechanism induced by thermal chock is not treated in MAAP and MELCOR codes and deactivated in DRS calculation, it may explain the observed lowering of the hydrogen release during reflood for those participants.

In addition, a remarkable deviation arises at 1,25 m where both heated and unheated rods show a similar scatter around 300 μm which already existed in the same extent prior to reflood. It confirms the need for improved boundary conditions in the upper plenum. Besides, the sharp peak of the UZA and CMX oxide layer thicknesses at 1.05 m and 1.15 m elevation for the heated rod, respectively, give evidence of unexpected shattering in this region illustrating the difficulties arising due to facility modeling in this region.

4.7.3 Axial profile of accumulated debris

From the visual inspection of the bundle after the test no melt formation could be detected except for some local shroud melting. In the destructive post test analyses /7/ neither macroscopic melt release nor blockage or debris formation was detected.

As can be seen in Figure 4.43 some participants calculated massive material redistribution in the bundle, depending on the maximum temperature and the code capabilities. Such extreme values were not expected and may only be explained by user errors.

In case of DMM the relocated melt is mainly metallic Zircaloy as shown in Figure 8.41. In case of UZA a post processing error has to be assumed. The small debris value calculated by REZ at the uppermost levels is caused by an unexpected code error which collapsed artificially the uppermost nodes, as explained by the participant.

Figure 4.43 Axial profile of accumulated debris calculated by the participants for t=8000 s compared to experimental results.

5 SUMMARY

The International Standard Problem No. 45 of the OECD/NEA/CSNI on the out-of-pile reflood test QUENCH-06performed at FZK, fills the gap between various ISPs dedicated to reflood situations under design basis accidents and ISPs in the severe core damage area ISP-31 (CORA-13) and the LOFT LP-FP2.

Apart from obvious user errors, the calculated conditions prior to reflood do not deviate significantly from one another, so that a definition of a mainstream is justified. During quenching the lack of adequate hydraulic modeling becomes obvious: some participants could not match the observed cool-down rates, others had to use a very fine mesh to compensate code deficiencies. Even without any bundle damage, the calculated axial oxide layer thickness varied significantly. For a more detailed analysis and in order to assess the influence of code capability as well as user experience on the results, a coarse qualification was performed as shown in Table 5.1.

Code capability

The thermal-hydraulic packages of the codes span between detailed mechanistic versions, widely validated in the field of DBA experiments and single phase approaches, which can only handle either liquid or vapor in one cell. To overcome such deficiencies for both integral codes MAAP and MELCOR, new models for reflood were used. They will be discussed in detail in the OECD report /22/.

The results with respect to energy balance, thermal-hydraulics, and bundle degradation are considered to be reasonable if they are in the confidence range as indicated in Table 5.1, forming the so called “mainstream”. That mainstream comprises app. 80 % of the participants.

The energy balance of the different code systems showed unexpected large deviations compared to experimental values and post-test analyses at the end of the pre-oxidation phase, when a quasi steady state situation in the bundle is given. This was not expected and may not be attributed to user effects alone.

During reflood various data such as water level and temperatures, reflect the different thermal-hydraulic capabilities of the codes. The results vary between no reflood effects, the temperatures simply drop to saturation value, and temperature increases up to 3100 K.

Simulation / user capability

In Table 5.1 the user’s experience is classified into four groups, and obvious errors are indicated (Remarks). The user’s experience ranged from start-up to code developer / experienced user, who knows the code deficiencies perfectly. It was found that code developers suggested wrong code options to the code users which deactivates the rod to rod radiative heat transfer, so that unrealistic high cladding temperatures were found.

The simulation capability of the codes with respect to the electrically heated out-of-pile test facility has been significantly improved with respect to previous ISPs (ISP-31, ISP-

36) hosted at FZK. Nevertheless, for some codes the simulation of non reactor specific environments causes difficulties. In the contest of the various codes the detailed mechanistic codes such as ICARE/CATHARE, SCDAP-3D, SCDAP/RELPA5, or SCDAPSIM have some in-built advantages due to their dedicated usage for experiment analyses (SCDAP designed for PBD, LOFT analyses and extended and optimized at FZK for CORA/QUENCH and Phebus experiments, ICARE2 for the Phebus SFD and Phebus FP programs).

Table 5.1 Code and user specific effects found during ISP-45 contest.

Code	Input source	Code variants	Energy balance	Thermal-hydraulics heat-up	Thermal-hydraulics reflood	Bundle degradation heat-up	Bundle degradation reflood	User experience	Remarks
ATHLET-CD	GRS	GRS	± OK	± OK	++	± OK	--	D/E	missing mechanical model
	RUB	"			±OK		++	E/D	shattering amplified by user
GENFLO	VTT	VTT	--	± OK	±OK	n/a	n/a	G	only static axial power profile
ICARE/ CATHARE	DRS	DRS	±OK	± OK	± OK	±OK	±OK	E/D	No shattering
	ENE	"	++			n/a	n/a	E	similar SR5 shattering option
IMPACT/ SAMPSON	NUP	NUP	± OK	±OK	±OK	±OK	n/a	D/E	similar to SR5 shattering option
MAAP 4.04	EDF	EDF	--	± OK	± OK	n/a	n/a	E/D	No shattering
	FRA	FRA	--			± OK	MR	E	No reflood model
MELCOR (R)	REZ/ SNL	SNL	± OK	± OK	± OK	±OK	± OK	E D	No shattering
MELCOR (-)	NK2 IJS	"	++	++	++	MR (IJS)	n/a	G	No reflood model
SCDAPSIM	ISS	ISS	++	++	++	n/a	++	D/G	R5 reflood model
	SIE	"	--	±OK	±OK	±OK	±OK	E	wrong code option
SCDAP-3D	INL	INL	/\/	++	++	±OK	±OK	D/E	outdated USNRC heater rod model
S/R5.irs	16 ax 32 ax	FZK	± OK	± OK	- ± OK	B B	-- ± OK	E	0.1 m nodalization insufficient for reflood
Confidence range:			*± 40%*	*± 15%*	*± 40%*	*± 15%*	*± 40%*		

results reasonable	**± OK**	n.a.	no sufficient information	D: code developer
underpredicted	**--**	B	ballooning with clad rupture	E: more experienced
overpredicted	**++**	MR	early melt relocation	G: less experienced
oscillating	*/\/*			

The ISP-45 is continued with user comments on this report and open calculations in order to eliminate obvious user errors. No perfect simulation of the QUENCH-06 using all adjustments of the codes was intended, but a reasonable simulation of all phenomena. So all participants were invited to participate in open calculations and to use other QUENCH experiments without modifying the main code parameters.

6 ACKNOWLEDGMENT

The broad support needed for preparation and execution of the OECD/NEA/CSNI ISP-45 is gratefully acknowledged. In particular, the authors would like to thank the QUENCH team at IMF for their successful performance of the QUENCH-06 test and all the work which is related to such a project. They also appreciate the contribution of all participants to clarify unexpected data. Especially we appreciate the careful reading of the manuscript and the valuable comments by Jacques Royen, Wolfgang Schütz, and Martin Wörner.

7 LITERATURE

/1/ Hofmann P., Homann C., Leiling W., Miassoedov A., Piel D., Schmidt L., Sepold L., Steinbrück M.; Results of the Commissioning Tests, Wissenschaftliche Berichte, FZKA-6099 (August 1998).

/2/ Hofmann P., Hering W., Homann C., Leiling W., Miassoedov A., Piel D., Schmidt L., Sepold L., Steinbrück M.; QUENCH-01 Experimental and Calculational Results, Wissenschaftliche Berichte, FZKA-6100 (November 98).

/3/ Hofmann P., Homann C., Leiling W., Miassoedov A., Piel D., Schanz G., Schmidt L., Sepold L., Steinbrück M.; Experimental and Calculational Results of the Experiments QUENCH-02 and QUENCH-03, Wissenschaftliche Berichte, FZKA-6295 (July 2000).

/4/ Hering W., Homann Ch., Improvement of the Severe Accident Code SCDAP/RELAP5 mod 3.2 with respect to the FZK QUENCH Facility, FZKA 6566 (December 2001).

/5/ PSF-Information: http://psf-nt-server.fzk.de/psfhome.htm

/6/ ZIRCONIA Insulation Boards and Discs Types ZYFB-6 and ZYFB-3 http://www.zircarzirconia.com/ZYFB-3ZYFB-6.htm

/7/ Sepold L., Homann C., Miassoedov A., Piel D., Schanz G., Schmidt L., Stegmaier U., Steinbrück M.; Experimental and Calculational Results of the QUENCH-06 Test (OECD ISP-45), Wissenschaftliche Berichte, FZKA-6664 (in preparation).

/8/ Hering W., Homann Ch., Miassoedov A., Steinbrück M., Specification of the International Standard Problem ISP-45 (QUENCH-06), OECD/NEA/CSNI/R(2001)1.

/9/ Hering W., Homann Ch., Lamy J.-S., First survey of global data of ISP-45 blind phase, Internal Report Nuklear-3359 (August 2001).

/10/ Frepoli C., Hochreiter L.E., Mahaffy J., Cheung F.B., A noding sensitivity analysis using COBRA-TF and the effect of spacer grids during core reflood, ICONE-8711, Proceedings of ICONE-8, April 2-6, 2000, Baltimore, MD, USA.

/11/ Olander D. R., “Materials chemistry and transport modeling for severe accident analyses in light water reactors, I: External cladding oxidation”, NED 148 (1994), pages 253-271.

/12/ Firnhaber M., Trambauer K., Hagen S., Hofmann P., CORA-13 experiment on severe fuel damage : OECD/NEA-CSNI international standard problem no. 31 ; ISP-31 ; comparison report, OECD/NEA/CSNI/R(93)17, Bericht KfK-5287, GRS-106, July 1993.

/13/ Firnhaber M., Trambauer K., Hagen S., Hofmann P., CORA-W2 experiment on severe fuel damage for a Russian type PWR; Comparison report; OECD/NEA-CSNI international standard problem ISP 36, Wissenschaftliche Berichte, FZKA-5711 (1996).

/14/ Analytis G. Th.; Developmental assessment of RELAP5/MOD3.1 with the separate-effect and integral experiments: Model changes and options. PSI-Ber.96-09 (April 1996).

/15/ Elias E., Sanchez V., Hering W.; Development and validation of a transition boiling model for RELAP5/MOD3 reflood simulations, NEDEA 183 177-332 (1998).

/16/ Cole, R., " MELCOR Core Reflood Modeling and Applications to QUENCH Experiments", CSARP Meeting, May 7-9, 2001, Bethesda, Maryland, USA.

/17/ Berdyshev A.V., Boldyrev A.V., Palagin A.V., Shestak V.E., Veshchunov M.S., SVECHA/QUENCH Code for The Modeling of Reflooding Phenomena in Severe Accidents Conditions. Proceedings of the Ninth International Topical Meeting on Nuclear Re-

actor Thermal Hydraulics (NURETH-9), paper Log_19 (CD-ROM edition), San Francisco, California, 1999. (http://www.ibrae.ac.ru/english/kiselevae.html)

/18/ Allison C., private communication, October 2001.

/19/ Mühl B., Programm Nukleare Sicherheitsforschung, Jahresbericht 2000, Wissenschaftliche Berichte, FZKA-6653, p. 239-250 (September 2001).

/20/ Stuckert J., private communication, November 2001.

/21/ Leskovar M., private communication, November 2001.

/22/ Hering W., Homann Ch., Lamy J.S., Miassoedov A., Schanz G., Sepold L., Steinbrück M., Interpretation and Comparison Report of the OECD International Standard Problem No. 45 Exercise (QUENCH-06), OECD/NEA/CSNI/R(2002)2, Wissenschaftliche Berichte, FZKA-6722 (to be published).

8 APPENDIX

8.1 Quality of data delivery

In total, figures of more than 400 physical quantities were prepared from the data delivered by the participants. A number of data contains redundant information but may be of interest for some participants.

8.1.1 Database received

In the following tables the figures used in the report are indicated by bold typing, whose printed in the appendix are given in bold italic.

Table 8.1 Global data

Power	**Pel6**	**Pel7**	**Pelb**	**Poxt**	**Pshi**
Temperature	**Tbp**	Tff9	**Tfg9**		
Mass flow rate	**mdh9**	**mdst9**	**mht**		

Table 8.2 Axial profiles at 6000 s, 6620 s, 7170 s, and at 8000 s, which is considered as end state of the QUENCH-06 experiment

	6000 s	6620 s	7170 s	8000 s
Power	**Plin_1**	**Plin_2**	**Plin_3**	
Temp. Cladding Rod 1	**Tcl1o_1**	**Tcl1o_2**	**Tcl1o_3**	
Temp. Cladding Rod 2	Tcl2o_1	Tcl2o_2	Tcl2o_3	
Temp. Cladding Rod 3	Tcl3o_1	Tcl3o_2	Tcl3o_3	
Temp. Cladding Rod 4	Tcl4o_1	Tcl4o_2	Tcl4o_3	
Gas temperature	Tfg_1	Tfg_2	Tfg_3	
Liquid temperature	Tfl_1	Tfl_2	Tfl_3	
Shroud temperature	Tshi_1	Tshi_2	Tshi_3	
Flow area				**af_4**
Oxide Layer Rod 1	**dox1_1**	**dox1_2**	**dox1_3**	**dox1_4**
Oxide Layer Rod 2	dox2_1	dox2_2	dox2_3	dox2_4
Oxide Layer Rod 3	dox3_1	dox3_2	dox3_3	***dox3_4***
Oxide Layer Rod 4	dox4_1	dox4_2	dox4_3	***dox4_4***
Oxide Layer Shroud	doxsh_1	doxsh_2	doxsh_3	***doxsh_4***
Debris distribution				**mdeb_4**
Hydrogen mass	mdh_1	mdh_2	mdh_3	
Steam mass	mdst_1	mdst_2	mdst_3	
Oxide mass				***mzro_4***
Zircaloy mass				***mzry_4***

For completeness the following figures are enclosed but were not included in Section 4 due to redundant contents. For some participants, however, these results may be of

worth and some comments concerning axial profiles refer to figures in this section.

Table 8.3 specification of oxidation and material behavior versus time

#	Cross sec-tion	Oxide layer rod 2	Oxide layer rod 3	Oxide layer shroud	Debris mass	ZrO2 mass	Zircaloy mass	Hydrogen mass
1	af.01	dox2.01	dox3.01	doxsh.01	mde 01	mzro.01	mzry.01	mdhs.01
2	af.02	dox2.02	dox3.02	doxsh.02	mde 02	mzro.02	mzry.02	mdhs.02
3	af.03	dox2.03	dox3.03	doxsh.03	mde 03	mzro.03	mzry.03	mdhs.03
4	af.04	dox2.04	dox3.04	doxsh.04	mde 04	mzro.04	mzry.04	mdhs.04
5	af.05	dox2.05	dox3.05	doxsh.05	mde 05	mzro.05	mzry.05	mdhs.05
6	af.06	dox2.06	dox3.06	doxsh.06	mde 06	mzro.06	mzry.06	mdhs.06
7	af.07	dox2.07	dox3.07	doxsh.07	mde 07	mzro.07	mzry.07	mdhs.07
8	af.08	dox2.08	dox3.08	doxsh.08	mde 08	mzro.08	mzry.08	mdhs.08
9	af.09	dox2.09	dox3.09	doxsh.09	mde 09	mzro.09	mzry.09	mdhs.09
10	af.10	dox2.10	dox3.10	doxsh.10	mde 10	mzro.10	mzry.10	mdhs.10
11	af.11	dox2.11	dox3.11	doxsh.11	mde 11	mzro.11	mzry.11	mdhs.11
12	af.12	dox2.12	dox3.12	doxsh.12	mde 12	mzro.12	mzry.12	mdhs.12
13	af.13	dox2.13	dox3.13	doxsh.13	mde 13	mzro.13	mzry.13	mdhs.13
14	af.14	dox2.14	dox3.14	doxsh.14	mde 14	mzro.14	mzry.14	mdhs.14
15	af.15	dox2.15	dox3.15	doxsh.15	mde 15	mzro.15	mzry.15	mdhs.15
16	af.16	dox2.16	dox3.16	doxsh.16	mde 16	mzro.16	mzry.16	mdhs.16

Table 8.4 Data calculated during quench-phase

#	Tempera-ture drop	Heat transfer fluid	Heat trans-fer gas	Number of zones	Local void	Misc
1	DT1.01	hf.01	hg.01	ndz.01	void.01	ndz
2	DT1.02	hf.02	hg.02	ndz.02	void.02	ses.void
3	DT1.03	hf.03	hg.03	ndz.03	void.03	ses.zTq
4	DT1.04	hf.04	hg.04	ndz.04	void.04	***ses.zwlv***
5	DT1.05	hf.05	hg.05	ndz.05	void.05	**zTq**
6	DT1.06	hf.06	hg.06	ndz.06	void.06	**zwlv**
7	DT1.07	hf.07	hg.07	ndz.07	void.07	
8	DT1.08	hf.08	hg.08	ndz.08	void.08	
9	DT1.09	hf.09	hg.09	ndz.09	void.09	
10	DT1.10	hf.10	hg.10	ndz.10	void.10	
11	DT1.11	hf.11	hg.11	ndz.11	void.11	
12	DT1.12	hf.12	hg.12	ndz.12	void.12	
13	DT1.13	hf.13	hg.13	ndz.13	void.13	
14	DT1.14	hf.14	hg.14	ndz.14	void.14	
15	dT1.15	hf.15	hg.15	ndz.15	void.15	

16	dT1.16	hf.16	hg.16	ndz.16	void.16	

Table 8.5 General results, various temperatures versus time

	T center Rod 1	**T inner clad Rod 1**	**T clad Rod 1**	**T clad Rod 2**	**T clad Rod 3**	**T shroud**	**T fluid Gas**	**T fluid Liquid**
1	Tcl1c.01	Tcl1i.01	Tcl1o.01	Tcl2o.01	Tcl3o.01	Tshi.01	Tfg.01	Tfl.01
2	Tcl1c.02	Tcl1i.02	Tcl1o.02	Tcl2o.02	Tcl3o.02	Tshi.02	Tfg.02	Tfl.02
3	Tcl1c.03	Tcl1i.03	Tcl1o.03	Tcl2o.03	Tcl3o.03	Tshi.03	Tfg.03	Tfl.03
4	Tcl1c.04	Tcl1i.04	Tcl1o.04	Tcl2o.04	Tcl3o.04	Tshi.04	Tfg.04	Tfl.04
5	Tcl1c.05	Tcl1i.05	Tcl1o.05	Tcl2o.05	Tcl3o.05	Tshi.05	Tfg.05	Tfl.05
6	Tcl1c.06	Tcl1i.06	Tcl1o.06	Tcl2o.06	Tcl3o.06	Tshi.06	Tfg.06	Tfl.06
7	Tcl1c.07	Tcl1i.07	Tcl1o.07	Tcl2o.07	Tcl3o.07	Tshi.07	Tfg.07	Tfl.07
8	Tcl1c.08	Tcl1i.08	Tcl1o.08	Tcl2o.08	Tcl3o.08	Tshi.08	Tfg.08	Tfl.08
9	Tcl1c.09	Tcl1i.09	Tcl1o.09	Tcl2o.09	Tcl3o.09	Tshi.09	Tfg.09	Tfl.09
10	Tcl1c.10	Tcl1i.10	Tcl1o.10	Tcl2o.10	Tcl3o.10	Tshi.10	Tfg.10	Tfl.10
11	Tcl1c.11	Tcl1i.11	Tcl1o.11	Tcl2o.11	Tcl3o.11	Tshi.11	Tfg.11	Tfl.11
12	Tcl1c.12	Tcl1i.12	Tcl1o.12	Tcl2o.12	Tcl3o.12	Tshi.12	Tfg.12	Tfl.12
13	Tcl1c.13	Tcl1i.13	Tcl1o.13	Tcl2o.13	Tcl3o.13	Tshi.13	Tfg.13	Tfl.13
14	Tcl1c.14	Tcl1i.14	Tcl1o.14	Tcl2o.14	Tcl3o.14	Tshi.14	Tfg.14	Tfl.14
15	Tcl1c.15	Tcl1i.15	Tcl1o.15	Tcl2o.15	Tcl3o.15	Tshi.15	Tfg.15	Tfl.15
16	Tcl1c.16	Tcl1i.16	Tcl1o.16	Tcl2o.16	Tcl3o.16	Tshi.16	Tfg.16	Tfl.16

8.1.2 Errors in delivered database

In Table 8.6 the data errors as well as our attempts to correct obvious errors are given. Also some user remarks to user errors are included.

Table 8.6 Remarks on data delivered by participants

Token	Remarks
cmx	gives strange results for Pel7 (including < 0). In cmx.global.f mdst-955000000 is changed into mdst9-55000000
dmm	gives stepwise maximum temperature, perhaps due to inappropriate data format and has very high values for Pshi; the energy balance should be checked
drs	sent a wrong time vector (not ascending monotonously). Therefore results look somewhat strange; the thick line in Figure 4.1 is in fact a number (»1) of lines.
edf	Poxt, mdh9 data have a sharp peak at t = 0, probably post processing problem
ljs	Power data (Pel6, Pelb, Pel7 given in kW instead of W), data for water level in the bundle (zwlv) missing, only local collapsed water level given.
inl	uses user variable testda-1, which does not exist, for mdh9. It was replaced by bgth-0, as usual for sr5. It has very high values for Pshi; energy balance should be checked
neh	underestimates mdh9 by about 1 order of magnitude
nk1	has very high data for Pel6; bgnhg-0 is used instead. mdst9 and mdh9 required additional adaptation. For Pel6, Pelb, Pel7 the same user variable is used.
nk2	data in nk2_mdat are not delivered as specified in SI units, hence unusable
rez	delivered wrong scaled data for Pshi, corrected manually
rub	Pel6, Pelb, Pel7 data were delivered for 18 rods only, Tff9 and Tfg9 were given in °C, and Pshi didn't include radiation, the values were corrected manually.
sie	has very high data for Pel6; bgnhg-0 is used
ses	Data for water level in the bundle (zwlv) missing, only local collapsed water level given.
vtt	replaced probably wrong data (august). The code didn't model the temperature feedback of the heater rod tungsten wire.

8.2 Normal usage of codes

In the ISP-45 specification report /8/ all participants were asked to give some information about normal application of their code, impact of ISP-45 results on their work on reactor safety, and experience to reactor safety, AMM, licensing, etc. The following sections comprise all available statements of the participants.

GRS: ATHLET-CD

The code system ATHLET-CD is developed by GRS especially for the investigation of beyond design basis accidents and accident management measures. For this the knowledge of the impact of quench processes on fuel elements is very important. The results of the well defined and instrumented ISP experiment are a good basis to be compared with the analytical investigation with ATHLET-CD and for further improvements of the model. The ISP will be added to the validation matrix for the code and thus has a significant influence on the further development of ATHLET-CD.

RUB: ATHLET-CD

The range of application of the code ATHLET-CD comprises the whole spectrum of leaks and large breaks, as well as operational and abnormal transients for PWRs, BWRs, and VVERs. At present the analyses cover the in-vessel thermal-hydraulics, the core degradation processes in the core region, as well as fission products and aerosol release from the core and their transport in the reactor coolant system. The aim of the code development is to extend the simulation of core degradation up to failure of the reactor pressure vessel and to cover all physically reasonable accident sequences for western and eastern LWRs including RBMKs

VTT: GENFLO

At present, the GENFLO (GENeral FLOw) code is being used in three different applications. In a code called RECRIT, the model is coupled with the 2-D transient neutronics model TWODIN for calculating thermal hydraulics during re-criticality accidents in a BWR plant. Then the whole BWR vessel is modeled for GENFLO. In APROS-SA application, the model is used to calculate the PWR pressure vessel thermal hydraulics during a severe accident until the core melting and relocation and pool generation at the bottom of the reactor vessel is simulated. In the current FRAPTRAN application the model is coupled with a transient fuel behavior code to study complex fuel transients whereby special attention is given to realistic description of the thermal hydraulics in the sub-channel.

The thermal hydraulics solution principles of GENFLO are based on the models developed for the SMABRE. The SMABRE code has been used twenty years for the safety analyses in Finland.

DRS: ICARE/CATHARE

The ICARE2 module of the ICARE/CATHARE code was developed at IPSN and is primarily devoted to calculate the behavior of a Light Water Reactor (LWR) vessel during a

severe accident, but it is also intensively used to simulate core-degradation experiments.

In the actual V3mod1 version, ICARE2 is able to represent the structures and the fluid of the vessel, as well as the degradation phenomena during the early phase of an accident (heat-up, oxidation and early material interactions) and during the late phase (melting and creation of a debris bed, progression and flowing of the corium until the formation of a magma pool). Reflooding issues are accounted for, but partial validation is confirmed only in intact geometry.

ICARE2 already benefits from a large validation matrix on separate effect tests and on integral experiments concerning the different aspects of degradation phenomena. In particular, calculations of the CORA tests exhibited a large under-estimation of the hydrogen production during the quench phase. In order to investigate further this phenomenon and to evaluate the capability of the code to predict the thermal-hydraulics of reflooding, a part of the QUENCH program is included in the validation matrix of ICARE2: the QUENCH-01 test was calculated to assess the modeling of the test section and to validate the different code parameters; the present exercise belongs to the validation matrix too and is the occasion to check the prediction capability of the code.

ENE: ICARE/CATHARE

There are no nuclear power plants in operation in Italy. At present, the main objectives of our nuclear safety research is to maintain the knowledge and the expertise in this field, through the participation in international projects and collaborations with other institutions, looking forward to advanced reactors with new safety concepts including passive systems.

With this aim, we participate in various research projects on severe accidents promoted by the European Commission (Framework Program on Nuclear Fission) and the OECD/CSNI. We also have a bilateral agreement with IPSN-France. In this framework, we are largely involved in the development and validation of computer codes used in the analysis of severe accident, such as ICARE/CATHARE. Therefore, our main interest is not in nuclear plant applications, but in code model development, validation and testing.

Code models for the reflood phase computation are still under development. The ISP-45 is providing a good opportunity to assess the capability of the code (including a simple quench model), in evaluating hydrogen generation under reflood conditions starting from hot core temperatures, by comparing the results with experimental data and other code calculations.

Because of the particular situation in Italy, without nuclear power plants in operation, there are no information regarding the application of ISP5-45 results to AMM, licensing, etc.

NUP: IMPACT/SAMPSON

n/a

EDF: MAAP

For the last decade, Electricité de France has been using the MAAP code for severe accident analyses. MAAP stands for Modular Accident Analysis Program. It is developed under the leadership of EPRI (USA) by the contractor Fauske & Associates Inc. (FAI, USA). The last official version (MAAP 4.04) has been released in fall 1999.

Because of the modular structure of MAAP, it is possible for users to adapt and run the code to model experiments for validation and benchmarking purposes. However it still requires a few modifications in the code to model specific geometry and physical phenomena and to define initial and boundary conditions.

FRA: MAAP

MAAP code is the reference scenario code in FRAMATOME ANP SAS. Numerous severe accident studies have been performed for French existing plants and for plants under development, such as the European Pressurized water Reactor (EPR).

Regarding existing reactors, Framatome used MAAP code in several studies for EDF. Regarding the EPR, severe accidents consequences were taken into account since the very beginning of the reactor design, and in particular to design mitigation equipment, such as recombiners and corium core-catcher. MAAP is the reference code for EPR in-vessel analysis. It has been used for several scenarios, including reflooding scenario, to define the source terms (water, steam, H_2, fission products, corium) for the reactor building.

IJS: MELCOR

At “Jožef Stefan Institute”, MELCOR code is primarily used for simulations of possible severe accidents in “Krško” PWR Nuclear Power Plant, in Slovenia, where MAAP code has been used for the same purposes. The results of the ISP-45 will help to estimate the reliability and accuracy of the MELCOR calculations of hydrogen production during the emergency cooling of the core with the safety injection systems, which will be important also in comparisons with the corresponding MAAP calculations.

An impact of ISP-45 may become important in future if the results of MELCOR simulations of severe accidents in the "Krsko" Nuclear Power Plant are compared with the corresponding results of MAAP simulations, maybe for some licensing purposes. The research institutions - Jozef Stefan Institute in Ljubljana and University of Maribor, and Slovenian Nuclear Safety Administration use MELCOR, whereas "Krsko" Nuclear Power Plant uses MAAP.

At this moment, we do not have any research or development projects for "Krsko" NPP, in which the use of MELCOR is requested or necessary, but there is a certain probability for such a project in a near future.

NK2: MELCOR

n/a

REZ: MELCOR

The MELCOR code is very extensively used for the analysis of severe accident of nuclear reactors in Czech Republic. The code is used for analysis of both types of VVER reactors - VVER-440/213 (Dukovany NPP) and VVER-1000 (Temelin NPP) with the topics of the source term estimation and severe accident progress evaluation. The extended experience obtained from the work on the ISP-45 will significant improve, for example, the capability for the SAMG validation framework, which will include also the sequences with reflooding of overheated or partly damaged core.

SES: MELCOR

Studsvik EcoSafe has many years of experience in safety and severe accident analyses. Previously, the main code for severe accident was SCDAP/RELAP5 but from now on MELCOR will be the main code. One NPP accident analyses has been performed with MELCOR for a PWR on behalf of the Swedish authorities. A BWR study is under performance. The main purpose for EcoSafe to participate in the ISP-45 is mainly to get better knowledge about code behavior and better understanding of the modeling of the quench processes.

SNL: MELCOR

The MELCOR simulation code is being developed at Sandia National Laboratories for the U.S. Nuclear Regulatory Commission. It is available to United States citizens and to members of CSARP. MELCOR is a fully integrated, engineering-level computer code that has the ability to model a broad spectrum of severe accident phenomena in both boiling and pressurized water reactors in a unified framework. These phenomena include thermal-hydraulic response in the reactor coolant system, reactor cavity, containment, and confinement buildings; core heat up, degradation, and relocation; core-concrete attack; hydrogen production, transport, and combustion; fission product release and transport behavior.

MELCOR serves as a second-generation plant risk assessment tool, the successor to the Source Term Code Package. As such, it is used to model the progression of severe accidents in light water reactor nuclear power plants, including estimation of severe accident source terms and their sensitivities and uncertainties in a variety of applications. One current major application at Sandia National Laboratories involves characterizing the hydrogen source term.

Most of the modeling in MELCOR is quite general, and makes relatively few assumptions about the details of reactor design. Therefore, MELCOR has been used for analysis of reactors, including VVERs, with designs quite different from commercial United States power reactors. The generality also allows MELCOR to be used for non-reactor problems involving coupled fluid flow, heat transfer, and the transport of aerosols and trace gases. Such applications have included analysis of contamination accidents involving facilities and shipping containers.

Current regulatory policy in the United States does not include severe accident analysis or accident management as part of the licensing process. However, MELCOR has been

used as a research tool to provide guidance when considering the impact of severe accidents or the consequences of proposed accident management strategies.

Until recently, MELCOR had no specialized models for reflooding and quenching of a reactor core, and calculations conducted for ISP-45 (including preliminary tests on QUENCH-01) represent the first real test of these new models. We anticipate that comparisons with data from various QUENCH experiments will allow us to determine and validate appropriate default values for the parameters in the model.

CMX: SCDAPSIM

Application of Severe Accident Codes in the Mexican Regulatory Authority (CNSNS).

Since about ten years ago the CNSNS has been working with severe accident codes in order to evaluate different topics related with accident analysis. The first experience was with the package STCP (Source Term Code Package) that was used to obtain the source term of the different accident sequences that have high contribution to the core damage frequency. These source terms were used in the development of the APS level 2.

According with the Mexican regulation, the Individual Plant Examination (IPE) for Laguna Verde Nuclear Power Plant (two units with BWR-5 reactors) was requested to the utility, Comisión Federal de Electricidad (CFE). Ones of the computer codes to develop the IPE was MAAP3-B to evaluate the behavior of the nuclear station under severe accident condition. As independent evaluation of the IPE the CNSNS used the codes MAAP and MELCOR.

The codes SCDAPSIM and MELCOR, have been used by the CNSNS with the objective of carrying out studies related with the behavior of Laguna Verde Nuclear Power Plant during a severe accident and in a near future to evaluated the guides of accident administration for Laguna Verde Nuclear Power Station.

DMM: SCDAPSIM

n/a

ISS: SCDAPSIM

RELAP/SCDAPSIM is being developed under the sponsorship of the SDTP software development and training program. Organizations contributing to the development include the International Atomic Energy Agency (IAEA), Comision Nacional de Seguridad Nuclear y Salvaguardias (Mexico), Framatome-ANP (Germany), Institute of Nuclear Safety (Japan), Computer Software Development Co, Ltd (Japan), Hacettepe University (Turkey), University of Pisa, Texas A&M, University of Bochum, University of Michigan, Seoul National University, Carleton University (Canada), Hanyang University (Korea), Lappeenranta University (Finland), University of Catalunya (Spain), Shanghai Jiao Tong University (China), Idaho State University (US), University of Florida (US), University of Zageb (Croatia), and the University of Mexico. Software configuration control and the administration of the program are handled by Innovative Systems Software LLC (ISS). ISS is located in Idaho Falls. Funding for the development of the software

and the administration of the program comes from a combination of commercial sources and licensing fees for the use of the software.

RELAP/SCDAPSIM/MOD3.2(bd)
RELAP/SCDAPSIM/MOD3.2 uses models taken from the RELAP/MOD3.2 and SCDAP/RELAP/MOD3.2 codes publicly released by the US Nuclear Regulatory Commission, but with a number of improvements that allow the code to run significantly faster and more reliably. The code also includes a number of added user options and models. The improvements in speed and reliability are due to improvements in the code's numerical algorithms and programming as well as the correction of numerous coding errors in the original US NRC codes. The unique user features include the interactive 3D orthographic displays, Quick Plot options, integrated renodalization options, run display console, more automated time step control, and improved output. The unique modeling options include improved fuel rod simulator and shroud models.

The improved fuel rod simulator and shroud models were incorporated into the latest experimental version of RELAP/SCDAPSIM/MOD3.2(bd). Previously versions relied on the original INEEL model (which as noted below contained a serious error). The improved simulator model incorporated many of the features originally developed by FZK (Draft Report FZKA 6566, "Improvements of the SCDAP/RELAP5 Code with respect to the FZK QUENCH Facility") with a few added options. This new model allows the user to describe the simulator rod in much more detail including the use of Copper and/or Molybdenum portions of the electrode, electrode dimensions, contact resistances, and the type of pellets to be included (ZrO2 or UO2). The new model also accounts for the properties of the electrodes in the heat conduction solution. The improved shroud model allows the user to specify the properties of the shroud as a function of axial elevation so that the change in insulation in the upper portion of the bundle could be included.

NEH: SCDAPSIM

n/a

NK1: SCDAPSIM

n/a

SIE: SCDAPSIM

Framatome ANP GmbH uses SCDAPSIM mainly for the design and assessment of accident management measures for all kinds of LWRs (existing as well as future ones). In addition, it is used for the validation of the in-vessel results generated by simplified codes (e.g. MAAP) by benchmarking of key scenarios. Typical examples for the latter case are benchmark exercises mainly with respect to the mass- and energy release into the containment for the reference scenarios for the EPR hydrogen mitigation concept and the validation of training exercises for the plant operators and members of the Technical Support Center.

Our validation work for SCDAPSIM is strongly limited to the most risk relevant phenomena and the qualification of the user. Another related activity is the assessment of the potential of 'fast running'. By the improvements of the numerics performed in the last

years by Innovative Systems Software LLC almost real time plant calculation (on PCs 2GHz) are already possible. Under these conditions we intend to replace simplified integral codes by coupled mechanistic codes for whole plant analyses in the near future.

UZA: SCDAPSIM

n/a

INL: SCDAP-3D

n/a

FZK: SCDAP/RELAP5mod3.2irs

S/R5 mod3.2.irs is used for analyses within the CSARP agreement, for support of QUENCH experiments and analyses of safety features of existing and advanced nuclear power plants. Part of this work is done within the 5th Framework Program of the European Community, (COLOSS, EVITA, HPLWR), taking credit from the RELAP5 experience gained within the USNRC CAMP agreement.

Besides, code improvements /4/ were performed and transmitted to the customers of the QUENCH-program using SCDAP/RELAP5 based codes to take credit from our experience. Furthermore, model developments are under way to identify the basic mechanisms leading to increased hydrogen release during reflood situation, a major concern of hydrogen management measures in the containment.

8.3 Additional Figures

8.3.1 Axial profiles

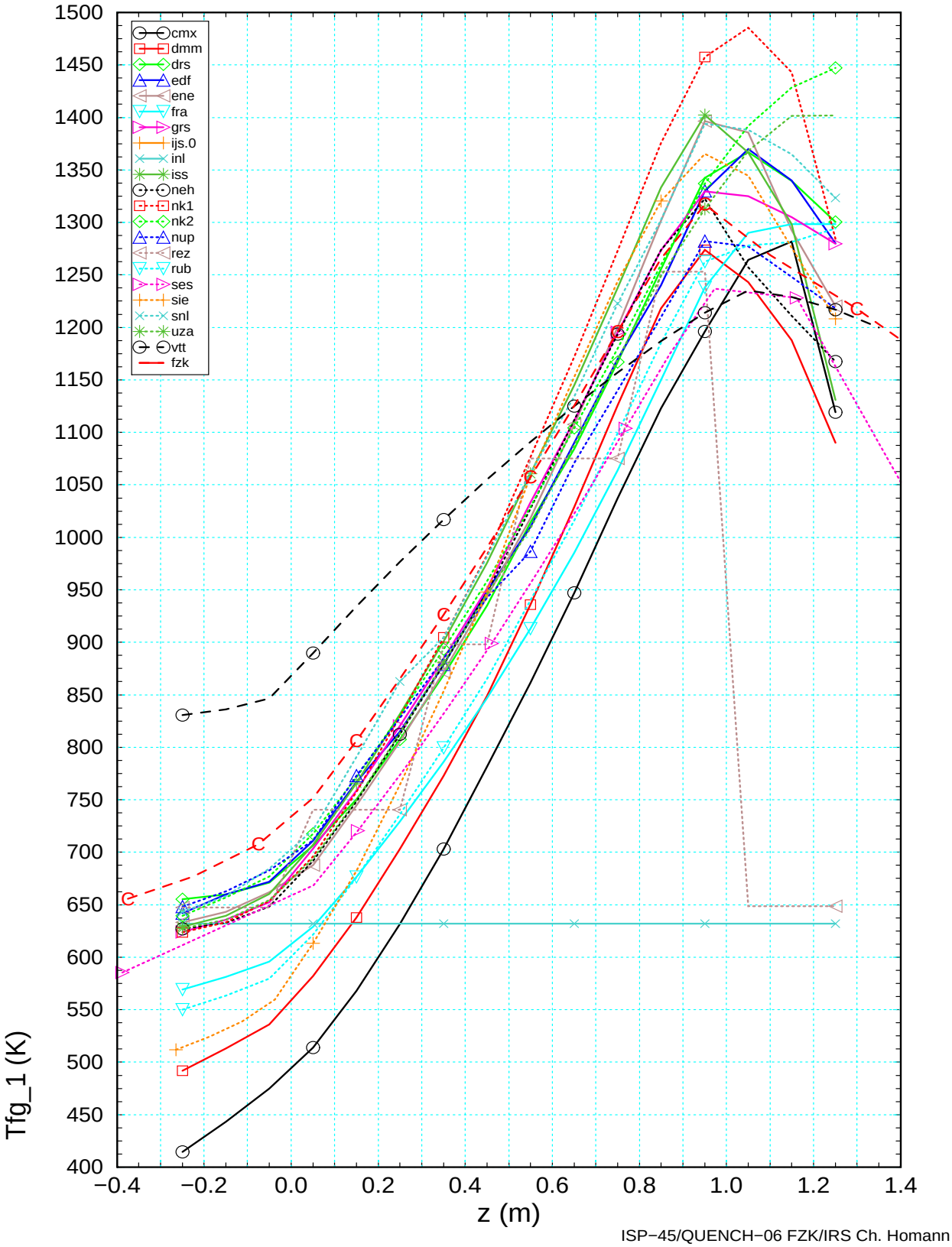

Figure 8.1 Axial profile of the fluid temperature (Tfg_1) calculated by the participants for t=6000 s compared to the results of FZK post-test calculations (-C-).

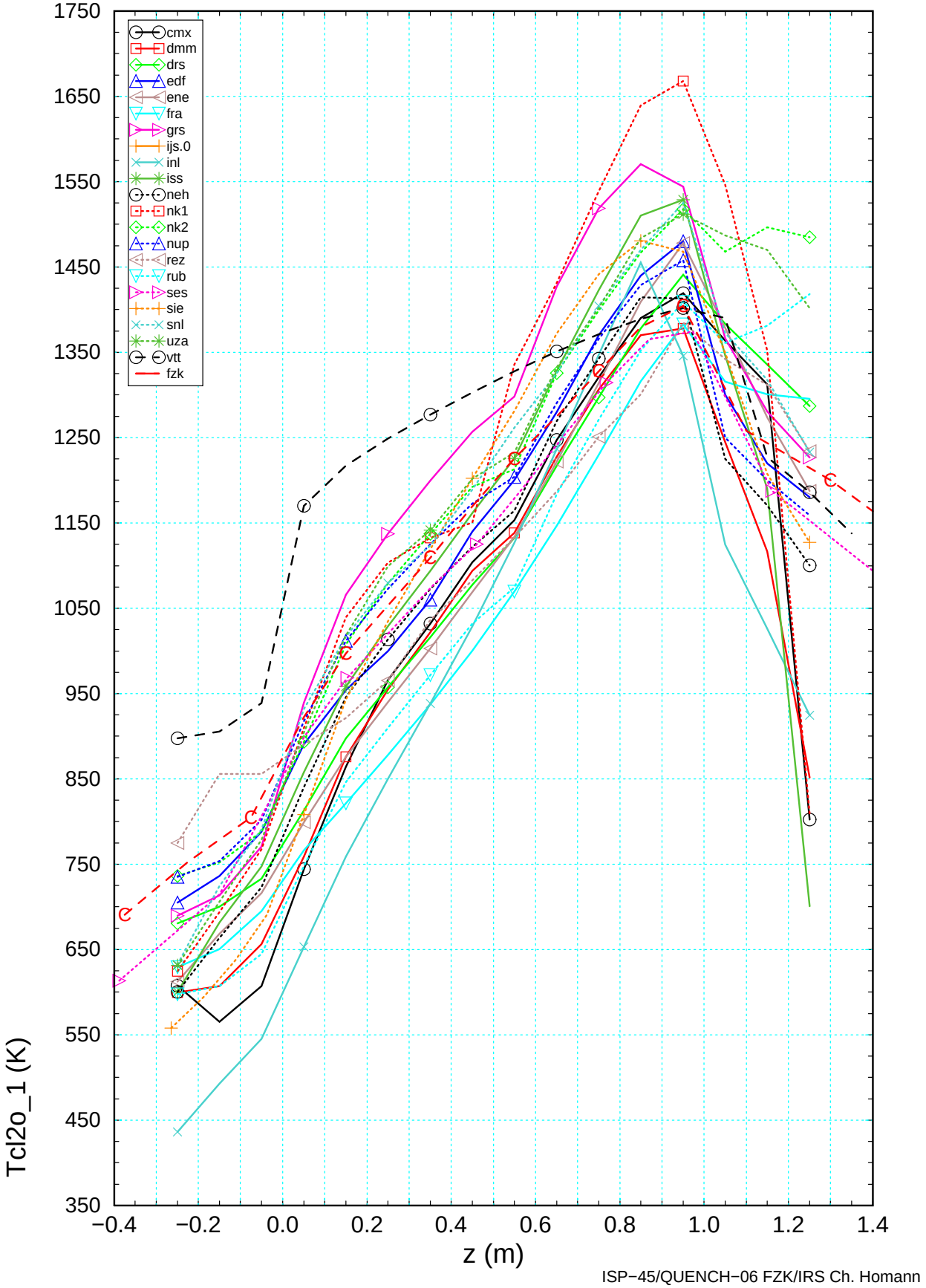

Figure 8.2 Axial cladding temperature profile for the inner ring of heater rods (Tcl2o_1) calculated by the participants for t=6000 s compared to the results of FZK post-test calculations (-C-).

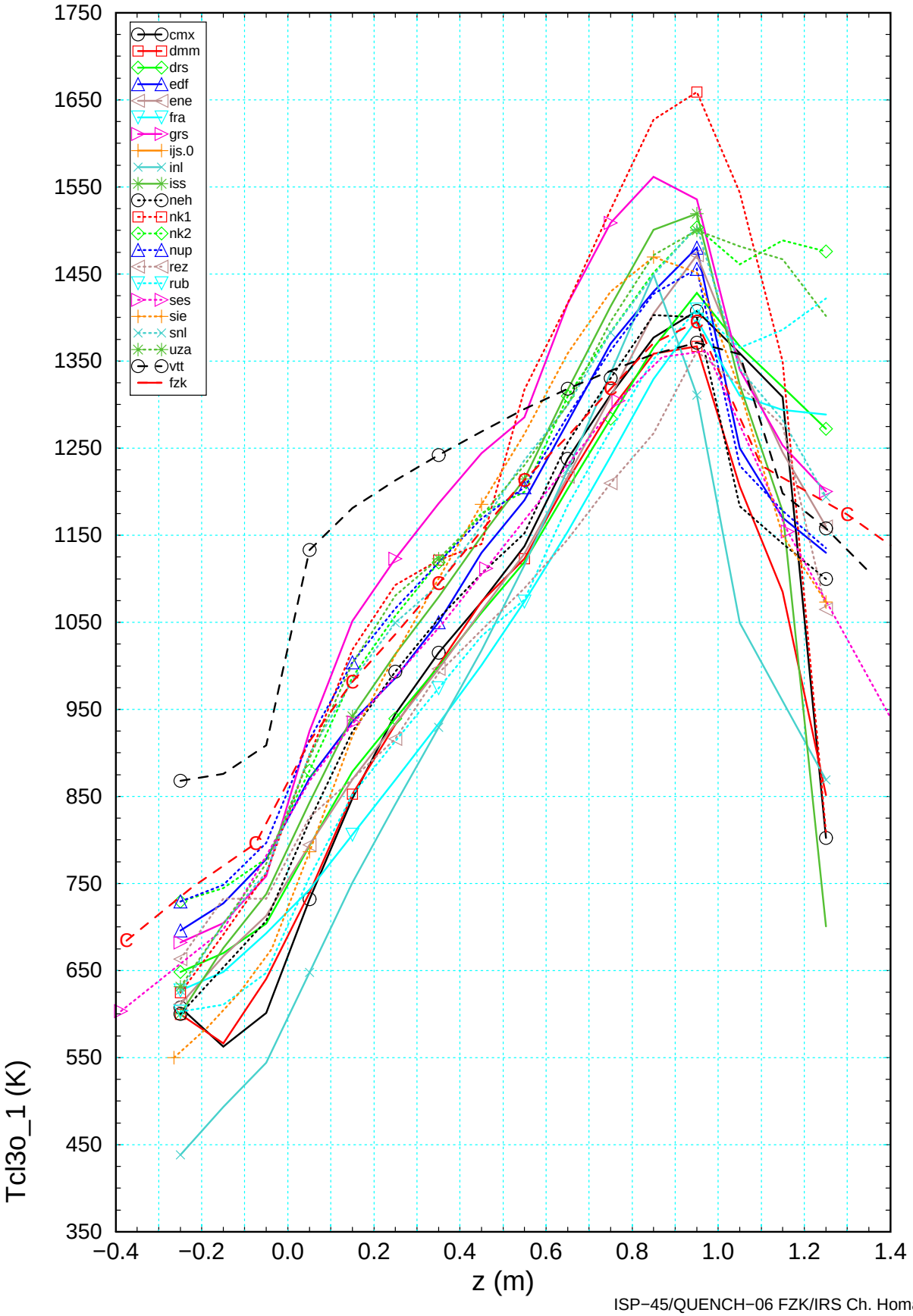

Figure 8.3 Axial cladding temperature profile for the outer ring of heater rods (Tcl3o_1) calculated by the participants for t=6000 s compared to the results of FZK post-test calculations (-C-).

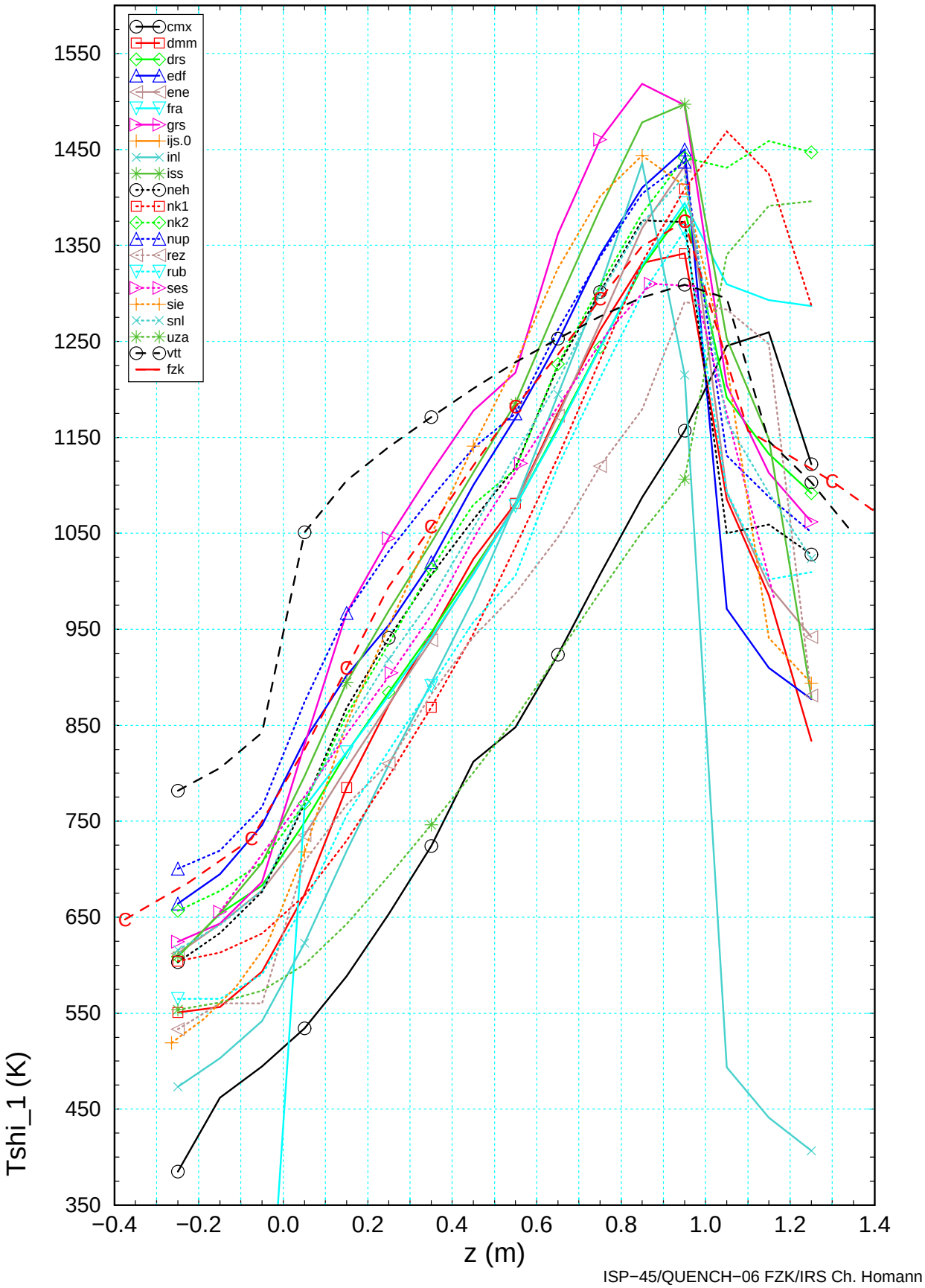

Figure 8.4 Axial profile for the shroud temperature (Tshi_1) calculated by the participants for t=6000 s compared to the results of FZK post-test calculations.

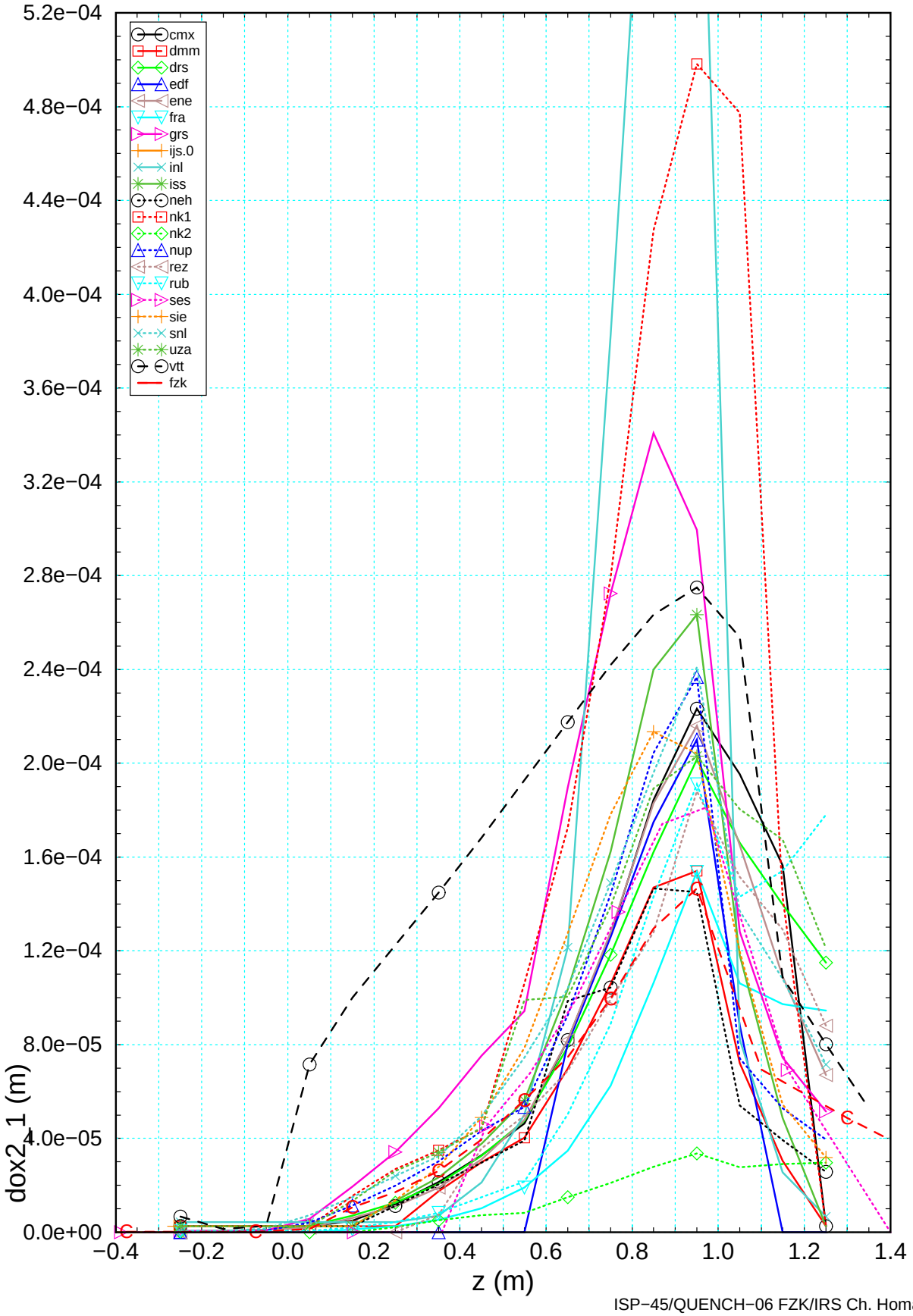

Figure 8.5 Axial oxide layer profile of the inner ring of heated rods (dox2_1) calculated by the participants for t=6000 s compared to the results of the FZK post-test calculations (-C-).

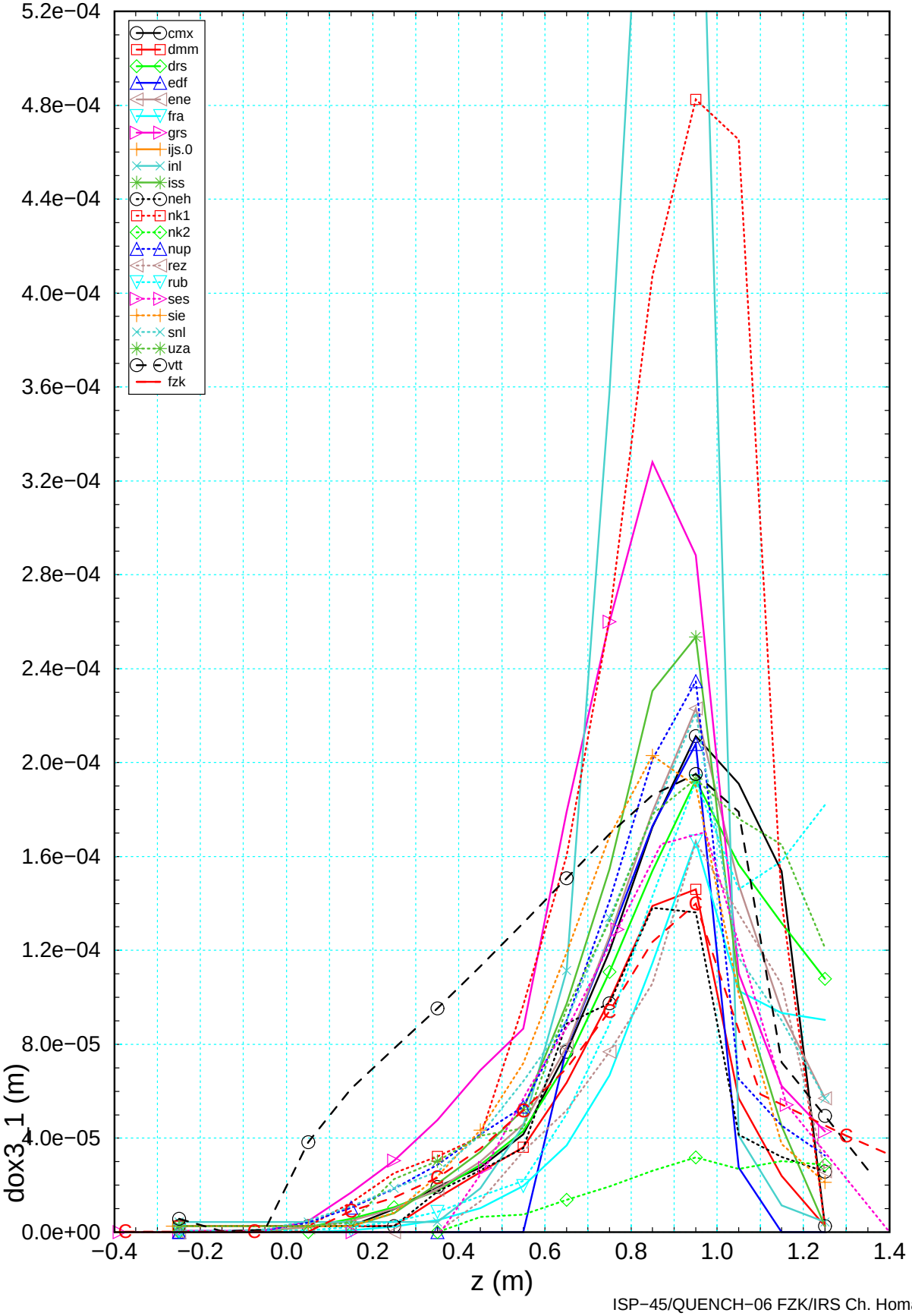

Figure 8.6 Axial oxide layer profile of the outer ring of heated rods (dox3_1) calculated by the participants for t=6000 s compared to the results of the FZK post-test calculations (-C-).

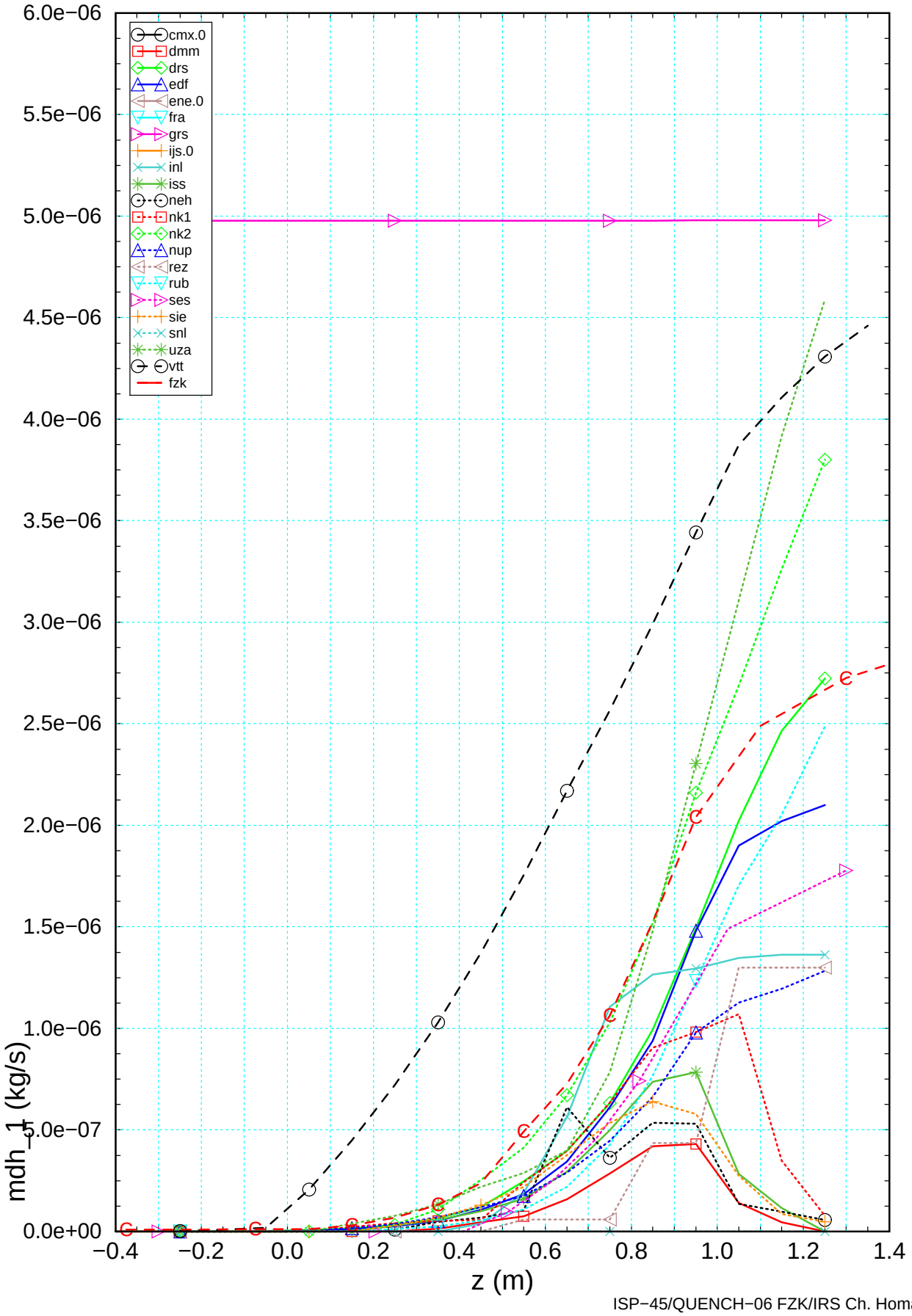

Figure 8.7 Axial distribution of hydrogen source calculated by the participants for t=6000 s compared to the results of FZK post-test calculations.

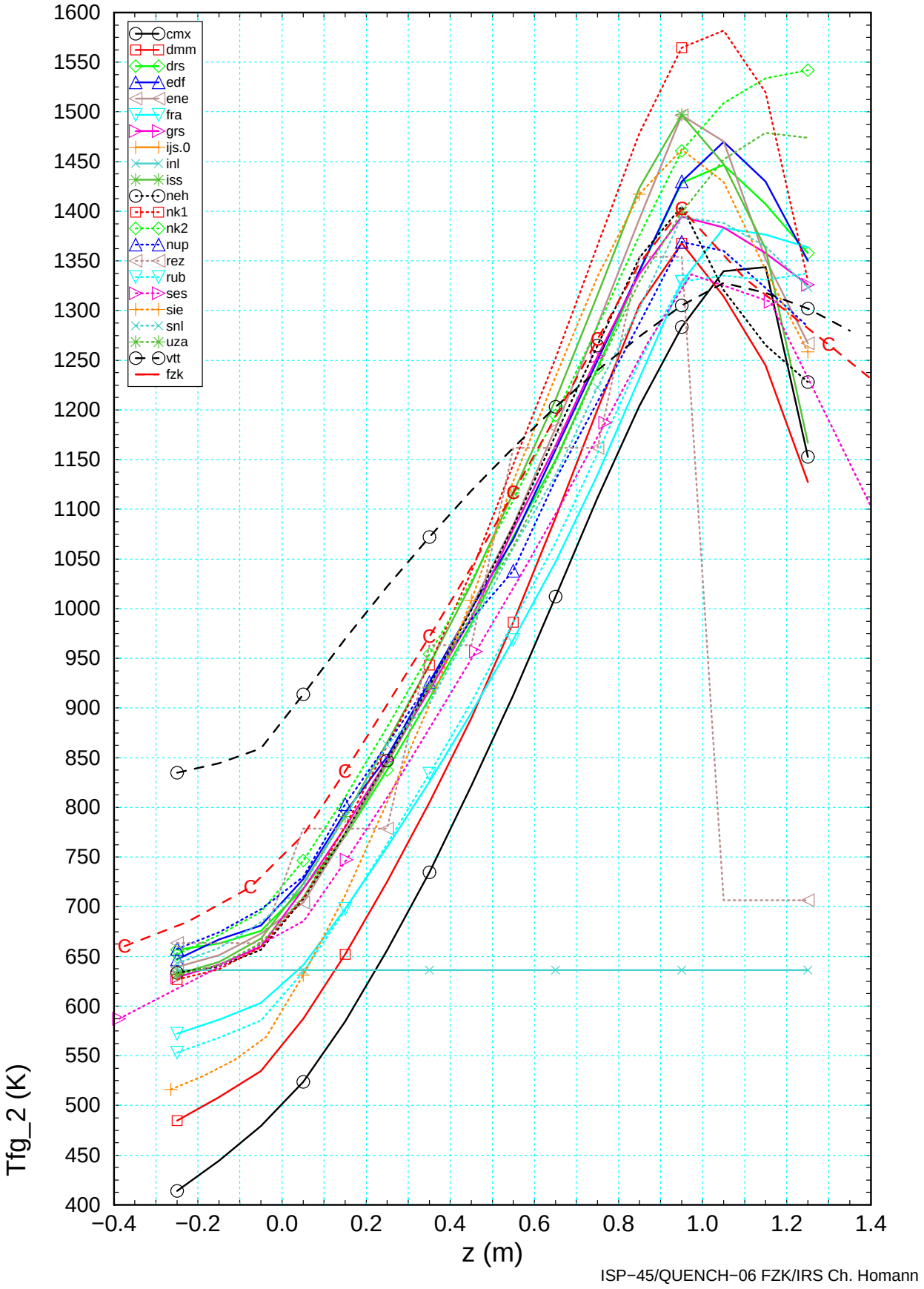

Figure 8.8 Axial profile of the fluid temperature (Tfg_2) calculated by the participants for t=6620 s compared to the results of FZK post-test calculations (-C-).

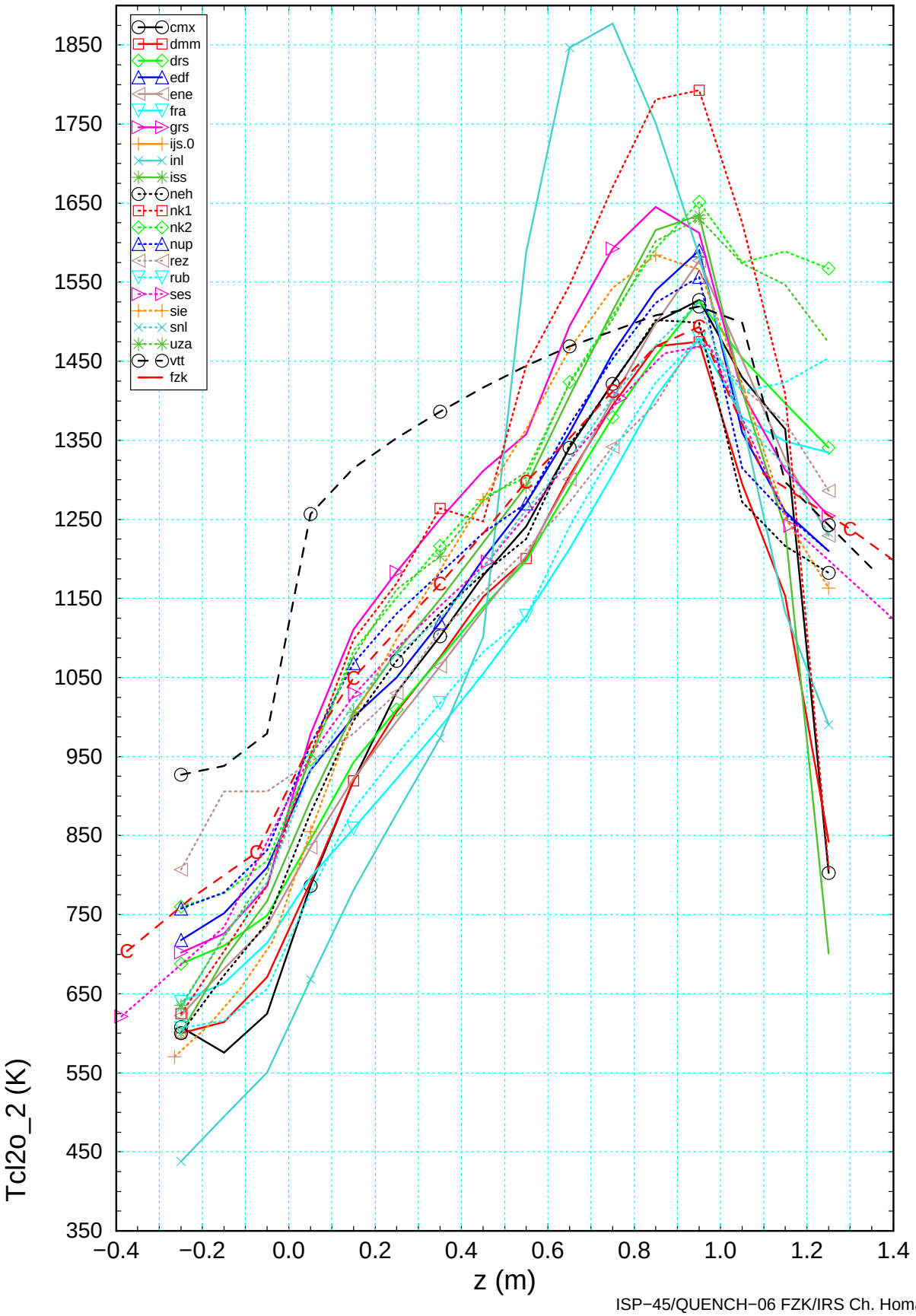

Figure 8.9 Axial cladding temperature profile for the inner ring of heater rods (Tcl2o_2) calculated by the participants for t=6620 s compared to the results of FZK post-test calculations (-C-).

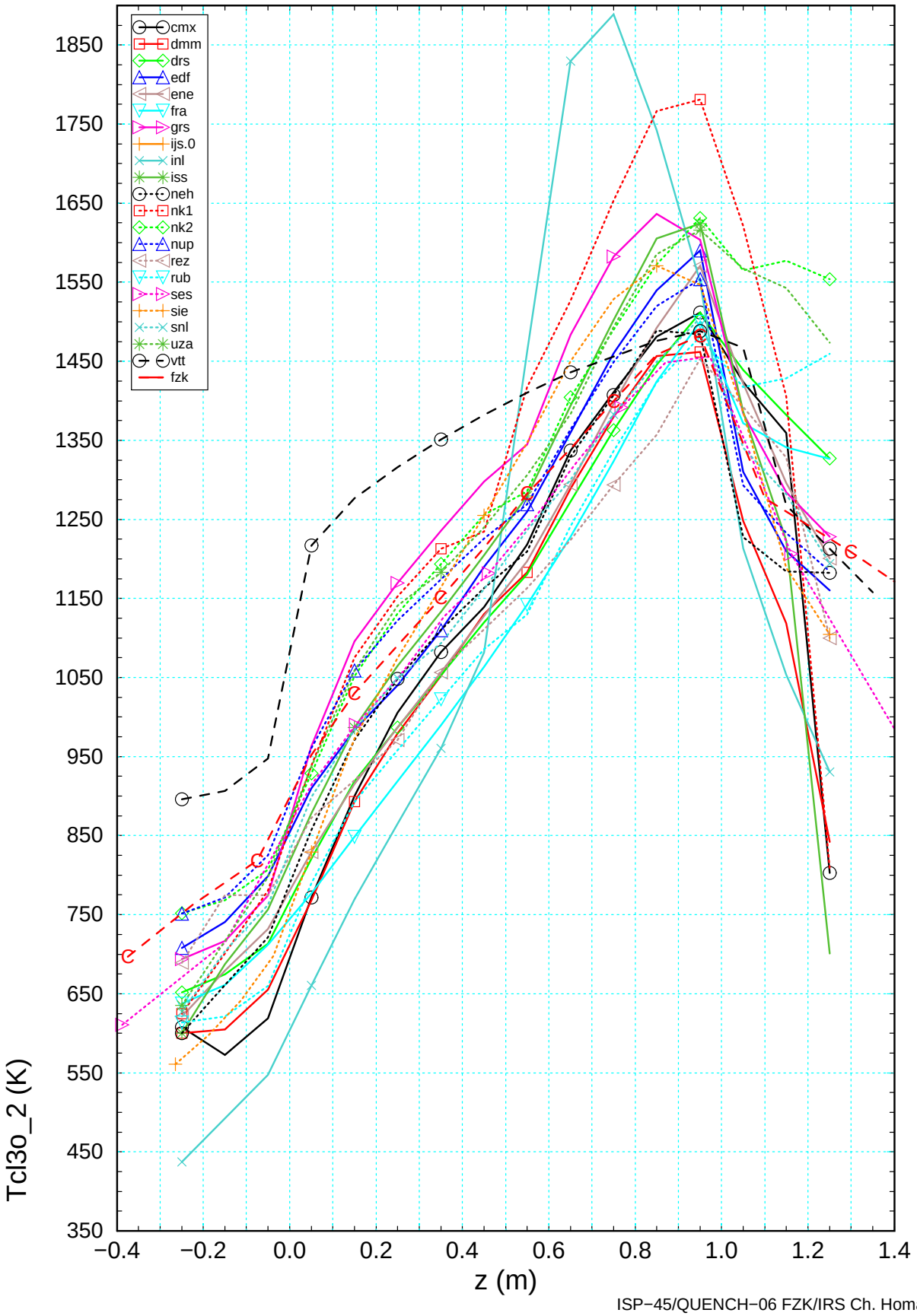

Figure 8.10 Axial cladding temperature profile for the outer ring of heater rods (Tcl3o_2) calculated by the participants for t=6620 s compared to the results of FZK post-test calculations (-C-).

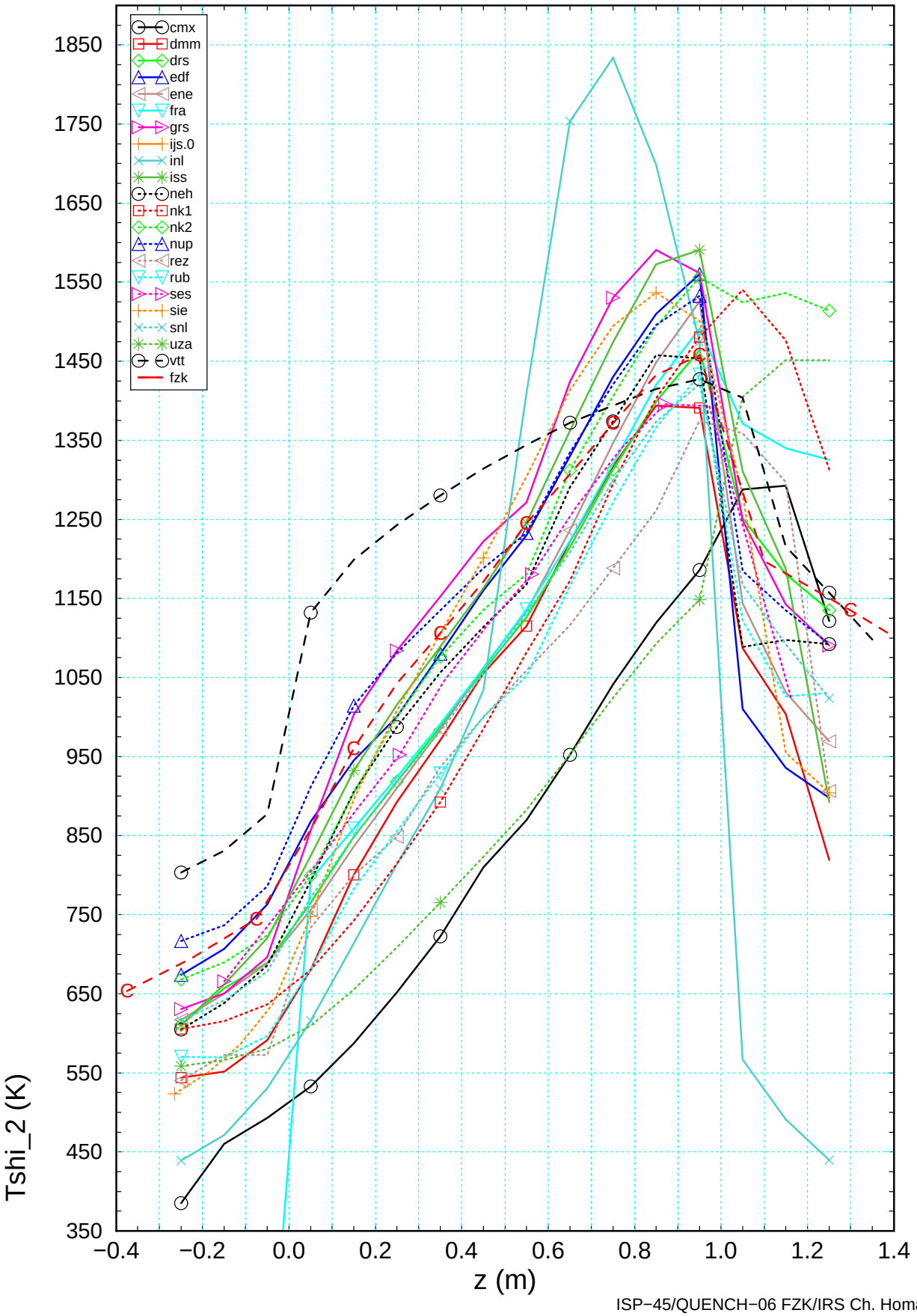

Figure 8.11 Axial profile for the shroud temperature (Tshi_2) calculated by the participants for t=6620 s compared to the results of FZK post-test calculations.

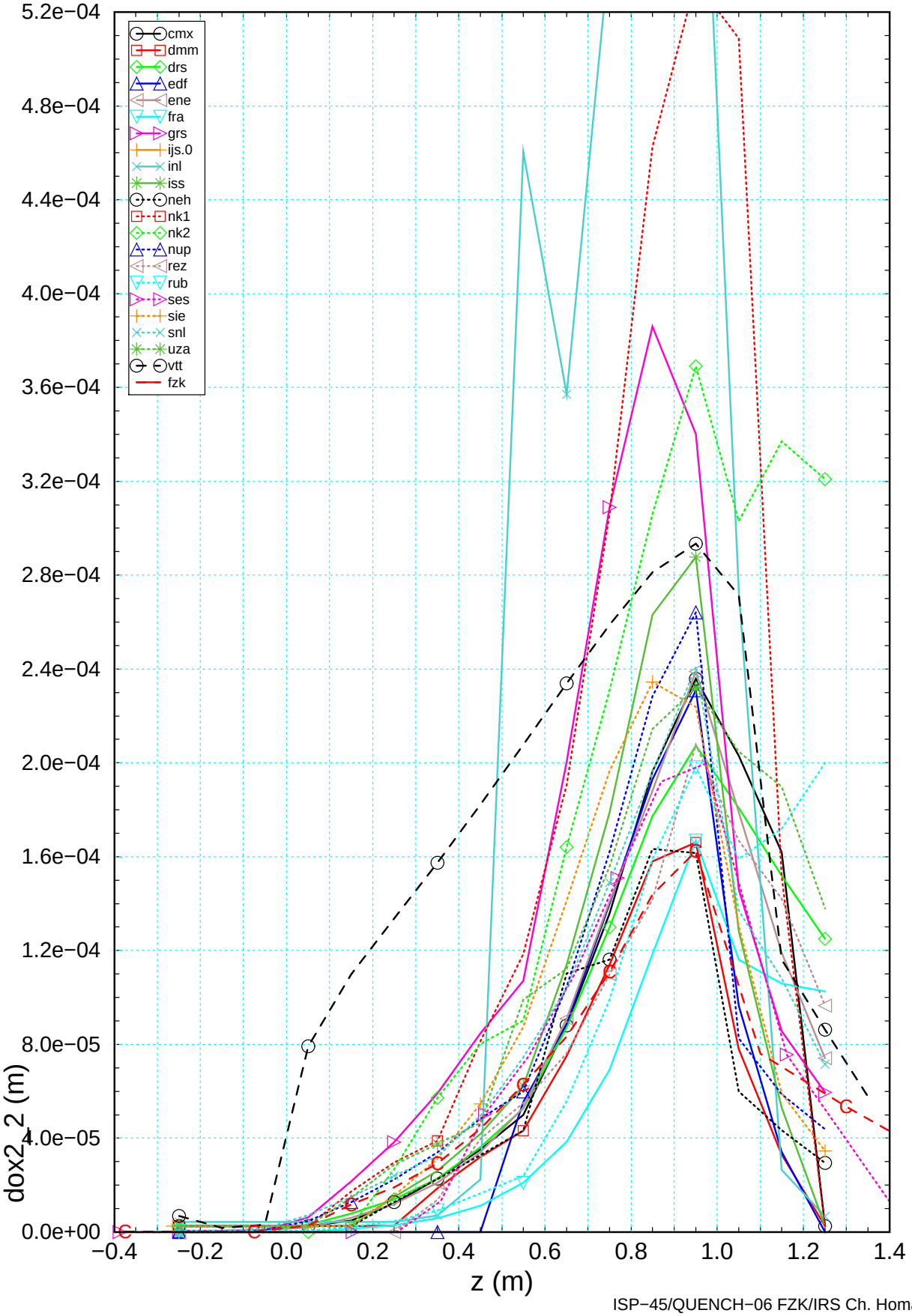

Figure 8.12 Axial oxide layer profile of the inner ring of heated rods (dox2_2) calculated by the participants for t=6620 s compared to the results of the FZK post-test calculations (-C-).

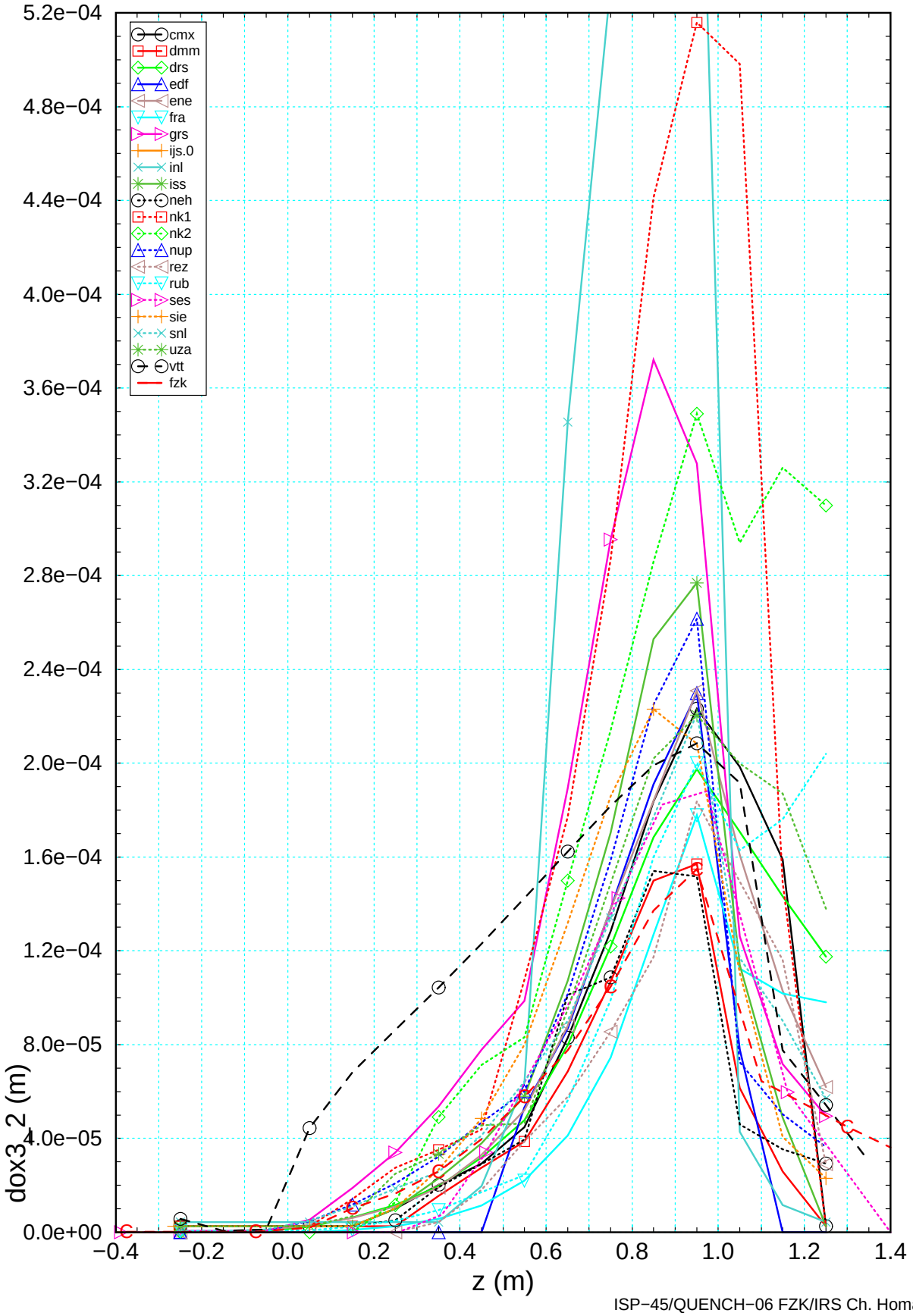

Figure 8.13 Axial oxide layer profile of the outer ring of heated rods (dox3_2) calculated by the participants for t=6620 s compared to the results of the FZK post-test calculations (-C-).

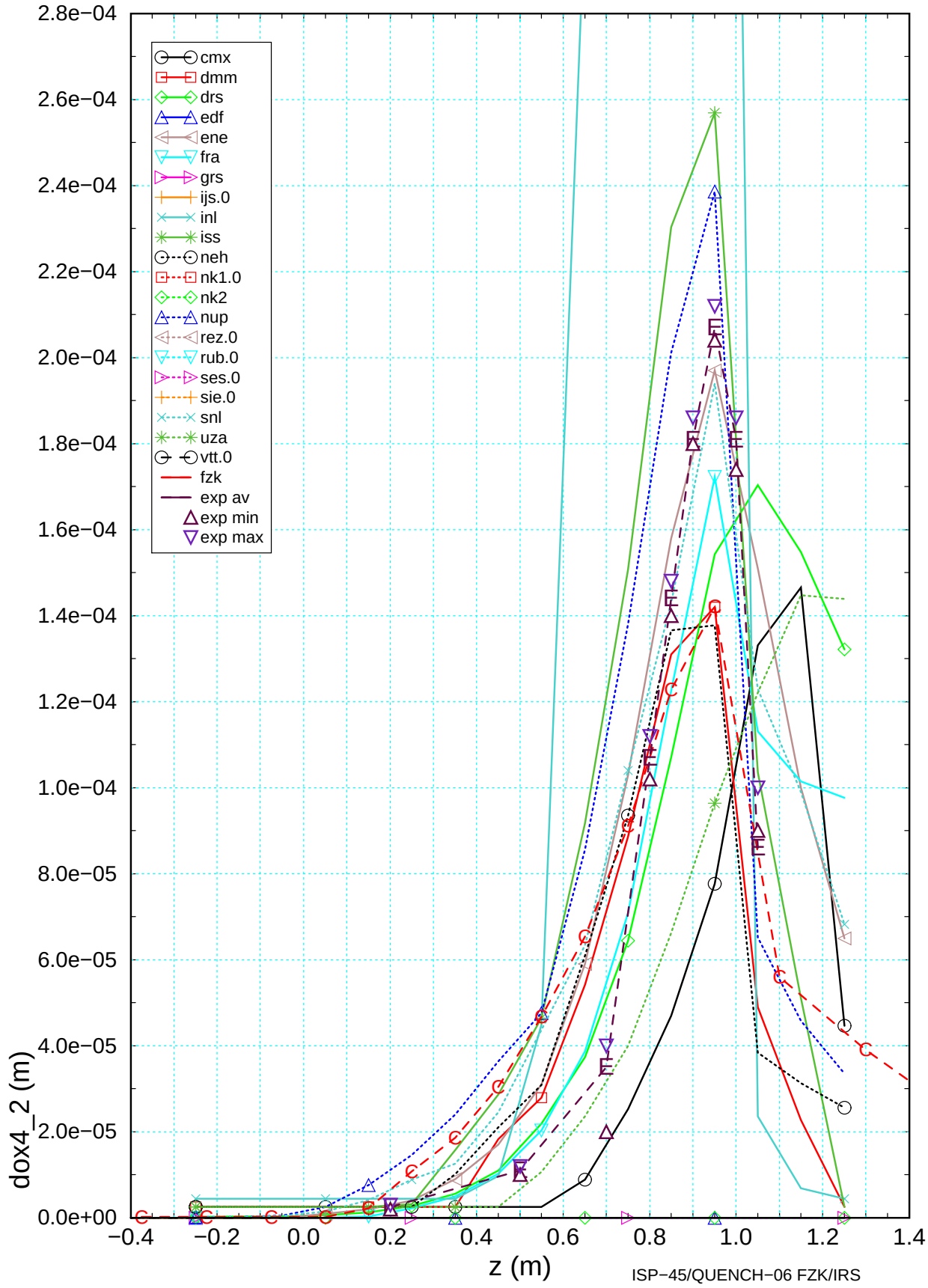

Figure 8.14 Axial oxide layer profile of the corner rods (dox4_2) calculated by the participants for t=6620 s compared to the results pots test investigations based on the removed corner rod (min/max, average) plus results of FZK post-test calculations (-C-).

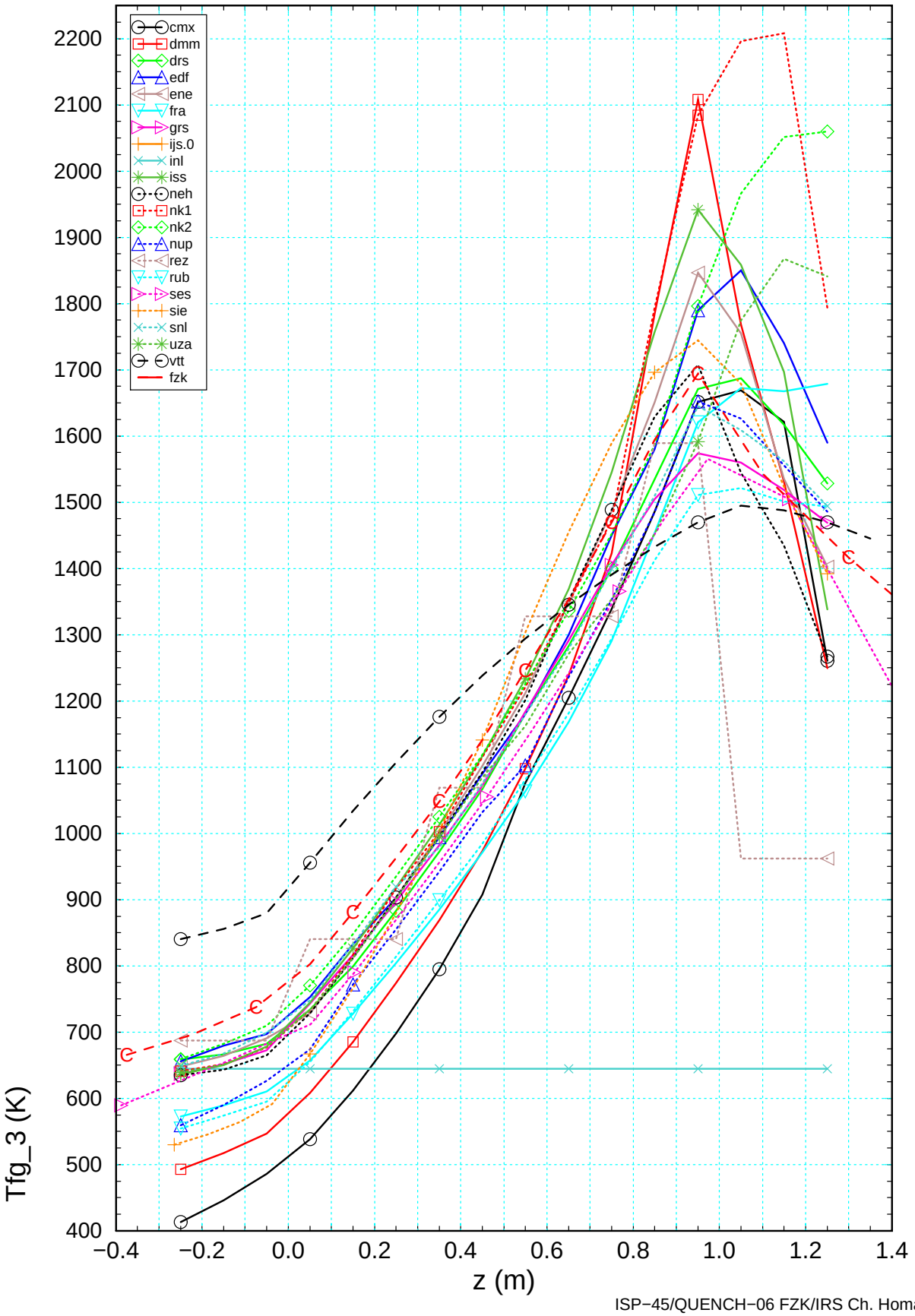

Figure 8.15 Axial profile of the fluid temperature (Tfg_3) calculated by the participants fort=7170 s compared to the results of FZK post-test calculations (-C-).

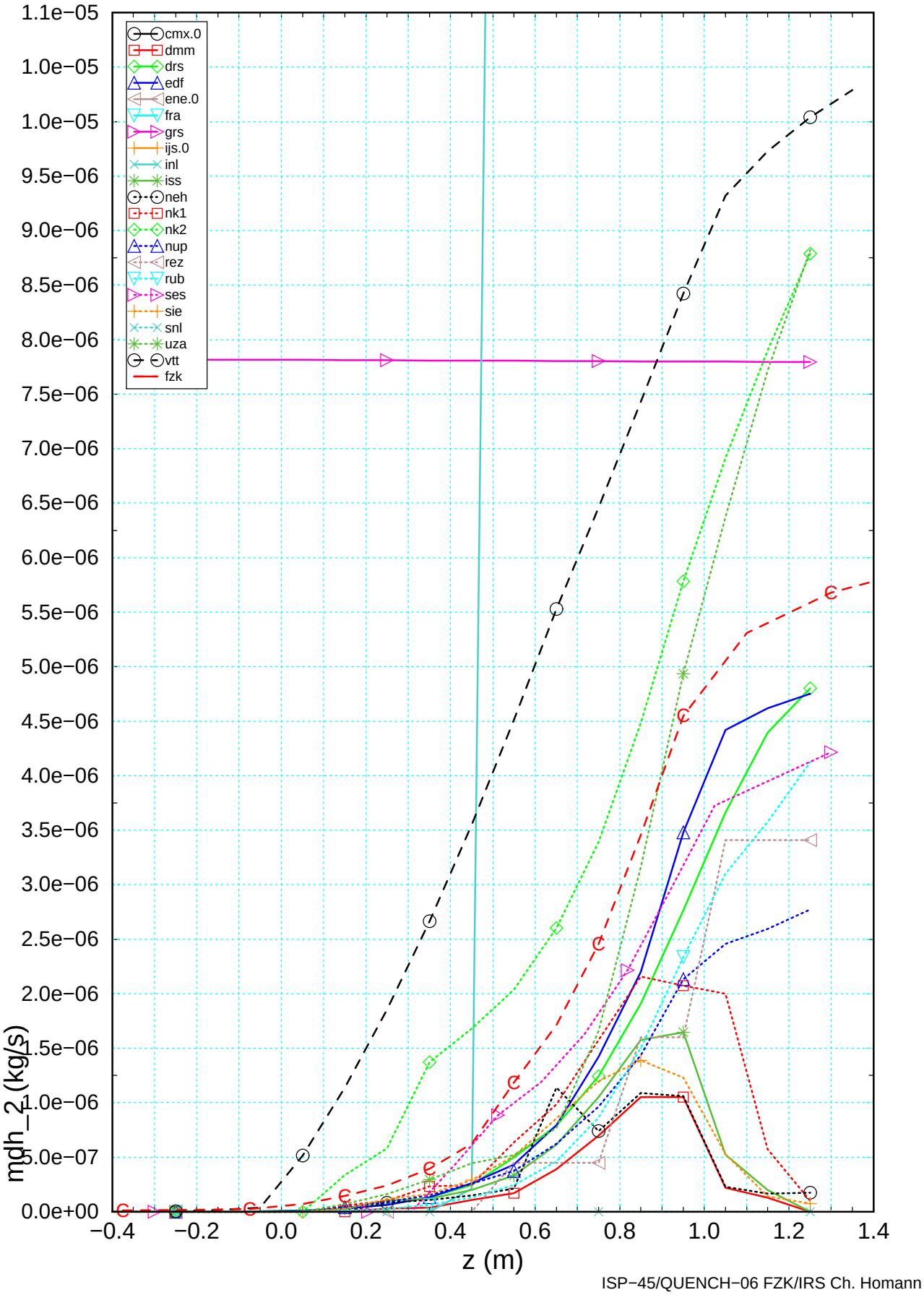

Figure 8.16 Axial distribution of hydrogen source calculated by the participants for t=6620 s compared to the results of FZK post-test calculations.

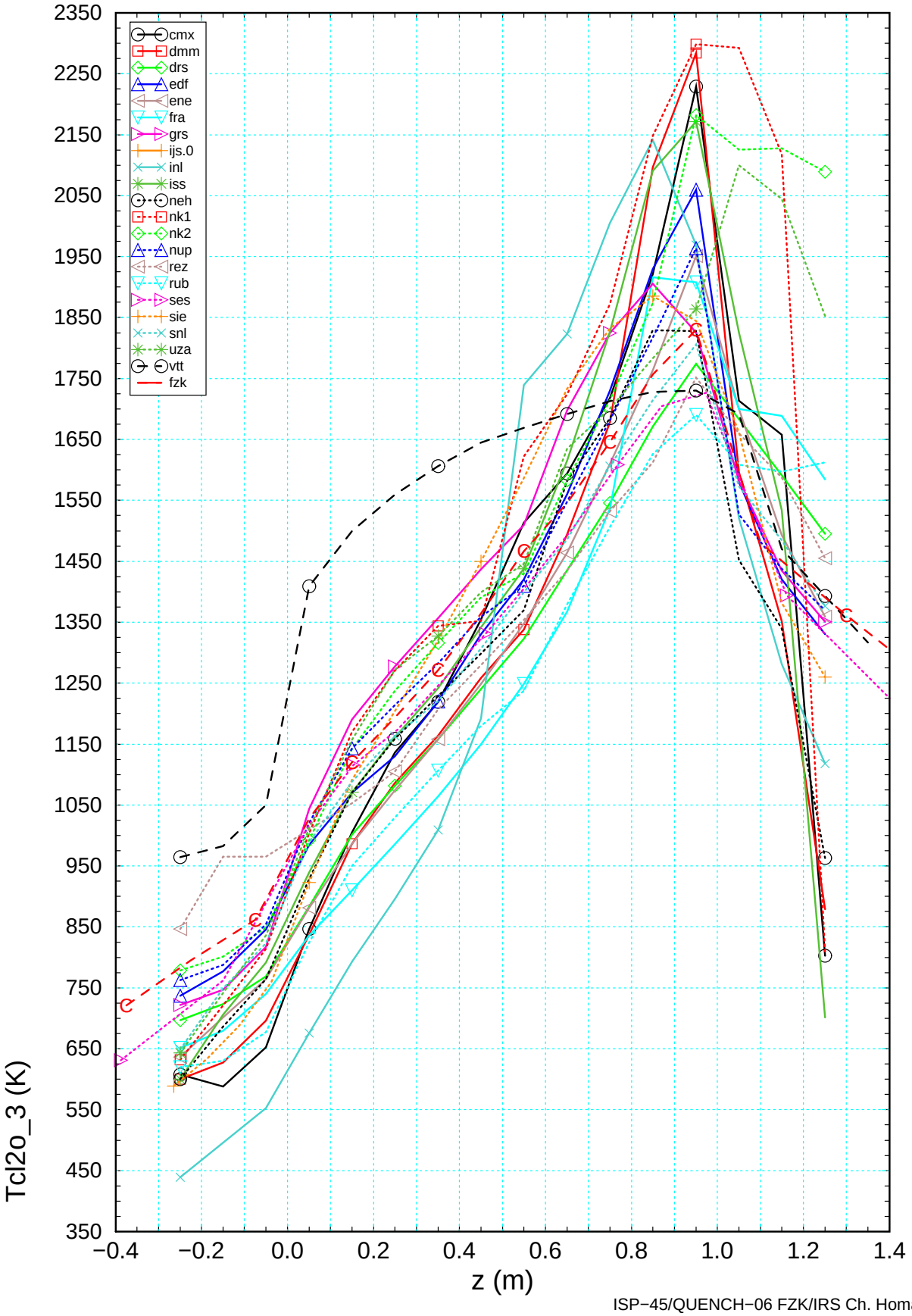

Figure 8.17 Axial cladding temperature profile for the inner ring of heater rods (Tcl2o_3) for t=7170 s compared to the results of FZK post-test calculations (-C-).

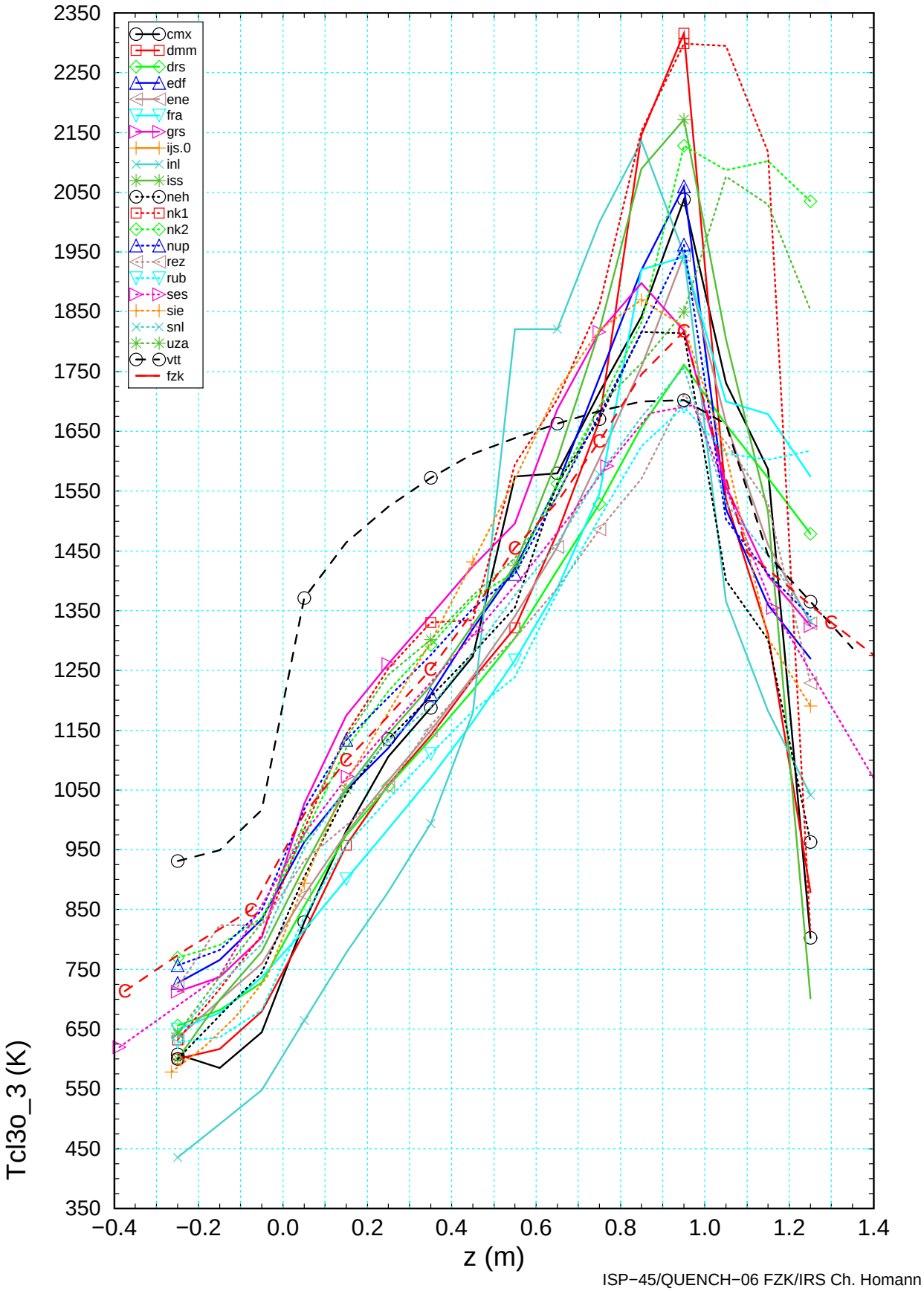

Figure 8.18 Axial cladding temperature profile for the outer ring of heater rods (Tcl3o_3) for t=7170 s compared to the results of FZK post-test calculations (-C-).

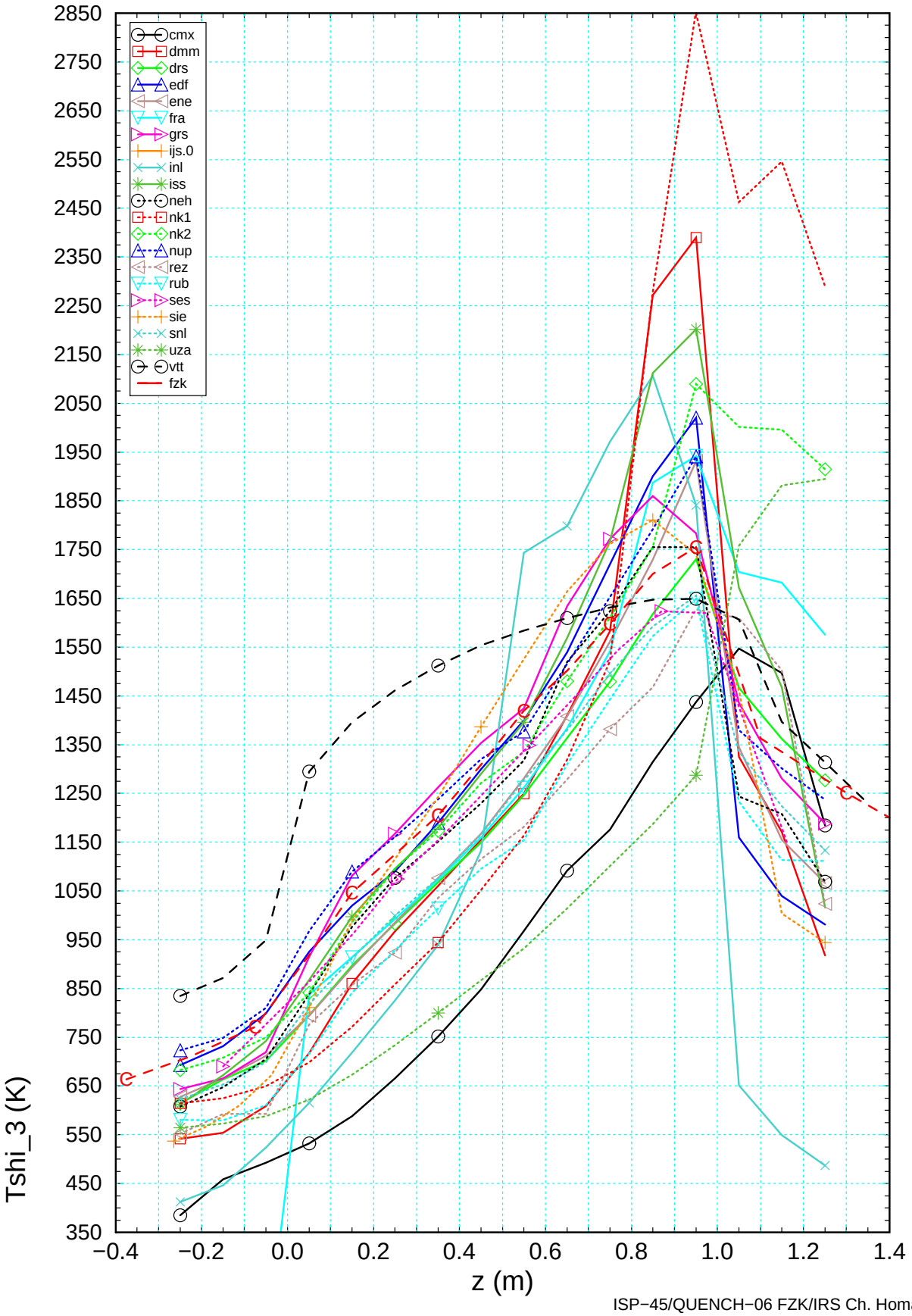

ISP−45/QUENCH−06 FZK/IRS Ch. Homann

Figure 8.19 Axial profile for the shroud temperature (Tshi_3) calculated by the participants for t=7170 s compared to the results of FZK post-test calculations.

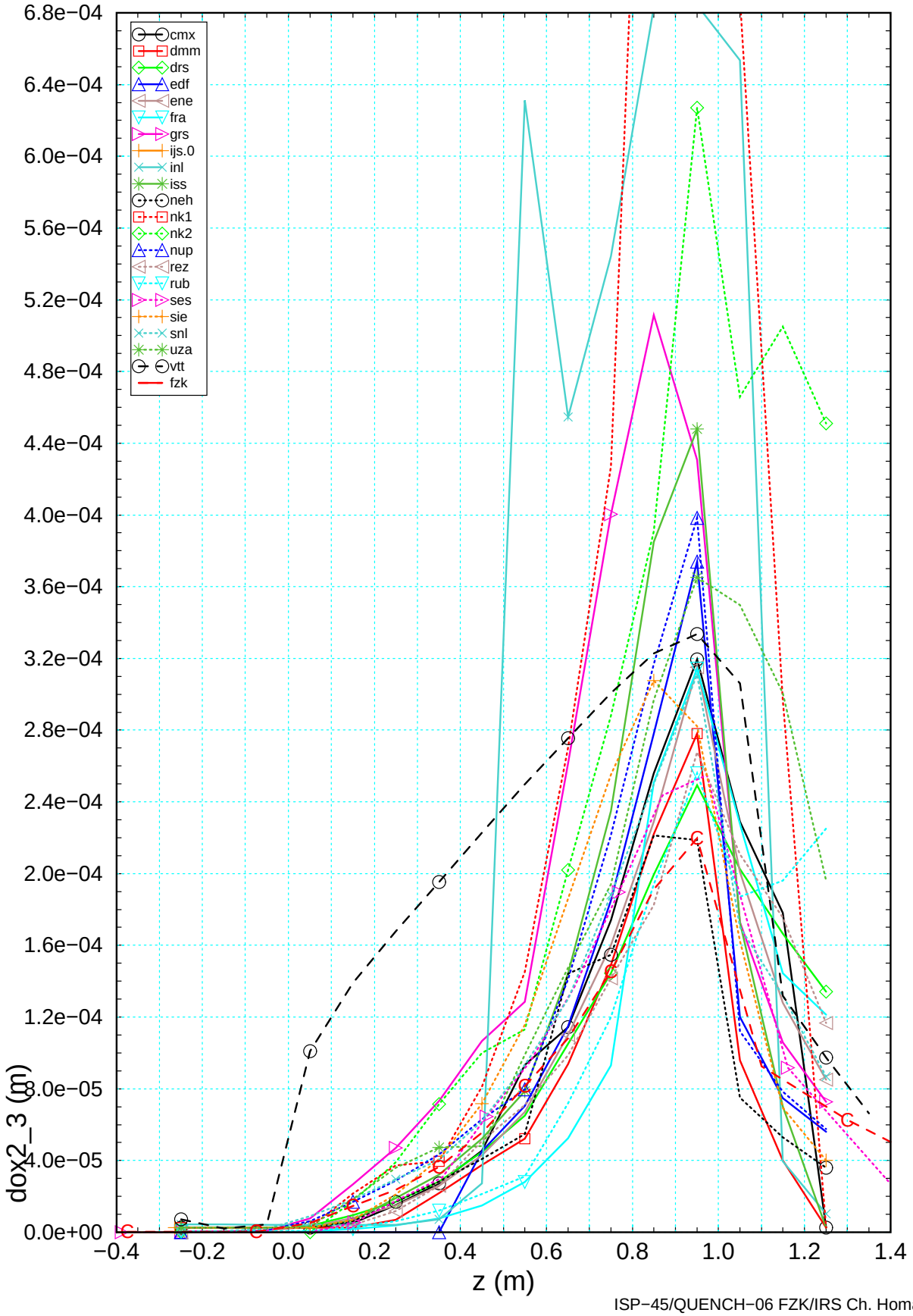

Figure 8.20 Axial oxide layer profile of the inner ring of heated rods (dox2_3) for t=7170 s compared to the results of the FZK post-test calculations (-C-).

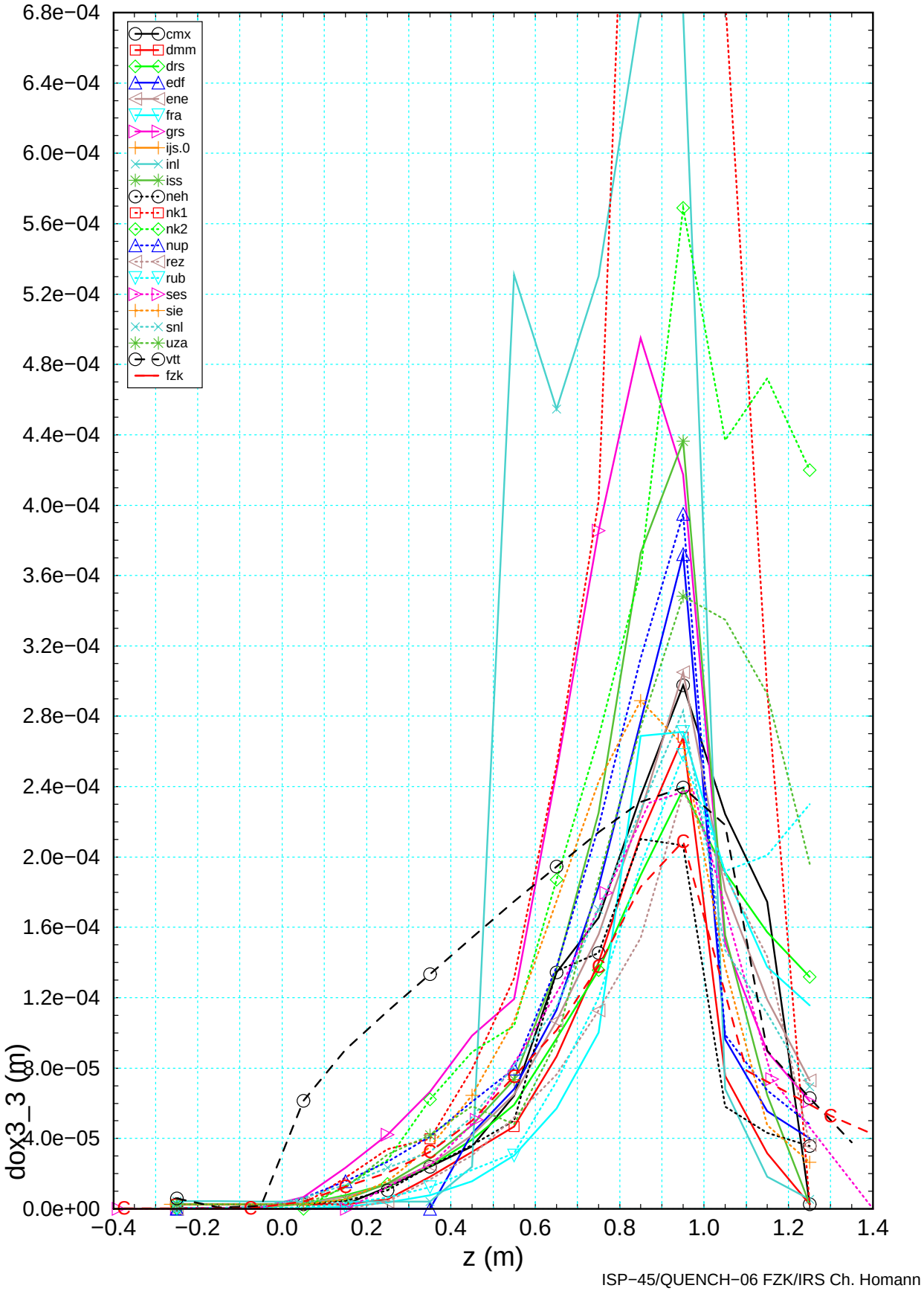

Figure 8.21 Axial oxide layer profile of the outer ring of heated rods (dox3_3) for t=7170 s compared to the results of the FZK post-test calculations (-C-).

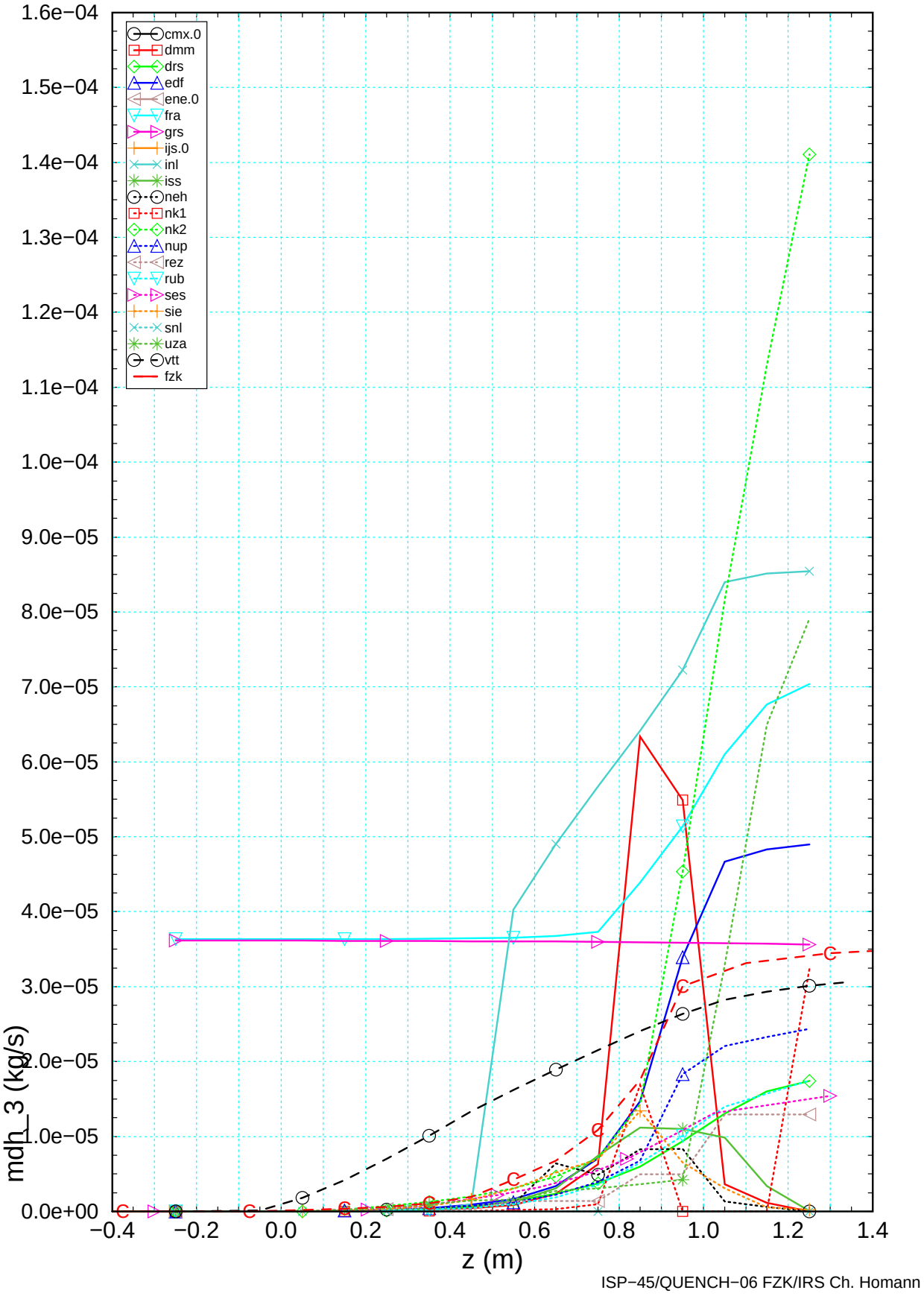

Figure 8.22 Axial distribution of hydrogen source calculated by the participants for t=7170 s compared to results of FZK post-test calculations

8.3.2 Bundle degradation

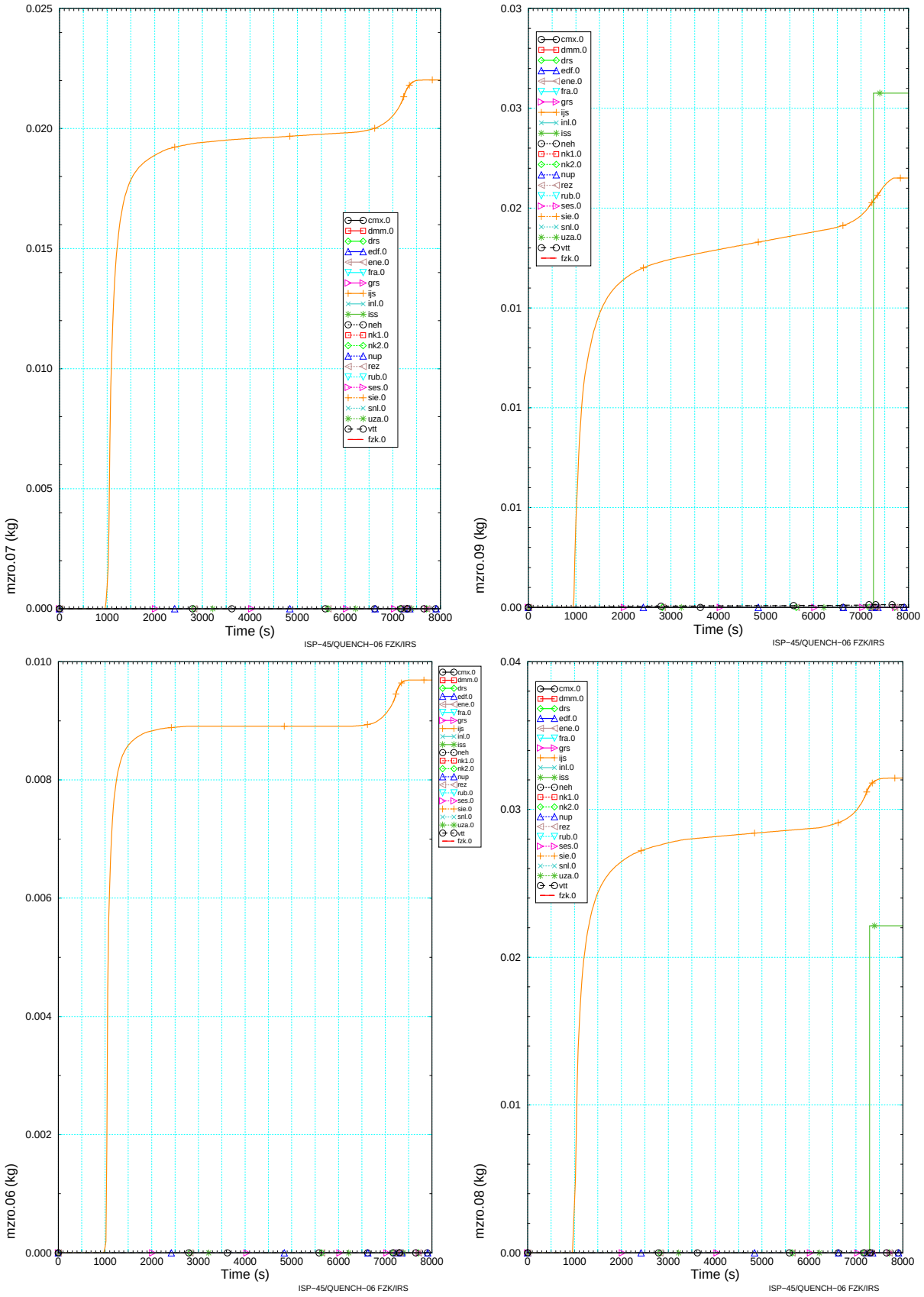

Figure 8.23 Calculated zirconium oxide mass at bundle zone 6 to 9.

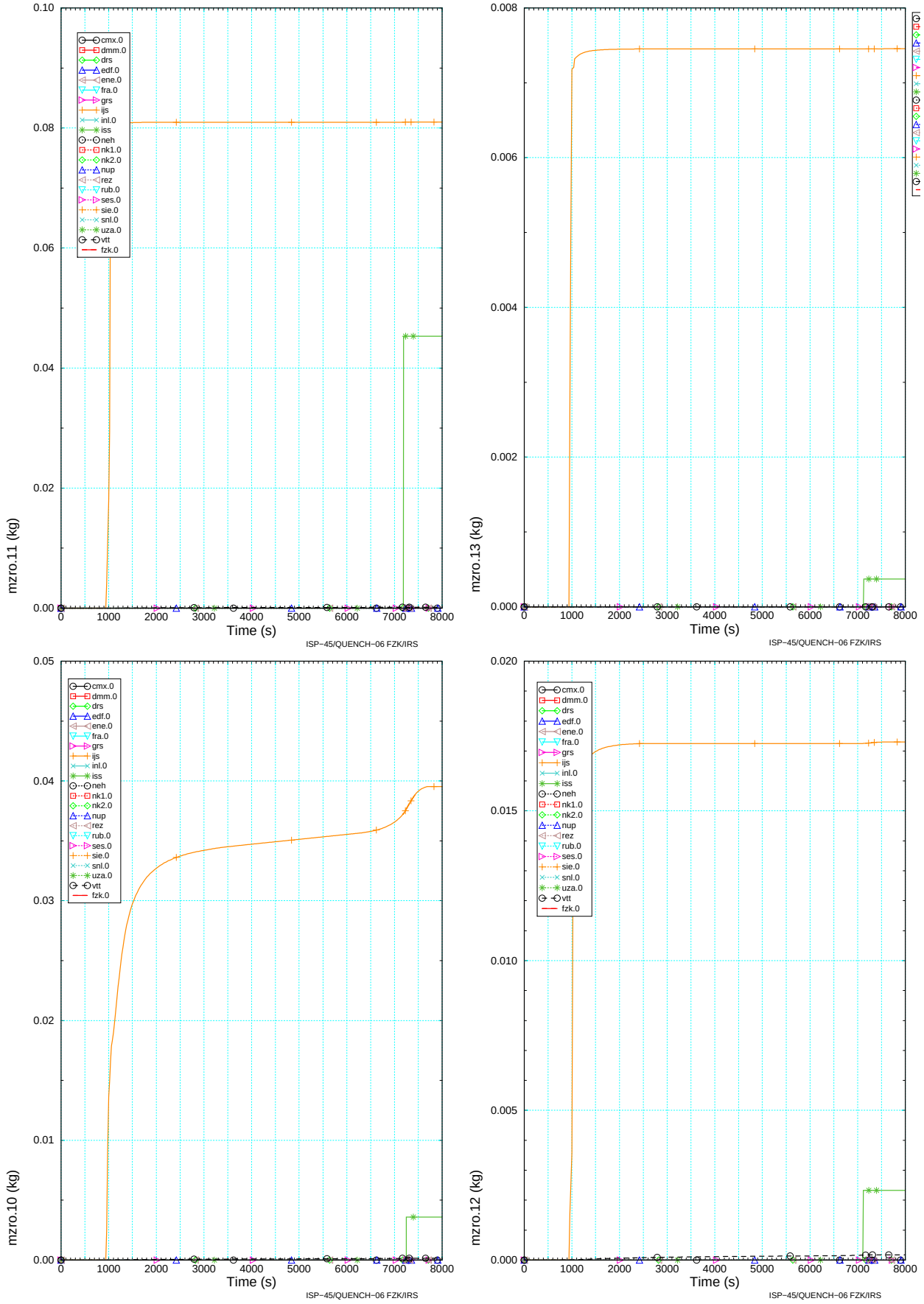

Figure 8.24 Calculated zirconium oxide mass at bundle zone 10 to 13.

8.3.3 Additional data during reflood phase

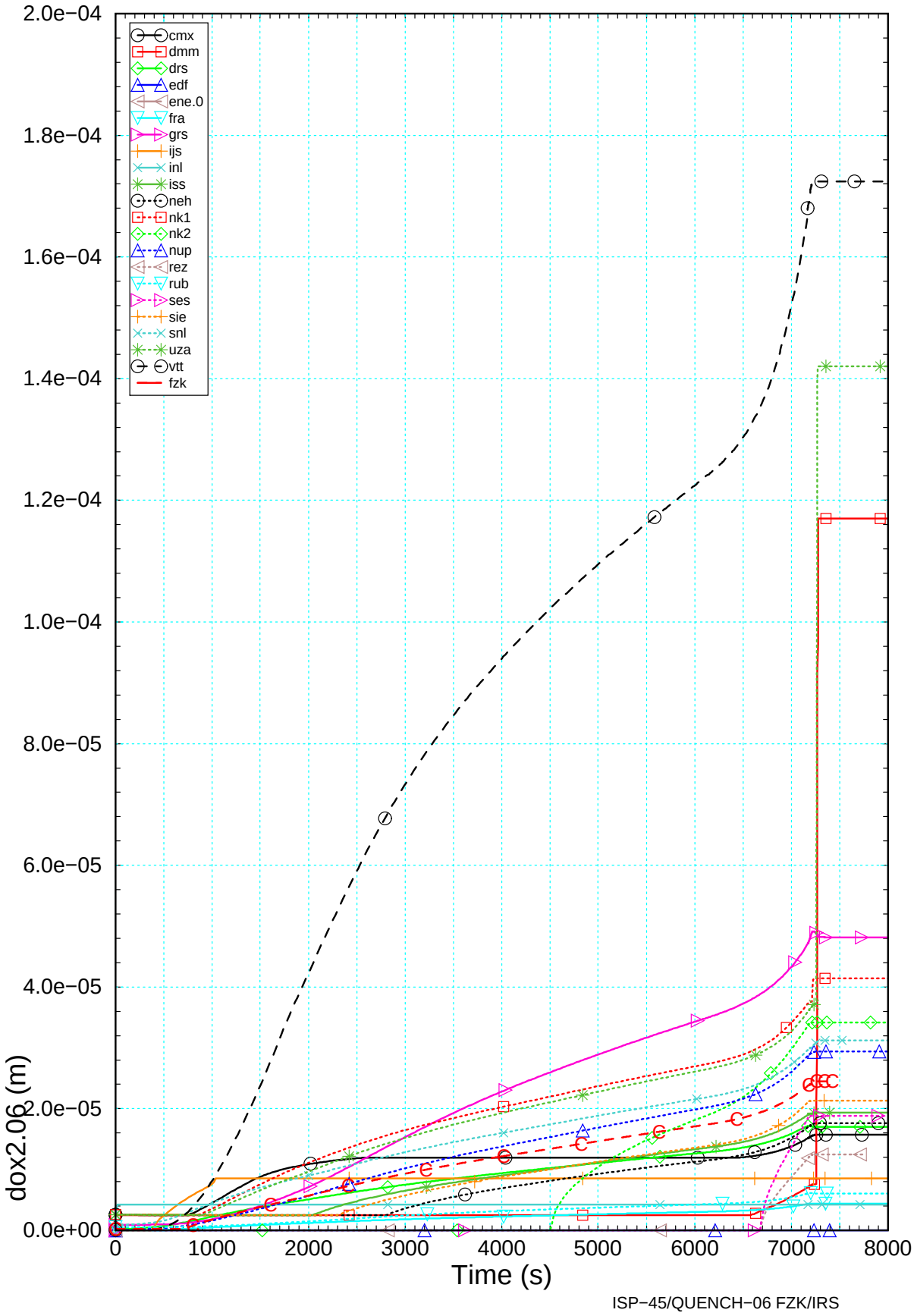

Figure 8.25 Heated rod (2nd ring) oxide layer thickness at elevation 0.25 m calculated by the participants and compared to the results of FZK post-test calculation (-C-)

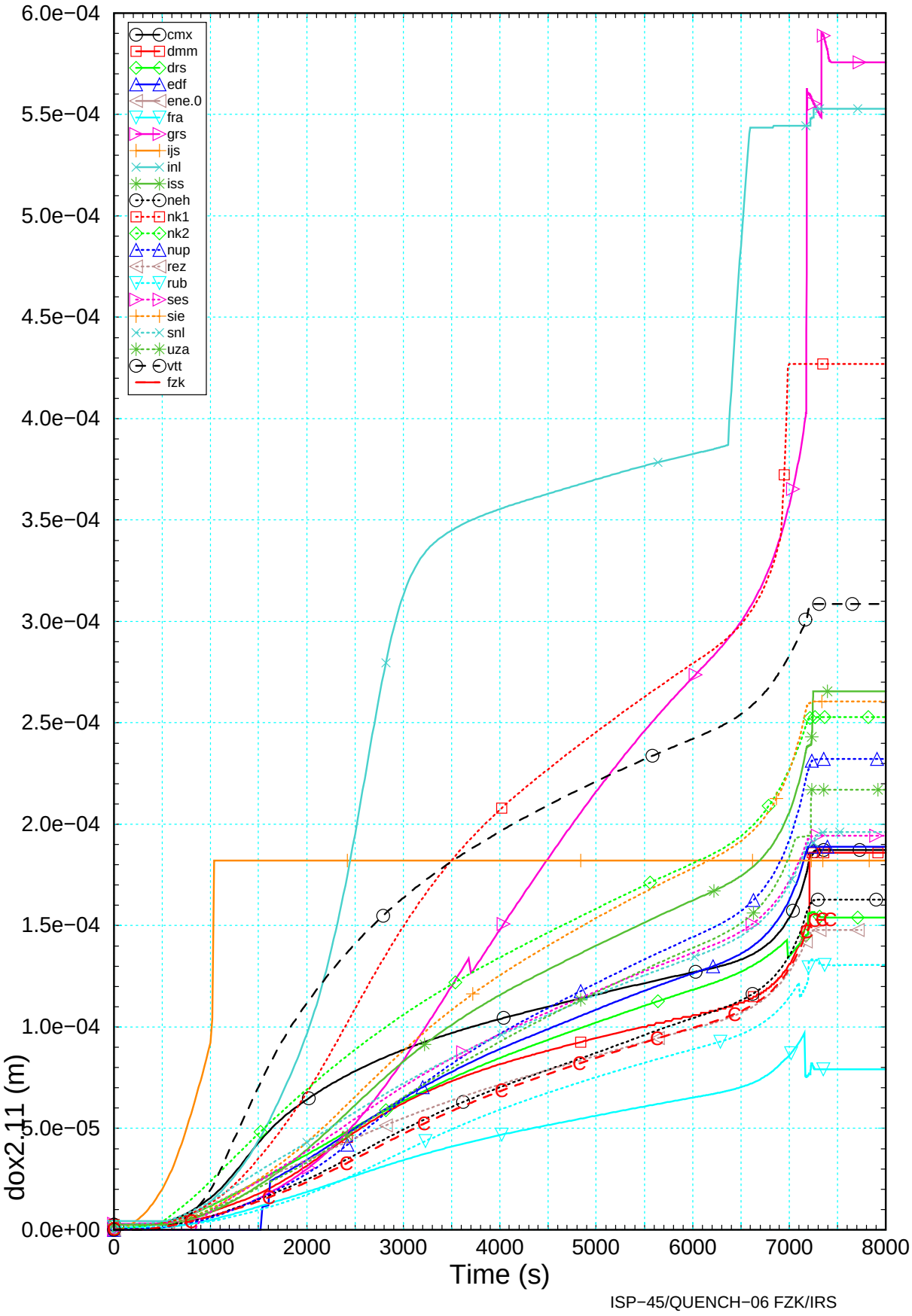

Figure 8.26 Heated rod (2nd ring) oxide layer thickness at elevation 0.75 m calculated by the participants and compared to the results of FZK post-test calculation (-C-)

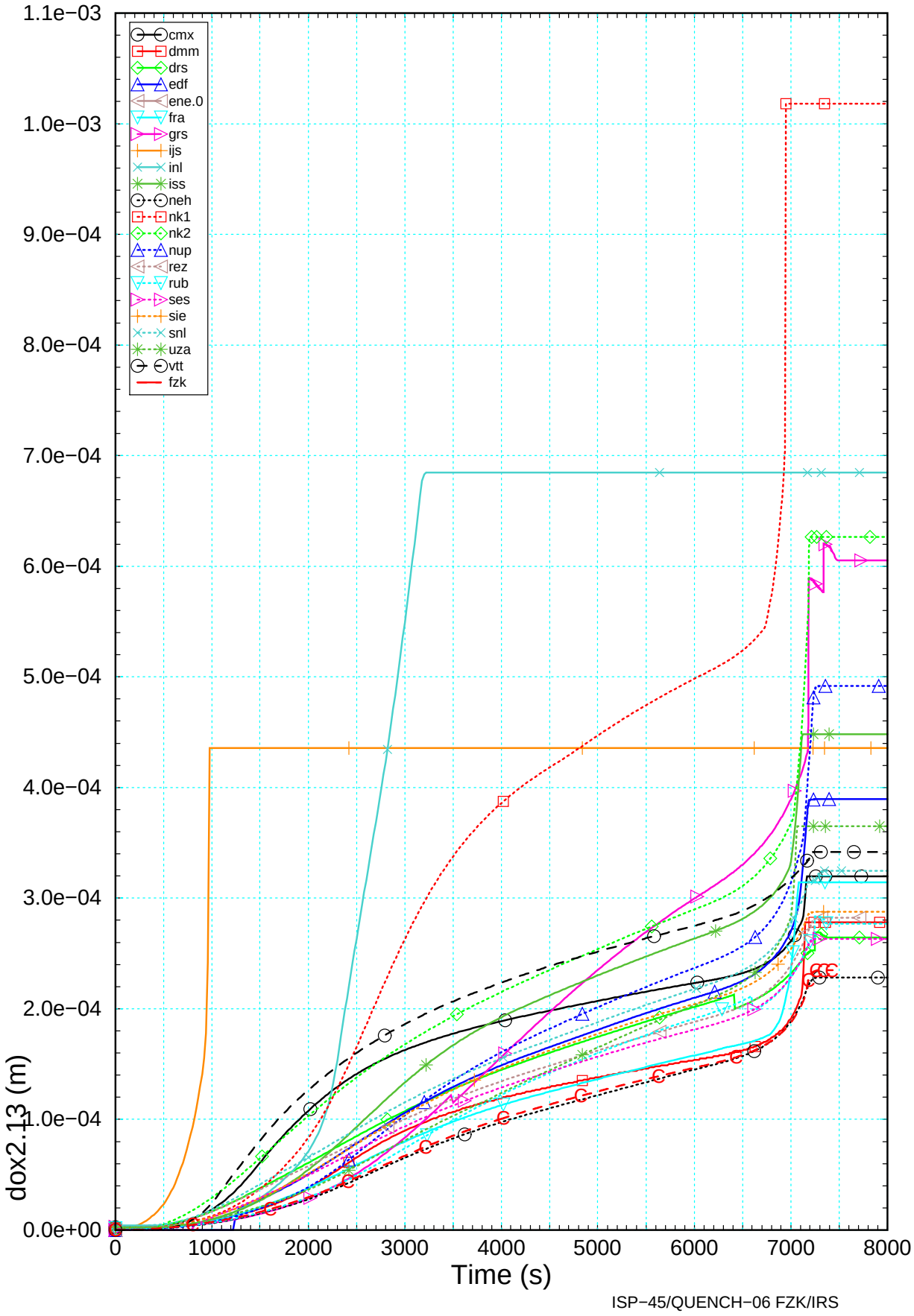

Figure 8.27 Heated rod (2nd ring) oxide layer thickness at elevation 0.95 m calculated by the participants and compared to the results of FZK post-test calculation (-C-)

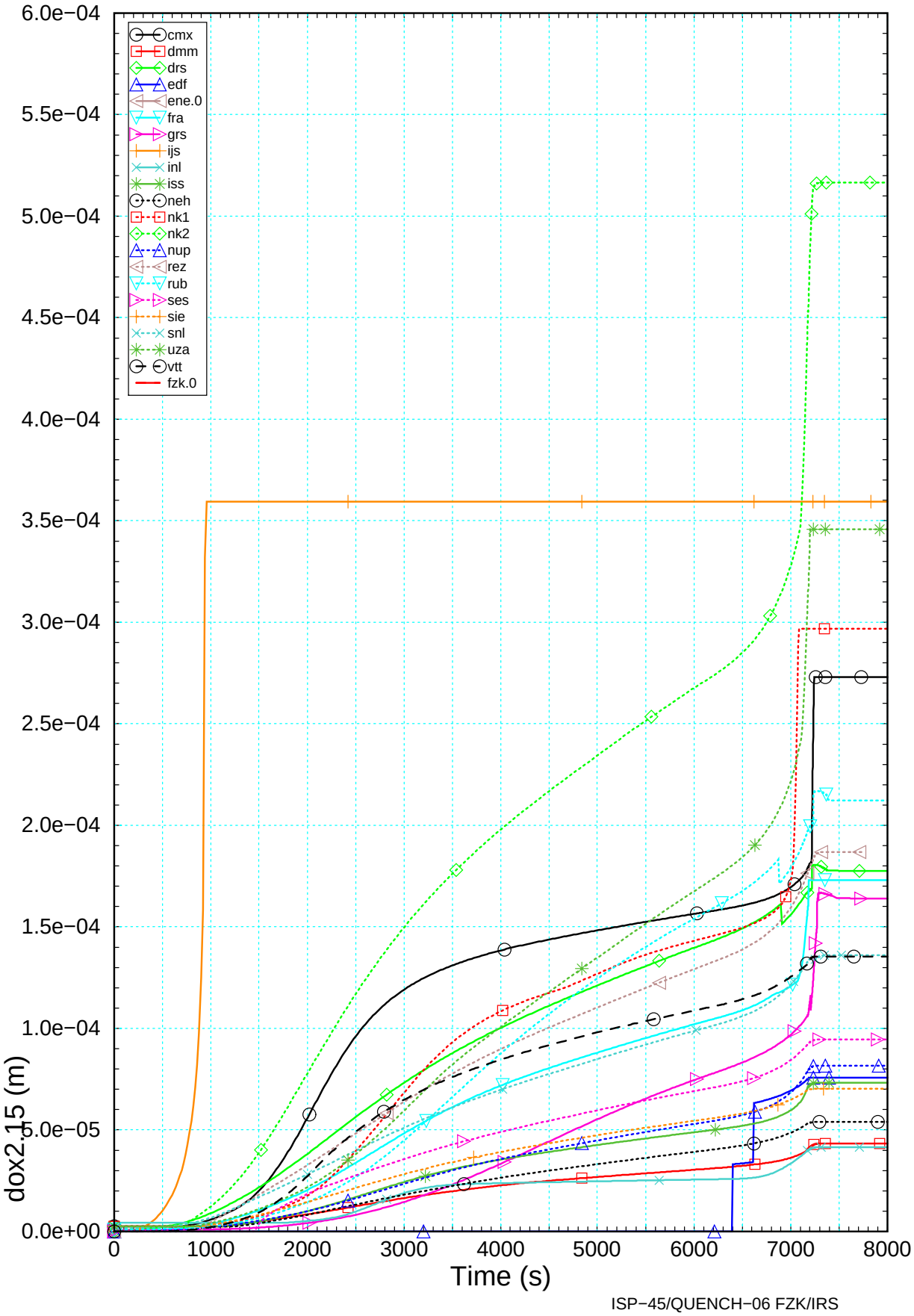

Figure 8.28 Heated rod (2nd ring) oxide layer thickness at elevation 1.15 m calculated by the participants.

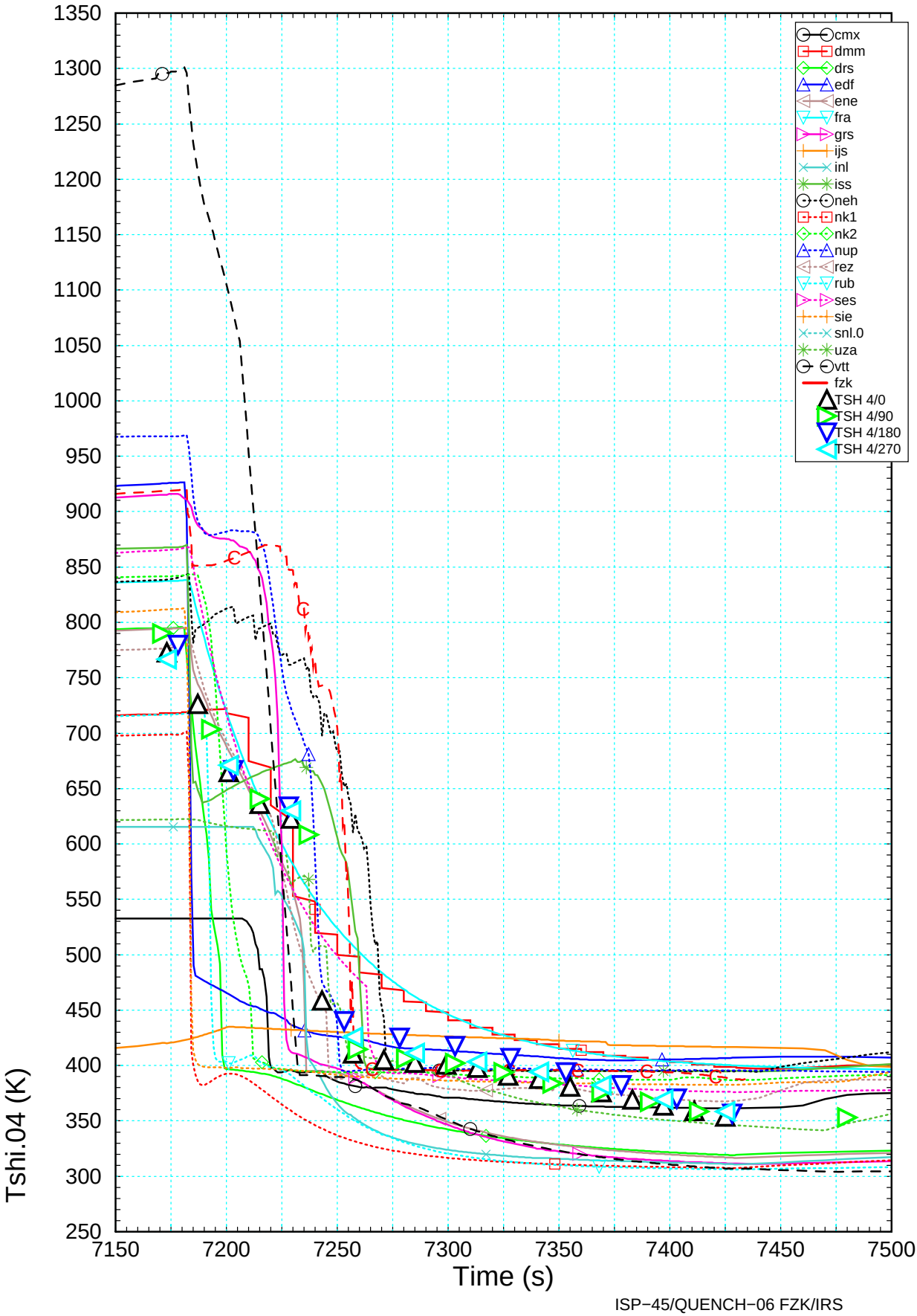

Figure 8.29 Shroud temperature at elevation 0.05 m calculated by the participants and compared to experimental results TSH4/[0;90;180;270] and the results of FZK post-test calculation (-C-)

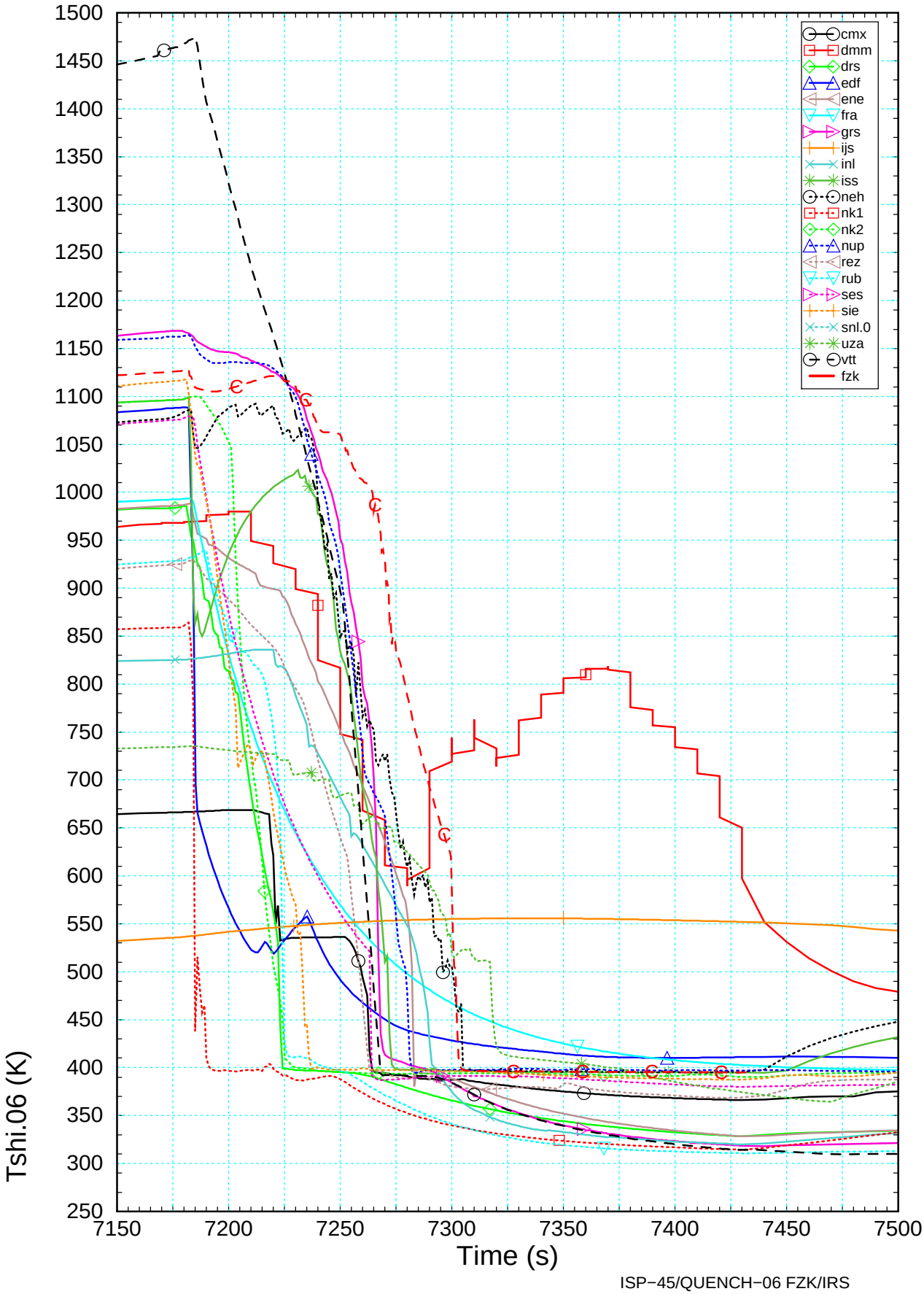

Figure 8.30 Shroud temperature at elevation 0.25 m calculated by the participants and compared to the results of FZK post-test calculation (-C-)

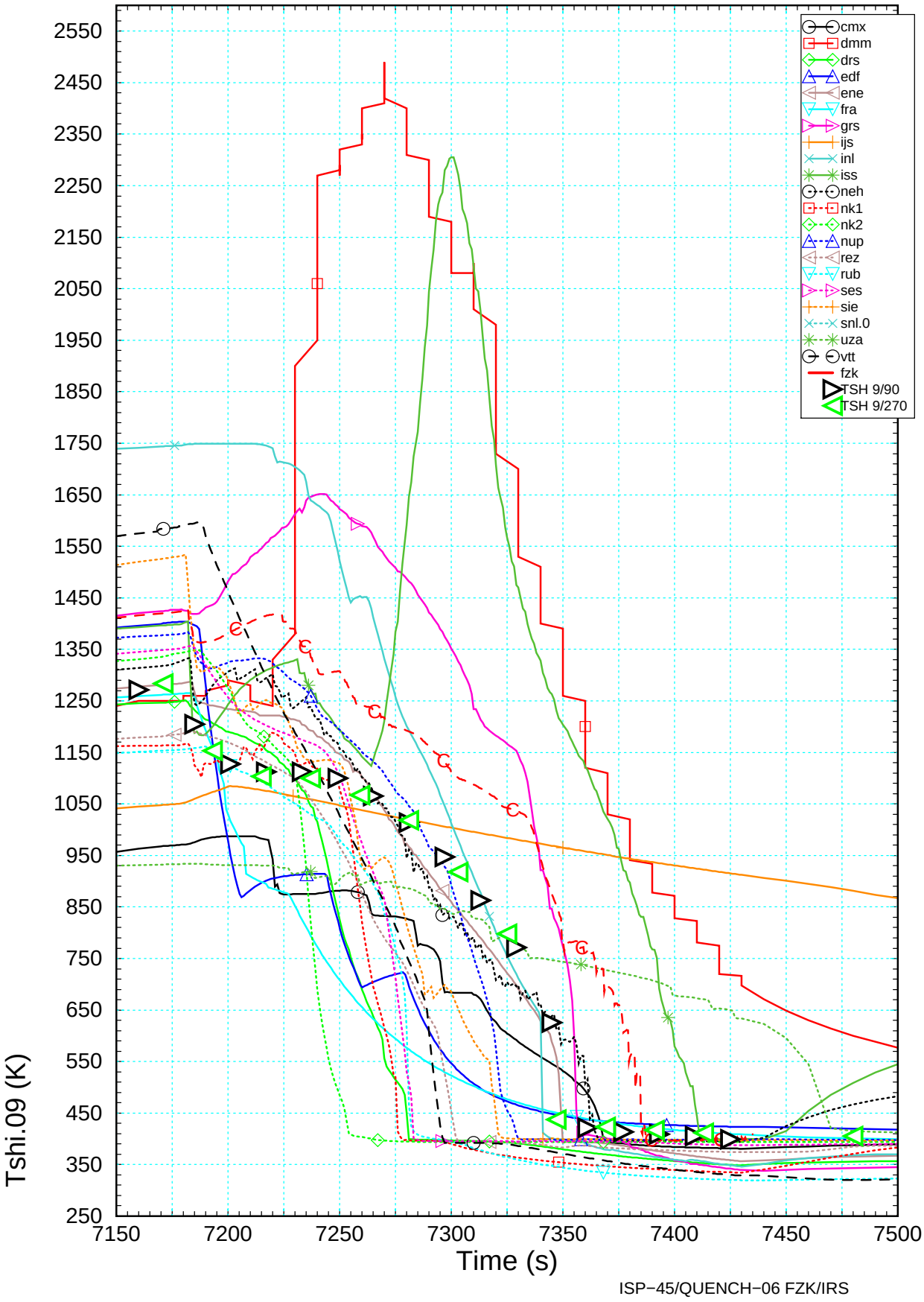

Figure 8.31 Shroud temperature at elevation 0.55 m calculated by the participants and compared to TC measurements TSH9/[90;270] (opaque triangles) and to the results of FZK post-test calculation (-C-)

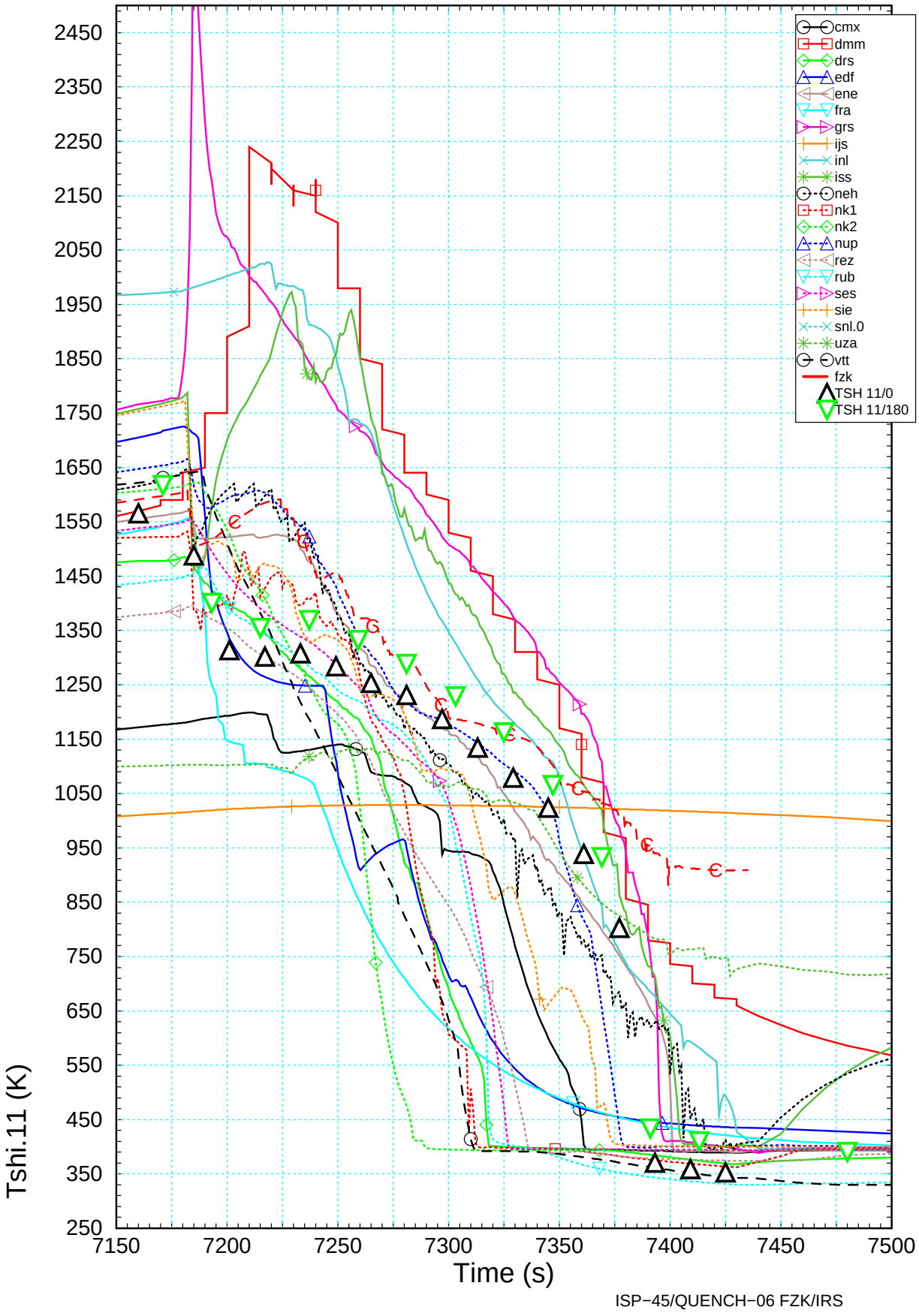

Figure 8.32 Shroud temperature at elevation 0.75 m calculated by the participants and compared to TC measurements TSH11/[0;180] (opaque triangles) and to the results of FZK post-test calculation (-C-)

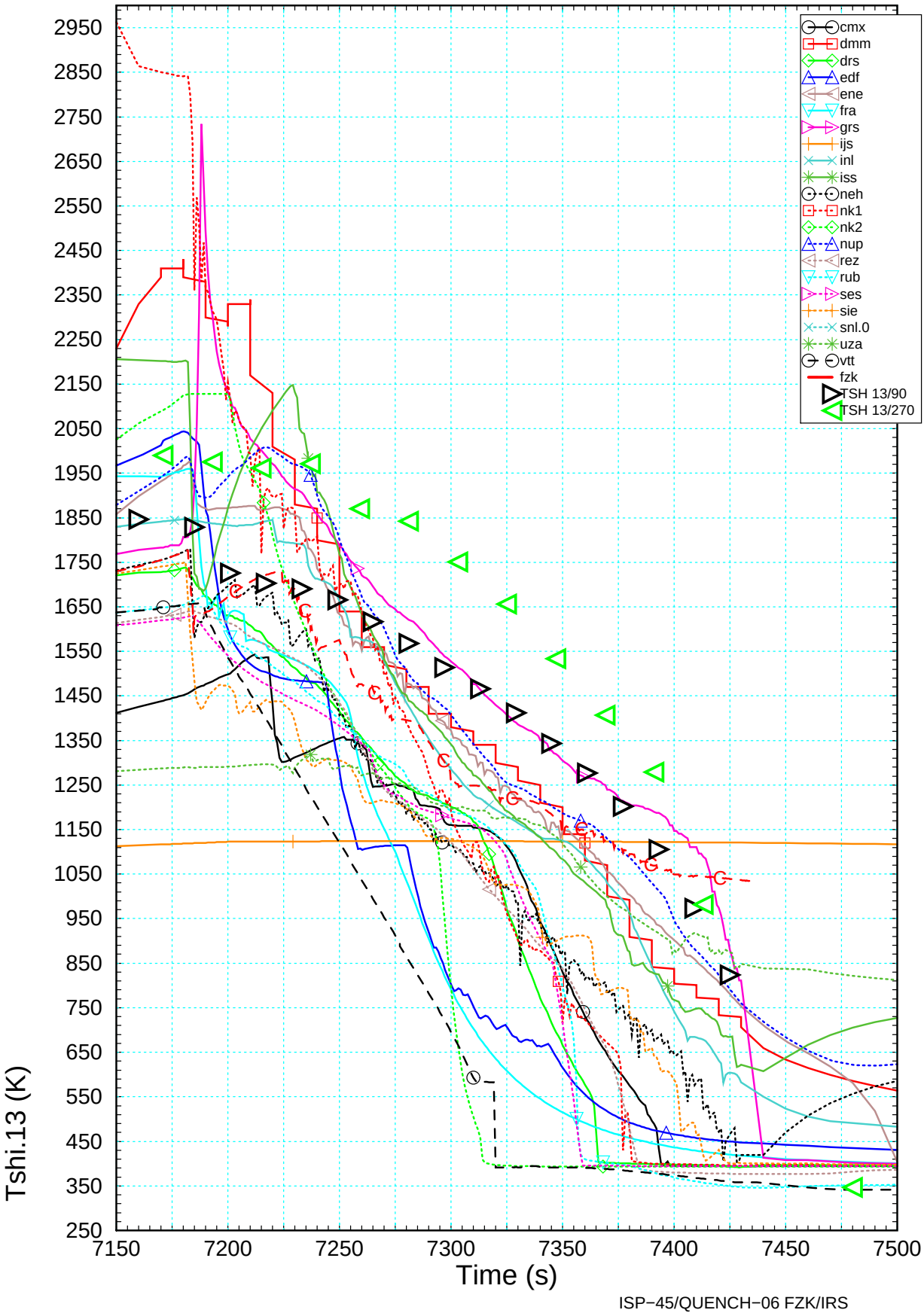

Figure 8.33 Shroud temperature at elevation 0.95 m calculated by the participants and compared to TC measurements TSH13/[90;270] (opaque triangles) and to the results of FZK post-test calculation (-C-)

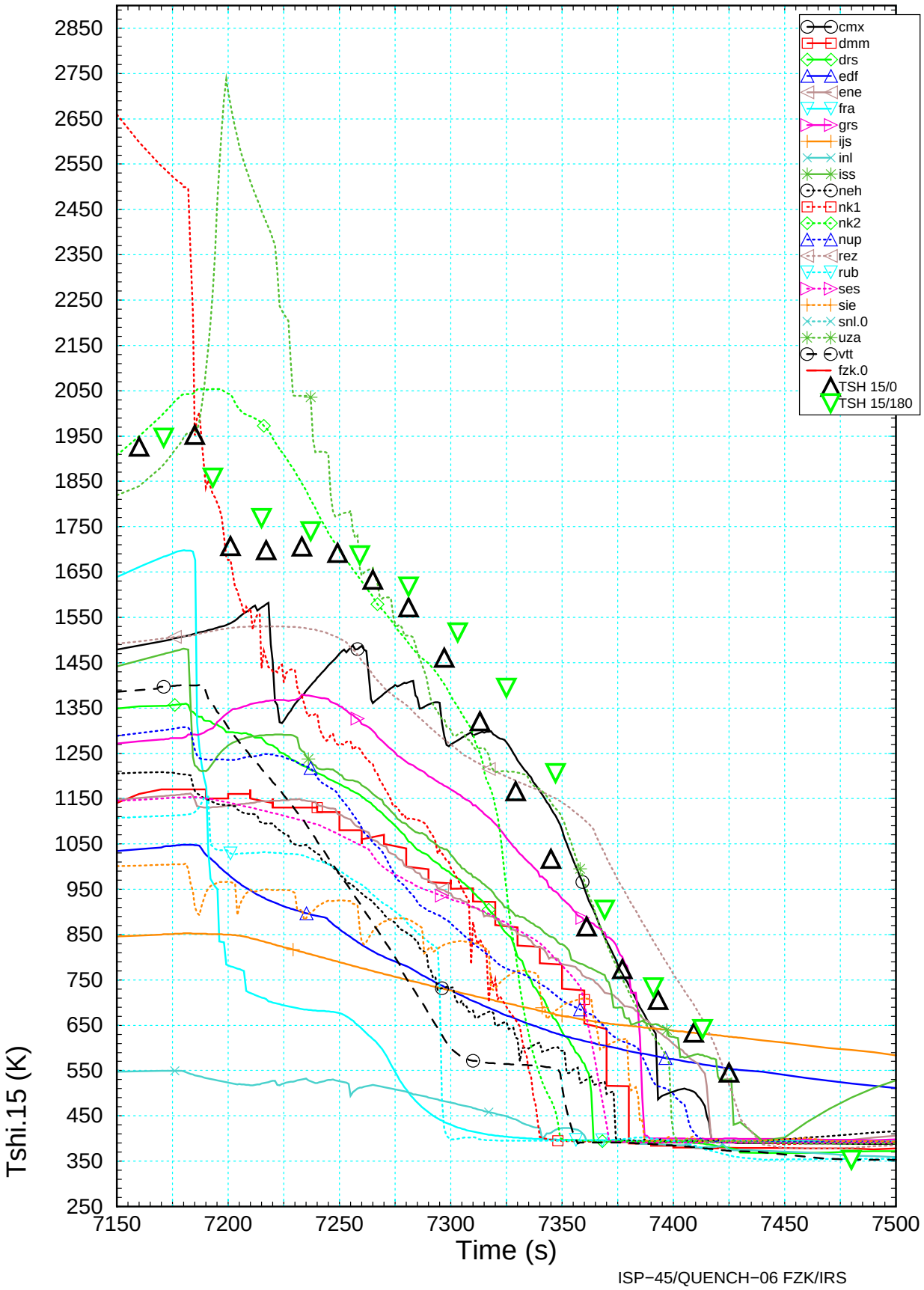

Figure 8.34 Shroud temperature at elevation 1.15 m calculated by the participants and compared to TC measurements TSH15/[0;180] (opaque triangles) and to the results of FZK post-test calculation (-C-)

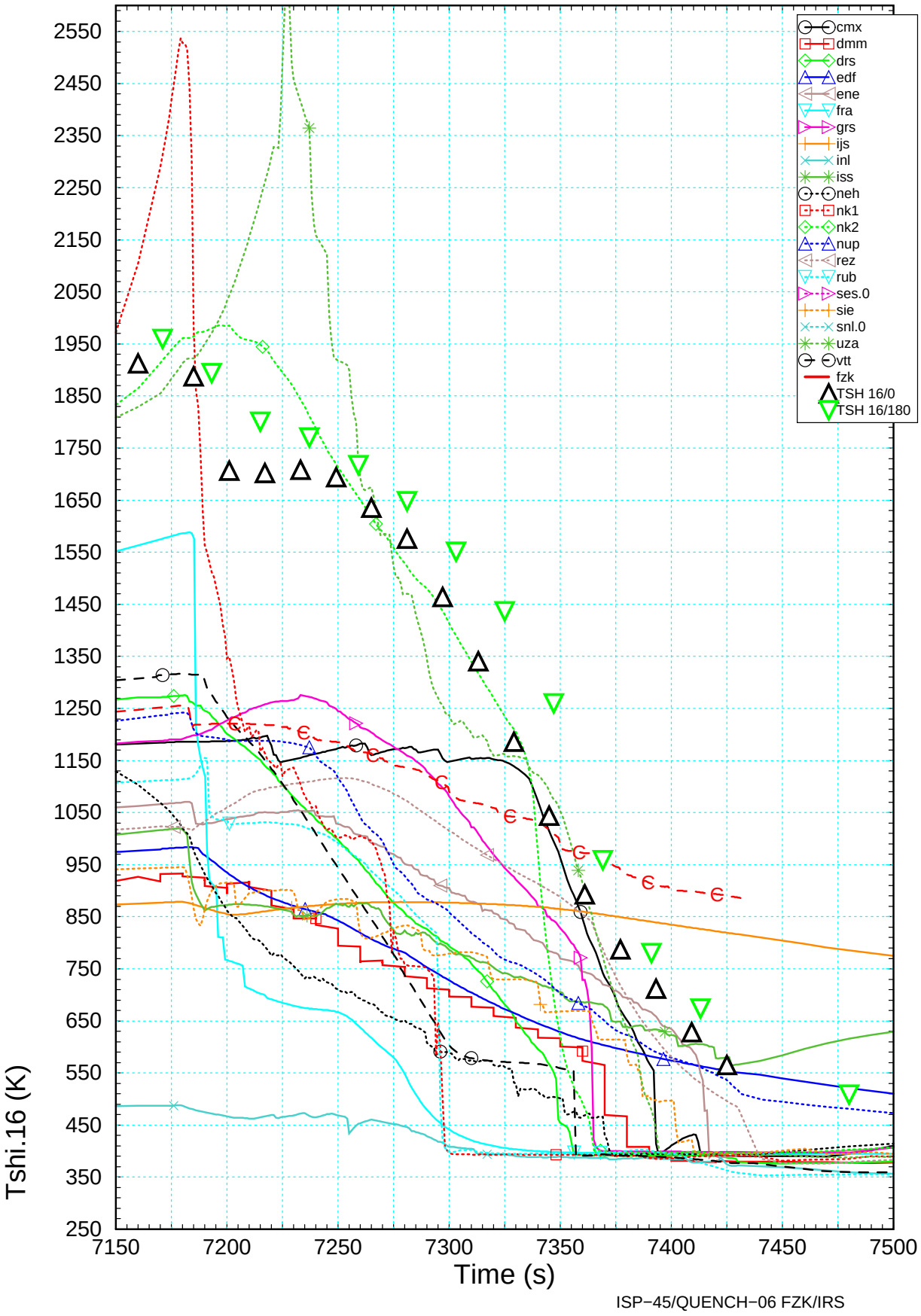

Figure 8.35 Shroud temperature at elevation 1.25 m calculated by the participants and compared to experimental results TSH16/[0;180] and the results of FZK post-test calculation (-C-)

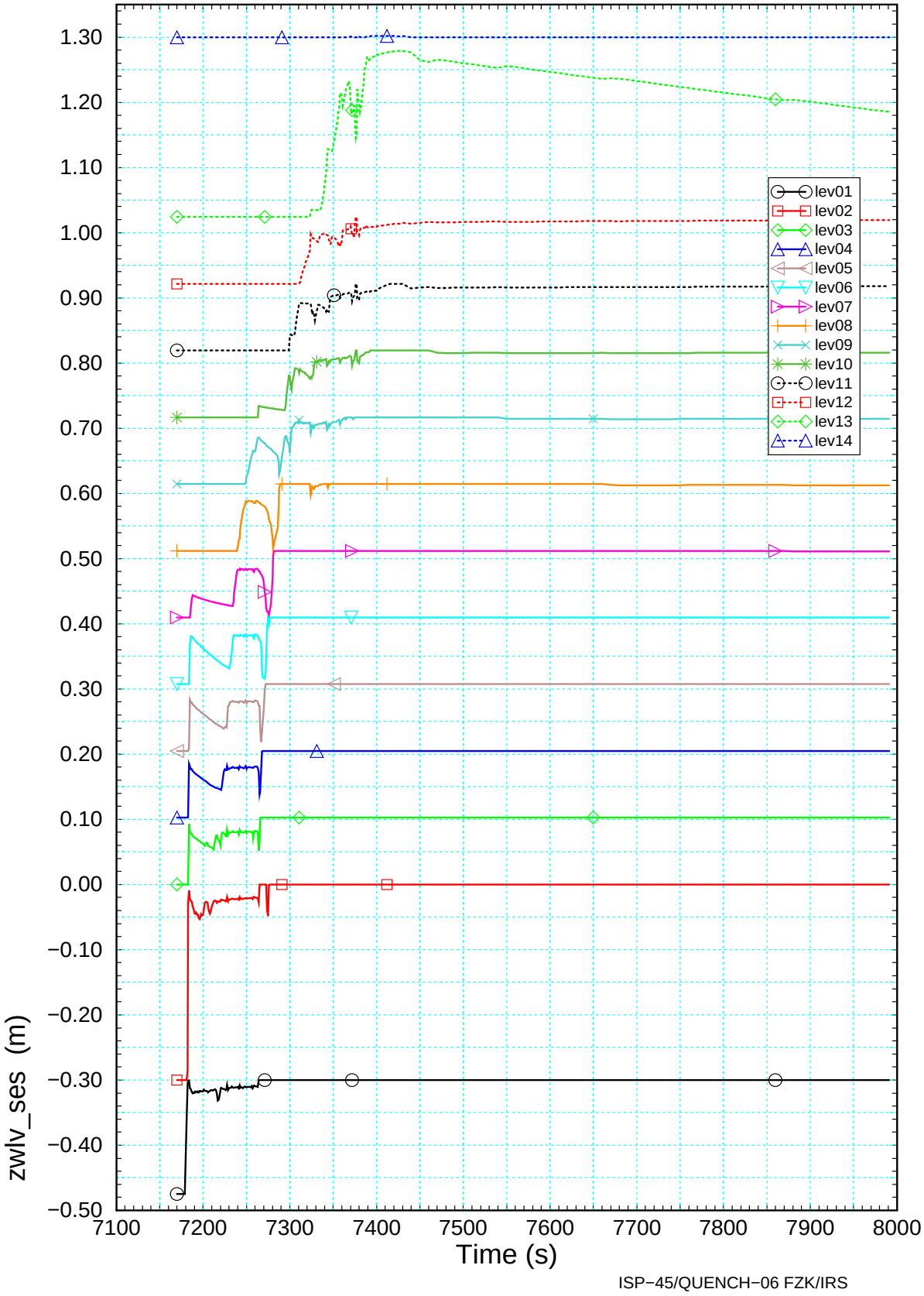

Figure 8.36 Water mass inventory for each axial zone delivered instead of a global water level as requested for comparison with collapsed water level as shown in **Figure 4.28**

8.3.4 Final state of calculations

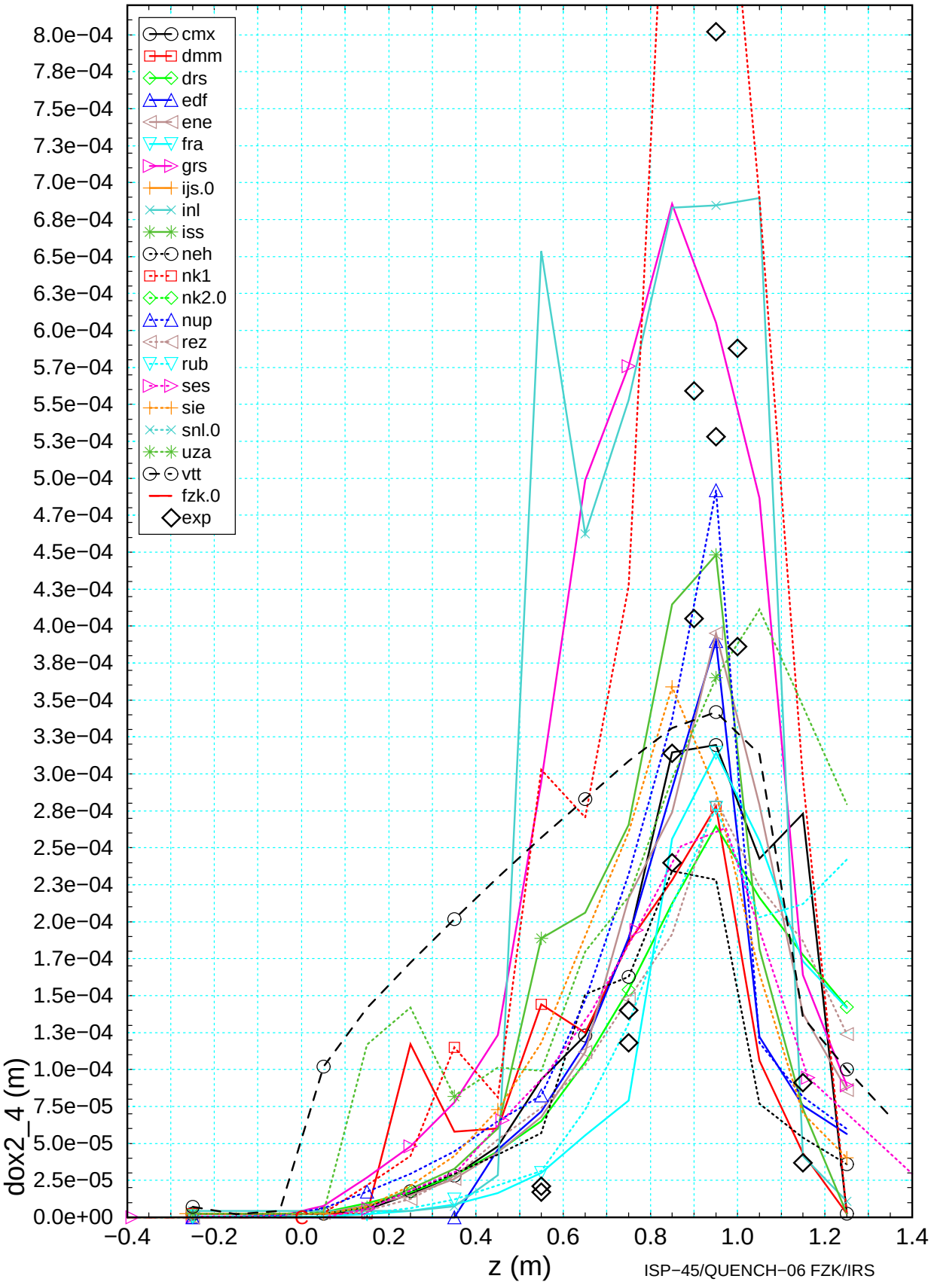

Figure 8.37 Axial oxide layer profile of the inner ring of heater rods calculated by the participants for t=8000 s compared to experimental results.

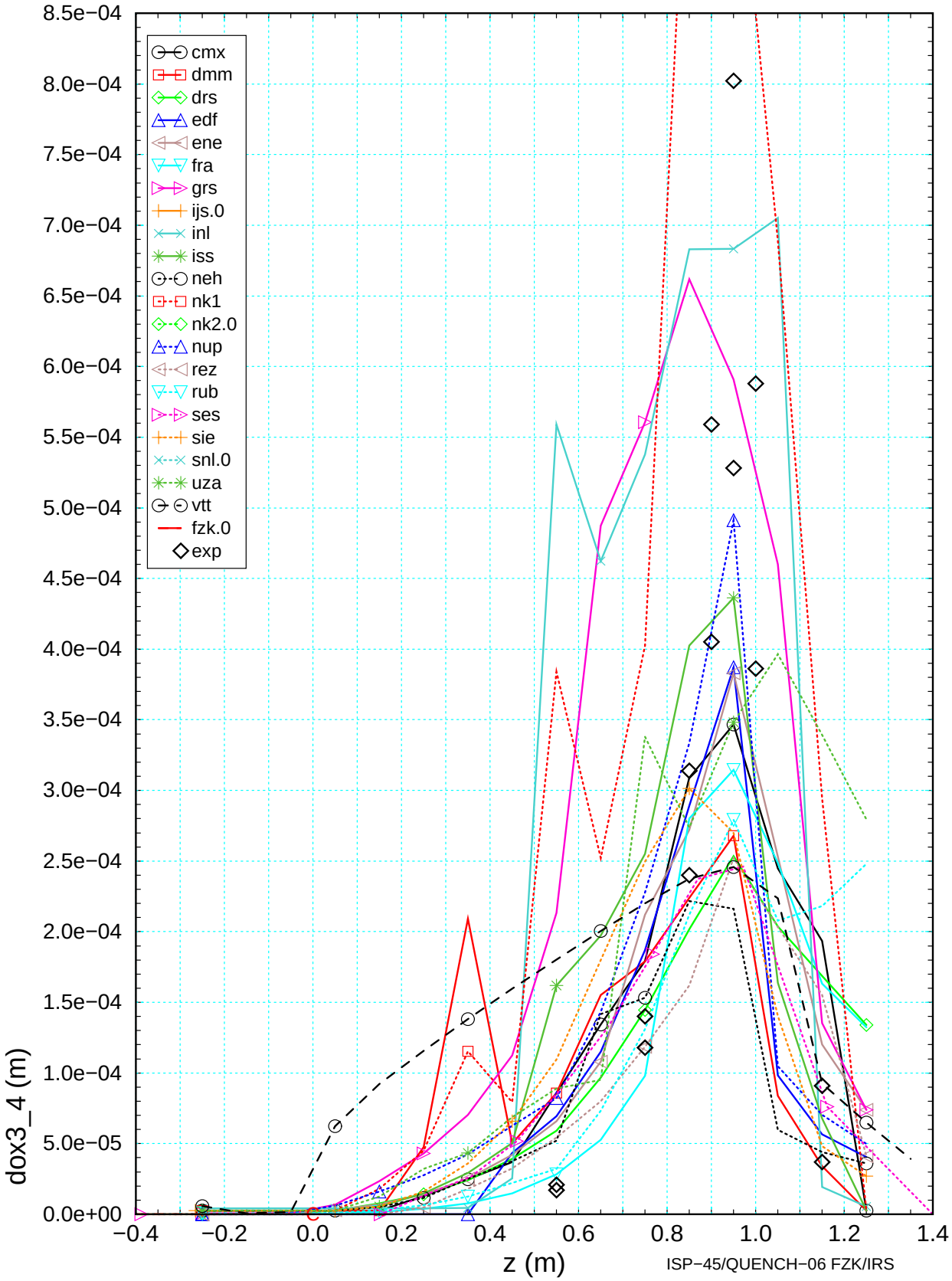

Figure 8.38 Axial oxide layer profile of the outer ring of heater rods calculated by the participants for t=8000 s compared to experimental results.

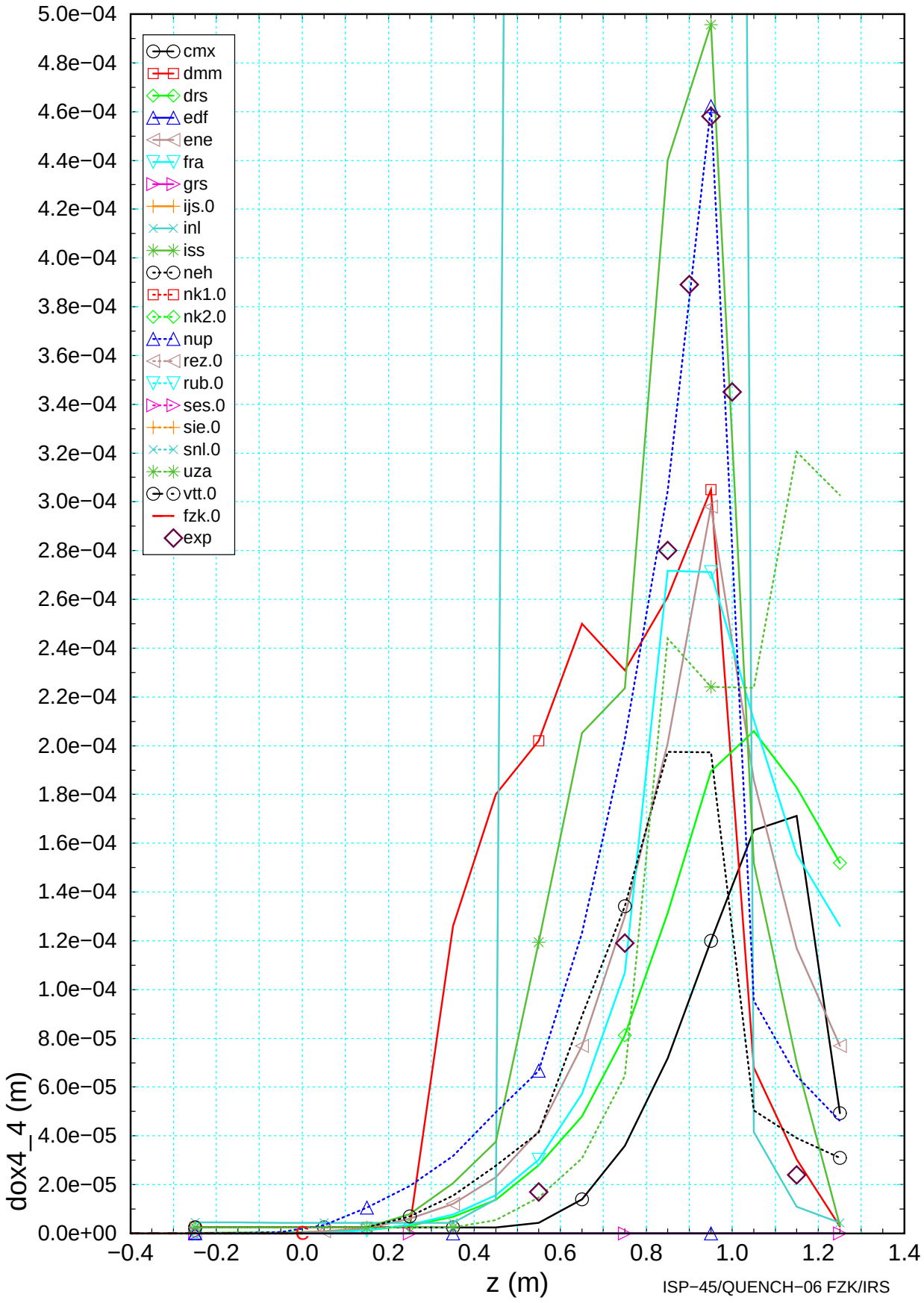

Figure 8.39 Axial oxide layer profile of the corner rods calculated by the participants for t=8000 s compared to experimental results

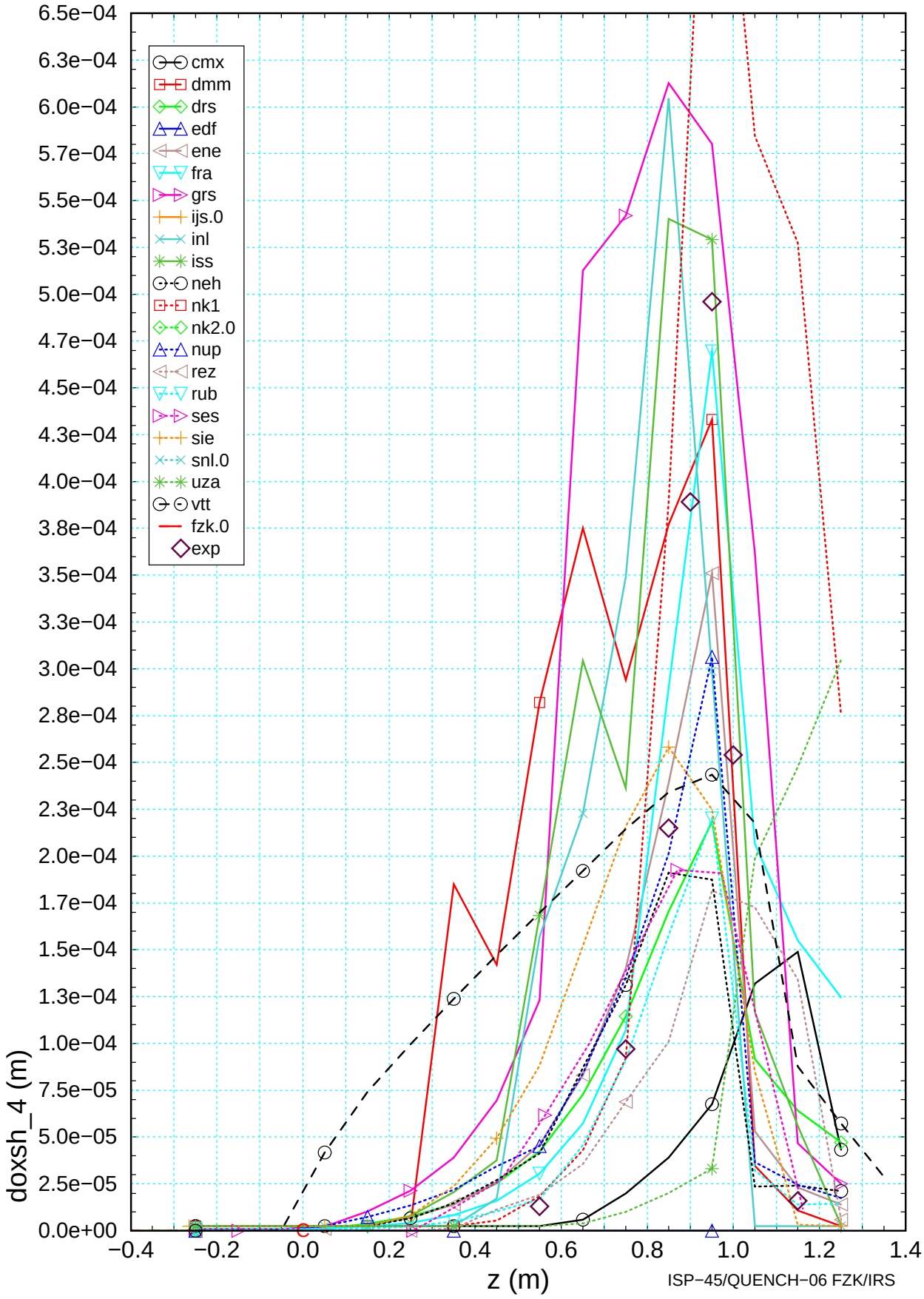

Figure 8.40 Axial oxide layer profile of the Zircaloy shroud calculated by the participants for t=8000 s compared to experimental results.

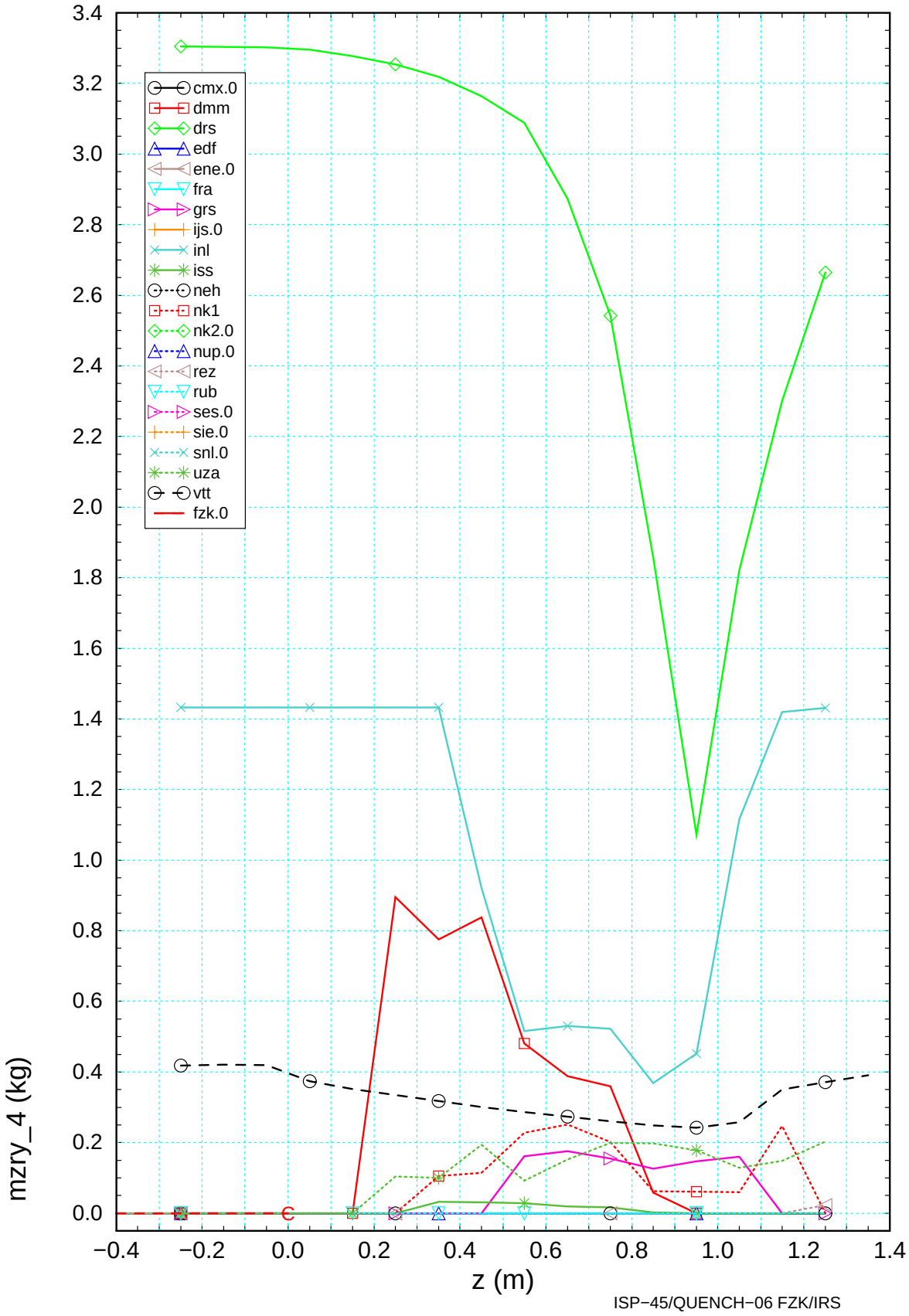

Figure 8.41 Axial distribution of metallic Zircaloy mass calculated by the participants for t=8000 s.

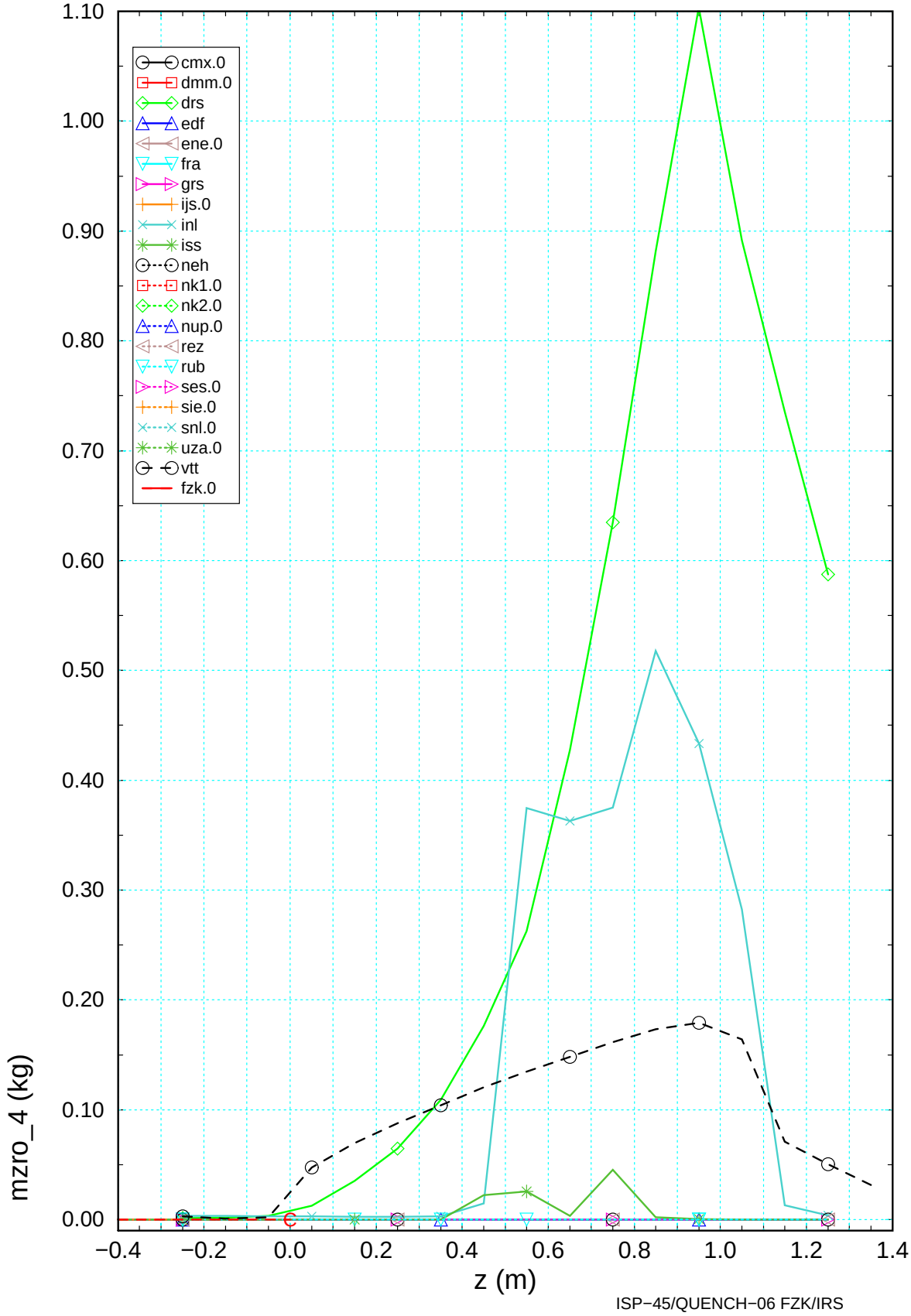

Figure 8.42 Axial distribution of Zirconium dioxide mass calculated by the participants for t=8000 s.